Microtechnology and MEMS

Zhong Lin Wang

Piezotronics and Piezo-Phototronics

Springer

Microtechnology and MEMS

Series Editors

Professor Dr. Hiroyuki Fujita
Institute of Industrial Science, University of Tokyo, Tokyo, Japan

Professor Dr. Dorian Liepmann
Department of Bioengineering, University of California, Berkeley, USA

For further volumes:
www.springer.com/series/4526

The series Microtechnology and MEMS comprises text books, monographs, and state-of-the-art reports in the very active field of microsystems and microtechnology. Written by leading physicists and engineers, the books describe the basic science, device design, and applications.Theywill appeal to researchers, engineers, and advanced students.

Zhong Lin Wang

Piezotronics and Piezo-Phototronics

Springer

Zhong Lin Wang
School of Materials Science
Georgia Institute of Technology
Atlanta, USA
and
Beijing Institute of Nanoenergy
and Nanosystems
Chinese Academy of Sciences
Beijing, China

ISSN 1615-8326 Microtechnology and MEMS
ISBN 978-3-642-34236-3 ISBN 978-3-642-34237-0 (eBook)
DOI 10.1007/978-3-642-34237-0
Springer Heidelberg New York Dordrecht London

Library of Congress Control Number: 2012955558

© Springer-Verlag Berlin Heidelberg 2012
This work is subject to copyright. All rights are reserved by the Publisher, whether the whole or part of the material is concerned, specifically the rights of translation, reprinting, reuse of illustrations, recitation, broadcasting, reproduction on microfilms or in any other physical way, and transmission or information storage and retrieval, electronic adaptation, computer software, or by similar or dissimilar methodology now known or hereafter developed. Exempted from this legal reservation are brief excerpts in connection with reviews or scholarly analysis or material supplied specifically for the purpose of being entered and executed on a computer system, for exclusive use by the purchaser of the work. Duplication of this publication or parts thereof is permitted only under the provisions of the Copyright Law of the Publisher's location, in its current version, and permission for use must always be obtained from Springer. Permissions for use may be obtained through RightsLink at the Copyright Clearance Center. Violations are liable to prosecution under the respective Copyright Law.
The use of general descriptive names, registered names, trademarks, service marks, etc. in this publication does not imply, even in the absence of a specific statement, that such names are exempt from the relevant protective laws and regulations and therefore free for general use.
While the advice and information in this book are believed to be true and accurate at the date of publication, neither the authors nor the editors nor the publisher can accept any legal responsibility for any errors or omissions that may be made. The publisher makes no warranty, express or implied, with respect to the material contained herein.

Printed on acid-free paper

Springer is part of Springer Science+Business Media (www.springer.com)

Preface

The fundamental principles of piezotronics and piezo-phototronics were introduced by my group in 2007 and 2010, respectively. Due to the polarization of ions in a crystal that has non-central symmetry in materials such as the wurtzite structured ZnO, GaN, and InN, a piezoelectric potential *(piezopotential)* is created in the crystal by applying a stress. Owing to the simultaneous possession of piezoelectricity and semiconductor properties, the piezopotential created in the crystal has a strong effect on the carrier transport at the interface/junction. *Piezotronics* concerns the devices fabricated using the piezopotential as a "gate" voltage to tube/control charge carrier transport at a contact or junction. The *piezo-phototronic effect* is to use the piezopotential to control the carrier generation, separation, transport, and/or recombination for improving the performance of optoelectronic devices, such as photon detector, solar cell, and LED. The functionality offered by piezotronics and piezo-phototronics are complementary to CMOS technology. By an effective integration of piezotronic and piezo-phototronic devices with silicon-based CMOS technology, some unique applications can be found in areas such as human–computer interfacing, sensing and actuating in nanorobotics, smart and personalized electronic signatures, smart MEMS/NEMS, nanorobotics, and energy sciences. This book introduces the fundamentals of piezotronics and piezo-phototronics.

I would like to thank my group members and collaborators who contributed to the development of piezotronics and piezo-phototronics (not in particular order): Jun Zhou, Wenzhuo Wu, Youfan Hu, Qing Yang, Yan Zhang, Ying Liu, Xudong Wang, Caofeng Pan, Jr-Hau He, Yifan Gao, Xiaonan Wen, Weihua Han, Yusheng Zhou and many others. We acknowledge generous financial support from DARPA, NSF, DOE, NASA, Airforce, NIH, Samsung, MANA NIMS, Chinese Academy of Sciences, and Chinese Scholars Council. I like to thank Georgia Tech and the Center for Nanostructure Characterization (CNC) for support in facility and infrastructure.

Lastly and most importantly, I thank my wife and our daughters for their years of support and understanding. It would not have been possible to carry out such a research without their support.

Atlanta — Zhong Lin Wang

Contents

Chapter 1
Introduction of Piezotronics and Piezo-Phototronics

Abstract Starting from the road map for microelectronics, the focus of future electronics will be on functionalities toward personal, portable, polymer, sensor, and self-powering applications. The integration of these characteristics with the fast speed and high density as defined by Moore's law will lead to the development of smart systems and self-powered systems. This chapter first introduces the basic physics of piezotronics and piezo-phototronics from band structure theory. Then blue-prints for future impacts and applications of piezotronics and piezo-phototronics are presented. The role anticipated to be played by piezotronics in the era of "Beyond Moore" is similar to the mechanosensation in physiology that provides a direct human "interfacing" with CMOS technology. It presents a paradigm shift for developing revolutionary technologies for force/pressure triggered/controlled electronic devices, sensors, MEMS, human–computer interfacing, nanorobotics, touch-pad, solar cell, photon detector and light-emitting diodes.

1.1 Beyond Moore's Law with Diversity and Multifunctionality

Moore's law has been the roadmap that directs and drives the information technology in the last few decades. With the density of devices on a single silicon chip doubles every 18 months, increasing CPU speed and building a system on a chip are the major developing directions for IT technology. With the line width reaching close to 10 nm, a general question is how small a device can we fabricate at industrial scale? What are the pros and cons with respect to stability and liability when devices get extraordinarily small? Is the speed the only driving parameter that we should look for? We know that Moore's law will reach its limit one day, and it is just a matter of time. Then, the question is: what should we look for beyond Moore's law?

Sensor network and personal health care have been predicted as the major driving force for the near term industry. As we have observed in today's electronic products, electronics is moving toward personal electronics, portable electronics and polymer-based flexible electronics. We are looking for multifunctionality and diversity associated with electronics. Take a cell phone as an example, having a super fast computer in a cell phone may not be the major drive for future markets, but the consumers are looking for more functionality, such as health care sensors for blood

Z.L. Wang, *Piezotronics and Piezo-Phototronics*, Microtechnology and MEMS,
DOI 10.1007/978-3-642-34237-0_1, © Springer-Verlag Berlin Heidelberg 2012

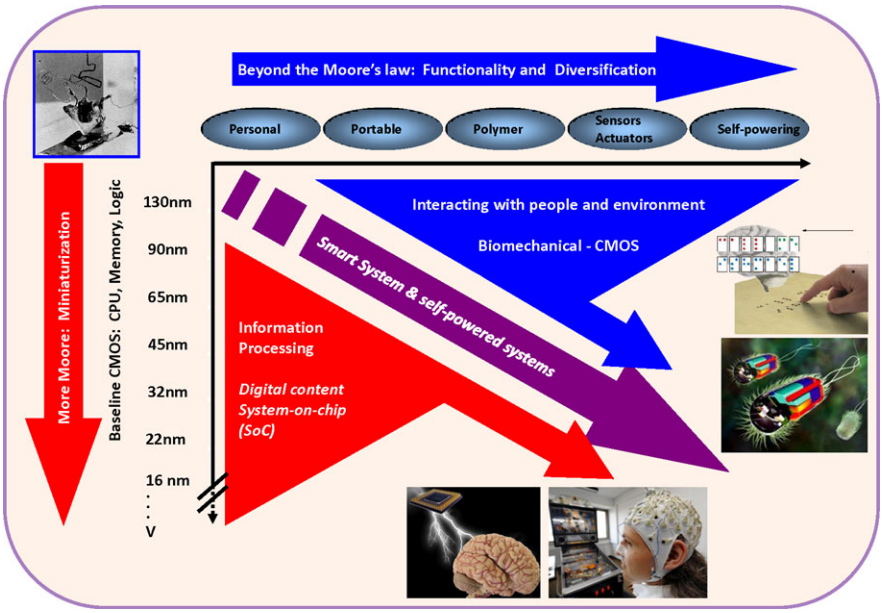

Fig. 1.1 Future perspective of electronics beyond Moore's law. The *vertical axis* represents a miniaturization and increase of device density, CPU speed and memory. The *horizontal axis* represents the diversity and functionality for personal and portable electronics. The future of electronics is an integration of CPU speed and functionality. It is anticipated that an integration of mechanical action through piezotronics in electronic systems is an important aspect of interfacing human and CMOS technologies

pressure, body temperature and blood sugar level, interfacing with environment with sensors for detecting gases, UV, and hazardous chemicals. In such a case, the IT technology is developing along another dimension, as presented in Fig. 1.1. A conjunction of speed and functionality will be the future trend of electronics. The near future development of electronics is moving toward personal, portable and (flexible or organic) polymer-based electronics with the integration of multifunctional sensors and self-powering technology. The goal is to directly interfacing with human and the environment in which we live in. A combination of CPU speed, density of memory and logic with the functionality tends to drive the electronics toward smart systems and self-powered systems, which are believed to be the major roadmaps for electronics.

1.2 Interfacing Human with Machine

Once we interface human with electronics, we are inevitably have to consider human activities and the "signals" generated by a human, which are mostly mechanical actions and a small portion of electrical signals. Electric signals transmitted

by neuron system have been studied for decades and various approaches have been developed to interface neuron signals with silicon-based technologies using field effect transistors. Mechanical actions, however, is not easy to directly interface with silicon technologies without innovative design and approaches. The most conventional approach is to use sensors that are sensitive to strain variation. The signals from sensors can be detected and recorded by conventional electronics, which is so called passive detection, but they are unable to be used to control Si electronics. The current on-going research in flexible electronics is to minimize and eliminate the effect of strain introduced by the substrate on the performance of the electronic components built on a substrate, which can be termed the *passive* flexible electronics. On the other hand, we can utilize the deformation introduced by the substrate to induce electrical signals that can be used directly for controlling Si-based electronics. A "mediator" or "translator" is needed for conjunction of biomechanical action with the operation of silicon-based electronics. Piezotronics and piezo-phototronics were invented for such purposes, and they are considered as the *active* flexible electronics or bio-driven electronics. This is an approach for directly generating digital signals and control using mechanical actions.

The role anticipated to be played by piezotronics is similar to the mechanosensation in physiology [1]. Mechanosensation is a response mechanism to mechanical stimuli. The physiological foundation for the senses of touch, hearing and balance, and pain is the conversion of mechanical stimuli into neuronal signals; the former is mechanical actuation and the latter is electrical stimulation. Mechanoreceptors of the skin are responsible for touch. Tiny cells in the inner ear are responsible for hearing and balance.

1.3 Piezopotential—The Fundamental Physics for Piezotronics and Piezo-Phototronics

Piezoelectricity, a phenomenon known for centuries, is an effect that is about the production of electrical potential in a substance as the pressure on it changes. The most well-known material that has piezoelectric effect is the provskite structured $Pb(Zr, Ti)O_3$ (PZT), which has found huge applications in electromechanical sensors, actuators, and energy generators. But PZT is an electric insulator and it is less useful for building electronic devices. Piezoelectricity has its own field and is being largely studied in the ceramic community. Wurtzite structures, such as ZnO, GaN, InN, and ZnS, also have piezoelectric properties but they are not extensively used as much as PZT in piezoelectric sensors and actuators due to their small piezoelectric coefficient. Therefore, the study of wurtzite structures is mainly in the electronic and photonic community due their semiconductor and photon excitation properties.

Silicon-based CMOS technology is operated by electrical driven charge transport process. To directly control the operation of CMOS by mechanical action, one must find an electric signal that can be generated as a result of mechanical action. The most nature choice is piezoelectricity. As for this purpose, we choose the Wurtzite

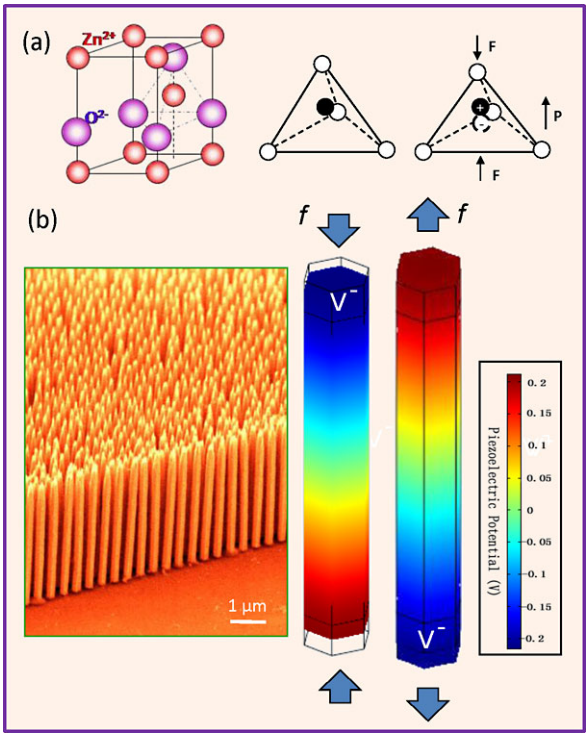

Fig. 1.2 Piezopotential in wurtzite crystal. (**a**) Atomic model of the wurtzite-structured ZnO. (**b**) Aligned ZnO nanowire arrays by solution based approach. Numerical calculated distribution of piezoelectric potential along a ZnO NW under axial strain. The growth direction of the NW is c-axis. The dimensions of the NW are $L = 600$ nm and $a = 25$ nm; the external force is $f_y = 80$ nN

materials, such as ZnO, GaN, InN, and ZnS, which simultaneously have piezoelectric and semiconductor properties. ZnO, for example, has a non-central symmetric crystal structure, which naturally produces piezoelectric effect once the material is strained. Wurtzite crystal has a hexagonal structure with a large anisotropic property in c-axis direction and perpendicular to the c-axis. Simply, the Zn^{2+} cations and O^{2-} anions are tetrahedrally coordinated and the centers of the positive ions and negatives ions overlap with each other. If a stress is applied at an apex of the tetrahedron, the center of the cations and the center of anions are relatively displaced, resulting in a dipole moment (Fig. 1.2(a)). A constructive add-up occurs of the dipole moments created by all of the units in the crystal results in a macroscopic potential drop along the straining direction in the crystal. This is the piezoelectric potential (*piezopotential*) (Fig. 1.2(b)) [2]. Piezopotential can serve as the driving force for the flow of electrons in the external load once subject to mechanical deformation, which is the fundamental of the nanogenerator [3–6].

The distribution of piezopotential in a c-axis ZnO nanowire (NW) has been calculated using the Lippman theory [7–9] without considering the doping in ZnO. For a NW with a length of 1200 nm and a hexagonal side length of 100 nm, a tensile force of 85 nN creates a potential drop of approximately 0.4 V between the two ends, with the $+c$ side positive (Fig. 1.2(b)). When the applied force changes to a compressive strain, the piezoelectric potential reverses with the potential difference

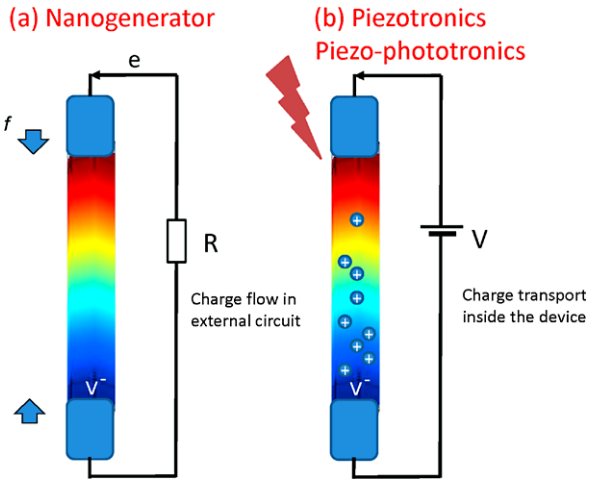

Fig. 1.3 Piezopotential created inside a nanostructure, as represented by the color code, is the fundamental physics for nanogenerator and piezotronics. (**a**) Nanogenerator is based on a process of piezopotential driven flow of electrons in the external load. (**b**) Piezotronics is about the devices fabricated using a process of piezopotential tuned/controlled charge carrier transport at the metal–semiconductor interface or p–n junction. Piezo-phototronics is about the devices fabricated using piezopotential to control charge carrier generation, separation, transport and recombination processes at the interface/junction

remaining 0.4 V but with the $-c$-axis side at a higher potential. The creation of this inner crystal potential is the core of piezotronics.

The presence of the piezopotential in the crystal has created a few new research fields. A nanogenerator has been developed for converting mechanical energy into electricity [10–13]. Once a strained piezoelectric crystal is connected at its two polar ends to an external electric load, the piezopotential creates a drop in the Fermi levels at the two contact ends, thus, the free electrons in the external load are driven to flow from one side to the other to "screen" the local piezopotential and reach a new equilibrium. The generated current in the load is a result of the transient flow of electrons. An alternating flow of electrons is possible if the piezopotential is continuously changed by applying a dynamic stress across the crystal. This means that the nanogenerator gives continuous output power if the applied stress is varying, which means inputting mechanical work (Fig. 1.3(a)). The nanogenerator has been extensively developed and it is now gives an output of ~3 V, and the output power is capable to drive a liquid crystal display (LCD), light-emitting diode and laser diode [14–17]. The nanogenerator will play an important role in energy harvesting as the sustainable and self-sufficient power source for micro/nanosystems.

1.4 Coining the Field of Piezotronics

In 2006, two independent research experiments were carried out in Wang's group. The first group of experiment was to measure the electric transport of a long ZnO

wire, the two ends of which were completely enclosed by electrodes, as its shape being bent inside a scanning electron microscopy (SEM) [18]. A dramatic drop in electric conductance was obtained as the degree of bending increased. The interpretation was that a piezoelectric potential drop was created across the wire when it is bent, which acted as a gate voltage for controlling the transport of charge carriers through the wire. This is referred to piezoelectric field effect transistor (PE-FET).

The second experiment was about a two-probe manipulation of a single ZnO NW and measurement of its transport property [19]. One probe held one end of a nanowire (NW) that laid on an insulator substrate, the other probe pushed the NW from the other end by in-contact with the tensile surface of the NW. The tungsten tips had Ohmic contact with the NW. The I–V curve changed from a linear shape to a rectifying behavior with the increase of the degree of NW bending. This phenomenon was interpreted as a result of creating a positive piezopotential at the interface region, which served as potential barrier for blocking the flow of electrons to one direction. This is the piezoelectric-diode (PE-diode).

Both the PE-FET and PE-diode were based on the presence of a strain induced piezoelectric potential in the NW. The induced flow of electrons in the external circuit by the piezoelectric potential is the energy generation process. The presence of the piezopotential can drastically change the transport characteristic of a NW-based FET. To systematically represent the piezoelectric-semiconductor coupled properties of such a system, Wang introduced the concept of nano-piezotronics on Nov. 24, 2006 and publicly disclosed it in the MRS fall conference in Boston a few days later [20]. Then, Wang first coined the word of piezotronics in a short paper published in 2007 [21, 22]. The basis of piezotronics is to use piezopotential to tune and control the transport of the carriers inside the nanowire (Fig. 1.3(b)). Ever since then, dramatic progress has been made in piezotronics, which will be described in the following chapters.

1.5 Piezotronic Effect

A most simple FET is a two ends bonded semiconductor wire, in which the two electric contacts at the ends are the source and drain, and the gate voltage can be applied either at the top of the wire through a gate electrode or at its bottom on the substrate. By applying a source to drain driving voltage, V_{ds}, the charge carrier transport process in the semiconductor device is tuned/gated by the gate voltage V_g, which is an externally applied potential.

Alternatively, the gate voltage can be replaced by the piezopotential generated inside the crystal (inner potential), so that the charge carrier transport process in FET can be tuned/gated by applying a stress to the device [20]. This type of devices is called piezotronic devices as triggered or driven by a mechanical deformation action. When a ZnO NW is strained axially along its length, two typical effects are observed. One is the *piezoresistance effect*, which is introduced because of the change in bandgap and possibly density of states in the conduction band. This effect

has no polarity so that it has equivalent/identical effect on the source and drain of the FET. On the other hand, piezopotential is created along its length. For an axial strained NW, the piezoelectric potential continuously drops from one side of the NW to the other, which means that the electron energy continuously increases from the one side to the other. Meanwhile, the Fermi level will be flat all over the NW when equilibrium is achieved, since there is no external electrical field. As a result, the effective barrier height and/or width of the electron energy barrier between ZnO and metal electrode will be raised at one side and lowered at the other side, thus, it has a non-symmetric effect on the barrier heights at the source and drain. Therefore, *piezotronic effect* is to use piezopotential to tune/control the charge transport across an interface/junction [22, 23].

1.5.1 Piezotronic Effect on Metal–Semiconductor Contact

A better understanding about the piezotronic effect is to compare it with the most fundamental structure in semiconductor devices: Schottky contact and p–n junction. When a metal and a n-type semiconductor forms a contact, a Schottky barrier (SB) ($e\phi_{SB}$) is created at the interface if the work function of the metal is appreciably larger than the electron affinity of the semiconductor (Fig. 1.4(a)). Current can only pass through this barrier if the applied external voltage is larger than a threshold value (ϕ_i) and its polarity is with the metal side positive (for n-type semiconductor). If a photon excitation is introduced, the newly generated electron–hole pairs not only largely increase the local conductance, but also the effective height of the SB is reduced as a result of charge redistribution at the interface (Fig. 1.4(b)).

Once a strain is created in the semiconductor that also has piezoelectric property, a negative piezopotential at the semiconductor side effectively increases the local SB height to $e\phi'$ (Fig. 1.4(c)), while a positive piezopotential reduces the barrier height. The polarity of the piezopotential is dictated by the direction of the c-axis for ZnO. The role played by the piezopotential is to effectively change the local contact characteristics through an internal field, thus, the charge carrier transport process is tuned/gated at the metal–semiconductor (M–S) contact.

Strain in the structure would produce piezo-charges at the interfacial region. It is important to note that the polarization charges are distributed within a small depth from the surface and they are ionic charges, which are non-mobile charges located adjacent to the interface. In such a case, free carriers can only partially screen the piezo-charges due to the finite dielectric permittivity of the crystal and the limited doping concentration, but they cannot completely cancel the piezo-charges. The piezo-charges may produce mirror charges at the meal side. The positive piezo-charges effectively may lower the barrier height at the local Schottky contact, while the negative piezo-charges increase the barrier height (Fig. 1.5(b) and (c)). The role played by the piezopotential is to effectively change the local contact characteristics through an internal field depending on the crystallographic orientation of the material and the sign of the strain, thus, the charge carrier transport process is

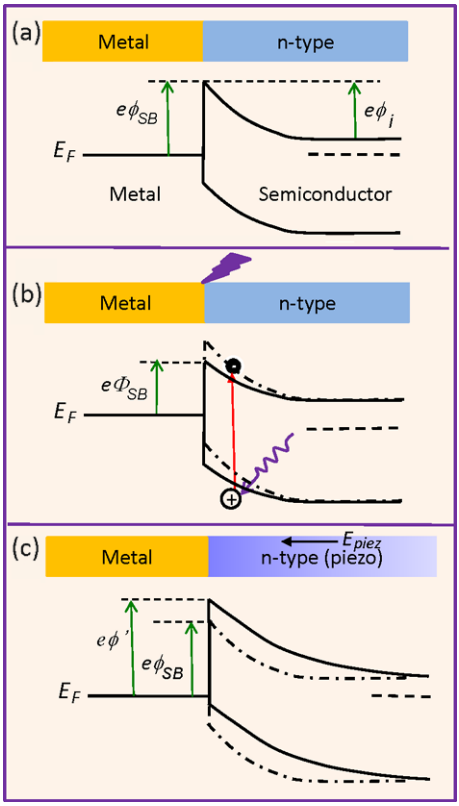

Fig. 1.4 Energy band diagram for illustrating the effects of laser excitation and piezoelectricity on a Schottky contacted metal–semiconductor interface. (**a**) Band diagram at a Schottky contacted metal–semiconductor interface. (**b**) Band diagram at a Schottky contact after exciting by a laser that has a photon energy higher than the bandgap, which is equivalent to a reduction in the Schottky barrier height. (**c**) Band diagram at the Schottky contact after applying a strain in the semiconductor. The piezopotential created in the semiconductor has a polarity with the end in contacting with the metal being low

tuned/gated at the M–S contact. Therefore, the charge transport across the interface can be largely dictated by the created piezopotential, which is the gating effect. With considering the change in piezopotential polarity by switching the strain from tensile to compressive, the local contact characteristics can be tuned and controlled by the magnitude of the strain and the sign of strain. These are the cores of the piezotronic effect.

1.5.2 Piezotronic Effect on p–n Junction

When a p-type and a n-type semiconductors form a junction, the holes in the p-type side and the electrons in the n-type side tend to redistribute to balance the local potential, the interdiffusion and recombination of the electrons and holes in the junction region forms a charge depletion zone. The presence of such a carrier-free zone can significantly enhance the piezoelectric effect, because the piezo-charges will be mostly preserved without being screened by local residual free carriers. As shown in Fig. 1.5(d), for a case that the p-type side is piezoelectric and a strain is applied, local net negative piezo-charges are preserved at the junction provided

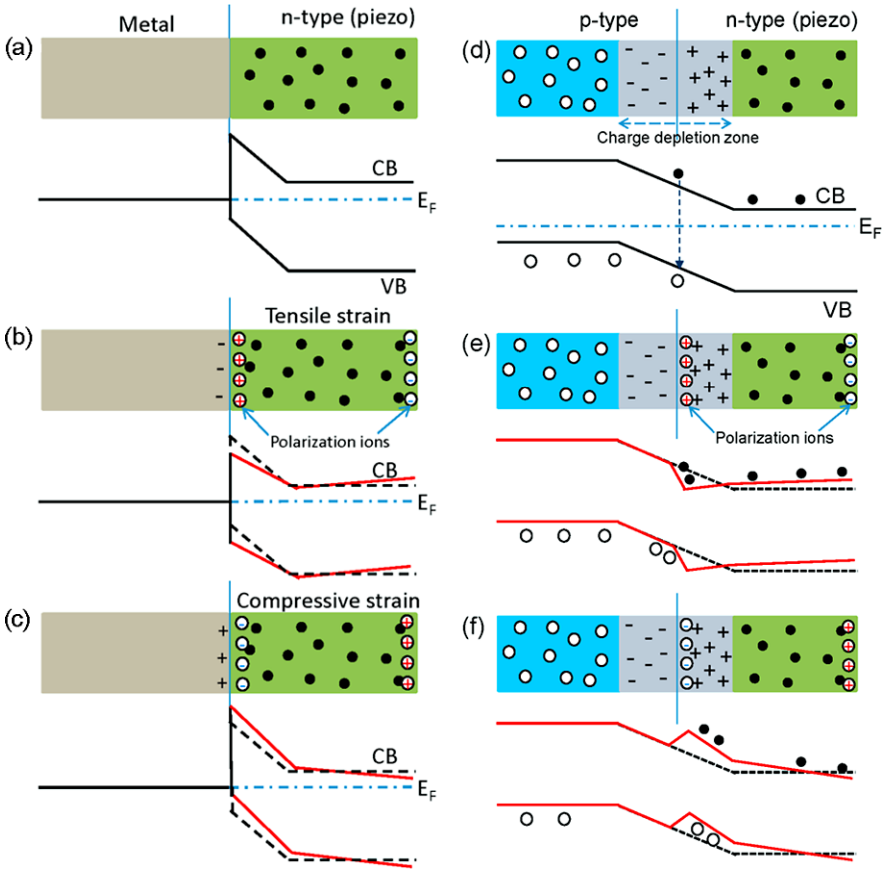

Fig. 1.5 (**a**)–(**c**) Energy band diagram for illustrating the effects of piezoelectric polarization charges on a Schottky contacted metal–semiconductor interface without and with the presence of non-mobile, ionic charges at the metal–semiconductor interface. The piezoelectric charges are indicated at the interface. (**d**)–(**f**) Energy band diagram for illustrating the effect of piezoelectricity on a p–n junction that is made of two materials of similar bandgaps. The distorted band with the presence of piezoelectric charges is indicated by *red lines*

the doping is relatively low so that the local free carriers are not enough to fully screen the piezo-charges. The piezopotential tends to raise the local band slightly and introduce a slow slope to the band structure. Alternatively, if the applied strain is switched in sign (Fig. 1.5(e)), the positive piezo-charges at the interface creates a dip in the local band. A modification in the local band may be effective for trapping the holes so that the electron–hole recombination rate can be largely enhanced, which is very beneficial for improving the efficiency of an LED. Furthermore, the inclined band tends to change the mobility of the carriers moving toward the junction.

With the creation of a piezopotential in one side of the semiconductor material under strain, the local band structure near the p–n junction is changed/modified. For

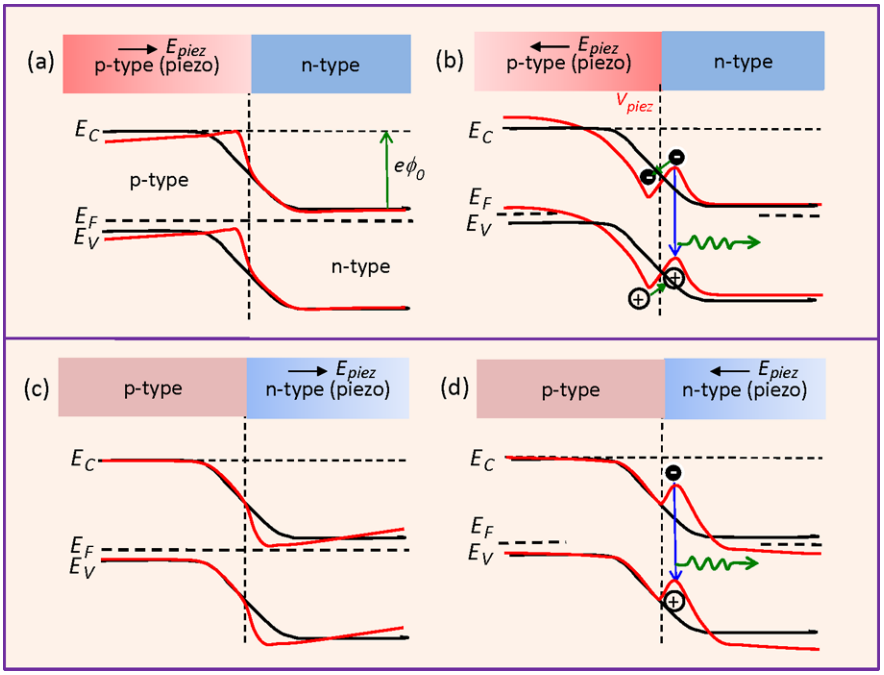

Fig. 1.6 Energy band diagram for illustrating the effect of piezoelectricity on a p–n junction that is made of two materials of similar bandgaps. The band diagrams for the p–n junction with and without the presence of piezoelectric effect for the four possible cases are shown using *dark* and *red curves*, respectively. The bandgap for the n-type and p-type are assumed to be about equal. The effect of reversal in polarity is presented

easy understanding, we include the screening effect of the charge carriers to the piezopotential in the discussion, which means that the positive piezopotential side in n-type material is largely screened by the electrons, while the negative piezopotential side is almost unaffected. By the same token, the negative piezopotential side in p-type material is largely screened by the holes, but leaves the positive piezopotential side almost unaffected. As shown in Fig. 1.6(b) for a case that the p-type side is piezoelectric and a strain is applied, the local band structure is largely changed, which significantly affects the characteristic of charge carriers flow through the interface. This is the core of the piezotronic effect.

In addition, the holes on the p-type side can drift to the n-type side to combine with the electrons in the conduction band, possibly resulting in an emission of photon. This is a process of piezopotential induced photon emission, e.g., *piezophotonics*. The following conditions may need to be met in order to observe the piezophotonic process. The magnitude of the piezopotential has to be significantly large in comparison to ϕ_i, so that the local piezoelectric field is strong enough to drive the diffusion of the holes across the p–n junction. The straining rate for creating the piezopotential has to be rather large, so that the charge carriers are driven across the interface within a time period shorter than the time required for charge recombina-

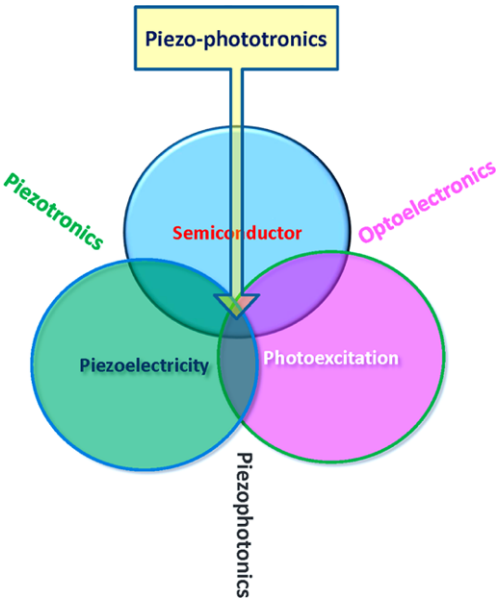

Fig. 1.7 Schematic diagram showing the three-way coupling among piezoelectricity, photoexcitation and semiconductor, which is the basis of piezotronics (piezo-electricity–semiconductor coupling), piezophotonics (piezoelectric–photon excitation coupling), optoelectronics, and piezo-phototronics (piezoelectricity–semicon-ductor–photoexcitation). The core of these coupling relies on the piezopotential created by the piezoelectric materials

tion. The width of the depletion layer has to be small so that there are enough charge carriers available in the acting region of the piezopotential. Finally, a direct bandgap material is beneficial for the observation of the phenomenon.

The fundamental working principles of the p–n junction and the Schottky contact are that there is an effective barrier that separates the charge carriers at the two sides to across. The height and width of the barrier are the characteristic of the device. In piezotronics, the role played by the piezopotential is to effectively change the width of p–n junction or height of SB by piezoelectricity.

1.6 Piezo-Phototronic Effect

Piezophototronics was first coined in 2010 [24–26]. For a material that simultaneously has semiconductor, photon excitation and piezoelectric properties, besides the well-known coupling of semiconductor with photon excitation process to form the field of optoelectronics, additional effects could be proposed by coupling a semiconductor with piezoelectric to form a field of piezotronics, and piezoelectric with photon excitation to form a field of piezophotonics. Furthermore, a coupling among semiconductor, photon excitation and piezoelectric is a field of *piezo-phototronics*, which can be the basis for fabricating piezo-photonic–electronic nanodevices. The *piezo-phototronic effect* is to use the piezopotential to tune/control the charge generation, separation, transport and/or recombination at an interface/junction for achieving superior optoelectronic processes (Fig. 1.7).

1.7 One-Dimensional Wurtzite Nanostructures for Piezotronics

The principles illustrated for piezotronics and piezo-phototronics apply to both of thin film and NWs. But the NWs are of great advantageous than thin films for the following reasons. First, ZnO NWs can be grown using a chemical approach at low temperature (<100 °C) on any substrate and any shape substrate, exhibiting a huge advantage for scaling up at a low cost; while it is practically difficult to make high quality single crystal thin film at low temperature. Secondly, owing to the largely reduced size, NWs exhibit extremely high elasticity that allows large degrees of mechanical deformation (up to 6 % in tensile strain according to theoretical calculation for very small wire [27]) without cracking or fracture, while thin film can easily generate cracks after applying even smaller strain. Third, the small size of the NWs largely increases the toughness and robustness of the structure so that it is almost fatigue free. Fourth, a relatively small force is required to induce the mechanical agitation, so that it can be very beneficial for building ultrasensitive devices. Finally, NWs may exhibit higher piezoelectric coefficient than thin film [28].

One-dimensional nanomaterials, such as nanowires and nanobelts, are ideal for piezotronics and piezo-phototronics, because they can tolerate a large mechanical strain. ZnO, GaN, InN and possibly doped PZT materials are potential candidate for piezotronics. Currently, the most popular structure is ZnO NWs for three main reasons. First, ZnO NWs can be easily grown at a large quantity using vapor-solid process or chemical approach at low temperature. Secondly, they are biological compatible and environmentally friendly. Finally, they can be grown on substrate and any shape substrate. The vapor-solid growth usually takes place in a tube furnace by vaporizing ZnO powders with the presence of carbon at a temperature of ~900 °C. Patterned growth is possible with the introduction of Au catalyst. Pulse laser deposition (PLD) can be used for NW growth. A KrF excimer laser (248 nm) was used as the ablation source to focus on a ceramic target, which is a stack of ZnO powder. A control of pressure can give nice NW array (Fig. 1.8(a)).

The most commonly used chemical agents for the hydrothermal synthesis of ZnO NWs are zinc nitrate hexahydrate and hexamethylenetetramine [29, 30]. Zinc nitrate hexahydrate salt provides Zn^{2+} ions, required for building up ZnO NWs. Water molecules in the solution provide O^{2-} ions. Even though the exact function of hexamethylenetetramine during the ZnO NW growth is still unclear, it is believed to act as a weak base, which would slowly hydrolyze in the water solution and gradually produce OH^{-}. This is critical in the synthesis process because, if the hexamethylenetetramine hydrolyzes very fast and produces a lot of OH^{-} in a short period of time, the Zn^{2+} ions in solution would precipitate out very quickly due to the high pH environment. Using a pattern generated by laser interference, well aligned NW arrays have been grown at a temperature around 85 °C (Fig. 1.8(b)).

NWs grown by vapor phase technique at high temperature usually have low defects and they are most adequate for studying piezotronic and piezo-phototronic effects [31, 32]. A treatment in oxygen plasmon can effectively reduce the vacancy concentration. The low-temperature chemically grown NWs have a relatively high concentration of defects, and they are most useful for piezoelectric nanogenerators.

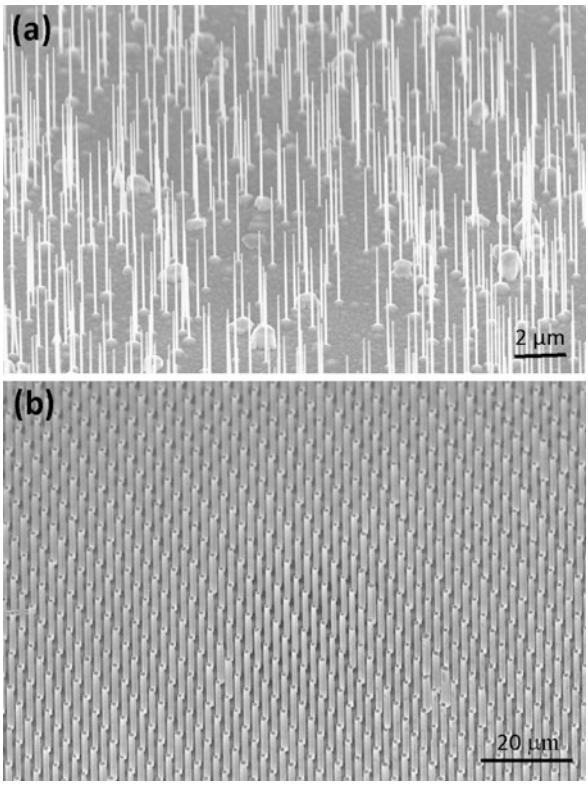

Fig. 1.8 ZnO nanowire arrays grown by (**a**) pulse laser deposition technique and (**b**) low-temperature solution based approach

1.8 Perspective

Today's electronics and optoelectronics are mostly based on Si, II–VI and III–V compound semiconductor materials, with focuses on CMOS technology, LED, photon detector and solar cell. Piezoelectricity, on the other hand, relies on PZT type of provskite materials, which are rarely used for electronics and optoelectronics. Owing to the gigantic difference in materials systems, the overlap between piezoelectricity and optoelectronics is rather limited. With the use of wurtzite materials, such as ZnO, GaN and InN, which simultaneously have piezoelectric and semiconductor properties, we have coupled piezoelectricity with optoelectronic excitation processes and coined a few new fields (Fig. 1.9). The core relies on piezopotential that is created in a piezoelectric material by applying a stress, and it is generated by the polarization of ions in the crystal. *Piezotronics* is about the devices fabricated using the piezopotential as a "gate" voltage to tube/control charge carrier transport at a contact or junction. *Piezo-phototronic effect* is to use the piezopotential to control the carrier generation, separation, transport, and/or recombination for improving the performance of optoelectronic devices, such as photon detector, solar cell and LED.

Z.L. Wang's group has devoted over 12 years for studying ZnO nanostructures and its wide range of applications. Our systematic studies and the field coined can

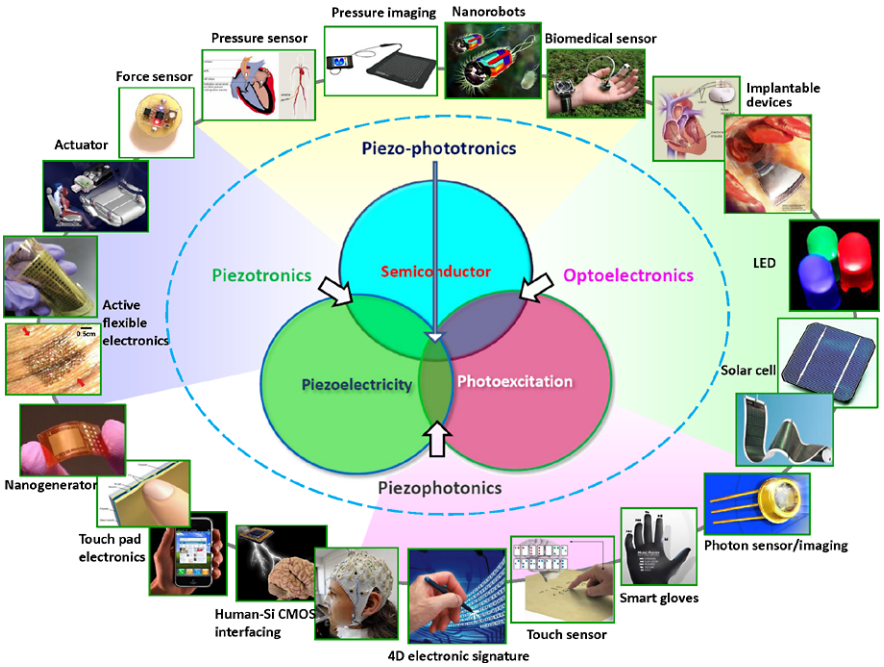

Fig. 1.9 Potential and perspective applications of piezotronics, piezo-phototronics, and nanogenerators [6], which are important future directions and fields in near future. *Middle*: schematic diagram showing the three-way coupling among piezoelectricity, photoexcitation and semiconductor, which is the basis of piezotronics (piezoelectricity–semiconductor coupling), piezophotonics (piezoelectric–photon excitation coupling), optoelectronics, and piezophototronics (piezoelectricity–semiconductor–photoexcitation)

be summarized using a "tree" structure, as shown in Fig. 1.10. The fundamental "root" of all these fields is: piezopotential and semiconductor as the basic physics, and wurtzite structure as the fundamental materials system; the "branches" are the fields we have coined; and the "fruits" are the important applications. Furthermore, fundamental quantum phenomena possibly arising from nano-scale piezo-physics can be explored in near future. Besides the wurtzite family, we have doped provskite type structures, such as PZT, $BaTiO_3$, for such studies.

Piezotronics is likely to have important application in sensors, human–silicon technology interfacing, MEMS, nanorobotics and active flexible electronics. The role played by piezotronics in interfacing human–CMOS technology is similar to the mechanosensation in physiology. Mechanosensation is a response mechanism to mechanical stimuli. The physiological foundation for the senses of touch, hearing and balance, and pain is the conversion of mechanical stimuli into neuronal signals. We anticipate near future applications of piezotronics and piezo-phototronics in sensor network, bioscience, human–machine interfacing and integration, and energy sciences.

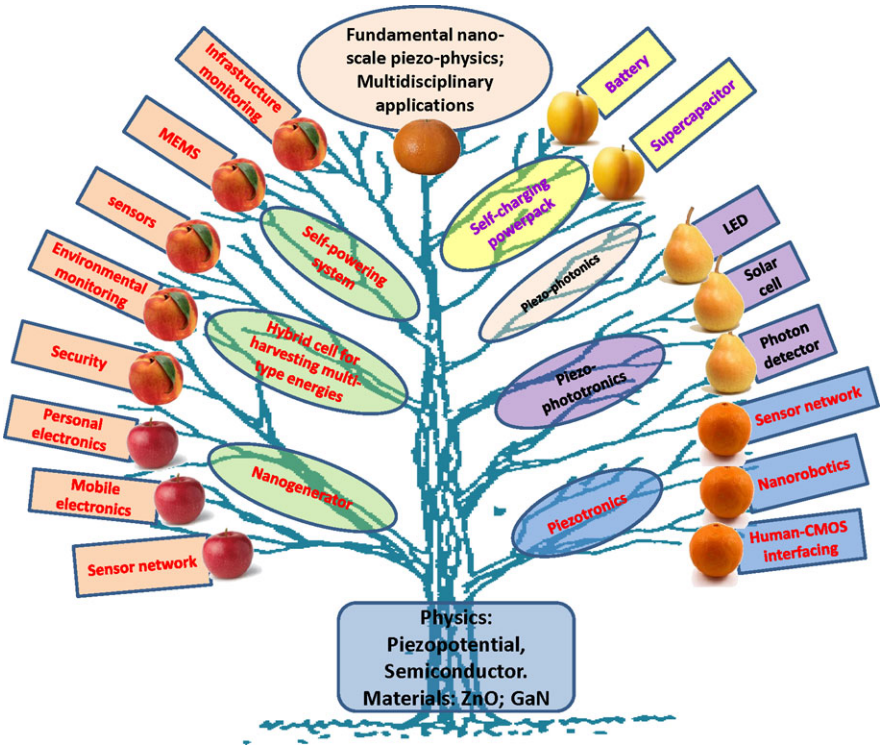

Fig. 1.10 A "tree" idea for summarizing the fields of nanogenerator, hybrid cell for harvesting multi-type energies [33–36], self-powered system [6], piezotronics, piezo-phototronics and possibly piezophotonics that have been developed by Wang's group in the last decade. The fundamental "root" of all these fields is: piezopotential and semiconductor as the basic physics, and ZnO as the fundamental materials system. All of the fields are derived based on these basics

References

1. http://en.wikipedia.org/wiki/Mechanosensation
2. Z.L. Wang, J.H. Song, Piezoelectric nanogenerators based on zinc oxide nanowire arrays. Science **312**, 242–246 (2006)
3. Z.L. Wang, Towards self-powered nanosystems: from nanogenerators to nanopiezotronics. Adv. Funct. Mater. **18**(22), 3553 (2008)
4. Z.L. Wang, ZnO nanowire and nanobelt platform for nanotechnology. Mater. Sci. Eng. Rep. **64**(3–4), 33–71 (2009)
5. Z.L. Wang, R.S. Yang, J. Zhou, Y. Qin, C. Xu, Y.F. Hu, S. Xu, Lateral nanowire/nanobelt based nanogenerators, piezotronics and piezo-phototronics. Mater. Sci. Eng. Rep. **70**(3–6), 320–329 (2010)
6. Z.L. Wang, Nanogenerators for self-powered devices and systems. Georgia Institute of Technology, SMARTech digital repository (2011). http://hdl.handle.net/1853/39262
7. Y.F. Gao, Z.L. Wang, Electrostatic potential in a bent piezoelectric nanowire. The fundamental theory of nanogenerator and nanopiezotronics. Nano Lett. **7**(8), 2499–2505 (2007)
8. Z.Y. Gao, J. Zhou, Y.D. Gu, P. Fei, Y. Hao, G. Bao, Z.L. Wang, Effects of piezoelectric potential on the transport characteristics of metal–ZnO nanowire–metal field effect transistor.

J. Appl. Phys. **105**(11), 113707 (2009)
9. C.L. Sun, J. Shi, X.D. Wang, Fundamental study of mechanical energy harvesting using piezoelectric nanostructures. J. Appl. Phys. **108**(3), 034309 (2010)
10. X.D. Wang, J.H. Song, J. Liu, Z.L. Wang, Direct-current nanogenerator driven by ultrasonic waves. Science **207**(316), 102–105 (2007)
11. Y. Qin, X.D. Wang, Z.L. Wang, Microfibre–nanowire hybrid structure for energy scavenging. Nature **451**, 809–813 (2008)
12. R.S. Yang, Y. Qin, L.M. Dai, Z.L. Wang, Power generation with laterally packaged piezoelectric fine wires. Nat. Nanotechnol. **4**, 34–39 (2009)
13. S. Xu, Y. Qin, C. Xu, Y.G. Wei, R.S. Yang, Z.L. Wang, Self-powered nanowire devices. Nat. Nanotechnol. **5**, 366–373 (2010)
14. G. Zhu, R.S. Yang, S.H. Wang, Z.L. Wang, Flexible high-output nanogenerator based on lateral ZnO nanowire array. Nano Lett. **10**(8), 3151–3155 (2010)
15. S. Xu, B.J. Hansen, Z.L. Wang, Piezoelectric-nanowire-enabled power source for driving wireless microelectronics. Nat. Commun. **1**, 93 (2010)
16. Y.F. Hu, Y. Zhang, C. Xu, L. Lin, R.L. Snyder, Z.L. Wang, Self-powered system with wireless data transmission. Nano Lett. **11**(6), 2572–2577 (2011)
17. Z.T. Li, Z.L. Wang, Air/liquid-pressure and heartbeat-driven flexible fiber nanogenerators as a micro/nano-power source or diagnostic sensor. Adv. Mater. **23**(1), 84–89 (2011)
18. X.D. Wang, J. Zhou, J.H. Song, J. Liu, N.S. Xu, Z.L. Wang, Piezoelectric field effect transistor and nanoforce sensor based on a single ZnO nanowire. Nano Lett. **6**(12), 2768–2772 (2006)
19. J.H. He, C.H. Hsin, L.J. Chen, Z.L. Wang, Piezoelectric gated diode of a single ZnO nanowire. Adv. Mater. **19**(6), 781–784 (2007)
20. Chemical and Engineering News, January 15 issue, p. 46 (2008). http://pubs.acs.org/cen/science/85/8503sci1.html
21. Z.L. Wang, Nanopiezotronics. Adv. Mater. **19**(6), 889–892 (2007)
22. Z.L. Wang, The new field of nanopiezotronics. Mater. Today **10**(5), 20–28 (2007)
23. Z.L. Wang, Piezopotential gated nanowire devices: piezotronics and piezo-phototronics. Nano Today **5**, 540–552 (2010)
24. Y.F. Hu, Y.L. Chang, P. Fei, R.L. Snyder, Z.L. Wang, Designing the electric transport characteristics of ZnO micro/nanowire devices by coupling piezoelectric and photoexcitation effects. ACS Nano **4**(2), 1234–1240 (2010)
25. Q. Yang, W.H. Wang, S. Xu, Z.L. Wang, Enhancing light emission of ZnO microwire-based diodes by piezo-phototronic effect. Nano Lett. **11**(9), 4012–4017 (2011)
26. Q. Yang, X. Guo, W.H. Wang, Y. Zhang, S. Xu, D.H. Lien, Z.L. Wang, Enhancing sensitivity of a single ZnO micro-/nanowire photodetector by piezo-phototronic effect. ACS Nano **4**(10), 6285–6291 (2010)
27. R. Agrawal, B. Peng, H.D. Espinosa, Experimental-computational investigation of ZnO nanowires strength and fracture. Nano Lett. **9**(12), 4177–4183 (2009)
28. M.H. Zhao, Z.L. Wang, S.X. Mao, Piezoelectric characterization of individual zinc oxide nanobelt probed by piezoresponse force microscope. Nano Lett. **4**(4), 587–590 (2004)
29. L. Vayssieres, Growth of arrayed nanorods and nanowires of ZnO from aqueous solutions. Adv. Mater. **15**(5), 464–466 (2003)
30. S. Xu, Z.L. Wang, One-dimensional ZnO nanostructures: solution growth and functional properties. Nano Res. **4**(11), 1013–1098 (2011)
31. Z.W. Pan, Z.R. Dai, Z.L. Wang, Nanobelts of semiconducting oxides. Science **291**, 1947–1949 (2001)
32. X.D. Wang, C.J. Summers, Z.L. Wang, Large-scale hexagonal-patterned growth of aligned ZnO nanorods for nano-optoelectronics and nanosensor arrays. Nano Lett. **4**(3), 423–426 (2004)
33. C. Xu, X.D. Wang, Z.L. Wang, Nanowire structured hybrid cell for concurrently scavenging solar and mechanical energies. J. Am. Chem. Soc. **131**(16), 5866–5872 (2009)
34. B.J. Hansen, Y. Liu, R.S. Yang, Z.L. Wang, Hybrid nanogenerator for concurrently harvesting biomechanical and biochemical energy. ACS Nano **4**(7), 3647–3652 (2010)

35. D. Choi, M.J. Jin, K.Y. Lee, M.J. Jin, S.G. Ihn, S. Yun, X. Bulliard, W. Choi, S.Y. Lee, S.W. Kim, J.Y. Choi, J.M. Kim, Z.L. Wang, Control of naturally coupled piezoelectric and photovoltaic properties for multi-type energy scavengers. Energy Environ. Sci. **4**(11), 4607–4613 (2011)
36. C.F. Pan, Z.T. Li, W.X. Guo, J. Zhu, Z.L. Wang, Fiber-based hybrid nanogenerators for/as self-powered systems in biological liquid. Angew. Chem., Int. Ed. Engl. **50**(47), 11192–11196 (2011)

Chapter 2
Piezopotential in Wurtzite Semiconductors

Abstract The most fundamental physics for piezotronics and piezo-phototronics is in the presence of a piezoelectric potential (piezopotential) in semiconductor structured materials, such as the wurtzite structure. This chapter introduces the fundamental theory for calculating the piezopotential distribution in nanostructures with and without considering the presence of doping. The finite conductivity possessed by the material can partially screen the regional piezopotential having an opposite polarity to the type of doping, but cannot completely cancel the polarization charge due to the dielectric property of the material and the moderate doping level. The effect of piezopotential on the local contact in electrical measurements is also discussed, and a through-end model is proposed for understanding the transport properties of nanowire-based devices. This model will be adopted in future chapters for understanding the I–V characteristics of the devices.

The core of piezotronics and piezo-phototronics relies on the piezoelectric potential (piezopotential) produced by piezoelectric effect in materials that simultaneously have piezoelectric, semiconductor and optoelectronic properties. Wurtzite family is an ideal system for this type of study, such as ZnO, GaN and InN. As a start, we first introduce the theory of piezoelectricity and calculation of the piezopotential. In the literature, numerous theories for 1D nanostructure piezoelectricity have been proposed, including first-principle calculations [1, 2], MD simulations [3] and continuum models [4]. However, first-principle theory and MD simulation are difficult to implement to nanopiezotronics system (the typical dimension of which is ~50 nm in diameter and ~2 micron in length) due to the huge number of atoms. The continuum model proposed by Michalski et al. is relevant in that it gives a criterion to distinguish between mechanically dominated regime and electrostatically dominated regime. In this section we propose a continuum model for the electrostatic potential in a laterally bent NW. A perturbation technique is introduced to solve the coupled differential equations, and the derived analytical equation gives a result that is within 6 % of that received from full numerical calculation. The theory directly establishes the physical basis of nanopiezotronics and nanogenerator as proposed previously.

Z.L. Wang, *Piezotronics and Piezo-Phototronics*, Microtechnology and MEMS,
DOI 10.1007/978-3-642-34237-0_2, © Springer-Verlag Berlin Heidelberg 2012

2.1 Governing Equations

Our theoretical objective is to derive the relationship between the potential distribution in a NW and the dimensionality of the NW and magnitude of the applied force at the tip. For this purpose, we start from the governing equations for a static piezoelectric material, which are three sets: mechanical equilibrium equation (see (2.1a) and (2.1b)), constitutive equation (see (2.2a), (2.2b) and (2.2c)), geometrical compatibility equation (see (2.3)) and Gauss equation of electric field (see (2.4)) [8]. The mechanical equilibrium condition when there is no body force $\vec{f}_e^{(b)} = 0$ acting on the nanowire is

$$\nabla \cdot \sigma = \vec{f}_e^{(b)} = 0 \tag{2.1a}$$

where σ is the stress tensor, which is related to strain ε, electric field $\vec{E}$ and electric displacement $\vec{D}$ by constitutive equations:

$$\begin{cases} \sigma_p = c_{pq}\varepsilon_q - e_{kp}E_k, \\ D_i = e_{iq}\varepsilon_q + \kappa_{ik}E_k. \end{cases} \tag{2.1b}$$

Here c_{pq} is the linear elastic constant, e_{kp} is the linear piezoelectric coefficient, and κ_{ik} is the dielectric constant. It must be pointed out that (2.1b) does not contain the contribution from the spontaneous polarization introduced by the polar charge on the $\pm(0001)$ polar surfaces [5], which are the top and bottom ends of the NW, respectively. The validity of this approximation will be elaborated later. To keep the notation compact, the so-called Nye two-index notation [6] is used. By considering the C_{6v} symmetry of a ZnO crystal (with wurtzite structure), c_{pq}, e_{kp} and κ_{ik} can be written as

$$c_{pq} = \begin{pmatrix} c_{11} & c_{12} & c_{13} & 0 & 0 & 0 \\ c_{12} & c_{11} & c_{13} & 0 & 0 & 0 \\ c_{13} & c_{13} & c_{33} & 0 & 0 & 0 \\ 0 & 0 & 0 & c_{44} & 0 & 0 \\ 0 & 0 & 0 & 0 & c_{44} & 0 \\ 0 & 0 & 0 & 0 & 0 & \frac{(c_{11}-c_{12})}{2} \end{pmatrix}, \tag{2.2a}$$

$$e_{kp} = \begin{pmatrix} 0 & 0 & 0 & 0 & e_{15} & 0 \\ 0 & 0 & 0 & e_{15} & 0 & 0 \\ e_{31} & e_{31} & e_{33} & 0 & 0 & 0 \end{pmatrix}, \tag{2.2b}$$

$$\kappa_{ik} = \begin{pmatrix} \kappa_{11} & 0 & 0 \\ 0 & \kappa_{11} & 0 \\ 0 & 0 & \kappa_{33} \end{pmatrix}. \tag{2.2c}$$

The compatibility equation is a geometrical constraint that must be satisfied by strain ε_{ij}:

$$e_{ilm}e_{jpq}\frac{\partial^2\varepsilon_{mp}}{\partial x_l \partial x_q} = 0. \tag{2.3}$$

In (2.3) the indices are in the normal definition and Nye notation is not used. e_{ilm} and e_{jpq} are Levi-Civita anti-symmetric tensors. For simplicity of the derivation, we assume that the NW bending is small.

Finally, by assuming no free charge $\rho_e^{(b)}$ in the nanowire, the Gauss equation must be satisfied:

$$\nabla \cdot \vec{D} = \rho_e^{(b)} = 0. \tag{2.4}$$

This assumption is a restriction in the sense that the governing equation, (2.4), applies to insulator piezoelectric materials. But this is a good start to develop more sophisticated models.

2.2 Theory for the First Three Orders of Perturbations

The typical setup of a vertical piezoelectric nanowire that is transversely deflected by a force at the tip. Equations (2.1a), (2.1b), (2.2a)–(2.2c), (2.3) and (2.4) along with appropriate boundary conditions give a complete description of a static piezoelectric system. However, the solution of these equations is rather complex, and an analytical solution does not exist in many cases. Even for a two-dimensional (2-D) system, the solution would entail a partial differential equation of order six [7]. In order to derive an approximate solution of the equations, we apply a perturbation expansion of the linear equations to simplify the analytical solution [8]. Then, we will examine the accuracy of the perturbation theory in reference to the exact results calculated by the finite element method.

In order to derive the piezoelectric potential distributed in the NW for the different orders of electro-mechanical coupled effect, we now introduce a perturbation parameter λ in the constitutive equations by defining $\tilde{e}_{kp} = \lambda e_{kp}$, which is introduced to trace the magnitudes of contributions made by different orders of effects in building the total potential. Consider a virtue material with linear elastic constant c_{pq}, dielectric constant κ_{ik} and piezoelectric coefficient $\tilde{e}_{kp}$. When $\lambda = 1$, this virtue material becomes the realistic ZnO. When $\lambda = 0$, it corresponds to a situation of no coupling between mechanical field and electric field. For virtue materials with λ between 0 and 1, the mechanical field and electric field are both functions of

parameter λ, which can be written as an expansion:

$$\begin{cases} \sigma_p(\lambda) = \sum_{n=0}^{\infty} \lambda^n \sigma_p^{(n)}, \\ \varepsilon_q(\lambda) = \sum_{n=0}^{\infty} \lambda^n \varepsilon_q^{(n)}, \\ E_k(\lambda) = \sum_{n=0}^{\infty} \lambda^n E_k^{(n)}, \\ D_i(\lambda) = \sum_{n=0}^{\infty} \lambda^n D_i^{(n)}, \end{cases} \tag{2.5}$$

where the superscript (n) represents the orders of perturbation results. By substituting (2.5) into (2.2a)–(2.2c) for a virtue material with piezoelectric coefficient $\tilde{e}_{kp}$, and comparing the terms in the equations that have the same order of λ, the first three orders of perturbation equations are given as follows:

$$\text{zeroth order:} \quad \begin{cases} \sigma_p^{(0)} = c_{pq}\varepsilon_q^{(0)}, \\ D_i^{(0)} = \kappa_{ik}E_k^{(0)}; \end{cases} \tag{2.6}$$

$$\text{first order:} \quad \begin{cases} \sigma_p^{(1)} = c_{pq}\varepsilon_q^{(1)} - e_{kp}E_k^{(0)}, \\ D_i^{(1)} = e_{kq}\varepsilon_q^{(0)} + \kappa_{ik}E_k^{(1)}; \end{cases} \tag{2.7}$$

$$\text{second order:} \quad \begin{cases} \sigma_p^{(2)} = c_{pq}\varepsilon_q^{(2)} - e_{kp}E_k^{(1)}, \\ D_i^{(2)} = e_{kq}\varepsilon_q^{(1)} + \kappa_{ik}E_k^{(2)}. \end{cases} \tag{2.8}$$

For (2.1a), (2.1b), (2.3), and (2.4), since there is no explicit coupling, no decoupling process is needed while seeking perturbation solution.

We now consider the solutions of the first three orders. For the zeroth order (see (2.6)), the solution is for a bent nanowire without piezoelectric effect, which means there is no electric field even in the presence of elastic strain. Here we ignore the contribution from the spontaneous polarization. For the case of ZnO NW, it normally grows with its c-axis parallel to the growth direction. The $\pm(0001)$ surfaces at the top and bottom end of the NW are terminated by Zn^{2+} and O^{2-} ions, respectively. The electric field due to spontaneous polarization arising from polar charges on the $\pm(0001)$ surface can be ignored for the following two reasons. First, since the NW has a large aspect ratio, the polar charges on the $\pm(0001)$ polar surfaces, which are the top and bottom ends of the NW in most of the cases, can be viewed as two point charges. Thus they do not introduce an appreciable intrinsic field inside of the NW. Second, the polar charges at the bottom end of the NW are neutralized by

the conductive electrode; while the ones at the top of the NW may be neutralized by surface adsorbed foreign molecules while exposed to air. Furthermore, even the polar charges at the top end introduce a static potential, it will not contribute to the power generated but shift the potential base line by a constant value, which goes to the background signal, because the polar charges are present and remain constant regardless the degree of NW bending. Therefore, we can take $E_k^{(0)} = 0$, $D_i^{(0)} = 0$. Consequently, from (2.7) and (2.8), we have $\sigma_p^{(1)} = 0$, $\varepsilon_p^{(1)} = 0$, $D_p^{(2)} = 0$, $E_p^{(2)} = 0$. Equations (2.5)–(2.7) thus become

$$\text{zeroth order:} \quad \sigma_p^{(0)} = c_{pq}\varepsilon_q^{(0)}, \tag{2.9}$$

$$\text{first order:} \quad D_i^{(1)} = e_{kq}\varepsilon_q^{(0)} + \kappa_{ik}E_k^{(1)}, \tag{2.10}$$

$$\text{second order:} \quad \sigma_p^{(2)} = c_{pq}\varepsilon_q^{(2)} - e_{kp}E_k^{(1)}. \tag{2.11}$$

The physical meaning of these equations can be explained as follows. Under the different order of approximation, these equations correspond to the decoupling and coupling between the electric field and mechanical deformation: the zeroth order solution is purely mechanical deformation without piezoelectricity; the first order is the result of direct piezoelectric effect that strain–stress generates an electric field in the NW; and the second order shows up the first feed back (or coupling) of the piezoelectric field to the strain in the material.

In our case as for nanowires bent by AFM tip, the mechanical deformation behavior of the material is almost unaffected by piezoelectric field in the NW. Therefore, as for the calculation of piezoelectric potential in the nanowire, the first order approximation may be sufficient. The accuracy of this approximation will be examined in reference to full numerical solutions of the coupled equations (2.1a), (2.1b), (2.2a)–(2.2c), (2.3) and (2.4).

2.3 Analytical Solution for a Vertical Nanowire

To simplify the analytical solution, we assume that the nanowire has a cylindrical shape with a uniform cross section of diameter $2a$ and length l. To further simplify the derivation, we approximate the material elastic constants by an isotropic elastic modulus with Young modulus E and Poisson ratio ν. This has been found to be an excellent approximation for ZnO. For the convenience of our calculation, we define $a_{pq}^{\text{isotropic}}$ to be the inverse of matrix $c_{pq}^{\text{isotropic}}$. The strain and stress relation is given

by

$$\begin{pmatrix} \varepsilon_{xx} \\ \varepsilon_{yy} \\ \varepsilon_{zz} \\ 2\varepsilon_{yz} \\ 2\varepsilon_{zx} \\ 2\varepsilon_{xy} \end{pmatrix} = \sum_q a_{pq}^{\text{isotropic}} \sigma_q$$

$$= \frac{1}{E} \begin{pmatrix} 1 & -\nu & -\nu & 0 & 0 & 0 \\ -\nu & 1 & -\nu & 0 & 0 & 0 \\ -\nu & -\nu & 1 & 0 & 0 & 0 \\ 0 & 0 & 0 & 2(1+\nu) & 0 & 0 \\ 0 & 0 & 0 & 0 & 2(1+\nu) & 0 \\ 0 & 0 & 0 & 0 & 0 & 2(1+\nu) \end{pmatrix} \begin{pmatrix} \sigma_{xx} \\ \sigma_{yy} \\ \sigma_{zz} \\ \sigma_{yz} \\ \sigma_{zx} \\ \sigma_{xy} \end{pmatrix}. \tag{2.12}$$

In the configuration of the nanogenerator, the root end of the nanowire is affixed to a conductive substrate, while the top end is pushed by a lateral force f_y. We assume that the force f_y is applied uniformly on the top surface so that there is no effective torque that twists the nanowire. By Saint–Venant theory of bending [9], the stress induced in the nanowire is given by

$$\sigma_{xz}^{(0)} = -\frac{f_y}{4I_{xx}} \frac{1+2\nu}{1+\nu} xy, \tag{2.13a}$$

$$\sigma_{yz}^{(0)} = \frac{f_y}{I_{xx}} \frac{3+2\nu}{8(1+\nu)} \left[a^2 - y^2 - \frac{1-2\nu}{3+2\nu} x^2 \right], \tag{2.13b}$$

$$\sigma_{zz}^{(0)} = -\frac{f_y}{I_{xx}} y(l-z), \tag{2.13c}$$

$$\sigma_{xx}^{(0)} = \sigma_{xy}^{(0)} = \sigma_{yy}^{(0)} = 0 \tag{2.13d}$$

where $I_{xx} = \int_{\text{CrossSection}} x^2 \, dA = \frac{\pi}{4} a^4$.

Equations (2.13a)–(2.13d) is the zeroth order mechanical solution to (2.1a), (2.1b), (2.3), and (2.12). Because the Saint–Venant principle is used to simplify the boundary condition, solution equations (2.13a)–(2.13d) is valid only for regions far away from the affixed end of the nanowire. Here by "far away" we mean a distance large enough in comparison to the NW diameter. Later, full numerical calculation shows that it would be safe to use (2.13a)–(2.13d) when the distance from the substrate is larger than twice the NW diameter.

Equations (2.4) and (2.10) give the direct piezoelectric behavior. By defining a remnant displacement $\vec{D}^R$ as

$$\vec{D}^R = e_{kq} \varepsilon_q^{(0)} \hat{i}_k \tag{2.14}$$

we have

$$\nabla \cdot \left(D_i^R + \kappa_{ik} E_k^{(1)} \right) = 0. \tag{2.15}$$

From (2.14), (2.13a–(2.13d), (2.12), and (2.2b), the remnant displacement is

$$\vec{D}^R = \begin{pmatrix} -\frac{f_y}{I_{xx}E}(\frac{1}{2}+\nu)e_{15}xy \\ \frac{f_y}{I_{xx}E}(\frac{3}{4}+\frac{\nu}{2})e_{15}(a^2-y^2-\frac{1-2\nu}{3+2\nu}x^2) \\ \frac{f_y}{I_{xx}E}(2\nu e_{31}-e_{33})y(l-z) \end{pmatrix}. \tag{2.16}$$

It should be noted that it is the divergence of $\vec{D}^R$ rather than $\vec{D}^R$ itself that induces $E_k^{(1)}$. If we simply assume $E_k^{(1)} = (\kappa_{ik})^{-1} D_i^R$, we would arrive at an absurd electric field with non-zero curl. Instead, by defining a remnant body charge:

$$\rho^R = -\nabla \cdot \vec{D}^R \tag{2.17}$$

and remnant surface charge:

$$\Sigma^R = -\vec{n} \cdot \left(0 - \vec{D}^R\right) = \vec{n} \cdot \vec{D}^R. \tag{2.18}$$

Equation (2.15) will be transformed into an elementary electrostatic problem with Poisson equation:

$$\nabla \cdot \left(\kappa_{ik} E_k^{(1)} \vec{i}_i\right) = \rho^R \tag{2.19}$$

with charge given by (2.18) on the cylindrical surface of the nanowire. From (2.17) and (2.16), we have

$$\rho^R = \frac{f_y}{I_{xx}E}\left[2(1+\nu)e_{15} + 2\nu e_{31} - e_{33}\right]y, \tag{2.20}$$

$$\Sigma^R = 0. \tag{2.21}$$

It is very important to note that, in (2.20) and (2.21), the remnant charge is independent of vertical height z. Therefore, electric potential $\varphi = \varphi(x, y) = \varphi(r, \theta)$ (in cylindrical coordinates) is also independent of z. (We will drop the superscript $^{(1)}$ for the first order approximation for simplicity from now on.) Physically, it suggests that the potential is uniform along z direction except for regions very close to the ends of the nanowire.

Noting that $\kappa_{11} = \kappa_{22} = \kappa_\perp$, the solution of (2.19), (2.20), and (2.21) is

$$\varphi = \begin{cases} \frac{1}{8\kappa_\perp}\frac{f_y}{I_{xx}E}[2(1+\nu)e_{15} + 2\nu e_{31} - e_{33}][\frac{\kappa_0+3\kappa_\perp}{\kappa_0+\kappa_\perp}\frac{r}{a} - \frac{r^3}{a^3}]a^3\sin\theta, & r < a, \\ \frac{1}{8\kappa_\perp}\frac{f_y}{I_{xx}E}[2(1+\nu)e_{15} + 2\nu e_{31} - e_{33}][\frac{2\kappa_\perp}{\kappa_0+\kappa_\perp}\frac{a}{r}]a^3\sin\theta, & r \geq a \end{cases} \tag{2.22}$$

where κ_0 is the permittivity in vacuum. Equation (2.22) is the potential inside and outside the NW.

From (2.22), we have the maximum potential at the surface ($r = a$) of the NW at the tensile (T) side ($\theta = -90°$) and the compressive (C) side ($\theta = 90°$), respectively, being

$$\varphi_{\max}^{(T,C)} = \pm\frac{1}{\pi}\frac{1}{\kappa_0 + \kappa_\perp}\frac{f_y}{E}\left[e_{33} - 2(1+\nu)e_{15} - 2\nu e_{31}\right]\frac{1}{a}. \tag{2.23}$$

By elementary elastic theory, under small deflection, the lateral force deflection f_y is related to the maximum deflection of the NW tip $v_{\max} = v(z = l)$ by

$$v_{\max} = \frac{f_y l^3}{3EI_{xx}}. \tag{2.24}$$

Thus the maximum potential at the surface of the NW is

$$\varphi_{\max}^{(T,C)} = \pm\frac{3}{4(\kappa_0 + \kappa_\perp)}\left[e_{33} - 2(1+\nu)e_{15} - 2\nu e_{31}\right]\frac{a^3}{l^3}v_{\max}. \tag{2.25}$$

This means that the electrostatic potential is directly related to the aspect ratio of the NW instead of its dimensionality. For a NW with a fixed aspect ratio, the piezoelectric potential is proportional to the maximum deflection at the tip.

2.4 Piezopotential for a Transversely Deflected Nanowire

In the first case, the wire diameter is $d = 50$ nm, length is $l = 600$ nm, and the lateral force applied by the AFM tip is 80 nN. To further confirm the validity of omitting the higher order terms in our analytical derivation, we performed a finite element method (FEM) calculation for a fully coupled electro-mechanical system using (2.1a), (2.1b), (2.2a)–(2.2c), (2.3) and (2.4) for a simplified medium of isotropic elastic modulus tensor and with cylindrical geometry. The boundary condition assumed is that the bottom end of the NW is affixed. The electrical boundary condition at the root is that the substrate is perfectly conductive. ZnO was considered as a dielectric medium. Figures 2.1(a) and (b) are, respectively, the potential distributions calculated by full FEM in the bent NW as viewed from side and in cross section, clearly presenting the "parallel plate capacitor" model of the piezoelectric potential except at the bottom. As for the nanogenerator and nanopiezotronics, only the potential distribution in the upper body of the NW matters. Using the analytical equation (2.22), the calculated potential distribution across the NW cross section for a lateral defection of 145 nm when pushed by a force if 80 nN is presented in Fig. 2.1(c), with the two side surfaces having ± 0.28 V piezoelectric potential, respectively. Again we emphasize that, in (2.22), the potential is independent of z_0 except near the top and the bottom.

A similar calculation has been done for a large size NW with $d = 300$ nm, length $l = 2$ μm, and a lateral force of 1000 nN. The value of the pushing force is esti-

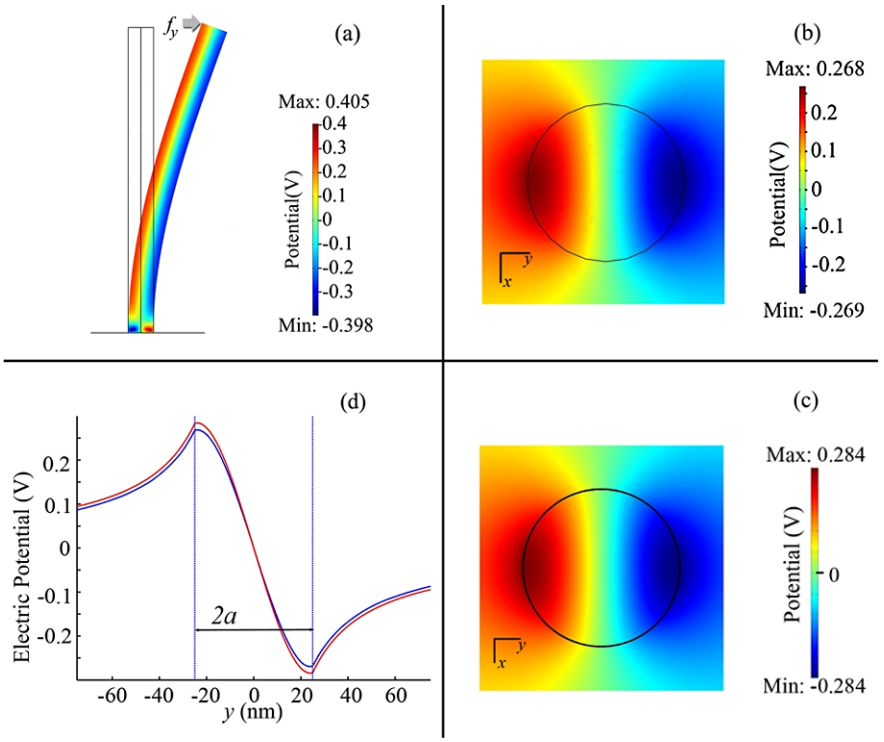

Fig. 2.1 Potential distribution for a ZnO nanowire with $d = 50$ nm, $l = 600$ nm at a lateral bending force of 80 nN. (**a**) and (**b**) are side and top cross-sectional (at $z_0 = 300$ nm) output of the piezoelectric potential in the NW given by finite element calculation using fully coupled equations (2.1a), (2.1b), (2.2a)–(2.2c), (2.3) and (2.4), respectively, while (**c**) is the cross-sectional output of the piezoelectric potential given by analytical equation (2.22). The maximum potential in (**b**) is smaller than that in (**a**), because here the potential in the bottom reverse region is larger than that in upper "parallel-plate capacitor" regions. (**d**) A comparison of the line scan profiles from both (**b**) and (**c**) (*blue* is for full FEM, *red* is for (2.22)) to show the accuracy of (2.22) and the approximations used for deriving it. From [8]

mated based on the lateral deflection observed experimentally. In analogy to the case shown for the smaller NW in Fig. 2.1, this large NW gives a potential distribution of ± 0.59 V across its cross section. Again, the analytical solution is within 6 % of the FEM full numerical calculation; this clearly proves the validity of our analytical solution. Therefore, the perturbation theory we have presented here is an excellent representation for calculating the piezoelectric potential across a NW, and the analytical results given by (2.22)–(2.25) can be applied to quantitative understanding of the experimentally measured results. From the calculation presented above, a 0.3 V is created between the NW and the AFM tip during mechanical bending.

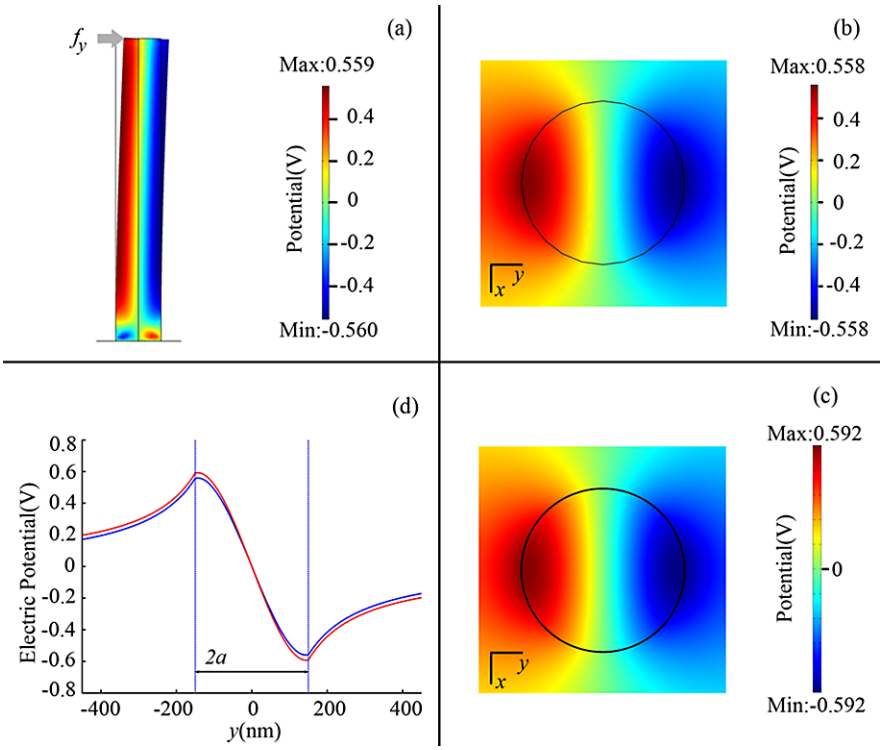

Fig. 2.2 Potential distribution for a nanowire with $d = 300$ nm, $l = 2$ μm at a lateral bending force of 1000 nN. (**a**) and (**b**) are side and top cross-sectional (at $z_0 = 1$ μm) output of the piezoelectric potential in the NW given by finite element calculation using fully coupled equations (2.1a), (2.1b), (2.2a)–(2.2c), (2.3) and (2.4), respectively, while (**c**) is the cross-sectional output of the piezoelectric potential given by analytical equation (2.22). The maximum potential in (**b**) is almost the same as in (**a**). (**d**) A comparison of the line scan profiles from both (**b**) and (**c**) (*blue* is for full FEM, *red* is for (2.22)) to show the accuracy of (2.22) and the approximations used for deriving it. From [8]

2.5 Probing the Piezopotential of a Transversely Deflected Nanowire

The piezopotentials at the stretched and compressed sides of the PFW have been measured by using a metal tip that is placed either at the tensile side or the compressive side of the NW, while the NW is deflected by air blowing [10]. When a periodic gas flow pulse was applied to a ZnO wire, the wire was bent and a corresponding periodic negative voltage output (Fig. 2.3(a)) was detected by connecting the surface of compressed side of the NW with external measurement circuit. The voltage output detected here was −25 mV. Correspondingly, a periodic positive voltage output (Fig. 2.3(b)) was detected at the stretched side of the wire using a Au coated needle when the ZnO wire was periodically pushed by the Au coated needle. Such measurements were done with the use of a voltage amplifier.

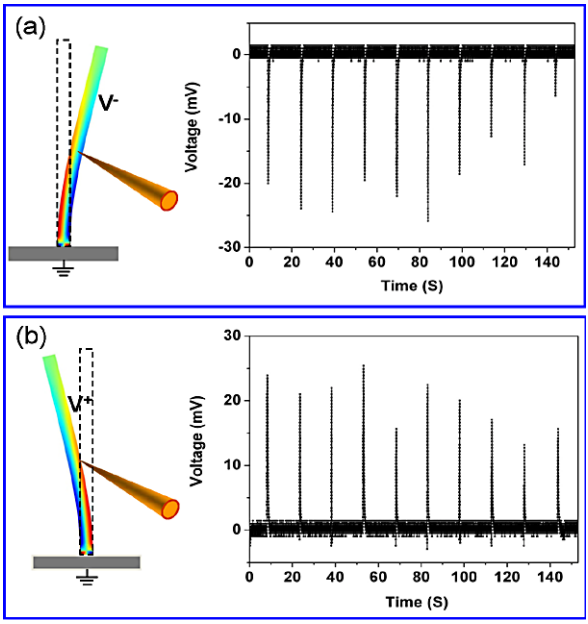

Fig. 2.3 Direct measurements of the asymmetric voltage distribution on the tensile and compressive side surfaces of a ZnO wire. (**a**) By placing a metal tip at the right-hand side and blowing Ar pulses at the left-hand side, negative voltage peaks of ~25 mV were observed once the pulse was on. (**b**) By quickly pushing and releasing the wire at the right-hand side by a metal tip, a positive voltage peak of ~25 mV was observed for each cycle of the deflection. The frequency of the deflection was once every 15 s

2.6 Piezopotential for an Axial Strained Nanowire

The main part of a typical two-terminal nanoelectronic device is a hexagonal ZnO nanowire grown along c-axis with its two ends and short segments adjacent to the ends fully embraced by electrodes, where several kinds of force, including tensile, compression, twisting and combinations of them, act on the nanowire. Our first task is to calculate the piezoelectric potential distribution throughout the nanowire under these forces [11]. In order to simply the system and concentrate on observing how the piezoelectric potential would vary with different applied strain, we assume there is no body force and no free charge in the nanowire by neglecting its conductivity. The fully coupled equations (2.1a), (2.1b), (2.2a)–(2.2c), (2.3) and (2.4) can be solved with the finite element method (FEM). For simplicity of illustrating the proposed physical model, the charge carriers in ZnO have been ignored, which greatly simplifies the numerical approach. Figure 2.4(a) shows a ZnO nanowire without any applied force. The total length of the nanowire is 1200 nm with a 100 nm length of contact domain at each end, and the side length of the hexagonal is 100 nm.

When a stretching force of 85 nN is uniformly acting on the nanowire surfaces surrounded by electrodes in the direction parallel to c-axis, the length of the nanowire would increase for 0.02 nm, which produces a tensile strain of 2×10^{-5}. As shown in Fig. 2.4(b), it creates a potential drop of approximately 0.4 V between the two end sides of the nanowire with the $+c$-axis side of higher potential. When the applied force changes to a compressive, the piezoelectric potential reverses with the potential difference remaining 0.4 V but with the $-c$-axis side at a higher potential. As presented in Fig. 2.4(c), the nanowire length decreases for 0.02 nm, revealing a compressive strain of -2×10^{-5}. Note that to produce the same amount of

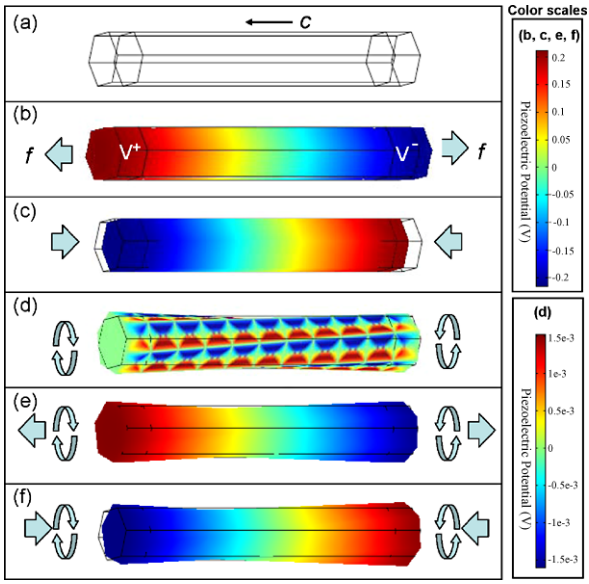

Fig. 2.4 Numerical calculation of the piezoelectric potential distribution in a ZnO nanowire without doping. (**a**) An unstrained ZnO nanowire grown along *c*-axis with a length of 1200 nm and a hexagonal side length of 100 nm. Two ends of the nanowire are assumed to be surrounded by electrodes for a length of 100 nm. Three-dimensional views of the piezoelectric potential distribution together with deformation shape for the nanowire (**b**) at a stretching force of 85 nN, (**c**) at a compressing force of 85 nN, (**d**) at a twist force pair of 60 nN, (**e**) at a combination of 85 nN stretching force and 60 nN twist force, (**f**) at a combination of 85 nN compressing force and 60 nN twist force. The stretching and compressing forces are supposed to uniformly act on both the end surfaces and side surfaces of the nanowire segments surrounded by electrodes, and the twist force is uniformly applied on the side surfaces of the nanowire segments surrounded by electrodes. The *red side* is the positive potential side and the *blue side* is the negative potential side. The potential difference is around 0.4 V. Note that the color scale is the same for (**b**), (**c**), (**e**) and (**f**), but (**d**) has a much smaller scale [11]

piezoelectric potential, the deformation needed here is much smaller than that in the case of bending a nanowire by a transverse force as we previously demonstrated. Thus the force along the polarization direction (*c*-axis) is easy to produce a high piezoelectric potential.

No matter stretching or compressing, the piezoelectric potential continuously drops from one side of the nanowire to the other, which means that the electron energy continuously increases from the one side to the other. Meanwhile, the Fermi level will be flat all over the nanowire when equilibrium is achieved, since there is no external electrical field. As a result, the electron energy barrier between ZnO and metal electrode will be raised at one side and lowered at the other side, which can be observed experimentally as an asymmetric I–V characteristic. This is the governing principle for understanding the experimental results presented in the following section. As the strain is unavoidable during nanowire device fabrication, we would

observe rectifying transport behavior for so many as-fabricated nanowire devices even with two identical electrodes [12].

One type of force that cannot be ignored during nanowire manipulation is the twist force. Figure 2.4(d) shows the simulation results when the nanowire has been twisted at its two ends in the opposite direction. There is no electric potential drop along the wire growth direction. Note that the magnitude of the created local potential is in the order of mV, much smaller than the case for stretching or compressing. When contacting with electrodes and across the cross section at the end, the energy barrier between metal and ZnO at one side of the nanowire would be equivalent, thus, a symmetric contact is expected.

For most of the cases in practice, the force is a combination of twist plus tensile, or twist plus compress. As shown in Fig. 2.4(e) and (f), there will be a piezoelectric potential drop produced along the wire, while the potential distribution in the cross section of the nanowire is not uniform but with one half higher and the other half lower, similar to the case of pure axial straining.

There are several things to be pointed out here: first, the effect of piezoelectricity on the transport characteristics of metal–ZnO nanowire contains two parts: one is the spontaneous polarization charge effect introduced by the Zn^{2+} and O^{2-} terminating layers at the $+c$ and $-c$ end surfaces; the other is the piezoelectric potential effect. The polarized charges exist at the end surface of the nanowire and cannot freely move. They would modulate the local Fermi energy to change the Schottky barrier height and shape. However, in practice metal–ZnO contacts are not just at the very end surface of nanowire, but also largely at the side surface due to the large contact area of the metal and the nanowire. For most of the time, the contact area in the side surface is much larger than at the end surface. If we only consider the polarization charge effect, electrons can pass by the side surface contact where there is no energy barrier.

Second, the above calculation is based on Lippman theory, since we assume there is no free charge carriers for simplicity and the whole system is isolated. The as-synthesized ZnO nanostructures are typically n-type with a typical donor concentration of 1×10^{17} cm^{-3}. Theoretical calculations based on statistical electron distribution in conduction band show that the free electrons tend to accumulate at the positive potential side of the nanowire at thermal equilibrium. Therefore, the effect of the free carriers is to partially, if not wholly, screen the positive piezoelectric potential, while no change to the negative piezoelectric potential. In such a case, the calculation results presented in Fig. 2.4 can still be adopted for explaining practical experimental results except the magnitude of the positive potential has to be reduced to balance the effect of the free carriers.

Third, strain will not only induce piezoelectric effect in ZnO, but also cause band-structure variation. The generated deformation potential can also change the Schottky barrier height: under tensile strain the barrier will be lowered, and under compressive strain the barrier will be raised. However, the variations at two ends of nanowire are identical and in the same tendency, and it cannot change a symmetric I–V curve into a rectifying I–V behavior. This is the piezoresistance effect.

2.7 Equilibrium Piezopotential in a Doped Semiconductive Nanowire

Lippman theory can be used to describe bent piezoelectric nanowires when the donor concentration is extremely low, so that the conductivity can be neglected. However, the as-grown ZnO nanowires are typically n-type due to unavoidable point defects. For semiconductor materials with a significant amount of free electrons, the Lippman theory cannot be directly applied, because the free charge carriers are able to distribute all over the material. The statistics of electrons/holes must be considered besides the phenomenological thermal dynamics. The main objective of this section is to present a macroscopic-statistical model of piezoelectricity in a laterally bent semiconductive nanowire by considering its moderate conductivity in a normal doping range.

2.7.1 Theoretical Frame

Previous results indicated that, for a ZnO NW with zero free charge carrier density, the tensile surface would show a positive piezoelectric potential, and the compressive side would show a negative potential. (In this context, by "piezoelectric potential" we mean that the potential is created by the polarizations of anions and cations in the NW; these charges cannot freely move as long as the strain is preserved.) In order to focus on the core physics by preventing digression to the less relevant problems about the interface heterojunctions, we assume that the substrate is also made of ZnO. Such a situation occurs for the ZnO nanowires grown on GaN substrates via the VLS method, because a thin ZnO film or ZnO walls usually form beneath the nanowires. Our task is to calculate the piezoelectric potential when thermodynamic equilibrium is achieved in the laterally bent nanowires [13].

It is well known that when free electrons/holes are present in a piezoelectric material, the carriers will redistribute due to the electric field established by the polarization. One famous application of such a redistribution effect is in the GaN/AlGaN HEMTs, where electrons are accumulated at the heterojunction to create a 2D Electron Gas (2DEG) [14]. For piezoelectric nanowire applications, the mechanical behavior is more complicated, but the physical pictures are essentially the same. Instead of using a fully coupled constitutive equation, we only write the mechanical equilibrium and the direct piezoelectric effect:

$$\begin{cases} \sigma_p = c_{pq}\varepsilon_q, \\ D_i = e_{iq}\varepsilon_q + \kappa_{ik}E_k \end{cases} \tag{2.26}$$

where σ is the stress tensor, ε is the strain, $\vec{E}$ is the electric field, and $\vec{D}$ is the electric displacement. κ_{ik} is the dielectric constant, e_{kp} is the piezoelectric constant, and c_{pq}

is the mechanical stiffness tensor. The Voigt–Nye notation is used. Substituting the second equation into the Gauss law, we get the equation for the electric field:

$$\nabla \cdot \vec{D} = \frac{\partial}{\partial x_i}(e_{iq}\varepsilon_q + \kappa_{ik}E_k) = \rho_e^{(b)} = ep - en + eN_D^+ - eN_A^- \tag{2.27}$$

where p is the hole concentration in the valance band, n is the electron concentration in the conduction band, N_D^+ is the ionized donor concentration, and N_A^- is the ionized acceptor concentration. Because the as-grown ZnO NWs are usually n-type, we adopt $p = N_A^- = 0$. By introducing

$$\vec{D}^R = e_{kq}\varepsilon_q \hat{i}_k \tag{2.28a}$$

as the polarization due to piezoelectricity and

$$\rho^R = -\nabla \cdot \vec{D}^R \tag{2.28b}$$

as the corresponding piezoelectric charge, (2.27) can be rewritten for the electric potential φ [13]:

$$\kappa_{ik}\frac{\partial^2}{\partial x_i \partial x_k}\varphi = -\left(\rho^R - en + eN_D^+\right). \tag{2.29}$$

The surface charge due to piezoelectricity is calculated by $\Sigma^R = -\vec{n} \cdot \Delta\vec{D}^R$, where $\Delta\vec{D}^R$ is the change of $\vec{D}^R$ astride the material surface and $\vec{n}$ is the normal to the surface. For simplicity, we have ignored the surface charges introduced by polar surfaces of ZnO.

The redistribution of electrons under thermodynamic equilibrium is given by Fermi–Dirac statistics:

$$n = N_c F_{1/2}\left(-\frac{E_c(\vec{x}) - E_F}{kT}\right), \tag{2.30a}$$

$$N_c = 2\left(\frac{2\pi m_e kT}{h^2}\right)^{\frac{3}{2}} \tag{2.30b}$$

where the conduction band edge $E_c(\vec{x})$ is a function of space coordinates. N_c, the effective state density of conduction band, is determined by the effective mass of conduction band electrons m_e and the temperature T. Due to the large strain, the deformation potential might be important. To be specific, the band edge shift ΔE_c is the sum of the electrostatic energy part and the deformation potential part:

$$E_c - E_{c_0} = \Delta E_c = -e\varphi + \Delta E_c^{\text{deform}} = -e\varphi + a_c\frac{\Delta V}{V} \tag{2.31}$$

where E_{c_0} is the conduction band edge of a free-standing undeformed semiconductor material; $\Delta E_c^{\text{deform}} = a_c \Delta V/V$ is the band edge shift due to the deformation potential [15], which is proportional to the relative volume change $\Delta V/V$, and a_c

is the deformation potential constant. Finally, the activation process of the donors is given by

$$N_D^+ = N_D \frac{1}{1 + 2\exp(\frac{E_F - E_D}{kT})} \tag{2.32}$$

where $E_D(\vec{x}) = E_C(\vec{x}) - \Delta E_D$ is the position-dependent donor energy level. The constant ΔE_D is the activation energy of the donors. N_D is the concentration of the donors.

2.7.2 Calculated Piezopotential with Considering Doping

The piezoelectric potential in a bent ZnO nanowire with moderate charger carrier density can be calculated. It should be pointed out that (2.29)–(2.32) are valid only when the system dimension is not too small. For small systems, strong confinement requires quantum mechanical considerations due to discrete bound states. Such an elaboration in theory is necessary for 2DEG in GaN/AlGaN HEMTs, in which the quantum effect is important. In the following section we will conduct the calculation for nanowires with diameter ~50 nm or larger, where non-quantum mechanical calculation is still acceptable.

The Fermi level E_F is flat all over the bent semiconductor nanowire when thermodynamic equilibrium is assumed. Because the nanowires are assumed to be grown on a substrate whose dimension is much larger than the nanowire, the substrate can be taken as a vast reservoir that pins the Fermi level. In this paper we assume that the substrate is made of the same material as the nanowire itself. For nanowires making direct heterogeneous junctions with the substrate, depletion regions or charge-accumulation regions may form at the bottom junctions, which will not be elaborated on in this paper.

Symmetry is used so we only need to solve for the half-space of $x > 0$. Solution in the other half of space can be immediately derived by using the mirror symmetry of the $x = 0$ plane. In order to help the convergence, we first linearize (2.30a) and (2.32) by introducing an extreme case of ultra-high temperature T_{high}. For the convenience of calculations as presented in (2.30a) and (2.32), we define the following variables:

$$\eta = -\frac{E_c(\vec{x}) - E_F}{kT} \quad \text{and} \quad \eta_D = \frac{E_F - E_D}{kT} = \eta + \frac{\Delta E_D}{kT}. \tag{2.33}$$

When $T = T_{\text{high}}$ is large, η and η_D are no longer position-dependent; the problem is thus linearized for easy solution. As a convergence tool, T_{high} by itself is not required to have a realistic physical meaning. Nevertheless, the solutions under high temperature $T = T_{\text{high}}$ do evince some meaningful insight in physics. In fact, $\eta \approx \eta_D \approx \ln(\frac{N_D}{N_C})$ when $T = T_{\text{high}}$, therefore $N_D^+ = n$ and (2.29) would give an unscreened solution as though there were neither donors nor free charge carriers in

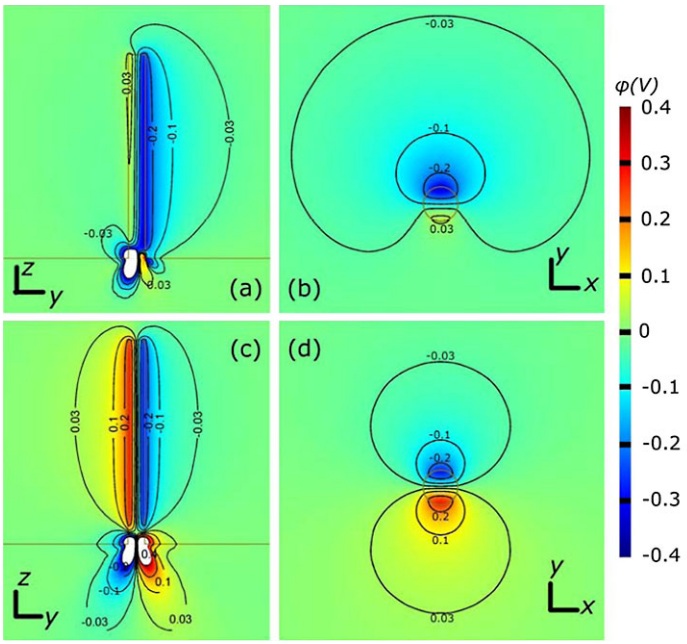

Fig. 2.5 Plot of calculated piezoelectric potential φ for $N_D = 1 \times 10^{17}$ cm^{-3}. For easy plot, the bending shape of the nanowire is not presented. Besides the color plot, equipotential contours for $\varphi = -0.4, -0.2, -0.1, -0.03, 0.03, 0.1, 0.2$ and 0.4 V are also superimposed. The dimensions of the nanowire are: $a = 25$ nm, $l = 600$ nm and the external force is $f_y = 80$ nN. (**a**) Plot of φ for $T = 300$ K at a cross section of $x = 0$. The blank region at the bottom is the region where $\varphi < -0.4$ V. The detail in this region is over saturated for display purposes, to optimize the color scale in order to show φ in the nanowire. In this paper, we mainly focus on the behavior in the nanowire and will leave aside the details regarding the bottom reverse region for future research. (**b**) Cross section plot of the electric potential for $T = 300$ K at the height $z = 400$ nm. Here only half of the space $x > 0$ is calculated using the mirror symmetry of $x = 0$ plane. The plot in the $x < 0$ region is derived by a simple reflection of the solution in $x > 0$ region. (**c**) and (**d**) Calculation for an extremely high temperature case of $T = T_{\text{high}} = 300000$ K to test the convergence of the result in reference to the result received from nanowires without doping. Again the extreme peaks are over saturated. (**c**) shows the cross section $x = 0$, (**d**) is the cross section plot of the electric potential for the height $z = 400$ nm. From [14]

ZnO. As the system "cools down" from T_{high} to the realistic temperature, the equations become more and more non-linear. The value of η dictates how degenerate the system is, with $\eta > -3$ being regarded as the highly degenerate case. As we will see later in the results, the problem will involve some degree of degeneracy even when the donor concentration is relatively low. This is analogous to the 2DEG regions in GaN/AlGaN HEMTs, where electrons accumulate even when the local doping level is small.

Figure 2.5(a) shows the equal-potential lines for $N_D = 1 \times 10^{17}$ cm^{-3} and $T = 300$ K on the cross section plane $x = 0$, which is right through the axis of the nanowire. Figure 2.5(b) gives the equal-potential lines on a cross section per-

pendicular to the nanowire axis and at a height of $z = 400$ nm. The electrostatic calculation is done under a small strain assumption, in which the difference between the Lagrangian reference frame and Eulerian reference frames is neglected. For comparison purposes, the results received under the un-realistic temperature of $T = T_{\text{high}} = 300{,}000$ K is also plotted in Figs. 2.5(c) and (d), which correspond to the situation when ZnO were an insulator without any free charge carriers.

The electric potential maximum at the positive side of the nanowire is significantly reduced from ~0.3 V in Fig. 2.5(d), which corresponds to an insulator case, to less than 0.05 V in Fig. 2.5(b), which agrees with moderate doping in ZnO. On the other hand, the potential at the compressed side (negative potential side) is very well preserved. This is consistent with the experimental observation that only negative pulses are observed in an AFM-based nanogenerator experiment using n-type ZnO nanowires. It is also consistent with the observation that the output negative potential peak appears only when the AFM tip touches the compressed side of the nanowire. The decrease of positive potential in this model is due to the in-flow of electrons from the substrate where free charges are abundant. When positive polarization charges $\rho^R > 0$ try to create a positive local potential $\varphi > 0$, it would result in a downward bending of the local conduction band. When η gets close to or gets even bigger than zero, a large amount of free electrons would be injected from the substrate reservoir into the nanowire to screen the positive potential.

In the negative potential side (compressed side of the nanowire), however, free charge carriers are depleted due to large negative value of η, leaving only $\rho^R + eN_D^+$ as the net charge in (2.4). Let us use the analytical equation derived in Sect. 2.3 to evaluate the concentration of ionic polarization charge. Substituting $a = 25$ nm, $l = 600$ nm and $f_y = 80$ nN into $\rho^R = \frac{f_y}{I_{xx}E}[2(1+\nu)e_{15} + 2\nu e_{31} - e_{33}]y$, where $I_{xx} = \frac{\pi}{4}a^4$, one gets the typical piezoelectric polarization charge density $\rho_R^{y=a}/e \sim -8.8 \times 10^{17}$ cm^{-3} near the wire surface $y = a$, where e is the charge of a single electron. When $N_D = 1 \times 10^{17}$ cm^{-3}, ρ_R cannot be totally screened in the negative side even if all of the electrons are depleted because N_D is much smaller than $\rho_R^{y=a}/e$. For a nanowire with a very high donor concentration $N_D > 10^{18}$ cm^{-3}, total neutralization with $\varphi \approx 0$ could occur everywhere. Namely, a NW with a high concentration of free charge carriers is expected to exhibit very small piezoelectric potential. This result agrees with the experimental measurement of a nanogenerator under the illumination of UV light. In reality, the doping level in as-grown un-intentionally doped ZnO nanowires is much smaller than 10^{18} cm^{-3}.

The band edge shift ΔE_c comprises two parts: the electric potential part and the deformation potential part. The Saint–Venant solution for stress in the nanowire is $\sigma_{zz} = -\frac{f_y}{I_{xx}}y(l-z)$, $\sigma_{xx} = \sigma_{xx} = 0$, therefore,

$$\begin{aligned}\left|\Delta E_c^{\text{deform}}\right| &= a_c|\Delta V/V| = a_c\left|\text{Tr}(\varepsilon)\right| = a_c\left|\frac{1-2\nu}{E}\text{Tr}(\sigma)\right| \\ &= \left|-a_c\frac{1-2\nu}{E}\frac{f_y}{I_{xx}}y(l-z)\right| < a_c\frac{1-2\nu}{E}\frac{f_y}{I_{xx}}\cdot a\cdot l = 46\text{ meV}.\end{aligned}$$

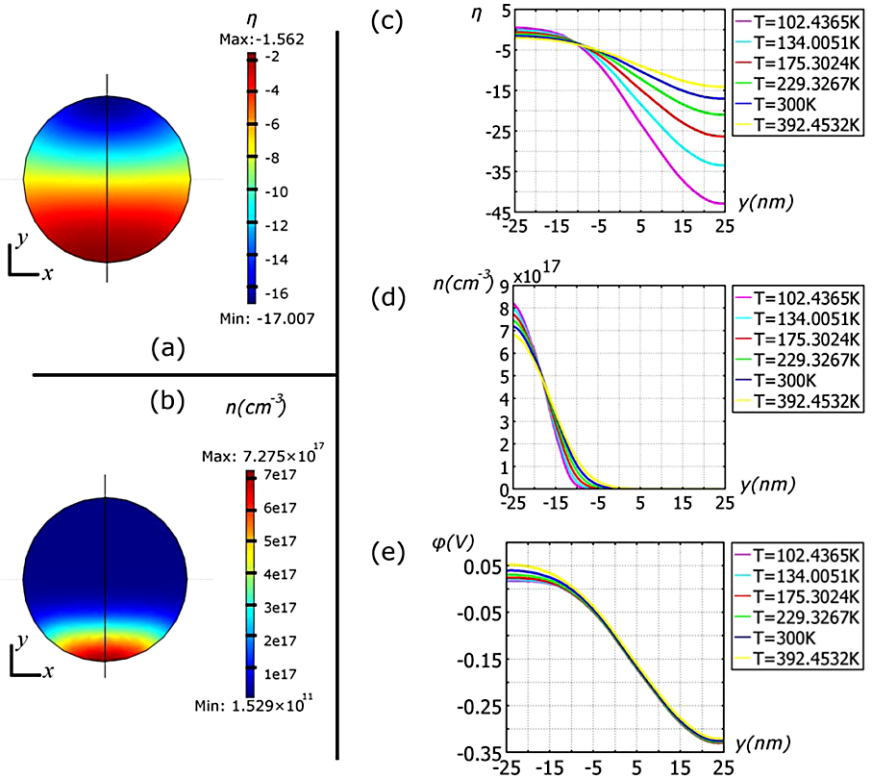

Fig. 2.6 (**a**) and (**b**) Cross section color plot of parameters η (**a**) and local electron density n (**b**) for $N_D = 1 \times 10^{17}$ cm^{-3} and $T = 300$ K at the height $z = 400$ nm. Here only half of the space $x > 0$ is calculated using the mirror symmetry of $x = 0$ plane. The plot in $x < 0$ region is derived by a simple reflection of the solution in $x > 0$ region. (**c**)–(**e**) Line plot of η, n and φ under different temperatures along the diameter in (**a**) and (**b**). The *horizontal axis* is the y-coordinate

As a posterior observation, this value is much smaller than the negative side value of $|e\varphi|$, therefore the deformation potential could have been neglected before the calculation if the potential magnitude in the negative side is the main concern. It also indicates that the negative potential observed in experiments should not be due to the deformation potential band-structure shift, but mainly be due to the piezoelectric effect.

Degeneracy is significant at the screened positive side as seen in the η plot in Fig. 2.6(a). The degeneracy in the charge-accumulation region is due to the piezoelectric effect but not due to large donor concentration or low temperature. Before deformation, $\eta = \eta_0 = -3.77$ for $N_D = 1 \times 10^{17}$ cm^{-3} at $T = 300$ K; this is below the degeneracy criterion. In order to investigate how temperature affects the free charge carrier distribution and the final electric potential, we plotted n, η and φ for different temperatures (Figs. 2.6(c), (d) and (e)). The variance of n, η and φ is small for temperatures in a range of $100 < T < 400$ K. The free carrier concen-

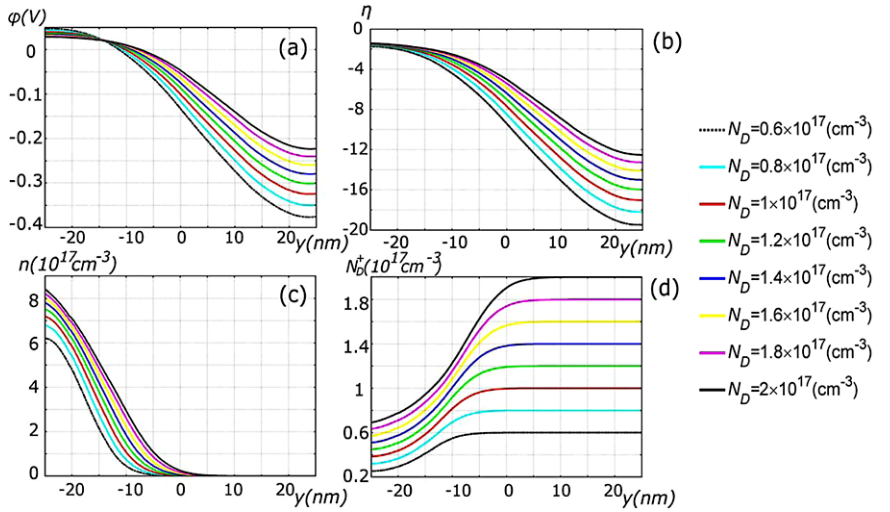

Fig. 2.7 (**a**) Piezoelectric potential φ, (**b**) parameter η, (**c**) free electron concentration n and (**d**) activated donor center concentration N_D^+ for different donor concentrations $0.6 \times 10^{17} < N_D < 2.0 \times 10^{17}$ cm^{-3}. The dimensions of the nanowire are: $a = 25$ nm, $l = 600$ nm and the external force is $f_y = 80$ nN, $T = 300$ K

tration is $n \sim 10^{15}$ cm^{-3} in the depletion region and $n \sim \rho_R/e + N_D \sim 10^{18}$ cm^{-3} in the charge-accumulation region, as seen in Fig. 2.6(b). The boundary between the charge-accumulation region and the depletion region is quite sharp. We notice that the width of the charge-accumulation region is much smaller than the wire diameter a, which implies strong confinement of the conduction band electrons. This strong confinement might result in a stronger quantum effect than that seen in the NW's undeformed state.

In order to investigate how the variance of N_D affects the piezoelectric potential, we plot the (a) electric potential φ, (b) parameter η, (c) free electron concentration n and (d) activated donor center concentration N_D^+ for different donor concentrations $0.6 \times 10^{17} < N_D < 2.0 \times 10^{17}$ cm^{-3} under $T = 300$ K in Fig. 2.7. It is seen that the electric potential φ is rather insensitive to the donor concentration in this regime. However, it is expected that φ will be completely neutralized when $N_D > 10^{18}$ cm^{-3}, as we have already discussed. In the $y < 0$ region (stretched side of the nanowire), degeneracy is always significant due to large η value (Fig. 2.7b). Therefore, electrons will be accumulated at the $y < 0$ side as seen in Fig. 2.4(c) and depleted in the compressed side of the nanowire ($y > 0$). On the other hand, the donor centers are not well activated at the $y < 0$ side as seen in Fig. 2.7(d), which makes the local electric charge density $\rho^R - en + eN_D^+$ at the $y < 0$ side even smaller.

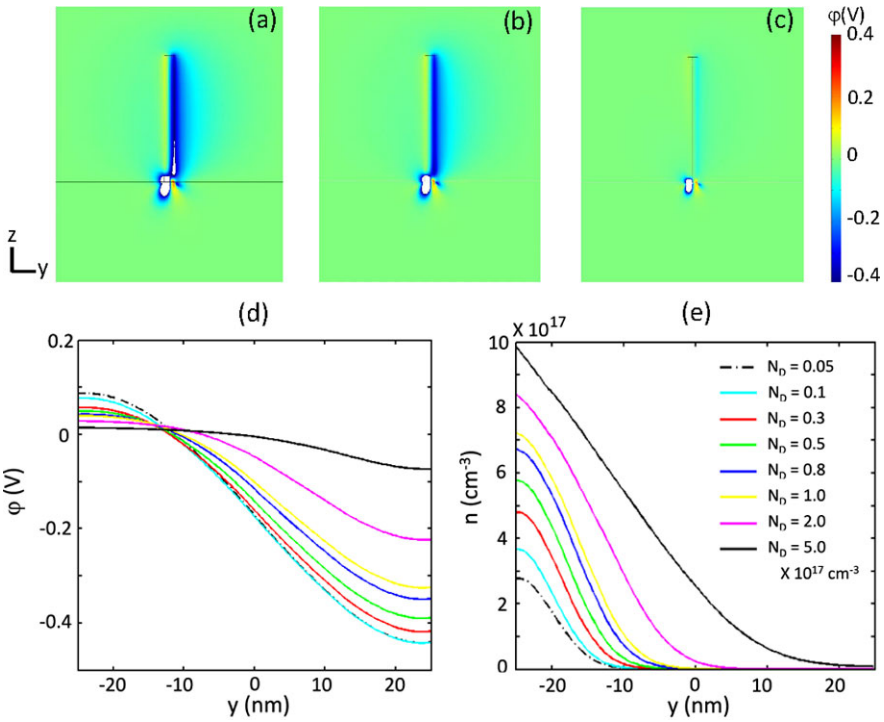

Fig. 2.8 Color plot of the calculated piezoelectric potential at a cross section of $x = 0$, for donor concentrations $N_D = 0.5 \times 10^{17}$ cm^{-3} (**a**), $N_D = 1 \times 10^{17}$ cm^{-3} (**b**) and $N_D = 5 \times 10^{17}$ cm^{-3} (**c**). The dimensions of the nanowire are $L = 600$ nm and $a = 25$ nm; the external force is $f_y = 80$ nN. (**d**) Piezoelectric potential and (**e**) local electron density for different donor concentrations $0.05 \times 10^{17} < N_D < 5 \times 10^{17}$ cm^{-3}, for $T = 300$ K. The line plot is along the diameter of the nanowire, at $z = 400$ nm [16]

2.7.3 *Effect of Doping Concentration*

The main objective of this section is to investigate the influence of different parameters on the equilibrium piezoelectric potential distribution in a deformed ZnO semiconductive NW. In particular, we will calculate the electric potential distribution when the thermodynamic equilibrium among free charge carriers is achieved, for NWs under different doping concentrations, different applied forces and different geometric configurations [16].

A ZnO nanowire epitaxially grown along the c-axis is laterally bent by a force f_y exerted at the top. An axial symmetric model is chosen in order to simplify the calculations. This means that the equation are solved for the half-space $x > 0$ and the solutions are eventually derived using the mirror symmetry of the $x = 0$ plane.

Figure 2.8 shows the influence of the donor concentration on both the equilibrium piezoelectric potential and the local electron density. The color plot of the piezoelectric potential in Figs. 2.8(a), (b), and (c) represents the result of low

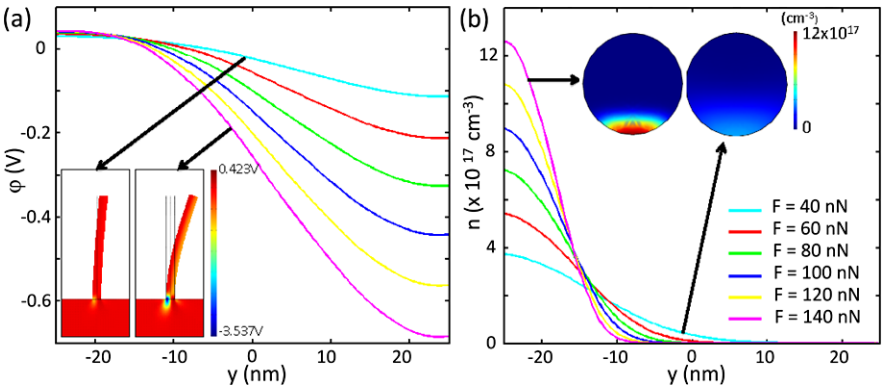

Fig. 2.9 (**a**) Piezoelectric potential and (**b**) local electron density for different external forces $40 < F < 140$ nN. (**a**) Also shows the color plot of the calculated potential at a cross section of $x = 0$ for $F = 40$ nN and $F = 140$ nN. (**b**) Also shows the color plot of the calculated free electron distribution at a cross section of the nanowire at the height of 400 nm, for $F = 40$ nN and $F = 140$ nN. Here only half of the space $x > 0$ is calculated using the mirror symmetry of the $x < 0$ plane. The plot in the $x < 0$ region is derived by a simple reflection of the solution in the $x > 0$ region. From [17]

(0.5×10^{17} cm^{-3}), medium (1×10^{17} cm^{-3}) and high (5×10^{17} cm^{-3}) donor concentrations N_D, respectively. In Figs. 2.8(d) and (e) we plot the electric potential φ and the free electron concentration n for different donor concentrations between 0.05×10^{17} and 5×10^{17} cm^{-3}, under $T = 300$ K. The electric potential φ in the stretched side, showing a positive potential, is less sensitive than the compressed negative side to the increase of donor concentration N_D. The electric potential φ is almost completely screened for $N_D = 5 \times 10^{17}$ cm^{-3}. The reason for the screening of the potential in the compressed side of the nanowire is that free electrons will be depleted in this region, while they will accumulate at the stretched side. Moreover, the decrease of the positive potential is due to the in-flow of free electrons from the substrate reservoir, where free charges are abundant. This increase in free electron concentration is clearly evident in Fig. 2.8(e).

Figure 2.9 shows the influence of the applied force to the equilibrium potential distribution and local electron density. All of the other parameters are kept constant: nanowire length 600 nm, radius 25 nm and donor concentration $N_D = 1 \times 10^{17}$ cm^{-3}. The force has been chosen to vary in the range $40 < F < 140$ nN. In the calculations, the force has been applied to the top surface of the nanowire in order to avoid punctual deformations. When increasing the applied force, the electric potential (in Fig. 2.9(a)) of the compressed side increases, reaching the value of about 0.7 V for the maximum applied force. The free electron concentration (Fig. 2.9(b)) also increases in the stretched side when increasing the force, because of the increase in the polarization charges due to highest strains. Figure 2.9(a) also shows the color plots of the electric potential and the scaled deformations for lower and higher applied forces. Figure 2.9(b) shows the color-plot for the free electron

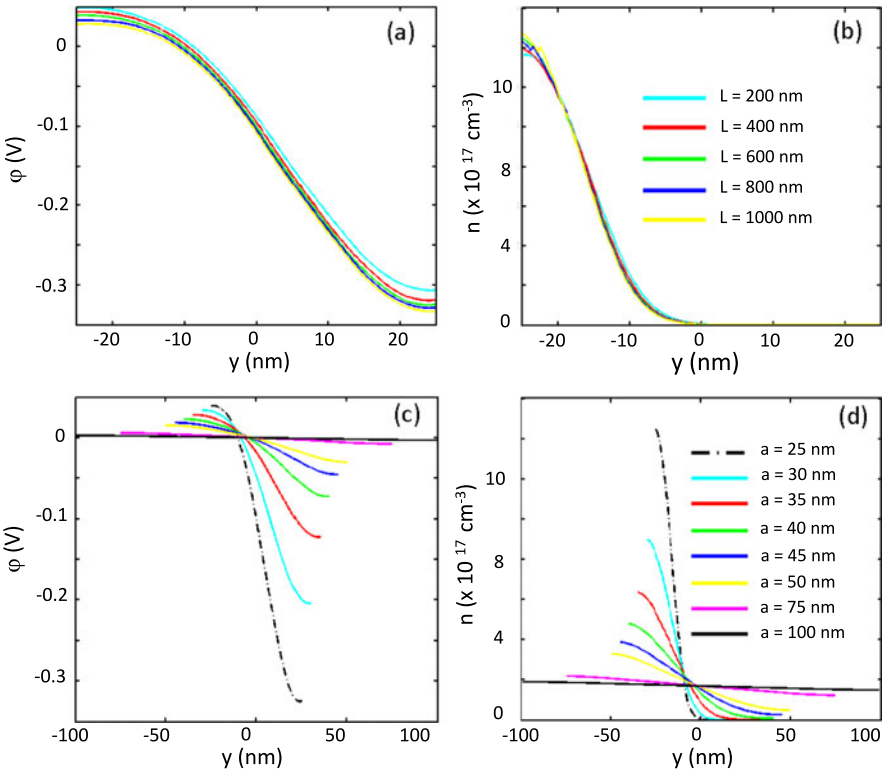

Fig. 2.10 (**a**) Piezoelectric potential and (**b**) local electron density for different lengths of the nanowire $200 < L < 1000$ nm. (**c**) Piezoelectric potential and (**d**) local electron density for different radius of the nanowire in $25 < a < 100$ nm. The donor concentration is $N_D = 10^{17}$ cm^{-3}, at $T = 300$ K; the external force is $f_y = 80$ nN. The line plot is along the diameter of the nanowire, at $z = 400$ nm

concentration, at the cross section at $z = 400$ nm. This last figure is obtained by means of the mirror symmetry of the $x = 0$ plane.

The influence of the geometric dimensions of the nanowire on the electric potential and local electron density has also been investigated, as shown in Figs. 2.10 and 2.11. While keeping the radius of the nanowire at 25 nm, the donor concentration at $N_D = 10^{17}$ cm^{-3} and the applied force at 80 nN, the length of the nanowire has been varied in the range $200 < L < 1000$ nm. Figures 2.9(a) and (b) show that the length of the nanowire does not influence either the electric potential distribution or the free electron density.

When keeping the length of the nanowire constant at 600 nm, the effect of the variation of the radius has been investigated in the range $25 < a < 100$ nm. The results are shown in Figs. 2.9(c) and (d) for electric potential and free electron concentration, respectively. The increase in the radius decreases both parameters; the electric potential is almost neutralized for a radius of 100 nm. It is to be noted that

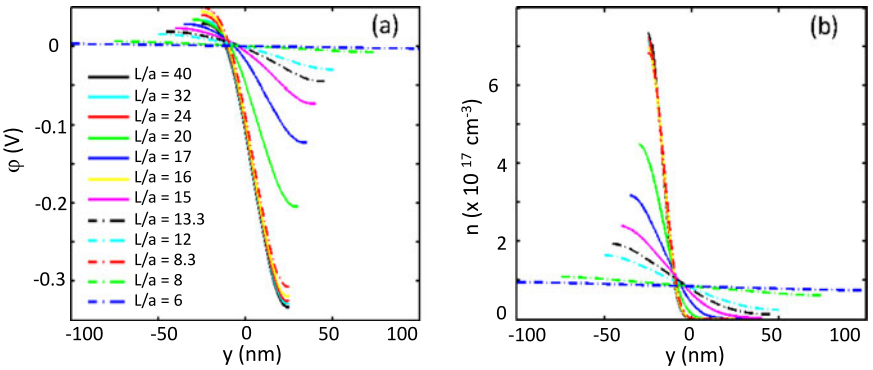

Fig. 2.11 (**a**) Piezoelectric potential and (**b**) local electron density for different aspect ratio of the nanowire in $6 < L/a < 40$. The donor concentration is $N_D = 10^{17}$ cm^{-3}, at $T = 300$ K; the external force is $f_y = 80$ nN. The line plot is along the diameter of the nanowire, at $z = 400$ nm

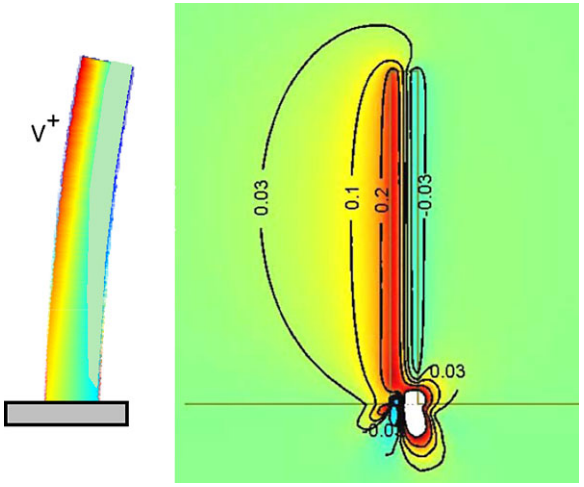

Fig. 2.12 Calculated piezoelectric potential distribution in a p-type ZnO nanowire when it is deflected from the left hand side by a transverse force

the increase of the radius also decreases the magnitude of the strain experienced by the nanowire, as we are keeping the applied force constant.

Figure 2.10 shows the influence of the aspect ratio L/a, on the electric potential and free electron distribution. It summarizes the results previously described in Fig. 2.9: the length variation does not affect the variables, while the increase in the radius dimension decreases both of them.

2.7.4 Effect of Carrier Type

Instead of assuming the n-type doping as for as-synthesized ZnO nanowires, it is possible to obtain stable p-type ZnO nanowires. The stability of the p-type doping

in nanowires is possibly due to the dislocation free volume and the presence of high concentration of vacancies near the surface of the nanowires. We have calculated the piezoelectric potential in a bent p-type NW taking a finite carrier density into consideration. For a laterally bent ZnO NW without any doping, the stretched side exhibiting positive piezoelectric potential and the compressed side negative piezoelectric potential. With a finite p-type doping, the holes tend to accumulate at the negative piezoelectric potential side. The negative side is thus partially screened by holes while the positive side of the piezoelectric potential preserves. Using the Poisson equation and the statistical Fermi-Dirac distribution of charge carriers, for a typical ZnO NW with diameter 50 nm, length 600 nm, acceptor concentration $N_A = 1 \times 10^{17}$ cm^{-3} under a bending force of 80 nN, the piezoelectric potential in the negative side is > -0.05 V and is $\sim$0.3 V at the positive side (Fig. 2.12). This means that the piezopotential in p-type nanowire is dominated by the positive piezopotential at the tensile side of surface [17].

2.8 Effect of Piezopotential on Local Contact Characteristics

Owing to the deformation shape of a nanowire, the piezopotential has a spatial distribution in the micro/nanowires depending on the applied tensile, compressive and/or deflecting force. The distribution of the piezopotential in the nanowire can be different at the top and bottom side surfaces of the nanowire. Such a non-uniform spatial distribution of piezopotential is likely to affect the performance of the piezotronic devices, which will be elaborated on in the following chapters.

In this section, we present the theoretical and experimental analysis on the effect of the piezopotential spatial distribution on the local charge transport characteristic at the contact [18]. Such a study is likely to reveal new features of the piezopotential and its effect on fabricating piezotronic devices. The piezotronic effect arising from the local tuning of the Schottky barrier height (SBH) is inevitable in practical device fabrication of nanowires because tensile and twist strain are usually introduced. Our study sets the model for the related research and applications.

2.8.1 Theoretical Analysis

To be simple and most plausible, the ZnO micro/nanowire is assumed to grow along the c-axis with length of $l = 5$ μm and radius of $a = 0.5$ μm (Fig. 2.13(a)). Although a circular cross-sectional beam is proposed in Fig. 2.13(a), the presented methodology applies to nanowires of arbitrary cross sections. In general, the externally applied force can be decomposed into vertical and parallel components in reference to the wire's direction. Using the finite element method (FEM), we calculate the distribution of the piezopotential in the ZnO micro/nanowires with a vertical force $\vec{F}_x$ and parallel external force $\vec{F}_z$, as shown in Fig. 2.13(a). For simplicity,

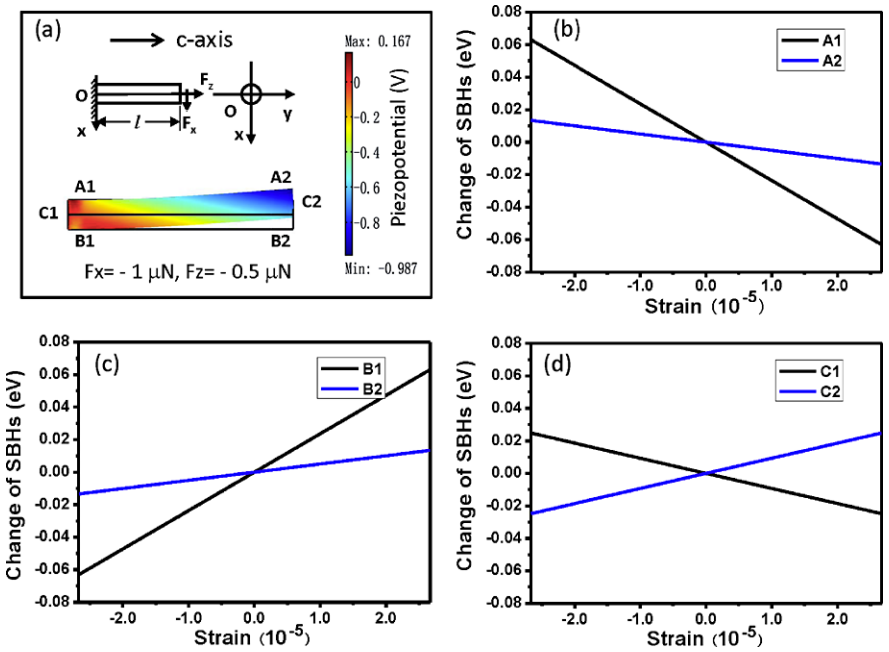

Fig. 2.13 (**a**) Schematic of a ZnO cantilever beam and its cross section, as well as the calculated piezopotential distribution in a one-end fixed ZnO cantilever beam under strain using the finite element method (FEM). The color represents the local piezopotential in unit of volt; the arrowhead indicates the strain increase direction. Predicted change in SBHs for the devices with electrical contact at positions at A1 and A2 (**b**), B1 and B2 (**c**), and (**d**) C1 and C2, respectively [18]

we ignored the finite doping in the nanowire, thus its electrical conductance is neglected. The two components of the applied forces are chosen as $\vec{F}_x = -1000$ nN and $\vec{F}_z = -500$ nN. Figure 2.13(a) shows the distribution of piezopotential in the nanowire at its side cross section parallel to its axis. The piezopotential at points A1 and A2 decreases with increase of vertical force component, while it increases at points B1 and B2 under the same condition; for the positions at C1 and C2, the piezopotential, which is largely determined by the parallel force component, increases at one end, and decreases at the other end with the increase of the tensile force. For a metal–semiconductor–metal back-to-back Schottky contacted ZnO micro/nanowire device, the changing of the piezopotential tunes the effective heights of the Schottky barriers at the electrical contact. As a result, the characteristic of I–V transport measured depends sensitively on where the positions of the electrical contacts had been made.

Now we begin to describe the change of SBHs related to the piezopotential variation if we fabricate the electrical contact at different positions at the nanowire. Assuming a small uniform mechanical strain S_{jk} [19], we can write the polarization P vector in terms of strain S as

$$(\mathbf{P})_i = (\mathbf{e})_{ijk}(\mathbf{S})_{jk} \tag{2.34}$$

where the third order tensor $(\mathbf{e})_{ijk}$ is the piezoelectric tensor. According to the conventional theory of piezoelectric and elasticity, the constituting equations can be written as

$$\begin{cases} \boldsymbol{\sigma} = \mathbf{c}_E \mathbf{S} - \mathbf{e}^{\mathrm{T}} \mathbf{E}, \\ \mathbf{D} = \mathbf{e}\mathbf{S} + \mathbf{k}\mathbf{E} \end{cases} \tag{2.35}$$

where $\boldsymbol{\sigma}$ is the stress tensor, $\mathbf{E}$ is the electric field, $\mathbf{D}$ is the electric displacement, $\mathbf{c_E}$ is the elasticity tensor, and $\mathbf{k}$ is the dielectric tensor. The material elastic constants are approximated to be the isotropic elastic modulus E and Poisson ratio ν and we obtain the solutions of stress by Saint–Venant theory of bending [8, 20]. Along the x-axis, the stress can be expressed as

$$\begin{cases} (\tau_{31})_{x=0} = \dfrac{(3+2\nu)}{8(1+\nu)} \dfrac{F_x a^2}{I_y} \left(1 - \dfrac{1-2\nu}{3+2\nu} \dfrac{y^2}{a^2}\right), \\ (\tau_{23})_{x=0} = 0, \\ (\tau_{33})_{x=0} = \dfrac{F_z}{\pi a^2}. \end{cases} \tag{2.36}$$

Thus, we can obtain the piezoelectric polarization on the electrical contact as

$$\begin{cases} P_x = \dfrac{2F_x}{\pi a^2 E} e_{15}(1+2\nu), \\ P_y = 0, \\ P_z = \dfrac{F_z}{\pi a^2 E}(2\nu e_{31} - e_{33}). \end{cases} \tag{2.37}$$

The effect of piezoelectric polarization on the electrical contact will shift the Fermi level at the interface and modify the charge distribution profile, which subsequently affects the SBH. The change in SBH by piezoelectric polarization is given approximately by [21]

$$\Delta\phi_B = \frac{\sigma_{\mathrm{pol}}}{D} \left(1 + \frac{1}{2q_s w_d}\right)^{-1} \tag{2.38}$$

where σ_{pol} is the volume density of the polarization charges (in units of the electron charge q), which is given by $\sigma_{\mathrm{pol}} = -\vec{n} \cdot \vec{P}/q, \vec{n}$ is the unit vector along normal direction of the device surface, D is a two-dimensional density of interface states at the Fermi level in the semiconductor band gap at the Schottky barrier, and w_d is the width of the depletion layer. Associated with the states in the band gap at the interface is a two-dimensional screening parameter $q_s = (2\pi q^2/\kappa_0)D$. In the last relationship, q is the electronic charge and κ_0 is the dielectric constant of the semiconductor. Substituting (2.37) into (2.38), we obtain

$$\Delta\phi_B = -\frac{4\pi q w_d \{2(\vec{n}_x \cdot \vec{F}_x)e_{15}(1+2\nu) + (\vec{n}_z \cdot \vec{F}_z)(2\nu e_{31} - e_{33})\}}{\kappa_0(1 + 2(2\pi q^2/\kappa_0)D w_d)\pi a^2 E}. \tag{2.39}$$

It is very important that if we neglect the parallel component $\vec{F}_z$, from (2.37) and (2.39), the result agrees with the results of single ZnO/GaN nanowire nanogenerator that is transversely pushed by a conductive AFM tip. With $\vec{F}_x = 0$, this model is the working principle of a two-end bonded nanowire-based nanogenerator, piezoelectric diodes and piezo-phototronic device. From (2.39), the different position of the electrical contact is likely to affect the characteristics of the piezotronic devices. For the two-dimensional density of interface states D, in a large range from 1×10^{13} to 1×10^{18} $(\text{eV cm}^2)^{-1}$, the condition of $2(2\pi q^2/\kappa_0)Dw_d \ll 1$ always holds. Thus, (2.39) can be rewritten as

$$\Delta\phi_B = -\frac{4\pi q w_d\{2(\vec{n}_x \cdot \vec{F}_x)e_{15}(1+2\upsilon) + (\vec{n}_z \cdot \vec{F}_z)(2\upsilon e_{31} - e_{33})\}}{\kappa_0 \pi a^2 E}. \tag{2.40}$$

Then, if $w_d = 20$ nm, which is the typical value obtained from the experiments, $E = 129.0$ GPa, and $\upsilon = 0.349$, the trend of SBHs at different positions on the wire in responding to the applied strain can be obtained, as shown in Figs. 2.13(b)–(d). First of all, the change of SBHs has a linear relationship with strain. If the electrical contact is at positions A1 and A2, both SBHs will decrease with increasing strain but possessing different changing rate, as shown in Fig. 2.13(b). For contacting positions at B1 and B2, as shown in Fig. 2.13(c), we notice that the linear relations of the SBHs with strain have positive slope but with different magnitudes; the result has a reversed trend compared to that for contacting positions at A1 and A2. The change of SBHs on the electrical contact at C1 and C2 as plotted in Fig. 2.13(d) shows that the SBH at contact position C1 decreases and at C2 increases with increasing strain. These entirely different SBHs changes at different contacting positions will have remarkable effect on the devices transport properties.

2.8.2 Experimental Verification

We now present experimental observations on the piezopotential spatial distribution effect on electrical contact of ZnO microwire. The ultralong ZnO microwires used in our study were grown by a high-temperature thermal evaporation process. Three kinds of device were designed to present the idea, as shown in Fig. 2.14(a). The first one is the top electrode configuration. A ZnO microwire was first laid down on a polystyrene (PS) substrate, and then each end of the wire was fixed to the substrate using silver paste. This configuration corresponds to the case of making contacts at position A1 and A2. The second kind is the bottom electrode configuration. For this kind of device, a ZnO microwire was laid down on predefined electrodes on a Kapton film, and then the film will be attached to a PS substrate for manipulation. The microwire will be fixed to the Kapton film by the van der Waals force. This corresponds to the case of making electrical contact at positions B1 and B2. We called the third kind a fully enclosed electrodes configuration, which is the most conventional case. Compared to the second kind of contact, the third one adds a

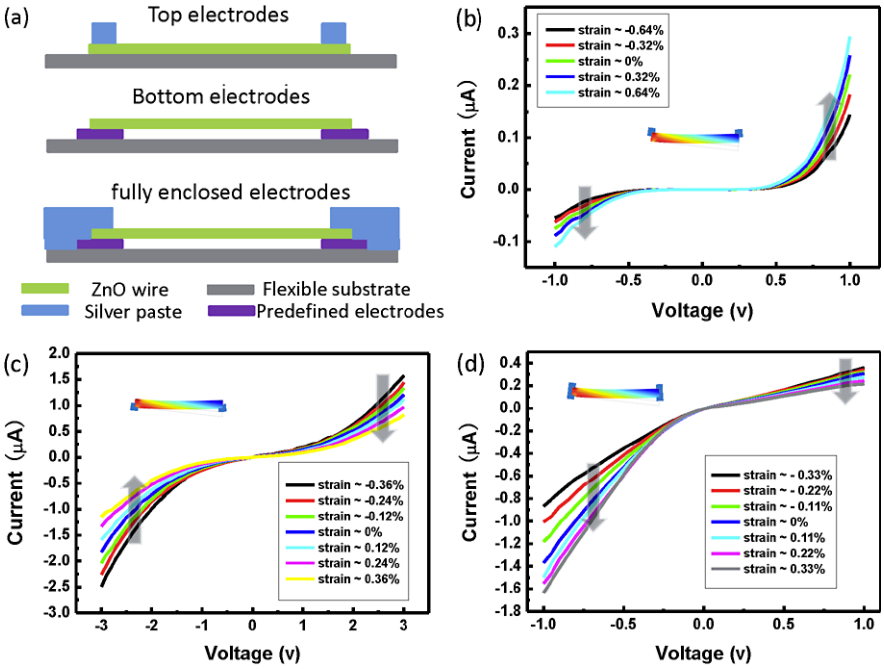

Fig. 2.14 (**a**) Schematic of three kinds of contact configuration to be examined experimentally, and the corresponding I–V characteristics as a function of the applied strain are to be presented in (**b**)–(**d**), respectively. (**b**) For the top electrode configuration, current increases in the entire voltage range with increasing of strain, but with different increasing rate in the negative and positive voltage ranges. (**c**) For the bottom electrode configuration, the current decreases in the entire voltage range with the increase of strain, but with different changing rate in the negative and positive voltage ranges. (**d**) For the fully enclosed electrode configuration, the current increases in the negative and decrease in the positive voltage range as the strain increases. The arrowheads indicate the trend of current change with the increase of the applied strain. The *insets* in (**b**)–(**d**) are the corresponding contacting configurations with the distribution of the strain presented [18]

silver paste covering the end of the microwire on the predefined electrode, making the end of the microwire fully surrounded by metal electrode. The electrical potential distribution on the side wall of the microwire cancels on average, and only the potential at the end surface has effect. This corresponds to the case of making contact at positions C1 and C2. For all of the devices, an additional very thin layer of polydimethylsiloxane (PDMS) was used to package the entire device, and it kept the device mechanically robust under repeated manipulation. The strain was introduced via bending the substrate by a precisely controlled linear stage with a motion resolution of 0.0175 μm. The piezo-response of these three kinds of device is shown in Figs. 2.14(b)–(d), respectively. For the top electrode configuration, according to the classic thermionic emission-diffusion theory [22], the change trend of SBHs at position A1 and A2, as shown in Fig. 2.13(b), will result in a current increase with increasing strain in the whole voltage range, but with different increasing rate in the

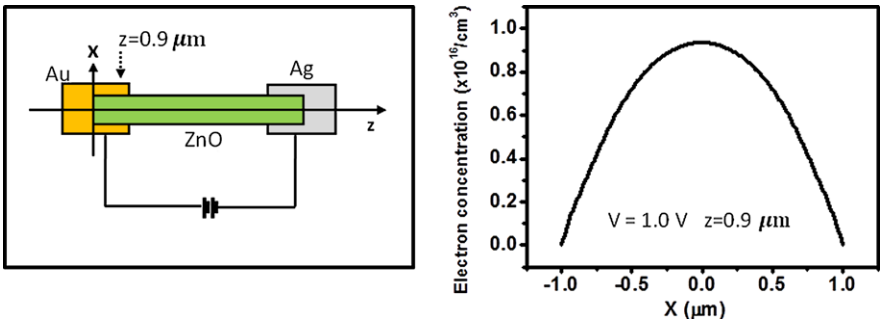

Fig. 2.15 The model and the carrier density distribution across a ZnO wire that is enclosed by an Au electrode as shown (at $z = 0.9$ μm, as indicated)

negative and positive voltage ranges. Besides this, a nonsymmetrical change of I–V curves in the positive and negative voltage ranges was observed, as predicted theoretically. For the device with bottom electrodes configuration, corresponding to the SBHs variation shown in Fig. 2.13(c), the current is decreased in the whole voltage range when the applied strain is increased, and nonsymmetrical variation characteristics were also observed due to the different positive slopes at contact position B1 and B2. When the fully enclosed electrodes are used, a pure nonsymmetrical change of I–V curves is observed, as shown in Fig. 2.14(d).

In summary, the effect of piezopotential spatial distribution on the electrical contact of the piezotronic devices has been studied. Using an external force that has a vertical and parallel component in reference to the nanowire length, the I–V transport behavior depends on the position at which the electrical contact is formed. A strategy is proposed for changing the device performance by tuning the piezopotential spatial distribution. This study has practical implication for understanding the I–V characteristic of piezotronic and piezo-phototronic devices by controlling local contact position and contact size.

2.9 Through-End Model for Current Transport

When a ZnO nanowire is in contact with a metal contact, the metal contact can wrap up the end of the nanowire. Here we analyze the current to be transported through the end surface in comparison to the side surface of the nanowire. Electrons are the major carriers in n-type ZnO nanowire and the electrode. We have used a computer simulation to find the distribution of carriers inside the wire once it is enclosed by an electrode [23]. According to semiconductor physics theory, the carrier distribution across the ZnO wire toward the end of the wire is shown in Fig. 2.15. The calculations were made by assuming: (1) the surface states in ZnO are ignored; and (2) the nanowire is n-type without p-type doping.

From the carrier profile, the carriers are mostly concentrated at the center of the wire. In such a case, the end surface is likely to pass through the most carriers if the

side contact area is not too much larger than the end surface in areas. Although the Schottky barrier is formed at both the end and side interfaces of ZnO nanowire with gold electrode, the barrier height can only be changed at the end surface due to the presence of polar charges.

There are two components of contributors to the conducting channels at the interface: the end surface of the wire and its side surface. If the area of contact for the side surface with the electrode is not too large in comparison to that of the end surface, with considering the equal potential of the electrode at the contact and the much higher conductivity of Au than ZnO as well as the distribution of the carriers, the current that is transported through the end surface of the wire is substantial for the entire structure. Thus, this component may be responsible to the effect/change we have observed here, while the current transported through the side surface may show little contribution. Therefore, our discussion in the future chapters only focuses on the contact of the metal with the end polar surfaces of ZnO.

References

1. H.J. Xiang, J.L. Yang, J.G. Hou, Q.S. Zhu, Piezoelectricity in ZnO nanowires: a first-principles study. Appl. Phys. Lett. **89**(22), 223111 (2006)
2. Z.C. Tu, X. Hu, Elasticity and piezoelectricity of zinc oxide crystals, single layers, and possible single-walled nanotubes. Phys. Rev. B **74**(3), 035434 (2006)
3. A.J. Kulkarni, M. Zhou, F.J. Ke, Orientation and size dependence of the elastic properties of zinc oxide nanobelts. Nanotechnology **16**(12), 2749–2756 (2005)
4. P.J. Michalski, N. Sai, E.J. Mele, Continuum theory for nanotube piezoelectricity. Phys. Rev. Lett. **95**(11), 116803 (2005)
5. Z.L. Wang, X.Y. Kong, Y. Ding, P.X. Gao, W.L. Hughes, R.S. Yang, Y.S. Zhang, Semiconducting and piezoelectric oxide nanostructures induced by polar surfaces. Adv. Funct. Mater. **14**(10), 943–956 (2004)
6. J.F. Nye, *Physical Properties of Crystals* (Oxford University Press, Oxford, 1957)
7. Q.H. Qin, *Fracture Mechanics of Piezoelectric Materials* (WIT Press, Southampton, 2001)
8. Y.F. Gao, Z.L. Wang, Electrostatic potential in a bent Piezoelectric nanowire. The fundamental theory of nanogenerator and nanopiezotronics. Nano Lett. **7**(8), 2499–2505 (2007)
9. R.W. Soutas-Little, *Elasticity* (Dover, Mineola, 1999)
10. J. Zhou, P. Fei, Y.F. Gao, Y.D. Gu, J. Liu, G. Bao, Z.L. Wang, Mechanical–electrical triggers and sensors using piezoelectric micowires/nanowires. Nano Lett. **8**(9), 2725–2730 (2008)
11. Z.Y. Gao, J. Zhou, Y.D. Gu, P. Fei, Y. Hao, G. Bao, Z.L. Wang, Effects of piezoelectric potential on the transport characteristics of metal–ZnO nanowire–metal field effect transistor. J. Appl. Phys. **105**(11), 113707 (2009)
12. C.S. Lao, J. Liu, P.X. Gao, L.Y. Zhang, D. Davidovic, R. Tummala, Z.L. Wang, ZnO nanobelt/nanowire Schottky diodes formed by dielectrophoresis alignment across Au electrodes. Nano Lett. **6**(2), 263–266 (2006)
13. Y.F. Gao, Z.L. Wang, Equilibrium potential of free charge carriers in a bent piezoelectric semiconductive nanowire. Nano Lett. **9**(3), 1103–1110 (2009)
14. F. Sacconi, A. Di Carlo, P. Lugli, H. Morkoc, Spontaneous and piezoelectric polarization effects on the output characteristics of AlGaN/GaN heterojunction modulation doped FETs. IEEE Trans. Electron Devices **48**(3), 450–457 (2001)
15. W. Shan, W. Walukiewicz, J.W. Ager, K.M. Yu, Y. Zhang, S.S. Mao, R. Kling, C. Kirchner, A. Waag, Pressure-dependent photoluminescence study of ZnO nanowires. Appl. Phys. Lett. **86**(15), 153117 (2005)

16. G. Mantini, Y.F. Gao, A. D'Amico, C. Falconi, Z.L. Wang, Equilibrium piezoelectric potential distribution in a deformed ZnO nanowire. Nano Res. **2**, 624–629 (2009)
17. M.P. Lu, J.H. Song, M.Y. Lu, M.T. Chen, Y.F. Gao, L.F. Chen, Z.L. Wang, Piezoelectric nanogenerator using p-type ZnO nanowire arrays. Nano Lett. **9**(3), 1223–1227 (2009)
18. Y. Zhang, Y.F. Hu, S. Xiang, Z.L. Wang, Effects of piezopotential spatial distribution on local contact dictated transport property of ZnO micro/nanowires. Appl. Phys. Lett. **97**(3), 033509 (2010)
19. G.A. Maugin, *Continuum Mechanics of Electromagnetic Solids* (North-Holland, Amsterdam, 1988)
20. R.W. Soutas-Little, *Elasticity*, vol. XVI (Dover, Mineola, 1999), p. 431
21. K.W. Chung, Z. Wang, J.C. Costa, F. Williamsion, P.P. Ruden, M.I. Nathan, Barrier height change in GaAs Schottky diodes induced by piezoelectric effect. Appl. Phys. Lett. **59**(10), 1191 (1991)
22. S.M. Sze, *Physics of Semiconductor Devices* (Wiley, New York, 1981)
23. J.H. Song, Y. Zhang, C. Xu, W.Z. Wu, Z.L. Wang, Polar charges induced electric hysteresis of ZnO nano/microwire for fast data storage. Nano Lett. **11**(7), 2829–2834 (2011)

Chapter 3
Basic Theory of Piezotronics

Abstract Using the basic transport equations, this chapter gives the theory of charge transport in piezotronic devices. Besides presenting the formal theoretical frame work, analytical solutions are presented for cases like the metal–semiconductor contact and p–n junction under simplified conditions. Numerical calculations are given for predicting the current–voltage characteristics of a general piezotronic transistor: metal–ZnO nanowire–metal device. This study is important for understanding the working principle and characteristics of piezotronic devices, but also for providing guidance for device design.

Due to the coupling of piezoelectric and semiconducting properties, nano/microwires of piezoelectric semiconductor have been used as basic building blocks for fabricating various innovative devices, such as nanogenerators [1–3], piezoelectric field effect transistors [4], piezoelectric diodes [5], piezoelectric chemical sensors [6], and piezo-phototronic devices [7, 8]. Take a ZnO nanowire as an example. When a tensile strain is applied along the nanowire that grows in the *c*-axis direction, piezoelectric charges are created at its two ends, forming a piezoelectric potential inside the nanowire. This potential tunes the contact of the nanowire with the electrodes by changing the height of the local Schottky barrier, thus, the transport behavior of the charge carriers in the nanowire is controlled/tuned by the externally applied strain. This is the piezotronic effect. Electronics fabricated by using the inner-crystal piezopotential as a "gate" voltage to tune/control the charge transport behavior across a metal–semiconductor interface or a p–n junction is named *piezotronics*, which is different from the basic design of CMOS field effect transistor, and it has applications in force/pressure triggered/controlled electronic devices, sensors, MEMS, human–computer interfacing, nanorobotics and touch-pad technologies.

In this chapter, we present a fundamental theoretical framework of piezotronics for understanding and quantitatively calculating the carrier transport behavior in the devices [9]. We first give some analytical solutions for ZnO piezoelectric p–n junction and metal–semiconductor (M–S) contact under simplified conditions, which are useful for understanding the piezotronic behavior in general. Furthermore, using the FEM, the characteristics of a piezotronic transistor, ZnO nanowire metal–semiconductor–metal (M–S–M) structure, are simulated. The theoretical re-

Z.L. Wang, *Piezotronics and Piezo-Phototronics*, Microtechnology and MEMS,
DOI 10.1007/978-3-642-34237-0_3, © Springer-Verlag Berlin Heidelberg 2012

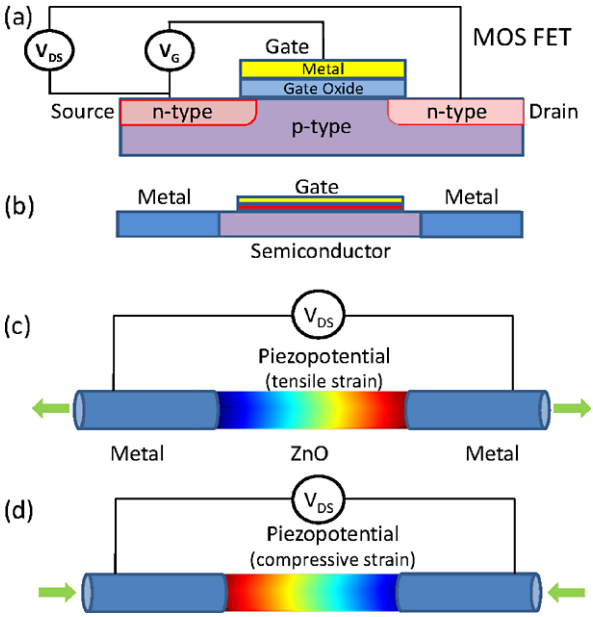

Fig. 3.1 Schematic of (**a**) an n-channel MOS FET and (**b**) a semiconductor nanowire FET; schematic of a piezotronic transistor with tensile strain (**c**) and compressive strain (**d**), where the gate voltage that controls the channel width is replaced by a piezopotential that controls the transport across the metal–semiconductor interface [9]

sults establish the basic physics for understanding the observed experimental results from piezotronic devices and guiding future device design.

3.1 Piezotronic Transistor vs. Traditional Field Effect Transistor

In order to illustrate the basic concept of piezotronics, we first start from a traditional metal oxide semiconductor field-effect transistor (MOS FET). For an n-channel MOS FET (Fig. 3.1(a)), the two n-type doped regions are the drain and source; a thin insulator oxide layer is deposited on the p-type region to serve as the gate oxide, on which a metal contact is made as the gate. The current flowing from the drain to source under an applied external voltage V_{DS} is controlled by the gate voltage V_G, which controls the channel width for transporting the charge carriers. In analogy, for a single channel FET fabricated using a semiconductor NW (Fig. 3.1(b)), the drain and source are the two metal electrodes at the two ends, and a gate voltage is applied at the top of the NW or through the base substrate.

A piezotronic transistor is a metal–NW–metal structure, such as Au–ZnO–Au or Ag–ZnO–Ag as shown in Fig. 3.1(c) and (d) [9]. The fundamental principle of the piezotronic transistor is to control the carrier transport at the M–S interface through a tuning at the local contact by creating a piezopotential at the interface region in the semiconductor by applying a strain. This structure is different from the CMOS design as stated in follows. First, the externally applied gate voltage is replaced by an inner-crystal potential generated by piezoelectric effect, thus, the "gate" electrode is eliminated. This means that the piezotronic transistor only has two leads: drain and

source. Secondly, the control over channel width is replaced by a control at the interface. Since the current transported across a M–S interface is the exponential of the local barrier height at the reversely biased case, the ON and OFF ratio can be rather high due to the non-linear effect. Finally, a voltage controlled device is replaced by an external strain/stress controlled device, which is likely to have complementary applications to CMOS devices.

When a ZnO NW device is under strain, there are two typical effects that may affect the carrier transport process. One is the piezoresistance effect because of the change in band gap, charge carrier density and possibly density of states in the conduction band of the semiconductor crystal under strain. This effect is a symmetric effect on the two end contact and has no polarity, which will not produce the function of a transistor. Piezoresistance is a common feature of any semiconductors such as Si and GaAs and is not limited to the wurtzite family. The other is the piezoelectric effect because of the polarization of ions in a crystal that has non-central symmetry, which has an asymmetric or non-symmetric effect on the local contacts at the source and drain owing to the polarity of the piezopotential. In general, the negative piezopotential side raises the barrier height at the local contact of metal n-type semiconductor, possibly changing a Ohmic contact to a Schottky contact, a Schottky contact to an "insulator" contact; while the positive piezopotential side lowers the local barrier height, changing a Schottky contact to an Ohmic contact. But the degree of changes in the barrier heights depends on the doping type and doping density in the NW. The piezoelectric charges are located at the ends of the wire, thus they directly affect the local contacts. The piezotronic effect is likely limited to the wurtzite family such as ZnO, GaN, CdS and InN. It is important to point out that the polarity of the piezopotential can be switched by changing tensile strain to compressive strain. Thus, the device can be changed from a control at source to a control at drain simply by reversing the sign of strain applied to the device.

3.2 Effect of Piezopotential on Metal–Semiconductor Contact

When a metal and a n-type semiconductor forms a contact, a Schottky barrier (SB) ($e\phi_{SB}$) is created at the interface if the work function of the metal is appreciably larger than the electron affinity of the semiconductor (Fig. 3.2(a)). Current can only pass through this barrier if the applied external voltage is larger than a threshold value (ϕ_i) and its polarity is at the metal side positive (for n-type semiconductor). If a photon excitation is applied at the interface, the newly generated electrons in conduction band tend to move away from the contact, while the holes tend to move close to the interface toward the metal side. The accumulated holes at the interface modify the local potential profile, so that the effective height of the Schottky barrier is lowered (Fig. 3.2(b)), which increases the conductance.

Once a strain is created in a semiconductor that also has the piezoelectric property, a negative piezopotential at the semiconductor side effectively increases the local SB height to $e\phi'$ (Fig. 3.2(c)) [10], while a positive piezopotential reduces

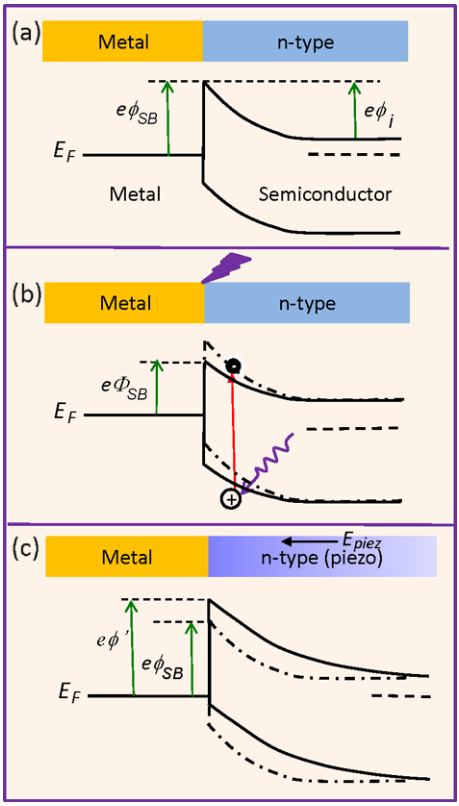

Fig. 3.2 Energy band diagram for illustrating the effects of laser excitation and piezoelectricity on a Schottky contacted metal–semiconductor interface. (**a**) Band diagram at a Schottky contacted metal–semiconductor interface. (**b**) Band diagram at a Schottky contact after exciting by a laser that has a photon energy higher than the bandgap, which is equivalent to a reduction in the Schottky barrier height. (**c**) Band diagram at the Schottky contact after applying a strain in the semiconductor. The piezopotential created in the semiconductor has a polarity with the end in contact with the metal being low [10]

the barrier height. The role played by the piezopotential is to effectively change the local contact characteristics through an internal field depending on the crystallographic orientation of the material and the sign of the strain, thus, the charge carrier transport process is tuned/gated at the metal–semiconductor (M–S) contact. Considering the change in piezopotential polarity by switching the strain from tensile to compressive, the local contact characteristics can be tuned and controlled by the magnitude of the strain and the sign of strain [11]. Therefore, the charge transport across the interface can be largely dictated by the created piezopotential, which is the gate effect. This is the core of piezotronics.

On the other hand, if we excited a MS contact by photons that have an energy larger than the bandgap of the semiconductor, electron-hole pairs are generated at the vicinity of the contact. The presence of free carriers at the interface can effectively reduce the Schottky-barrier height. Therefore, piezopotential can increase the local barrier height, while laser excitation can effectively reduce the local barrier height. The two effects can be applied in a complementary way for controlling the charge transport at the interface. This is a coupling between piezoelectricity and photon excitation.

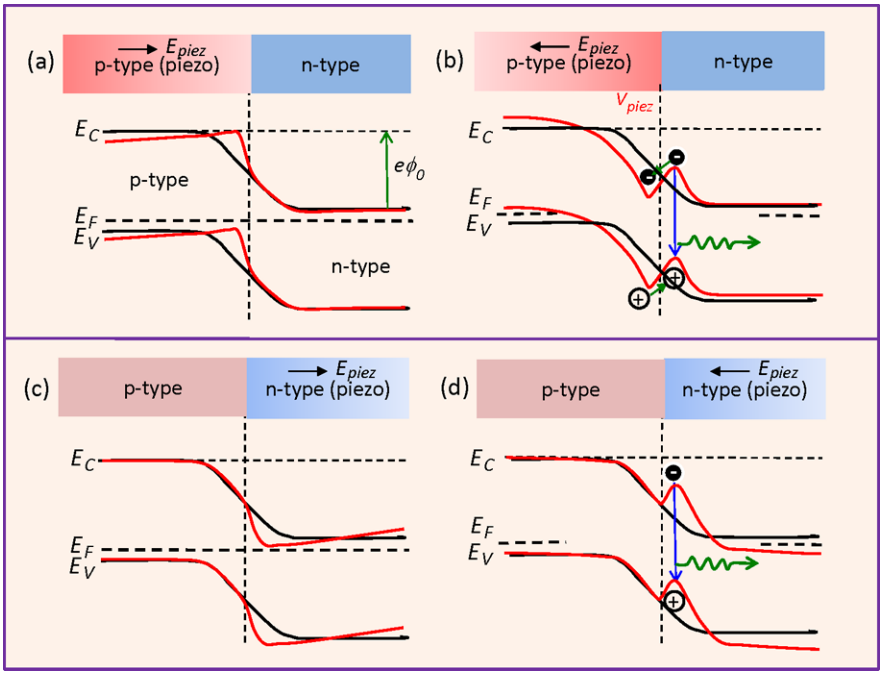

Fig. 3.3 Energy band diagram for illustrating the effect of piezoelectricity on a p–n junction that is made of two materials of similar bandgaps. The band diagrams for the p–n junction with and without the presence of piezoelectric effect for the four possible cases are shown using dark and red curves, respectively. The bandgap for the n-type and p-type are assumed to be about equal. The effect of reversal in polarity is presented [10]

3.3 Effect of Piezopotential on p–n Junction

When a p-type and a n-type semiconductors form a junction, the holes in the p-type side and the electrons in the n-type side tend to redistribute to balance the local potential, the interdiffusion and recombination of the electrons and holes in the junction region forms a charge depletion zone. The presence of such a carrier free zone can significantly enhance the piezoelectric effect, because the piezo-charges will be mostly preserved without being screened by local residual free carriers. As shown in Fig. 3.3(a), for a case that the p-type side is piezoelectric and a strain is applied, local net negative piezo-charges are preserved at the junction provided the doping is relatively low so that the local free carriers are not enough to fully screen the piezo-charges. The piezopotential tends to raise the local band slightly and introduce a slow slope to the band structure. Alternatively, if the applied strain is switched in sign (Fig. 3.3(b)), the positive piezo-charges at the interface creates a dip in the local band. A modification in the local band may be effective for trapping the holes so that the electron-hole recombination rate can be largely enhanced, which is very beneficial for improving the efficiency of an LED [12]. Furthermore, the inclined band tends to change the mobility of the carriers moving toward the junction.

By the same token, if the n-type side is piezoelectric, a similar band structure change can be induced from the piezoelectric effect, as shown in Figs. 3.3(c), (d). The band structure modification at the interface/junction by piezoelectric charges introduces some fundamental changes to the local band structure, which is effective for controlling the device performance.

For a p–n junction made of two materials with distinctly different bandgaps, local piezo-charges can also significantly affect the band profile, as shown in Fig. 3.4 [13], so that the transport of the charge carriers across the interface will be significantly modified. Take the case shown in Fig. 3.4(e) as an example: the barrier height at the interface as created by band misalignment can be reduced so that the electrons can be effectively transported across the interface. For the case of Fig. 3.4(f), the height and width of the barrier at the interface are increased by piezo-charges. As for the case presented in Fig. 3.4(b), the local trapping of holes can be significantly increased, which may be beneficial for LED. But for the case in Fig. 3.4(a), it may have negative effect on LED efficiency. Therefore, the presence of piezo-charges at the junction can be useful for some optoelectronic processes.

3.4 Theoretical Frame of the Piezotronic Effect

Since a piezotronic transistor involves a semiconductor that is piezoelectric, the fundamental governing equations for both semiconductor and piezoelectric theories are required. The basic equations for piezotronics are electrostatic equations, current–density equations, and continuity equations, which describe the static and dynamic transport behavior of the charge carriers in semiconductors [14–16], as well as the piezoelectric equations, which describe the piezoelectric behavior of the material under dynamic straining [18].

The Poisson equation is the basic equation for describing the electrostatic behavior of charges:

$$\nabla^2 \psi_i = -\frac{\rho(\mathbf{r})}{\varepsilon_s} \tag{3.1}$$

where ψ_i is the electric potential distribution and $\rho(\mathbf{r})$ is the charge density distribution, ε_s is the permittivity of the material.

The current–density equations that correlate the local fields, charge densities and local currents are

$$\begin{cases} \mathbf{J}_n = q\mu_n n\mathbf{E} + qD_n \nabla n, \\ \mathbf{J}_p = q\mu_p p\mathbf{E} - qD_p \nabla p, \\ \mathbf{J}_{\text{cond}} = \mathbf{J}_n + \mathbf{J}_p \end{cases} \tag{3.2}$$

where $\mathbf{J}_n$ and $\mathbf{J}_p$ are the electron and hole current densities, q is the absolute value of unit electronic charge, μ_n and μ_p are electron and hole mobilities, n and p are concentrations of free electrons and free holes, D_n and D_p are diffusion coefficients for electrons and holes, respectively, $\mathbf{E}$ is the electric field, and $\mathbf{J}_{\text{cond}}$ is the total current density.

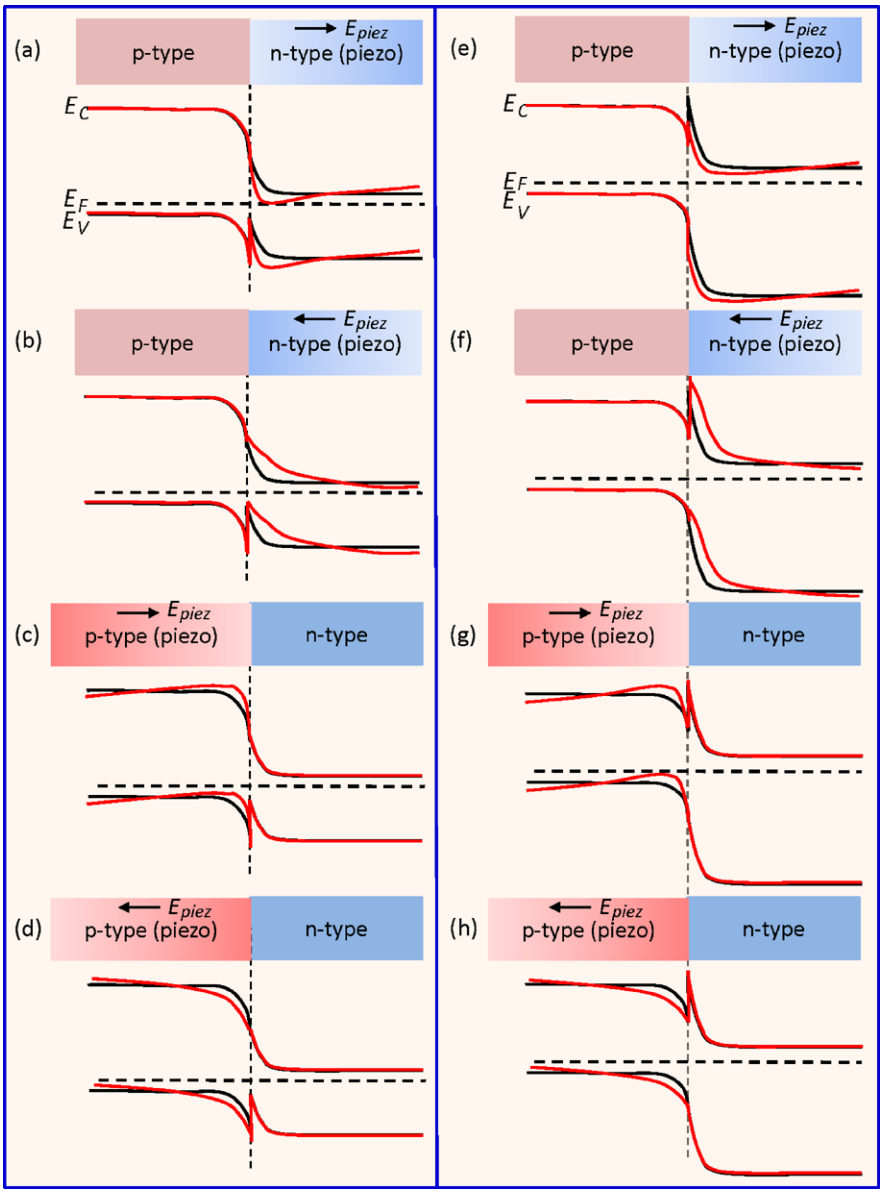

Fig. 3.4 Energy band diagram for illustrating the effect of piezoelectricity on a heterostructured p–n junction. The band diagrams for the p–n junction with and without the presence of piezoelectric effect for the eight possible cases are shown using *dark* and *red curves*, respectively. The effect of reversal in polarity is also presented [13]

The charge transport under the driving of a field is described by the continuity equations.

$$\begin{cases} \dfrac{\partial n}{\partial t} = G_n - U_n + \dfrac{1}{q}\nabla \cdot \mathbf{J}_n, \\ \dfrac{\partial p}{\partial t} = G_p - U_p - \dfrac{1}{q}\nabla \cdot \mathbf{J}_p \end{cases} \tag{3.3}$$

where G_n and G_p are the electron and hole generation rates, U_n and U_p are the recombination rates, respectively.

The piezoelectric behavior of the material is described by a polarization vector $\mathbf{P}$. For a small uniform mechanical strain S_{ik}, the polarization $\mathbf{P}$ vector is given in terms of strain $\mathbf{S}$ as

$$(\mathbf{P})_i = (\mathbf{e})_{ijk}(\mathbf{S})_{jk} \tag{3.4}$$

where the third order tensor $(\mathbf{e})_{ijk}$ is the piezoelectric tensor. According to the conventional theory of piezoelectric and elasticity, the constituting equations can be written as

$$\begin{cases} \boldsymbol{\sigma} = \mathbf{c}_E\mathbf{S} - \mathbf{e}^{\mathbf{T}}\mathbf{E}, \\ \mathbf{D} = \mathbf{e}\mathbf{S} + \mathbf{k}\mathbf{E} \end{cases} \tag{3.5}$$

where $\boldsymbol{\sigma}$ is the stress tensor, $\mathbf{E}$ is the electric field, $\mathbf{D}$ is the electric displacement, $\mathbf{c}_E$ is the elasticity tensor, and $\mathbf{k}$ is the dielectric tensor.

3.5 Analytical Solution for One-Dimensional Simplified Cases

In practical device modeling, the above basic equations can be solved under specific boundary conditions. For simplicity of illustrating the basic physics, we consider an one-dimension piezotronic device with ideal Ohmic contacts at the source and drain. This means that the Dirichlet boundary conditions of the carrier concentration and electrical potential will be applied at the device boundaries. The strain is applied normal to the M–S interface without introducing shear strain.

3.5.1 Piezoelectric p–n Junctions

The p–n junctions are most fundamental building blocks in modern electronic devices. Shockley theory provides the basic theory of current–voltage (I–V) characteristics of the p–n junctions. For better understanding about piezoelectric p–n junction, we describe the physics of the semiconductor using Shockley theory. For simplicity, we assume that the p-type region is non-piezoelectric and the n-type region is piezoelectric. Considering that ZnO grows along the direction of c-axis, the positive charges are created at the n-type side of the p–n junction by applying a compressive stress along the c-axis. For convenience in using piezoelectric theory, the piezoelectric charges are considered as surface charge at the bulk piezoelectric

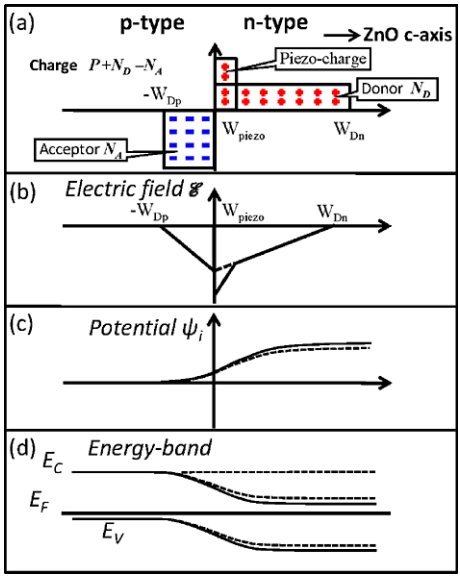

Fig. 3.5 Piezoelectric p–n junction with the presence of piezoelectric charges at applied voltage $V = 0$ (thermal equilibrium). (**a**) Piezoelectric charges, acceptor and donor charges distribution; (**b**) electric field; (**c**) potential distribution and (**d**) energy band diagram with the presence of piezoelectric charges. *Dashed lines* indicate electric field, potential and energy band in the absence of piezoelectric charges, and the *solid lines* are for the cases when a piezopotential is present at the n-type side

material, because the region within which the piezoelectric polarization charge distributes is much smaller than the volume of the bulk crystal, so it is reasonable to assume that the piezoelectric charges are distributed at a surface of zero thickness. But such an assumption is not valid for nanodevices and even microdevices. We assume that the piezoelectric charges distribute at the interface of the p–n junction within a width of W_{piezo} (Fig. 3.5(a)).

We use an abrupt junction model, in which the impurity concentration in a p–n junction changes abruptly from acceptor N_A to donor N_D, as shown in Fig. 3.5(a). The electrons and holes in the junction region form a charge depletion zone, which is assumed to have a box profile. We first calculate the electric field and potential distribution inside the p–n junction. For one-dimensional device, the Poisson equation (3.1) reduces to

$$-\frac{d^2\psi_i}{dx^2} = \frac{dE}{dx} = \frac{\rho(x)}{\varepsilon_s} = \frac{1}{\varepsilon_s}\left[qN_D(x) - qn(x) - qN_A(x) + qp(x) + q\rho_{\text{piezo}}(x)\right] \tag{3.6}$$

where $N_D(x)$ is the donor concentration, $N_A(x)$ is the acceptor concentration, and $\rho_{\text{piezo}}(x)$ is density of polarization charges (in units of electron charge). W_{Dp} and W_{Dn} are defined to be the depletion-layer widths in the p-side and the n-side, respectively. The electric field is then obtained by integrating the above equations, as shown in Fig. 3.5(b):

$$E(x) = -\frac{qN_A(x + W_{Dp})}{\varepsilon_s}, \quad \text{for } -W_{Dp} \le x \le 0, \tag{3.7a}$$

$$E(x) = -\frac{q[N_D(W_{Dn} - x) + \rho_{\text{piezo}}(W_{\text{piezo}} - x)]}{\varepsilon_s}, \quad \text{for } 0 \le x \le W_{\text{piezo}}, \tag{3.7b}$$

$$E(x) = -\frac{qN_D}{\varepsilon_s}(W_{Dn} - x), \quad \text{for } W_{\text{piezo}} \le x \le W_{Dn}. \tag{3.7c}$$

The maximum field E_m that exists at $\mathbf{x} = 0$ is given by

$$|E_m| = \frac{q(N_D W_{Dn} + \rho_{\text{piezo}} W_{\text{piezo}})}{\varepsilon_s}. \tag{3.8}$$

The potential distribution $\psi_i(x)$ is (as shown in Fig. 3.5(c))

$$\psi_i(x) = \frac{qN_A(x + W_{Dp})^2}{2\varepsilon_s}, \quad \text{for } -W_{Dp} \le x \le 0, \tag{3.9a}$$

$$\psi_i(x) = \psi_i(0) + \frac{q}{\varepsilon_s}\left[N_D\left(W_{Dn} - \frac{x}{2}\right)x + \rho_{\text{piezo}}\left(W_{\text{piezo}} - \frac{x}{2}\right)x\right], \quad \text{for } 0 \le x \le W_{\text{piezo}}, \tag{3.9b}$$

$$\psi_i(x) = \psi_i(W_{\text{piezo}}) - \frac{qN_D}{\varepsilon_s}\left(W_{Dn} - \frac{W_{\text{piezo}}}{2}\right)W_{\text{piezo}} + \frac{qN_D}{\varepsilon_s}\left(W_{Dn} - \frac{x}{2}\right)x, \quad \text{for } W_{\text{piezo}} \le x \le W_{Dn}. \tag{3.9c}$$

Thus, the built-in potential ψ_{bi} is given by

$$\psi_{bi} = \frac{q}{2\varepsilon_s}\left(N_A W_{Dp}^2 + \rho_{\text{piezo}} W_{\text{piezo}}^2 + N_D W_{Dn}^2\right). \tag{3.10}$$

Equation (3.10) presents the change in built-in potential as a result of piezoelectric charges due to tensile or compressive straining that defines the sign of the local piezoelectric charges. It is apparent that the piezopotential can change the semiconductor energy band relative to the Fermi level.

Next, we analyze the current–voltage characteristics of a piezoelectric p–n junction by using Shockley theory, which models an ideal junction based on four assumptions: (1) a piezoelectric p–n junction has an abrupt depletion layer; (2) piezoelectric semiconductors are nondegenerate so that the Boltzmann approximation applies; (3) the injected minority carrier concentration is smaller than the majority-carrier concentration so the low-injection assumption is valid; and (4) no generation-recombination current exists inside the depletion layer, and the electron and hole currents are constant throughout the p–n junction. If the width of the piezo-charges is much less than the width of the depletion zone, e.g., $W_{\text{piezo}} \ll W_{Dn}$, the effect of piezoelectric charges on ZnO energy band is considered as a perturbation. The total current density can be obtained by solving (3.2):

$$J = J_p + J_n = J_0\left[\exp\left(\frac{qV}{kT}\right) - 1\right] \tag{3.11}$$

where the saturation current

$$J_0 = \frac{qD_p p_{no}}{L_p} + \frac{qD_n n_{po}}{L_n},$$

p_{no} is the thermal equilibrium hole concentration in n-type semiconductor and n_{po} is the thermal equilibrium electron concentration in p-type semiconductor, and L_p and L_n are diffusion lengths of electrons and holes, respectively. The intrinsic carrier density n_i is given by

$$n_i = N_C \exp\left(-\frac{E_C - E_i}{kT}\right) \tag{3.12}$$

where N_C is the effective density of states in the conduction band, E_i is the intrinsic Fermi level, and E_C is the bottom edge of the conduction band.

For the simple case in which the n-type side has an abrupt junction with donor concentration N_D, and locally $p_{n0} \gg n_{p0}$, we have $J_0 \approx \frac{qD_p p_{no}}{L_p}$, where $p_{no} = n_i \exp(\frac{E_i - E_F}{kT})$, the total current density is given by

$$J = J_0\left[\exp\left(\frac{qV}{kT}\right) - 1\right] = \frac{qD_p n_i}{L_p}\exp\left(\frac{E_i - E_F}{kT}\right)\left[\exp\left(\frac{qV}{kT}\right) - 1\right]. \tag{3.13}$$

If J_{C0} and E_{F0} are defined to be the saturation current density and the Fermi level with the absence of piezopotential,

$$J_{C0} = \frac{qD_p n_i}{L_p}\exp\left(\frac{E_i - E_{F0}}{kT}\right). \tag{3.14}$$

According to (3.9a)–(3.9c), and (3.10), the Fermi lever E_F with the presence of piezopotential is given by

$$E_F = E_{F0} - \frac{q^2 \rho_{\text{piezo}} W_{\text{piezo}}^2}{2\varepsilon_s}. \tag{3.15}$$

Substituting (3.14) and (3.15) into (3.13), we obtain the current–voltage characteristics of the piezoelectric p–n junction [9]:

$$J = J_{C0}\exp\left(\frac{q^2 \rho_{\text{piezo}} W_{\text{piezo}}^2}{2\varepsilon_s kT}\right)\left[\exp\left(\frac{qV}{kT}\right) - 1\right]. \tag{3.16}$$

This means that the current transported across the p–n junction is an exponential function of the local piezo-charges, the sign of which depends on the strain. Therefore, the current to be transported can be effectively tuned or controlled not only by the magnitude of the strain, but also by the sign of the strain (tensile vs. compressive). This is the mechanism of the p–n junction-based piezotronic transistor.

3.5.2 Metal–Semiconductor Contact

The M–S contact is an important component in electronic devices. Similar to our analysis to the piezoelectric p–n junction, the M–S contact can be simplified in the

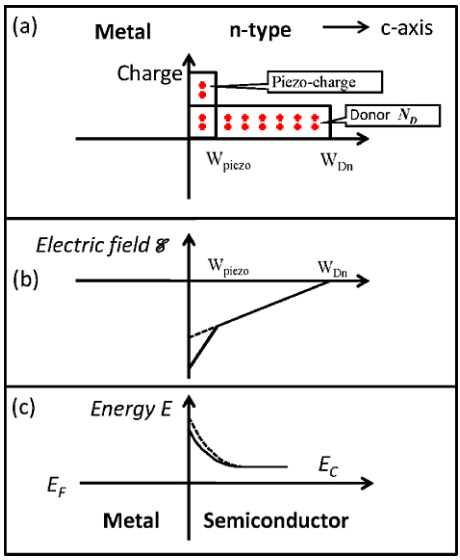

Fig. 3.6 Ideal metal–semiconductor Schottky contacts with the presence of piezoelectric charges at applied voltage $V = 0$ (thermal equilibrium). (**a**) Space charges distribution; (**b**) electric field and (**c**) energy band diagram with the presence of piezoelectric charges. *Dashed lines* indicate electric field and energy band in the absence of piezoelectric charges, and the *solid lines* are for the cases when a piezopotential is present in the semiconductor

charge distribution as shown in Fig. 3.6(a) in the presence of a Schottky barrier. The semiconductor side is assumed to be n-type, and the surface states and other anomalies are ignored for simplification. Under straining, the created piezo-charges at the interface not only change the height of the Schottky barrier, but also its width. Different from the method of changing the SBH by introducing dopants at the semiconductor side, the piezopotential can be *continuously* tuned by strain for a fabricated device.

There are several theories for the M–S Schottky contact, including thermionic-emission theory, diffusion theory and thermionic-emission-diffusion theory. Although the diffusion model is taken as an example for clearly describe the mechanism of piezotronic effect in this paper, the presented methodology also applies to thermionic-emission and thermionic-emission-diffusion model, etc.

The carrier transport in M–S contact is dominated by the majority carriers. The current density equation (3.2) can be rewritten as

$$J = J_n = q\mu_n nE + qD_n \frac{dn}{dx} \tag{3.17}$$

where

$$E = \frac{d\psi_i}{dx} = \frac{dE_c}{dx}.$$

According to the diffusion theory by Schottky, the solutions under forward bias (metal is positive bias) can be obtained as [15]

$$J_n \approx J_D \exp\left(-\frac{q\phi_{Bn}}{kT}\right)\left[\exp\left(\frac{qV}{kT}\right) - 1\right] \tag{3.18}$$

where

$$J_D = \frac{q^2 D_n N_C}{kT} \sqrt{\frac{2qN_D(\psi_{bi} - V)}{\varepsilon_s}} \exp\left(-\frac{q\phi_{Bn}}{kT}\right)$$

is the saturation current density. We define J_{D0} is the saturation current density in the absence of piezoelectric charges:

$$J_{D0} = \frac{q^2 D_n N_C}{kT} \sqrt{\frac{2qN_D(\psi_{bi0} - V)}{\varepsilon_s}} \exp\left(-\frac{q\phi_{Bn0}}{kT}\right) \tag{3.19}$$

where ψ_{bi0} and ϕ_{Bn0} are built-in potential and Schottky-barrier height in the absence of piezoelectric charges. In our case, the effect of piezoelectric charge can be considered as a perturbation to the conduction-band edge E_C. The change in effective Schottky-barrier height induced by piezoelectric charges can be derived from the potential distribution equations (3.9a)–(3.9c), and (3.10):

$$\phi_{Bn} = \phi_{Bn0} - \frac{q^2 \rho_{\text{piezo}} W_{\text{piezo}}^2}{2\varepsilon_s}. \tag{3.20}$$

Thus, the current density can be rewritten as

$$J_n \approx J_D \exp\left(\frac{q^2 \rho_{\text{piezo}} W_{\text{piezo}}^2}{2\varepsilon_s kT}\right)\left[\exp\left(\frac{qV}{kT}\right) - 1\right]. \tag{3.21}$$

This means that the current transported across the M–S contact is an exponential function of the local piezo-charges, the sign of which depends on the strain. Therefore, the current to be transported can be effectively tuned or controlled by not only the magnitude of the strain, but also by the sign of the strain (tensile vs. compressive). This is the mechanism of the piezotronic transistor for M–S case.

3.5.3 Metal–Wurtzite Semiconductor Contact

We now expand the result received in Sect. 3.4 for a special case of metal–wurtzite semiconductor contact, such as Au–ZnO or Ag–ZnO. For the ZnO nanowire grown along c-axis, the piezocoefficient matrix is written as

$$(\mathbf{e})_{ijk} = \begin{pmatrix} 0 & 0 & 0 & 0 & e_{15} & 0 \\ 0 & 0 & 0 & e_{15} & 0 & 0 \\ e_{31} & e_{31} & e_{33} & 0 & 0 & 0 \end{pmatrix}.$$

If the created strain is strain s_{33} along the c-axis, the piezoelectric polarization can be obtained from (3.4) and (3.5):

$$P_z = e_{33} s_{33} = q\rho_{\text{piezo}} W_{\text{piezo}}. \tag{3.22}$$

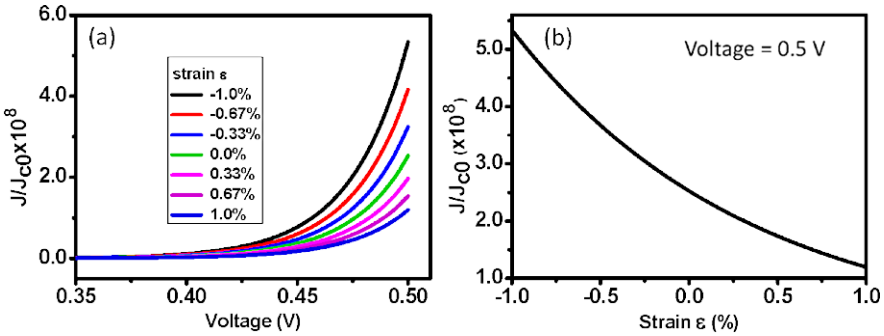

Fig. 3.7 The current–voltage characteristics of an ideal metal–semiconductor Schottky contact in the presence of piezoelectric charges. (**a**) Current–voltage curves at various strain from −1 % to 1 %; (**b**) relative current density as a function of strain at a fixed forward bias voltage of 0.5 V

The current density is

$$J = J_{D0} \exp\left(\frac{q e_{33} s_{33} W_{\text{piezo}}}{2\varepsilon_s kT}\right)\left[\exp\left(\frac{qV}{kT}\right) - 1\right]. \tag{3.23}$$

It is clear that the current transported across the M–S interface is directly related to the exponential of the local strain, which means that the current can be tuned on or off by controlling strain.

For numerical calculation, the material constants are piezoelectric constants $e_{33} = 1.22\ \text{C/m}^2$ and relative dielectric constant is $\varepsilon_s = 8.91$. The width of the piezocharges is $W_{\text{piezo}} = 0.25$ nm. The temperature is $T = 300$ K. Figure 3.7(a) shows the calculated J/J_{D0} as a function of the externally applied voltage V across the M–S interface as a function of the strain, clearly demonstrating its tuning effect on the transported current. When the external voltage is fixed at $V = 0.5$ V at forward bias, J/J_{D0} decreases when the strain changes from −1 % to 1 % (Fig. 3.7(b)). The theoretical result agrees qualitatively with our previous experiments. For reverse bias case, the dominant voltage dependence is mainly due to the change of Schottky barrier in our model.

3.6 Numerical Simulation of Piezotronic Devices

3.6.1 Piezoelectric p–n Junctions

The analytical solutions for one-dimensional simplified cases provide qualitative guidance for understanding the mechanism of how the piezopotential tunes/controls the carrier transport behavior. For a general case, the basic equations of piezotronic device can be solved numerically. For example, with considering the recombination of carriers in the depletion layer, we demonstrate the basic numerical method for simulating piezoelectric p–n junction.

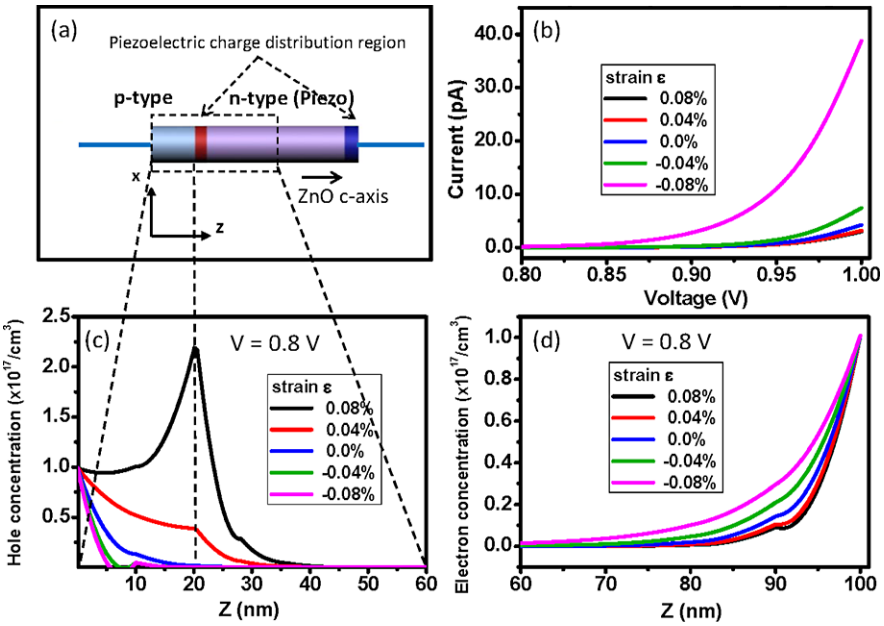

Fig. 3.8 (**a**) Schematic of a piezotronic ZnO nanowire p–n junction; (**b**) calculated current–voltage curves; (**c**) distribution of holes and (**d**) distribution of electrons at a fixed forward bias voltage of 0.8 V across the p–n junction under various applied strain (−0.09 % to 0.09 %) [9]

We first study the DC characteristics of the p–n junction with uniform strain. The piezoelectric charge distribution is obtained by numerically solving (3.4) and (3.5). Then the electrostatic equation, the convection and diffusion equations, and continuity equations are solved using the COMSOL software package. The electrical contacts at the ends of the p–n junction are assumed to be ideal Ohmic contacts, the Dirichlet boundary conditions are adopted for the carrier concentration and electrical potential at the device boundaries [19]. Figure 3.8(a) shows a sketch of a piezotronic nanowire p–n junction to be used for the calculation.

In order to have a reasonable comparison to a p–n junction diode, the dopant concentration function n can be approximately descried using Gaussian functions:

$$N = N_{Dn} + N_{Dn\max} e^{-(\frac{z-l}{ch})^2} - N_{Ap\max} e^{-(\frac{z}{ch})^2} \tag{3.24}$$

where N_{Dn} is the n-type background doping concentration due to the presence of intrinsic defects, $N_{Dn\max}$ is the maximum donor doping concentration and $N_{Ap\max}$ is the maximum acceptor doping concentration, l is the length of ZnO nanowire, ch controls the spreads width of the doping concentration. N is assigned to have a negative value in p-type region and a positive value in n-type region.

There is no external optical excitation in our model so that the electron and hole generation rates $G_n = G_p = 0$. For electron-hole recombination, there are two important recombination mechanisms, including band-to-band recombination and

trap-assisted recombination (named Shockley–Read–Hall recombination). Band-to-band recombination describes the energy transition from conduction band to the valence band by a radiation process (photon emission) or by transfer to another free electron or hole (Auger process). The Shockley–Read–Hall recombination is a general recombination process by traps in the forbidden band gap of the semiconductor. Taking it as an example in our model, the Shockley–Read–Hall recombination is given by

$$U_p = U_n = U_{\mathrm{SRH}} = \frac{np - n_i^2}{\tau_p(n + n_i) + \tau_n(p + n_i)} \tag{3.25}$$

where τ_p and τ_n are the carrier lifetimes. Thus, the basic semiconductor equations (3.1) and (3.3) are rewritten as

$$\begin{cases} \varepsilon_s \nabla^2 \psi_i = -q(p - n + N + \rho_{\mathrm{piezo}}), \\ -\nabla \cdot \mathbf{J}_n = -qU_{\mathrm{SRH}}, \\ -\nabla \cdot \mathbf{J}_p = -qU_{\mathrm{SRH}}. \end{cases} \tag{3.26}$$

For boundary conditions in contact with a metal electrode, the electrostatic potential is a constant. We assume infinite recombination velocity and no charge at the contact. Under an applied voltage, the electrostatic potential at the electrode is the potential corresponding to the quasi Fermi level plus the applied voltage V. The electrostatic potential and carrier concentrations at the electrode are given by [14–17, 20]:

$$\psi = V + \frac{q}{kT} \ln\left(\frac{\frac{N}{2} + \sqrt{(\frac{N}{2})^2 + n_i^2}}{n_i} \right), \tag{3.27a}$$

$$n = \frac{N}{2} + \sqrt{\left(\frac{N}{2}\right)^2 + n_i^2}, \tag{3.27b}$$

$$p = -\frac{N}{2} + \sqrt{\left(\frac{N}{2}\right)^2 + n_i^2}. \tag{3.27c}$$

Thus, we can calculate the above equations to obtain the boundary conditions of the electrostatic potential and carrier concentrator at the electrode.

In our simulation, we choose ZnO as the piezoelectric semiconductor material. The length and radius of the nanowire device are 100 nm and 10 nm, respectively. The p-type is assumed non-piezoelectric here so that it is not restricted to the wurtzite family. For simplicity, we neglect the difference in band gap between the p-type semiconductor and ZnO. The length of the p-type is 20 nm and the length of n-type ZnO is 80 nm. The relative dielectric constants are $\kappa_{\perp}^r = 7.77$ and $\kappa_{//}^r = 8.91$. The intrinsic carrier density is $n_i = 1.0 \times 10^6$ cm^{-3}. The electron and hole mobilities are $\mu_n = 200$ cm^2/V s and $\mu_p = 180$ cm^2/V s. The carrier lifetimes are $\tau_p = 0.1$ μs and $\tau_n = 0.1$ μs. The n-type background doping concentration is $N_{Dn} = 1 \times 10^{15}$ cm^{-3}. The maximum donor doping concentration

is $N_{Dn\max} = 1 \times 10^{17}$ cm^{-3} and the maximum acceptor doping concentration is $N_{Ap\max} = 1 \times 10^{17}$ cm^{-3}. The control constant $ch = 4.66$ nm. The temperature is $T = 300$ K. The piezoelectric charges are assumed to distribute uniformly at the two ends of the n-type segment within a region of 0.25 nm, as represented schematically by red and blue colored zones in Fig. 3.8(a). For easy of labeling, a z-axis is defined in Fig. 3.8(a), with $z = 0$ representing the end of the p-type. The p–n junction is located at $z = 20$ nm along the axis. The n-type ends at $z = 100$ nm.

The current–voltage curves at various strains are shown in Fig. 3.8(b). As for the negative strain (compressive strain) case in our model, the positive piezoelectric charges are at the p–n interface side, which attract the electrons to accumulate toward the p–n junction, resulting in a reduced built-in potential adjacent to the p–n junction. Thus, the corresponding saturation current density increases at a fixed bias voltage. Alternatively, for the positive strain (tensile strain) case, negative piezoelectric charges are created adjacent to the p–n interface, which attract the holes to the local region, resulting in an increase in the built-in potential and dropping in saturation current. Figure 3.8(c) show the distribution of hole concentrations at various strains from -0.08 % to 0.08 % at an applied voltage of $V = 0.8$ V, clearly displaying the effect of piezoelectric charges on the hole distribution. Under tensile strain, the hole concentration shows a peak right at the p–n junction interface where the negative piezoelectric charges accumulate. When a compressive strain is applied, the local positive piezoelectric charges push the holes away from the p–n junction, resulting in a disappearance of the peak. Correspondingly, Fig. 3.8(d) shows the electron distribution in the device at various strains from -0.08 % to 0.08 % at $V = 0.8$ V, showing a slight tendency of increasing. Since the right-hand electrode is an Ohmic contact ($z = 100$ nm), the carriers fully screen the piezoelectric charges at the contact. The electron concentration is rather low adjacent to the p–n junction. The piezoelectric charges at the p–n interface dominate the transport process. Therefore, the piezotronic effect is the result of tuning/controlling the carrier distribution by the device by the generated piezoelectric charges at the two ends.

Using our model, we also studied the DC characteristics and the carrier concentration distribution at various doping concentrations. The strain is fixed at -0.08 % and the n-type background doping concentration N_{Dn} is set to be 1×10^{15} cm^{-3}. By choosing $N_{Dn\max} = N_{Ap\max}$ and increasing $N_{Dn\max}$ from 1×10^{16} to 9×10^{16} cm^{-3}, the corresponding calculated current–voltage curves are plotted in Fig. 3.9(a). When the width of the depletion zone is fixed, the built-in potential increases with $N_{D\max}$. Therefore, the threshold voltage increases, which pushes the "take off" point of the I–V curve moving it to higher voltage. Then, by assuming $N_{Dn\max} = N_{Ap\max} = 1 \times 10^{17}$ cm^{-3} and increasing N_{Dn} from 5×10^{13} to 1×10^{15} cm^{-3}, the I–V curve shows little change, as shown in Fig. 3.9(b). The numerical results indicate that the DC characteristics depend on the distributions of donors and acceptor doping concentration in our model. Furthermore, the distributions of holes and electrons at an applied voltage of 0.8 V are shown in Figs. 3.9(c) and 3.9(d), respectively.

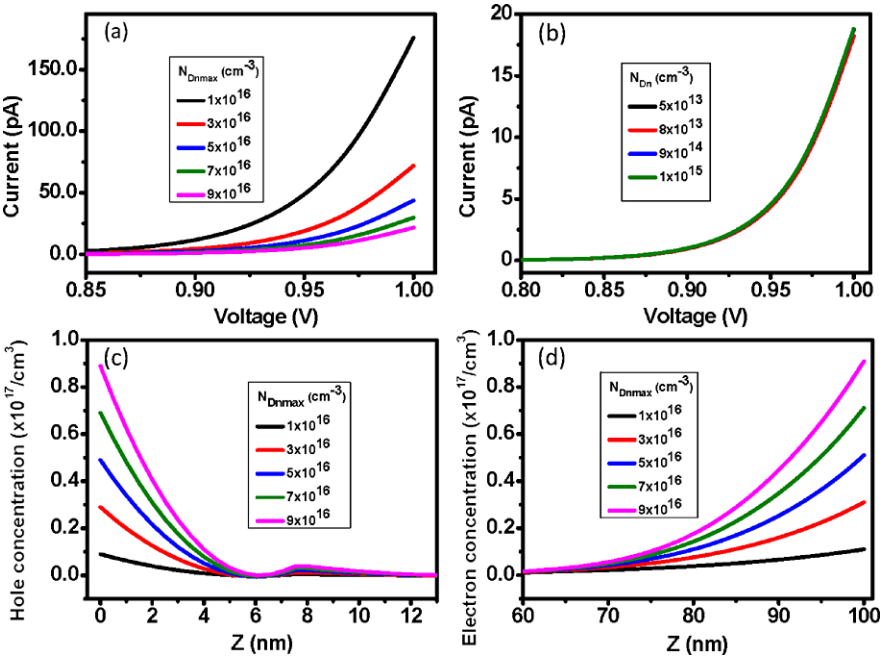

Fig. 3.9 (**a**) Calculated piezoelectric p–n junction current–voltage curves at various maximum donor doping concentration and maximum donor acceptor doping concentration; (**b**) calculated current–voltage curves at various n-type background doping concentration; (**c**) and (**d**) distributions of hole and electron concentrations along the length of the device at an applied forward voltage of 0.8 V at various maximum donor doping concentrations and maximum donor acceptor doping concentrations, respectively [9]

3.6.2 Piezoelectric Transistor

The M–S–M ZnO nanowire devices are the typical piezoelectric transistor in our experimental studies. Using FEM, we solved the basic equations of the M–S–M ZnO nanowire device with the applied strain along the nanowire length direction (*c*-axis). There are many types of M–S–M ZnO nanowire device, including different types of M–S contact and doping profile, etc. M–S contact can be fabricated as Ohmic contact or Schottky contact. The doping profile can be approximated as a box profile or a Gaussian distribution profile, etc. Our calculations are done based on a device model that has the following device property assumptions: the surface states in ZnO are ignored; the electrostatic potential are constants at the end electrodes; the nanowire is n-type without p-type doping; the doping concentration N is approximately descried using a Gaussian function; and, at equilibrium, the electron concentration at the metal contact is unaffected by the transported current; infinite recombination velocity and no charge at the contact. Although the M–S–M ZnO nanowire devices model is taken as a simplified model for clearly describing the mechanism of piezopotential tuning to carrier transport process, the basic principle

also applies to more complex cases, such as different surface states, arbitrary doping profiles and different piezoelectric semiconductor materials, etc.

Using the COMSOL software package, the piezoelectric equations (see (3.4)) are solved first. Then, the electrostatic equation, the convection and the diffusion equations are solved with the piezoelectric charge distribution provided. The doping concentration function N is approximately descried using a Gaussian function:

$$N = N_{Dn} + N_{Dn\max} e^{-(\frac{z-l}{ch})^2}. \tag{3.28}$$

The boundary conditions of the electrostatic potential at the electrode can be given by

$$\psi = V - \chi_{\mathrm{ZnO}} - \frac{E_g}{2} + \frac{q}{kT} \ln\left(\frac{\frac{N}{2} + \sqrt{(\frac{N}{2})^2 + n_i^2}}{n_i} \right) \tag{3.29}$$

where the electron affinity χ_{ZnO} of ZnO is 4.5 eV, and its band gap E_g is 3.4 eV. We assume the carrier concentration at the electrode to be the same as the value at thermal equilibrium. The boundary conditions of the carrier concentration at the electrode can be given by (3.27b).

We calculated the DC transport property of a M–S–M ZnO nanowire device with the presence of piezoelectric charges with the applied strain from -0.39 % to 0.39 %. Figure 3.10(a) shows the sketch of a piezotronic ZnO nanowire device. We choose $l = 50$ nm, which is half the length of the nanowire. The current–voltage curves are shown in Fig. 3.10(b). At negative strain (compressive strain), the positive and negative piezoelectric charges are at the left-hand and right-hand M–S contacts, respectively (as shown in Fig. 3.10(a)), which lower and raise the local Schottky-barrier heights at the corresponding contacts. When an external voltage is applied with the left-hand contact at positive bias, the dominant barrier that dictates the current–voltage curve is the reversely biased contact at the right-hand, at which the local barrier height is raised by piezoelectric charges. Thus, the transported current is lowered in comparison to the case of strain-free device. Alternatively, at positive strain (tensile strain) case and under the same biased voltage, by the same token, the I–V curve is largely determined by the M–S contact at the right-hand, which has a lowered barrier height, resulting in an increase in transported current in comparison to the strain-free case. The device displays 'ON' state at 0.39 % strain, and is 'OFF' at -0.39 % strain. Therefore, the piezopotential acts as a 'gate' voltage to tune/control the current of piezoelectric transistor at the M–S interface and the device can be switched "ON" and "OFF" by switching the applied strain, which is the piezotronic FET.

Figure 3.10(c) shows the electron concentration along the device at an applied voltage $V = 0.8$ V. When an external voltage is applied, the piezoelectric charges affect the peak height and position of the electron concentration distribution. With an increase in strain without applying bias voltage, not only the magnitude of the peak of the electron concentration increases, but also the position of the peak shifts from 44.2 to 55.8 nm when the strain varies from -0.39 % to 0.39 %, as shown in Fig. 3.10(d).

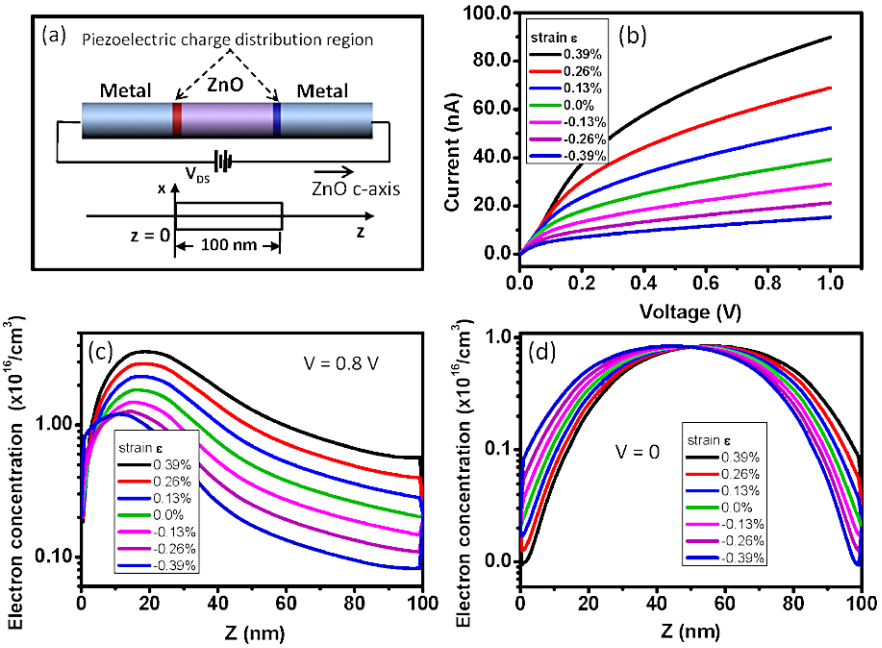

Fig. 3.10 (**a**) Schematic of piezotronic ZnO nanowire transistor; (**b**) calculated current–voltage curves of the device at various applied strain (−0.39 % to 0.39 %); electron distribution in the semiconductor segment (**c**) at a forward voltage of $V = 0.8$ V and (**d**) at $V = 0$ [9]

Furthermore, we study the DC characteristics and the carrier concentration with various doping concentration. In order to investigate how the variance of maximum donor doping concentration and maximum donor acceptor doping concentration affects the DC characteristics, we fix the strain at −0.08 % and the n-type background doping concentration N_{Dn} of 1×10^{15} cm^{-3}. When $N_{Dn\,\max}$ is increased from 1×10^{16} to 9×10^{16} cm^{-3}, the current increases as well (Fig. 3.11(a)). By fixing $N_{Dn\,\max} = N_{Ap\,\max} = 1 \times 10^{17}$ cm^{-3}, the current rises with increasing of N_{Dn} from 1×10^{13} to 1×10^{15} cm^{-3} (Fig. 3.11(b)). The numerical results indicate that the DC characteristics depend on the doping concentration in the piezoelectric transistor. The distribution of electrons at an applied voltage of 0.8 and 0.0 V are shown in Figs. 3.11(c) and (d), respectively.

3.7 Summary

We have presented the theoretical frame of piezotronics by studying the charge transport across the metal–semiconductor contact and p–n junction with the introduction of piezopotential [9]. The analytical solutions derived under simplified conditions are useful for illustrating the major physical pictures of the piezotronic

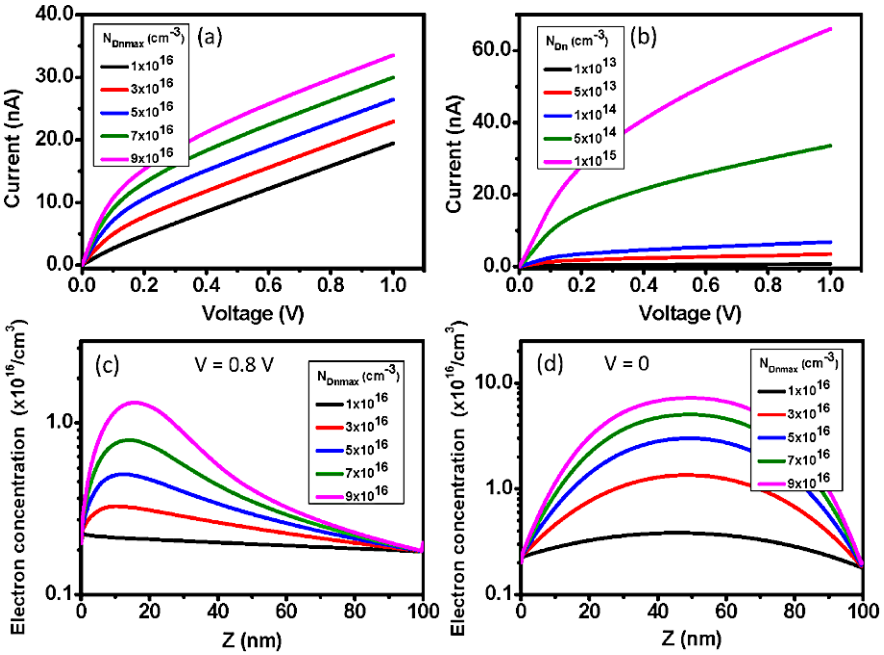

Fig. 3.11 Calculated transport characteristics of a piezotronic ZnO nanowire transistor. (**a**) Piezoelectric M–S–M nanowire transistor current–voltage curves at various maximum donor doping concentrations; (**b**) current–voltage curves at various n-type background doping concentrations; calculated electron distribution in the device at various maximum donor doping concentrations (**c**) at a forward bias of $V = 0.8$ V and (**d**) $V = 0$

devices, and the numerical calculated results are meant for understanding the transport characteristics of the piezotronic transistors in a practical case. The theory presented here not only establishes the solid physical background of piezotronics, but also provides theoretical support for guiding the experimental design of piezotronic devices.

References

1. Z.L. Wang, J.H. Song, Piezoelectric nanogenerators based on zinc oxide nanowire arrays. Science **312**, 242–246 (2006)
2. X.D. Wang, J.H. Song, J. Liu, Z.L. Wang, Direct-current nanogenerator driven by ultrasonic waves. Science **316**, 102–105 (2007)
3. Y. Qin, X.D. Wang, Z.L. Wang, Microfibre–nanowire hybrid structure for energy scavenging. Nature **451**, 809–813 (2008)
4. X.D. Wang, J. Zhou, J.H. Song, J. Liu, N.S. Xu, Z.L. Wang, Piezoelectric field effect transistor and nanoforce sensor based on a single ZnO nanowire. Nano Lett. **6**(12), 2768–2772 (2006)
5. J.H. He, C.H. Hsin, L.J. Chen, Z.L. Wang, Piezoelectric gated diode of a single ZnO nanowire. Adv. Mater. **19**(6), 781–784 (2007)

6. C.S. Lao, Q. Kuang, Z.L. Wang, M.C. Park, Y.L. Deng, Polymer functionalized piezoelectric-FET as humidity/chemical nanosensors. Appl. Phys. Lett. **90**(26), 262107 (2007)
7. Y.F. Hu, Y.L. Chang, P. Fei, R.L. Snyder, Z.L. Wang, Designing the electric transport characteristics of ZnO micro/nanowire devices by coupling piezoelectric and photoexcitation effects. ACS Nano **4**(2), 1234–1240 (2010)
8. Y.F. Hu, Y. Zhang, Y.L. Chang, R.L. Snyder, Z.L. Wang, Optimizing the power output of a ZnO photocell by piezopotential. ACS Nano **4**(7), 4220–4224 (2010)
9. Y. Zhang, Y. Liu, Z.L. Wang, Fundamental theory of piezotronics. Adv. Mater. **23**(27), 3004–3013 (2011)
10. Z.L. Wang, Piezopotential gated nanowire devices: piezotronics and piezo-phototronics. Nano Today **5**, 540–552 (2010)
11. J. Zhou, P. Fei, Y.D. Gu, W.J. Mai, Y.F. Gao, R.S. Yang, G. Bao, Z.L. Wang, Piezoelectric-potential-controlled polarity-reversible Schottky diodes and switches of ZnO wires. Nano Lett. **8**(11), 3973–3977 (2008)
12. Q. Yang, W.H. Wang, S. Xu, Z.L. Wang, Enhancing light emission of ZnO microwire-based diodes by piezo-phototronic effect. Nano Lett. **11**(9), 4012–4017 (2011)
13. Z.L. Wang, Progress in piezotronics and piezo-phototronics. Adv. Mater. **24**, 4632–4646 (2012)
14. S.M. Sze, *Physics of Semiconductor Devices*, 2nd edn. (Wiley, New York, 1981)
15. W. Schottky, Halbleitertheorie der Sperrschicht. Naturwissenschaften **26**(52), 843 (1938)
16. H.A. Bethe, MIT Radiation Lab. Report, vol. 43-12 (November, 1942)
17. C.R. Crowell, S.M. Sze, Current transport in metal–semiconductor barriers. Solid-State Electron. **9**(11–12), 1035–1048 (1966)
18. T. Ikeda, *Fundamentals of Piezoelectricity* (Oxford University Press, Oxford, 1996)
19. http://www.comsol.com/showroom/gallery/114/
20. S. Selberherr, *Analysis and Simulation of Semiconductor Devices* (Springer, Berlin, 1984)

Chapter 4
Piezotronic Transistors

Abstract By using the piezopotential as the "gating voltage" for tuning/controlling interface charge transport, this chapter presents the fundamental principle and fabrication of piezotronic transistors using horizontal and vertical oriented nanowires. The piezotronic transistor is a two-terminal transistor without a gate electrode. The replacement of an external voltage gating by an inner crystal potential gating makes it possible to fabricate arrays of devices using vertical nanowires that can be individually addressed/controlled. This is advantageous for fabricating a high density device matrix for electro-mechanical transduction, such as sensors and touch pad technology.

4.1 Piezotronic Stain Sensor

Research in the field of micro- and nano-electromechanical systems (MEMS) and NEMS is rapidly growing with considerable potential for ultra fast, high-sensitivity and low-power consumption devices. As for nano- and micro-scale strain/stress and pressure measurements, various sensors have been fabricated based on NWs [1] and carbon nanotubes (CNTs) [2, 3]. Commonly, these devices utilize the piezoresistance property of the material, i.e., under small strain, the conductance of the material changes with strain following a linear relationship. CNT is the most intensively studied material in this area, and a sensor device based on CNTs with gauge factor up to 850 have been achieved [4].

In the first part of this chapter, we present the fabrication and application of a fully packaged strain sensor device based on a single ZnO piezoelectric fine wire (PFW) (nanowire, microwire). The strain sensor was fabricated by bonding a ZnO PFW laterally on a polystyrene (PS) substrate. The *I–V* behavior of the device was modulated by strain due to the change in Schottky-barrier height (SBH). The PFW has Schottky contacts at its two ends but with distinctly different barrier heights. The *I–V* characteristic is highly sensitive to strain due to mainly the change in Schottky-barrier height (SBH) owing to the piezotronic effect, which scales linear with strain. The experimental data can well be described by the thermionic emission-diffusion model. A gauge factor of as high as 1250 has been demonstrated, which is 25 % higher than the best gauge factor demonstrated for carbon nanotubes. The strain

Z.L. Wang, *Piezotronics and Piezo-Phototronics*, Microtechnology and MEMS,
DOI 10.1007/978-3-642-34237-0_4, © Springer-Verlag Berlin Heidelberg 2012

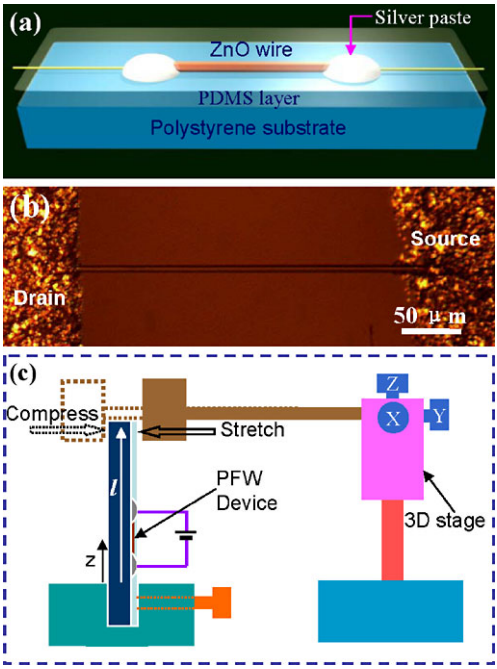

Fig. 4.1 (**a**) Schematic of a single ZnO PFW based strain sensor device. (**b**) Optical image of a strain sensor device. (**c**) Schematic of the measurement system to characterize the performance of the sensor device [5]

sensor developed here has application in strain and stress measurements in cell biology, biomedical sciences, MEMS devices, structure monitoring and more.

4.1.1 Sensor Fabrication and Measurement

The schematic of the strain sensor device is shown in Fig. 4.1(a) [5]. Ultra-long ZnO PFWs were synthesized by a high temperature thermal evaporation process, and they typically have diameters of 2–6 μm and lengths of several hundred micrometers to several millimeters. We choose large size wires for easy of manipulation under optical microscope. The same principle and methodology applies to nanowires. The typical PS substrate has a length of ∼3 cm, width of ∼5 mm and thickness of 1 mm. The substrate was sequence washed with deionized water and ethanol under sonication. After drying with flowing nitrogen gas and placing in a furnace at 80 °C for 30 minutes, the PS substrate was ready to be used as the substrate. ZnO PFW was placed on the PS substrate by using a probe station under optical microscopy. Silver paste was applied at both ends of the ZnO PFW to fix its two ends tightly on the substrate, silver paste was also used as source and drain electrodes. A thin layer of polydimethylsiloxane (PDMS) was used to package the device. The thickness of the PDMS layer is much thinner than the thickness of the PS substrate. The PDMS thin layer not only enhances the adherence of the silver paste to the PS substrate, but also prevents the ZnO wire from contamination or corrosion when it was exposed

to atmosphere. Then the entire device was annealing at 80 °C for 12 hours. Finally, a flexible, optically transparent, and well packaged strain sensor device was fabricated. Figure 4.1(b) shows an optical image of the strain sensor device, indicating that a smooth ZnO wire was placed on the substrate with two ends fixed.

The characterization of the *I–V* behavior of the sensor device with strain was carried out in atmosphere at room temperature, and the measuring system is schematically shown in Fig. 4.1(c). One end of the device was affixed on a sample holder that was fixed tightly on an optical air table, with another end free to be bent. An x–y–z mechanical stage with movement resolution of 1 μm was used to bend the free end of the sensor device to produce a compressive or tensile strain. Meanwhile a continuously sweeping triangle voltage was applied through the ZnO wire to measuring its *I–V* characteristics during deformation. To study the stability and response of the sensor devices, a resonator with controlled frequency and amplitude was used to periodically bend the sensor device. At the same time, a fixed bias voltage was applied between the source and drain.

Since the thin PDMS layer has a much smaller Young modulus ($E = 360$–870 kPa) than that of PS substrate ($E = 3$–3.5 GPa), and the silver paste electrodes have a much smaller area and thickness in comparison to those of the PS substrate, the PDMS layer and silver paste electrodes, which are bonded on the outer surface of the PS substrate, do not alter the mechanical properties of the PS film at any significant level. Therefore, the strain in the PFW is either purely tensile or compressive, depending on the bending direction of the PS substrate. The strain in the PFW is approximately equal to the strain of the site z where it was placed at on the outer surface of the PS substrate.

4.1.2 Calculation of Strain in the Piezoelectric Nanowire

For easiness of derivation, the origin of the coordinate system is set at the center of the cross section of one side of the film, while the z axis is parallel to the length l and x axis is parallel to the width w. In order to determine how the NW deforms as the substrate is deflected under an external bending force f_y, only the ε_{zz} component of the strain tensor needs to be calculated, where $\varepsilon_{zz} = \Delta L_{\text{wire}}/L_{\text{wire}}$. Meanwhile, $\sigma_{zz} = -f_y/I_{xx}\,y(l-z)$, $\sigma_{xx} = \sigma_{yy} = 0$, where I_{xx} is the geometrical moment of inertia for the beam cross section.

Therefore, $\Delta L_{\text{wire}}/L_{\text{wire}} = \varepsilon_{zz} = \sigma_{zz}/E$. The lateral deflection $D_{\max}$ of the substrate is experimentally easier to measure than the bending force f_y and the relationship between $D_{\max}$ and f_y is $D_{\max} = f_y l^3/3EI_{xx}$. Therefore [5],

$$\varepsilon_{zz} = -3\frac{y}{l}\frac{D_{\max}}{l}\left(1-\frac{z}{l}\right). \tag{4.1}$$

Here $y = \pm a$ and $z = z_0$ is the vertical distance between the fixed end of the Dura–Lar film substrate and the middle point of the ZnO NW. The positive and negative

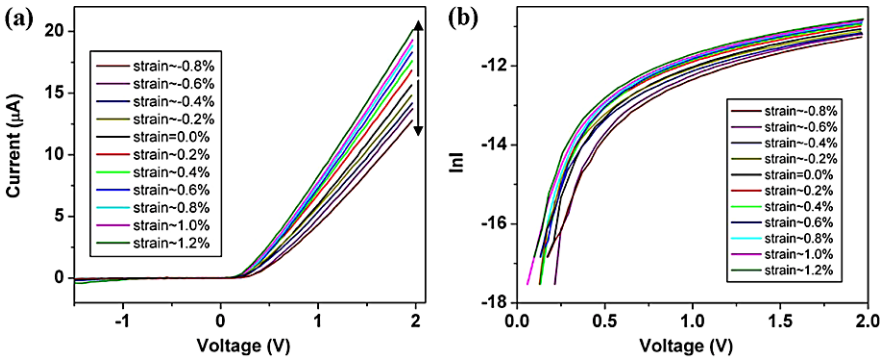

Fig. 4.2 (**a**) Typical *I–V* characteristics of the sensor at different strain. (**b**) Logarithm plot of the current under positive bias by using the data in (**a**) [5]

sign for y stand for the compressed side and tensile side of the beam, respectively. In practice, since the length of the substrate is much larger than the length of the PFW ($l \gg L$), the strain in the PFW is uniform to an excellent approximation.

4.1.3 Electromechanical Characterization of the Sensor

Before the electromechanical measurements, we have first measured the original *I–V* characteristic of the sensor device. We found various *I–V* characteristics for over 250 devices. The nonlinear *I–V* characteristics are commonly observed in measuring semiconductor devices [6, 7]. Generally the nonlinearity is caused by the Schottky barriers formed between the semiconductor and metal electrodes in the semiconductor device, and the shape of the *I–V* curve depends on the heights of the Schottky barriers formed at the source and drain due to different interface properties. In this study, we only focused on the devices that have Schottky contacts at the two ends of the PFW, but with distinctly different barrier heights. The *I–V* curve shape is quite asymmetric. Typical *I–V* characteristics under various strains are shown in Fig. 4.2(a). The *I–V* curves shift upward with tension strain and downward with compressive strain. The *I–V* curve fully recovered when the strain was relieved.

The stability and response of the sensor device was carefully studied. Figures 4.3(a) and (b) show the current response of the sensor over many cycles of repeatedly compressing and stretching at a frequency of 2 Hz under fixed bias of 2 V, respectively. It can be seen that the current decreases with compressive strain and increases with tensile strain, which is consistent with the phenomenon observed in Fig. 4.2(a). It should be noticed that the current reached almost the same value in each cycle of straining, and the current can fully recover when the strain was relived, indicating the sensor device had high reproducibility and good stability. A response time of ~10 ms of the sensor device can be derived.

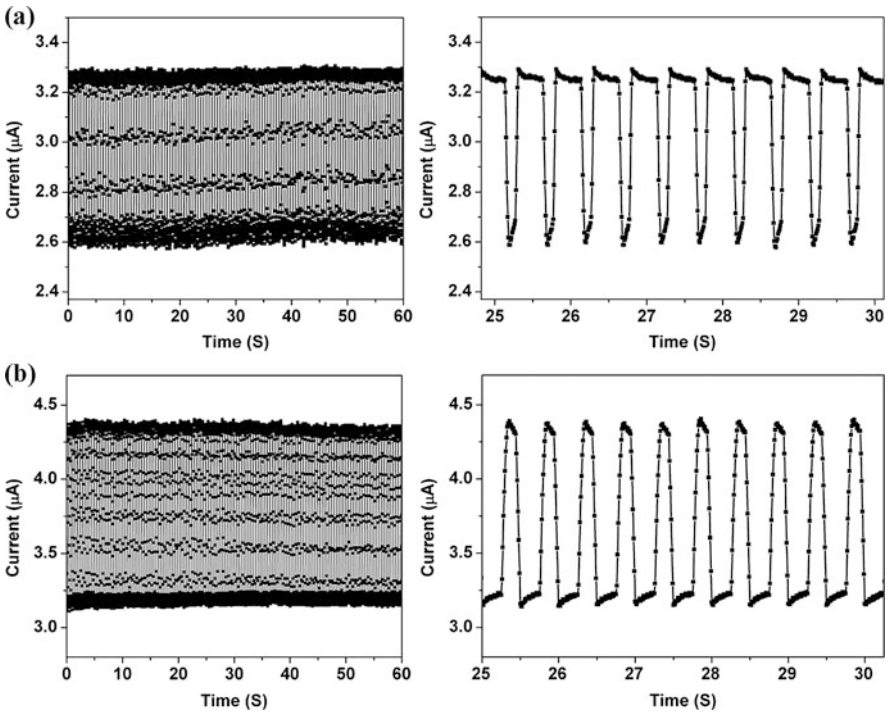

Fig. 4.3 Current response of a sensor device that was repeatedly stretched (**a**) and compressed (**b**) at a frequency of 2 Hz under fixed bias of 2 V [5]

4.1.4 Data Analysis Using the Thermionic Emission-Diffusion Theory

The *I–V* curve shown in Fig. 4.2(a) clearly demonstrates that there were Schottky barriers present at the contacts but with distinctly different barrier heights. The presence of a Schottky barrier at the metal/semiconductor interface [8] plays a crucial role in determining the electrical transport property of the metal–semiconductor–metal (M–S–M) structure. By simply looking at the *I–V* curve one is unable to identify the nature of the barriers either reversely biased or forward biased. It is important to quantitatively simulate the shape of the *I–V* curve in order to determine the nature of the electric transport across the M–S–M structure. After carefully studying the shape of the *I–V* curve, our device is considered as a single ZnO wire sandwiched between two opposite Schottky barriers, as shown in Fig. 4.4(a). We assume that the barrier height at the drain side ϕ_d (eV) is significantly higher than that at the source side. At a fixed bias voltage V, the voltage drop occurs mainly at the reversely biased Schottky barrier according to the measurement by in-situ scanning surface potential microscopy [9]. In our case, when a relatively large positive voltage V is applied across the drain and source with the drain positive, the voltage drop occurs mainly at the reversely biased Schottky barrier ϕ_s (eV) at the source

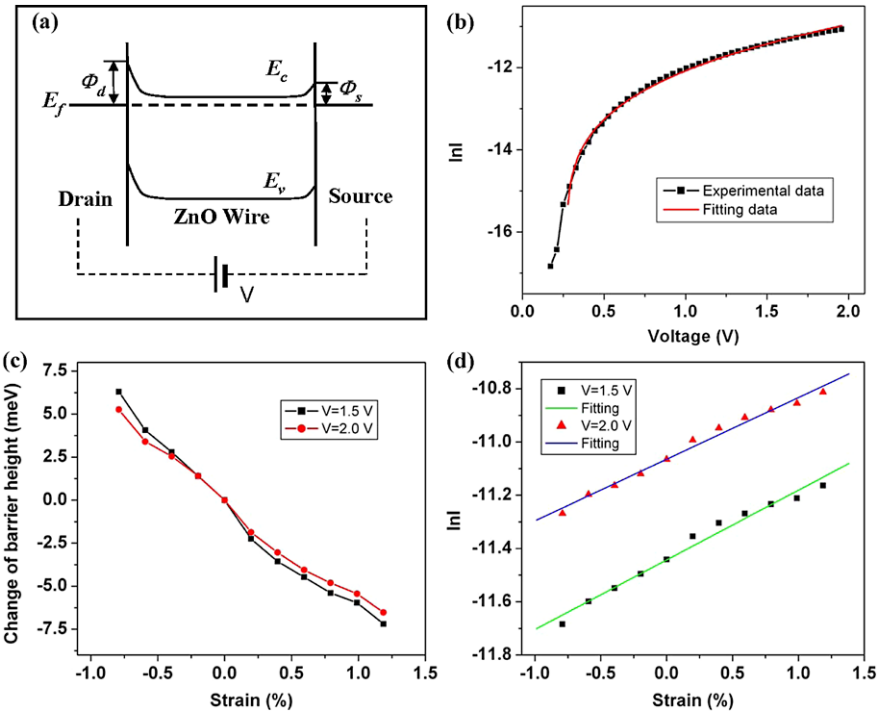

Fig. 4.4 (**a**) Energy band diagram illustrates the asymmetric Schottky barrier heights at the source and drain contacts of a PFW, where the offset by the applied drain-source voltage V was not included for easy discussion. (**b**) Fitting the $\ln I$–V data using the thermionic emission–diffusion theory at a given strain for a reversely biased Schottky barrier. The *black dotted* are experimental data points from Fig. 4.2(b) for strain = 0, and the *red line* is a fit. (**c**) The derived change in SBH based on the thermionic emission–diffusion model, as a function of stain at a drain-source bias of $V = 1.5$ and 2.0 V, respectively. (**d**) Logarithm plot of the current (in unit of Ampère) at fixed bias of $V = 1.5$ and 2.0 V as a function of strain [5]

side, and it is denoted by V_s. Here we assume $V_s \approx V$. Considering that our measurements were made at room temperature and the ZnO PFW had a low doping, the dominant transport property at the barrier is thermionic emission and diffusion, while the contribution made by tunneling can be ignored. Thus, as inspired by the shape of the $\ln I$–V curve in Fig. 4.4(b), and according to the classic thermionic emission–diffusion theory (for $V \gg 3kT/q \sim 77$ mV) for a reversal bias voltage V and at temperature T, the current through the reversely biased Schottky barrier ϕ_s is given by

$$I = SA^{**}T^2 \exp\left(-\frac{\phi_s}{kT}\right) \exp\left(\frac{\sqrt[4]{q^7 N_D (V + V_{bi} - kT/q)/(8\pi^2 \varepsilon_s^3)}}{kT}\right) \tag{4.2}$$

where S is the area of the source Schottky barrier, A^{**} is the effective Richardson constant, q is the electron charge, k is the Boltzmann constant, N_D is the donor im-

purity density, V_{bi} is the built-in potential at the barrier, and ε_s is the permittivity of ZnO. The $\ln I$–V curve shown in Fig. 4.4(b) quantitatively indicates that variation of $\ln I$ can be described by $V^{1/4}$ for reversely biased Schottky barrier instead of $\ln I$–V as for forward biased Schottky barrier. Therefore, (4.2) can be used to precisely fit the experimentally observed $\ln I$–V curve, from which the corresponding parameters can be derived. This not only indicates that the thermionic emission–diffusion model is the dominant process in our device, but also can be applied to derive the SBH as described in follows.

By assuming that S, A^{**}, T, N_D are independent of strain for small deformation [10], ϕ_s can, in principle, be derived from the logarithm of the current ($\ln I$)–V plot, which is shown in Fig. 4.4(b). Subsequently, the change of SBH can be determined by

$$\ln\left[I(\varepsilon_{zz})/I(0)\right] = -\Delta\phi_s/kT \tag{4.3}$$

where $I(\varepsilon_{zz})$ and $I(0)$ are the current measured through the PFW at a fixed bias with and without being strained, respectively. The results are plotted in Fig. 4.4(c) for two biases of 1.5 and 2 V, indicating that the change of SBH $\Delta\phi_s$ has an approximately linear relationship with strain. We also notice that the $\Delta\phi_s$ is not very sensitive to the choice of bias voltage V.

In the calculation presented above, we assumed that the applied voltage was totally consumed at the reversely biased Schottky barrier formed at the source electrode. In reality, $V_s < V$, thus the calculated $\Delta\phi_s$ value may be slightly affected by the choice of V, but the linear dependence of $\Delta\phi_s$ on strain will not be affected much. Figure 4.4(d) shows the change of $\ln I$ at fixed bias of $V = 1.5$ and 2.0 V as a function of strain. The change of $\ln I$ varies approximately linearly with the applied strain.

4.1.5 *Separating the Contributions Made by Piezoresistance and Piezotronic Effects*

It has been reported that the SBHs of GaAs [11], GaN [12], GaAlN [13] Schottky barrier shifts under stress/strain due the band structure change and piezoelectric effect. Experiments and calculations have shown that the band gap changes under strain/stress. Similarly, the SBH change for ZnO under strain can be viewed as a combination of band structure change (e.g., piezoresistance effect) and piezotronic effect. Using a simple Schottky model, the effect of the band structure change may be equivalently characterized by a change in semiconductor (ZnO) electron affinity under strain, which is denoted $\Delta\phi_{s-bs}$.

The effect of piezoelectric polarization on the SBH arises because the polarization produces surface charges at an interface where the divergence of the polarization is nonzero, i.e., at the metal–semiconductor interface and beneath the depletion region in the semiconductor [14]. At the latter position the associated polarization change may be screened by the conduction electrons. On the other hand, at the

metal-semiconductor interface the polarization change can be partially neutralized by an adjustment of the electronic charges in the interface states or in the metal. This effect will shift the Fermi level at the interface and subsequently affects the SBH. The change in SBH by piezoelectric polarization is given approximately by

$$\Delta\phi_{s-pz} = \frac{\sigma_{pz}}{D}\left(1 + \frac{1}{2q_s d}\right)^{-1}. \tag{4.4}$$

Here σ_{pz} is the area density of piezoelectric polarization changes (in units of electron charge), D is a two-dimensional density of interface states at the Fermi level in the semiconductor band gap at the Schottky barrier, and d is the width of the depletion layer. Associated with the states in the band gap at interface is the two-dimensional screening parameter $q_s = (2\pi q^2/k_0)D$, where q is the electronic charge and k_0 is the dielectric constant of the ZnO. Thus the total change in SBH of ZnO sensor can be expressed as

$$\Delta\phi_s = \Delta\phi_{s-bs} + \Delta\phi_{s-pz}. \tag{4.5}$$

In this study, $\Delta\phi_s$ decreases under tension strain, and increases under compressive strain, and the experimental observed strain effect is a combined result of $\Delta\phi_{s-bs}$ and $\Delta\phi_{s-pz}$. Experimentally, the contribution made by band structure change is stationary as long as the strain is preserved, while the contribution from the piezoelectric effect could be time dependent with a slight decay with considering the screening effect of the charge carriers, possibly because of charge trapping effect by impurity and vacancy states in ZnO, which may result in a slow change in conductivity, similar to the slow recovery of the ZnO conductivity after illuminating by UV light. Further study is required to fully understand this phenomenon.

4.1.6 Much Enhanced Gauge Factor by Piezotronic Effect

For practical application, the performance of a strain sensor is characterized by a gauge factor, which is defined to be the slope of the normalized current (I)–strain (ε) curve, $[\Delta I(\varepsilon)/I(0)]/\Delta\varepsilon$. The highest gauge factor demonstrated for our sensor device is 1250 (Fig. 4.5(b)), which exceeds the gauge factor of conventional metal strain gauges (1–5) and state-of-the-art doped-Si strain sensor (∼200), and even higher than the highest gauge factor reported for CNTs (∼1000). Figure 4.5(a) shows the I–V curve of another device as a function of the applied strain, which shows the same behavior as that presented in Fig. 4.2(a). The inset indicates that $\ln I$ linearly depends on the applied strain. The gauge factor determined as a function of the strain is presented in Fig. 4.5(b), and it is consistent with the calculated results [15].

In practice, some of the devices showed relatively low gauge factor, which may be attributed to the opposite signs of $\Delta\phi_{s-bs}$ and $\Delta\phi_{s-pz}$ because the piezoelectric effect depends on the orientation of the c-axis of the ZnO wire. We had 50 % chance in experiments to have the ZnO wire oriented along c or $-c$ direction.

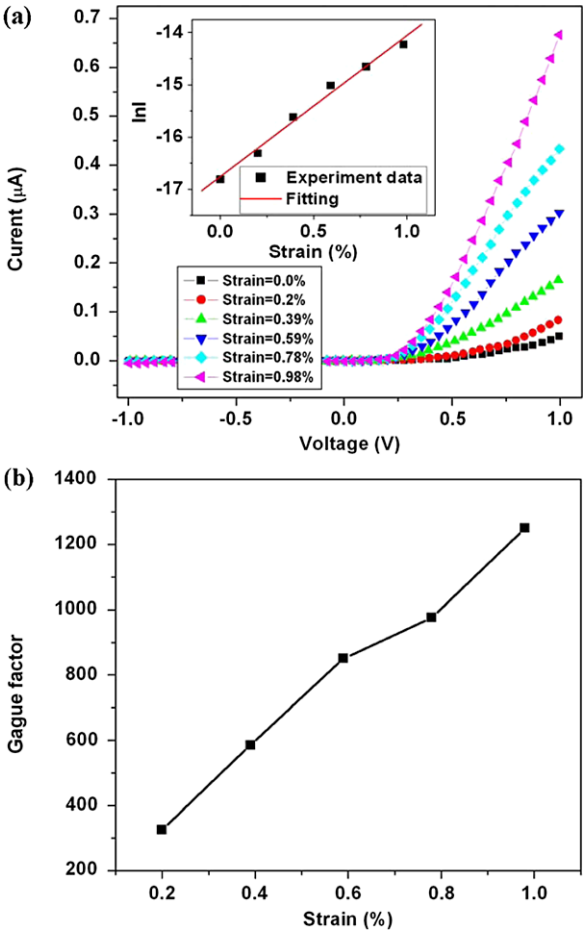

Fig. 4.5 (**a**) *I–V* characteristics of another sensor device under different strain. Inset is the dependence of ln *I* (in unit of Ampère) on the applied strain. (**b**) Gauge factors derived from (**a**) as a function of strain [5]

4.2 Piezoelectric Diodes

In this section, we report a new type flexible piezotronic switch device that is built using a single ZnO piezoelectric fine wire (PFW) (nanowire, microwire) [16]. Its operation mechanism relies on the piezoelectric potential induced asymmetric change in Schottky-barrier height (SBH) at the source and drain electrodes. The change of SBH is to the asymmetric change in Schottky-barrier heights at both source and drain electrodes as caused by the strain induced piezoelectric potential drop along the PFW, which have been quantified using the thermionic emission–diffusion theory. A new piezotronic switch device with an "on" and "off" ratio of ∼120 has been demonstrated. This work demonstrates a novel approach for fabricating diodes and switches that rely on a strain governed piezoelectric-semiconductor coupling process.

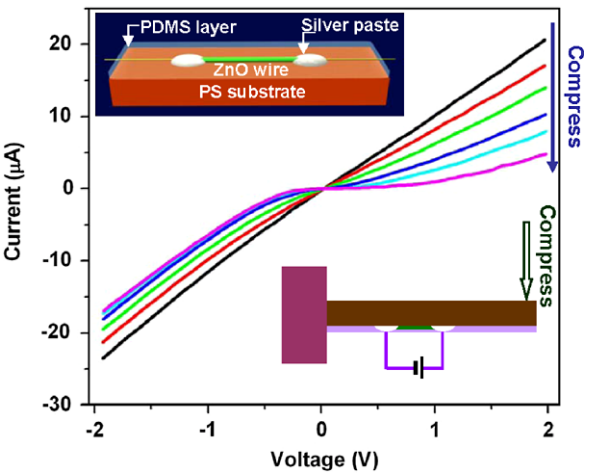

Fig. 4.6 Typical *I–V* characteristics of the sensor under different compressive strains (Device #1). The *black line* is the *I–V* curve without strain. The direction of the *blue arrowhead* indicates the increasing of applied compressive strain. The *upper inset* shows the schematic of a single ZnO PFW based device. The *lower inset* shows the schematic of the electromechanical measurement system

4.2.1 Piezotronic Induced Change from Ohmic to Schottky Contact

For this study, the device was fabricated by bonding an ultra-long ZnO PFW laterally on a polystyrene (PS) substrate, which has a thickness much larger than the diameter of the PFW, as schematically shown in the upper-inset of Fig. 4.6. Briefly, single ZnO PFW (typical diameter of several micrometers and length of several hundred micrometers to several millimeters), which was synthesized by a high temperature physical vapor deposition process, was placed on PS substrate (typical length of ~3 cm, width of ~5 mm and thickness of 1 mm) by using a probe station under optical microscopy. Then silver paste was applied at both ends of the ZnO PFW to fix its two ends tightly on the substrate, silver paste was also used as the source and drain electrodes. After the silver paste was dried, a thin layer of polydimethylsiloxane (PDMS) was used to package the device. Finally, a flexible, optically transparent, water proof and well packaged device was prepared.

The study of electromechanical properties of the device was carried out in atmosphere at room temperature. The lower-inset in Fig. 4.6 shows the measurement setup. One end of the device was affixed on a sample holder, with another end free to be bent. A three-dimension mechanical manipulation stage with displacement resolution of 1 μm was used to bend the free end of the device to produce a compressive strain. Meanwhile the *I–V* characteristics of the device during deformation were measured by a computer controlled measurement system.

Before the electromechanical measurements, we have first tested the original *I–V* characteristic of the device. We found various *I–V* characteristics for over 200 devices that were prepared under similar conditions, and most of them have nonlinear behavior. Previously, we focused on the devices which originally exhibit rectifying *I–V* behavior, and flexible piezotronic strain sensors based on those devices have been demonstrated. In this study, we focus only on the devices that have symmetric or nearly symmetric *I–V* behavior, which can be Ohmic or with symmetric Schottky contacts at the two ends. Typical *I–V* characteristics under various compressive

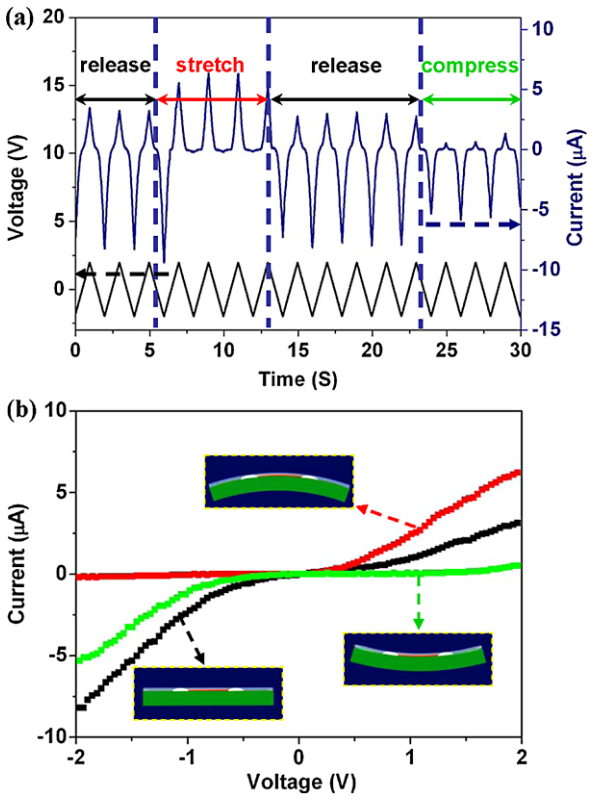

Fig. 4.7 (**a**) Current response under repeated compressing–releasing–stretching–releasing straining process (Device #2). The *blue line* and *black line* are current response and applied sweeping bias voltage over time, respectively, from which the *I–V* characteristic as a function of time was captured. (**b**) *I–V* characteristics under different strain: released (*black*), compressive strain (*green*) and tensile strain (*red*). The *inset* schematically shows the device under various straining conditions

strains are shown in Fig. 4.6. When the compressive strain was increased, the currents both under positive bias and negative bias were suppressed. Finally a downward diode-like *I–V* behavior is obtained. Some devices exhibited upward diode-like *I–V* behavior under compression strain. Statistic study showed that the ratio of the devices, which exhibited downward and upward diode-like *I–V* behavior under compressive strain, is nearly 1:1.

Figure 4.7(a) shows a current response under a repeated stretching–releasing–compressing–releasing straining cycle over a period of time for another device. The blue line and black line are current response and sweeping bias over time, respectively. The corresponding *I–V* behavior under each straining condition is shown in Fig. 4.7(b). When the device was under tensile straining, upward diode-like *I–V* behavior was observed (red line); downward diode-like *I–V* behavior (green line) was observed when the device was under compressive straining. The *I–V* curve (black line in Fig. 4.7(b)) fully recovered when the strain was relieved. Our extensive study indicates that the *I–V* behavior is introduced by strain rather than poor or unstable contact.

Transforming of symmetric or nearly symmetric *I–V* behavior to rectifying *I–V* behavior under strain is a novel phenomenon which was first reported by He et al. [17]. When they used an Au/Ti coated tungsten probe to bend an one-end fixed

ZnO nanowire, the linear *I–V* characteristic of the ZnO nanowire was changed to a rectifying behavior with a rectifying ratio of 8.7:1. They proposed that electrical transport of the ZnO nanowire was governed by a potential energy barrier induced by the strain induced piezoelectric potential. When the ZnO nanowire was bent, the outer surface is stretched and has positive piezoelectric potential, the inner surface is compressed and has negative piezoelectric potential, and thus a piezoelectric potential drop was produced across the diameter of the ZnO nanowire. The probe was in contact with the tensile surface of the nanowire. In our case, however, the ZnO PFW is fixed tightly at its two ends on the PS substrate, and both the outer and inner surfaces of the ZnO PFW are solely under tensile or compressive strain depending on the bending direction of the PS substrate; thus, the piezoelectric potential is along the axial direction of the PFW rather than across its diameter.

4.2.2 Quantifying the Change in Schottky-Barrier Height

The effect of piezoelectric polarization on the SBH arises because the polarization produces charges at the metal-semiconductor interface, which will shift the local Fermi level and modify the local conduction band profile. Thus, both the band structure and piezoelectric polarization effects will affect the SBH and consequently the transport property of the devices, as elaborated in what follows.

Figure 4.8(a) shows *I–V* characteristics under various compressive strains for a device. The currents both under positive bias and negative bias are suppressed, and finally an upward diode-like *I–V* behavior was observed under strain of $\sim -2.14\,\%$. The original *I–V* curve (black line) shown in Fig. 4.8 clearly demonstrates that there were Schottky barrier (SB) present at the contacts but with different barrier heights due to different interface properties. Therefore, the structure of the device can be considered as a single ZnO PFW sandwiched between two back-to-back SBs at the source and drain contacts with SBH of ϕ_s (in eV) and $\phi_d (\phi_d < \phi_s)$, which is shown in the inset of Fig. 4.8(a).

At a fixed bias voltage V, the voltage drop occurs mainly at the reversely biased Schottky barrier according to the measurement by in-situ scanning surface potential microscopy. In our case, when a positive bias voltage V is applied across the drain and source with the drain side positive, the voltage drop occurs mainly at the reversely biased Schottky barrier ϕ_s at the source side, and it is denoted by V_s; when a reversely biased voltage V is applied across the drain and source with the source side positive, the voltage drop occurs mainly at the reversely biased Schottky barrier ϕ_d at the drain side, and it is denoted by V_d. For simplify, here we define a positive voltage to be applied at the drain side and assume that most of the potential drop occur at the reversely biased SB, $V_s \approx V$. Considering that our measurements were made at room temperature and the ZnO PFW had a low doping/impurity level, the dominant transport property at the barrier is thermionic emission and diffusion, and the contribution made by tunneling is negligible. Thus, for a reversely biased SB under voltage V and at temperature T, the current through the reversely biased

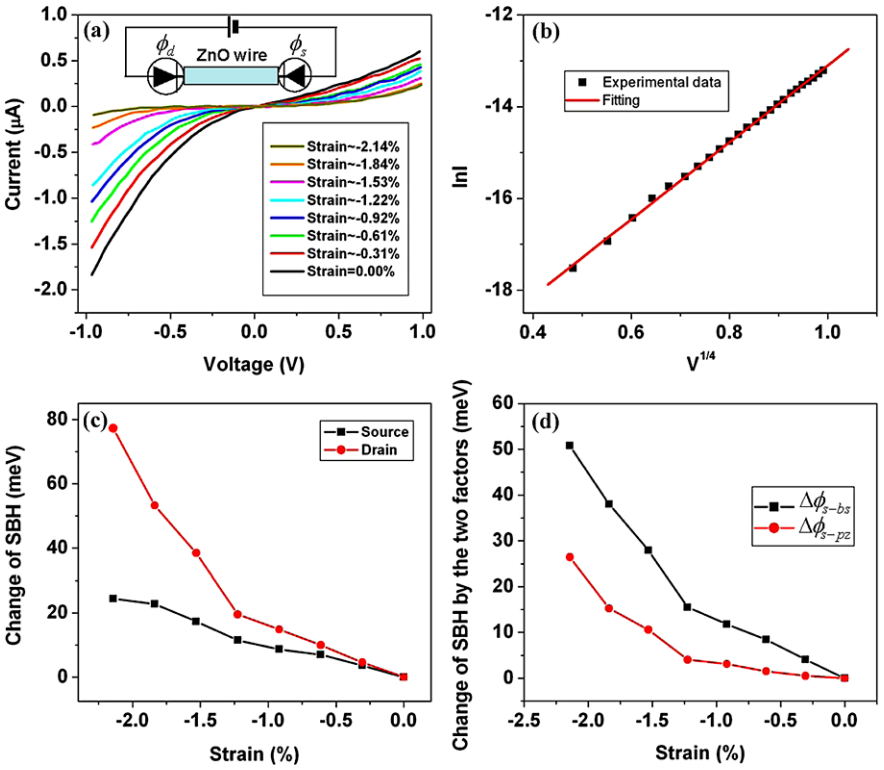

Fig. 4.8 (**a**) I–V characteristics of the sensor under different compressive strains. The decreased current indicates an increase in SBH. The inset is the proposed sandwich model of the device, i.e. two back-to-back Schottky diodes connected to a ZnO wire. (**b**) Plot of $\ln I$ as a function $V^{1/4}$, by using the data provided by the *black line* in (**a**). The *red lines* are theoretically fitting according to (4.2). (**c**) The derived change in SBH as a function of stain using the thermionic emission–diffusion model. The *black curve* and *red curve* are the SBH change for source contact and drain contact at a drain-source bias of $V = 1$ and -1 V, respectively. (**d**) The derived changes in SBH as contributed by band structure effect (*black curve*) and piezoelectric effect (*red curve*), respectively

Schottky barrier ϕ_s is as follows based on classic thermionic emission–diffusion theory (for $V \gg 3kT/q \sim 77$ mV), as presented in (4.2). To verify that (4.2) can precisely describe the observed phenomenon, we plot $\ln I$ as a function of V and $V^{1/4}$ by using the data provided by the black line in Fig. 4.8(a). Figure 4.8(b) shows that the $\ln I$–$V^{1/4}$ curve is very linear. This not only indicates that the thermionic emission–diffusion model is the dominant process in our device, but also shows that the theory can be applied to derive the SBH from experimental data, as described in what follows.

By assuming S, A^*, T and N_D are to be known, ϕ_s can, in principle, be derived from the $\ln I$–V plot [12]. Subsequently, the strain induced change in SBH can be

determined by

$$\ln\left[I(\varepsilon_{zz})/I(0)\right] \sim \Delta A^{**}/A^{**} - \Delta\phi_s/kT \tag{4.6}$$

where $I(\varepsilon_{zz})$ and $I(0)$ are the current measured through the PFW at a fixed bias V_a with and without being strained, respectively. Since the stress dependence of A^{**} arises only from the stress dependence of the effective mass, the first term is much smaller than the second term and is thus neglected in the following discussion. The change of SBH $\Delta\phi_s$ with strain for bias of 1.0 V is plotted in Fig. 4.8(c) (black curve). Similarly, under a bias of −1.0 V, the change of SBH $\Delta\phi_d$ with strain is calculated and the data are plotted in Fig. 4.8(c) (red curve). The result shows that both the SBH at the source and drain contacts were increased with increased compressive strain.

The SBH change for the Ag/ZnO/Ag device structure under strain is a combined effect from both strain induced band structure change and piezoelectric polarization. The contributions from band structure effect to SBH change in source and drain contacts are denoted $\Delta\phi_{s-bs}$ and $\Delta\phi_{d-bs}$, respectively. As discussed above, the axial strain in the ZnO PFW is uniform along its entire length, thus we can assume $\Delta\phi_{s-bs} = \Delta\phi_{d-bs}$ if the two contacts are identical. The contribution of piezoelectric effect to SBH can be described as follows.

As discussed above, the axial strain in the ZnO PFW is uniform along its entire length in our device. Under straining, the cations and anions in ZnO polarize along the straining direction, forming a piezoelectric charge induced polarization. It is important to point out that these piezoelectric ionic charges cannot freely move. They can be screened by the external electrons but cannot be completely depleted [16]. This means that the effect of piezoelectric charges is still preserved, although at a reduced level; even ZnO has a moderate conductivity. The effect of piezoelectric polarization on the SBH can be qualitatively described as follows. For a constant strain of ε_z along the length of the PFW, an axial polarization P_z is then created inside the wire and along the wire direction, $P_z = \varepsilon_z e_{33}$, where e_{33} is the piezoelectric tensor [18]. A potential drop of approximately $V_p^+ - V_p^- = |\varepsilon_z| L e_{33}$ is created along the length of the wire, where L is the length of the wire. Therefore, the modulations to the SBH at the source and drain sides are of the same magnitude but opposite sign ($V_p^+ = -V_p^-$), which are denoted by $\Delta\phi_{s-pz}$ and $\Delta\phi_{d-pz} (= -\Delta\phi_{s-pz})$. Thus the total strain induced changes in SBH at the source and drain contacts are

$$\text{Source:} \quad \Delta\phi_s = \Delta\phi_{s-bs} + \Delta\phi_{s-pz}; \tag{4.7}$$

$$\text{Drain:} \quad \Delta\phi_d = \Delta\phi_{s-bs} - \Delta\phi_{s-pz} \tag{4.8}$$

which yield $\Delta\phi_{s-bs} = (\Delta\phi_s + \Delta\phi_d)/2$ and $\Delta\phi_{s-pz} = (\Delta\phi_s - \Delta\phi_d)/2$. The $\Delta\phi_{s-bs}$ and $\Delta\phi_{s-pz}$ as a function of strain are plotted in Fig. 4.8, in which both show linear relationship under smaller strain and nonlinear behavior under larger strain. It has been reported that under small strain, both the band gap change and piezoelectric polarization have an approximately linear relationship with strain. The nonlinear effect under high strain needs to be analyzed using more sophisticated theory.

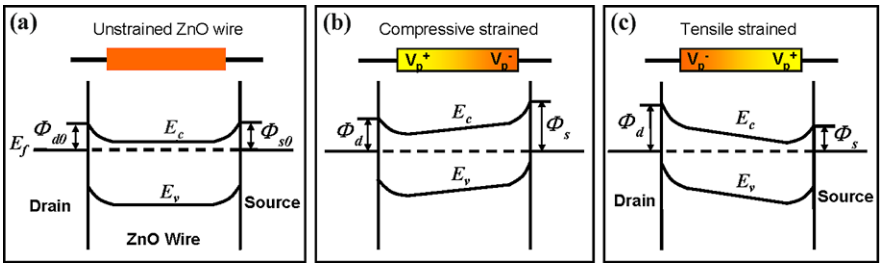

Fig. 4.9 Schematic energy band diagrams illustrating the Schottky barriers at the source and drain contacts of a unstrained (**a**), compressive strained (**b**), and tensile strained (**c**) PFW, which illustrates the effect of switching the piezoelectric potential either by strain or by wire orientation on the local band structure and SBH [18]

4.2.3 Mechanism of the Piezotronic Diode

Here we use a schematic energy band diagrams to illustrate how the piezoelectric polarization affects the Schottky barriers at the source and drain contacts. Figure 4.9(a) shows an unstrained device with the *c*-axis of ZnO pointing towards the source. When the device is under compressed strain, the drain has a higher piezoelectric potential (see Fig. 4.9(b)), resulting in higher SBH at source side. Alternatively, by changing the compressive straining to tensile straining simply by changing the bending direction of the PS substrate, the piezoelectric potential drop in the PFW reverses, as shown in Fig. 4.9(c), leading to a higher SBH at the drain side. If the modulation to SBH by band structure change is significantly smaller than that due to piezoelectric potential, the reversal in strain results in the reversal in rectifying polarity of the device, which is just what we observed experimentally in Fig. 4.7(b).

Furthermore, the profile of the piezoelectric potential depends not only on the sign of the strain (compressive ($\varepsilon_z < 0$); tensile ($\varepsilon_z > 0$)), but also the *c*-axis orientation of the PFW. A simple change in wire orientation can result in a reversal in the piezoelectric potential profile and thus the observed diode polarity. In our fabrication, the *c*-axis of the PFW is random. This is why the ratio of the devices that exhibit downward and upward diode-like *I*–*V* behavior under compressive strain is nearly 1:1.

4.2.4 Piezotronic Electromechanical Switch

Our device can act as an effective electromechanical switch. The inset in Fig. 4.10 shows the *I*–*V* characterization of Device #4 without (black curve) and with (red curve) stain. When the device is free of strain, it shows a symmetric *I*–*V* behavior; when the device is under strain, it shows a rectifying *I*–*V* behavior. The change is highly reversible. At a fixed bias of -2 V, the current across the device is $\sim$6 μA (defined as "on" state) and $\sim$0.05 μA (defined as "off" state) when the device is free

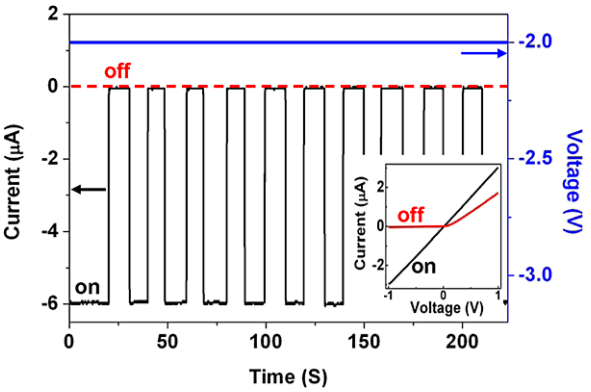

Fig. 4.10 Current response of Device #4 to periodic releasing-bending process under a fixed bias of −2 V, showing an "on"–"off" ratio of ∼120. The *inset* is *I*–*V* characterization of a device without (*black curve*) and with stain (*red curve*)

of strain and under strain, respectively. By periodically bending and releasing the device under a fixed bias of −2 V, an electromechanical switch with on-off ratio as high as ∼120 has been demonstrated (Fig. 4.10).

4.3 Piezotronic Transistors Based on Vertical Nanowires

In this section, we demonstrate strain-gated piezotronic transistor arrays using vertically aligned ZnO NWs [19]. Each ZnO NW with an Au droplet on the tip serves as a transistor. The stress-sensitive gate is the Au–ZnO Schottky junction at the NW tip and the other side is an Ag–ZnO junction. The piezotronic effect was observed in both forward and reversely biased piezoelectric transistors. The electrical transport characteristics of the transistors were investigated by conductive atomic force microscopy (AFM) in contact mode under different strains. Stable and repeatable current–voltage (*I*–*V*) characteristics were observed in our experiment. The current flowing through the NWs was successfully tuned/gated by external force applied to the NWs.

4.3.1 Reversely Biased Contact

The ZnO NWs were epitaxially grown on GaN thin films supported by sapphire substrates using Au nanoparticle catalysts, which were located at the tips of the NWs and served as the electrical contacts after the NW formation. To guarantee the measured electrical behavior is from a single isolated NW, we selected the NWs with low aspect ratios and low density for measurements.

There are two junctions in the piezoelectric transistor in this paper: Au–ZnO and Ag–ZnO. When a bias voltage is applied, one junction is forward biased while the other one is reversely biased. If the Schottky junction Au–ZnO is reversely biased, the Au droplet is connected to the negative voltage and the Ag paste electrode is

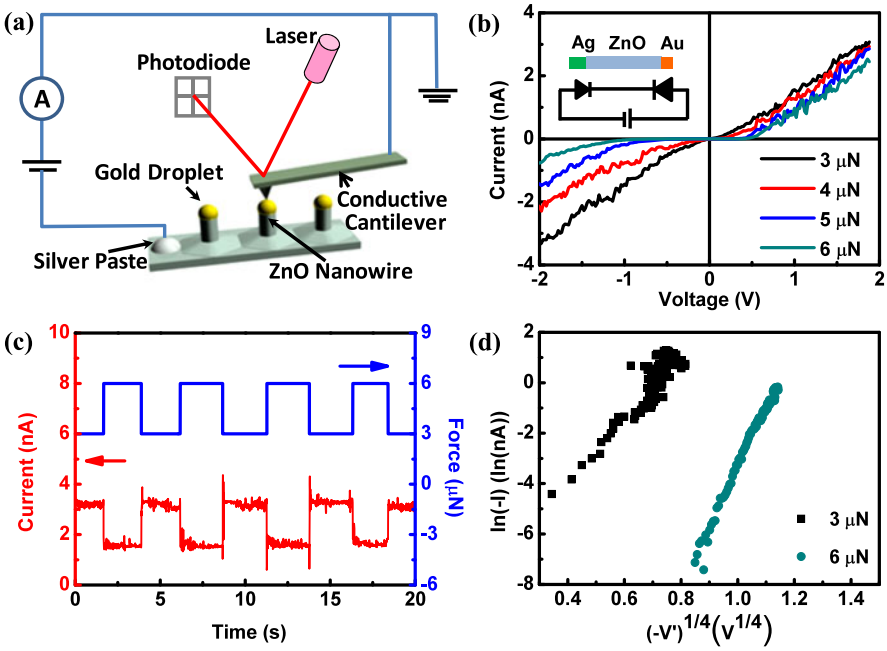

Fig. 4.11 (**a**) Schematic of the C-AFM system used for nanoscale positioning and electrical measurement; (**b**) typical *I–V* characteristics under various compressive force of a sample with double-Schottky junctions; (**c**) current response to a force pulse from 3 to 6 μN. The *blue line* is the applied force and the *red* is the resulting current; (**d**) plots of $\ln(-I)$ as a function of $(-V)^{1/4}$, by using the data from the negative biased region in (**b**)

connected to the positive. In this mode, the dominant piezotronic effect on the *I–V* characteristics if from the Au–ZnO junction due to the higher consumption of the voltage across this junction compared to the forward biased.

The *I–V* characteristics of the transistors were examined by conductive AFM. Figure 4.11(a) gives a schematic diagram of this measurement setup. A conductive AFM probe was used to perform nanometric contact on the transistors. The AFM probe was grounded and the bias voltage was applied from the bottom of sample stage. The structure of the piezoelectric transistor is Ag–ZnO–Au, and the Ag–ZnO junction is stress-free. One electrode is Ag paste coated on the as formed ZnO conductive layer which serves as the source, and the other electrode is the gold droplet formed at the tip of the NW which served as the drain. The "gate voltage" was created from the piezoelectric potential in the NW by applying an axial force using the AFM probe. The current through the NW was collected and measured using the conductive AFM system. During the electrical measurements, various compressive forces were applied to the NWs by adjusting the deflection voltage of the cantilever, which had a linear relationship to the magnitude of the contact force between the AFM tip and the samples.

Strain-dependent *I*–*V* characteristics have been observed in the ZnO NW transistors. Typical rectifying behavior under different forces of a transistor is presented in Fig. 4.11(b). After overcoming the influence of the contact resistance between the AFM tip and the gold droplet, a force from 3 to 6 μN was applied to the transistor. As shown in Fig. 4.11(b), the current decreased when the magnitude of the compressive force increased. At a lower strain with a force of 3 μN, the *I*–*V* characteristic is symmetric and close to linear (black line in Fig. 4.11(b)). By increasing the applied force, the shape of the *I*–*V* curves changed from symmetric into asymmetric and turned into a single Schottky-diode-like characteristic when the force was increased up to 6 μN. The current flowing through the NW has been tuned by the intensity of the external force.

The current response to periodically force pulses was also measured at constant biases. Figure 4.11(c) illustrates the dynamic response to a force pulse at a bias of −2 V. The blue line shows the applied force on the transistor alternating between 3 and 6 μN, and the red line is the response signal of current. This shows that the effect of the force on the current is reversible. At a fixed bias of −2 V, the current dropped from 3.6 to 0.5 nA after applying a 6 μN force on the NW, which can be considered as the "on" and "off" states in a switch transistor. The on-off ratio is about 7.2, which can be further tuned by increasing the strain.

The inset in Fig. 4.11(b) shows the device structure and an equivalent circuit of the transistor. The transistor can be equivalent to two back-to-back Schottky junctions. For back-to-back Schottky junctions, the voltage is mainly consumed at the reversely biased SB. The voltage dependence of the reverse current flowing through a SB is mainly due to the image-force induced barrier height lowering [19]. When an electron was injected from the metal electrode into the semiconductor, it induces a positive charge at the interface layer which acts like an image charge within the layer. The conduction band bends downward and the valence band bends upward, respectively. This effect leads to a reduction of the SBH. The dependence of the reverse current I_r to the reverse-bias follows (4.2). To verify that the model can be used to describe the observed phenomenon, the curves of $\ln(-I)$ as a function of $(-V)^{1/4}$ using the data from Fig. 4.11(b) ($V < 0$) are plotted in Fig. 4.11(d). Under two typical strains, 3 and 6 μN, both plots show a good linear relationship, as expected. It is reasonable to expect that the transportation behavior at the reversely biased side is dominated by the reversely biased SB.

4.3.2 Forward Biased Contact

In forward mode, the piezo Schottky junction (Au–ZnO) is forward biased. A positive voltage is applied between the Au droplet and the Ag paste. In this mode, the Ag–ZnO junction is reversely biased and it will consume most of the voltage if the barrier is high. To eliminate this effect, a device with a lower barrier height at the Ag–ZnO junction was obtained by annealing the device at 600 K in atmosphere for 12 hours. Figure 4.12(a) shows the SEM image (30°-tilted view) of ZnO NWs for a

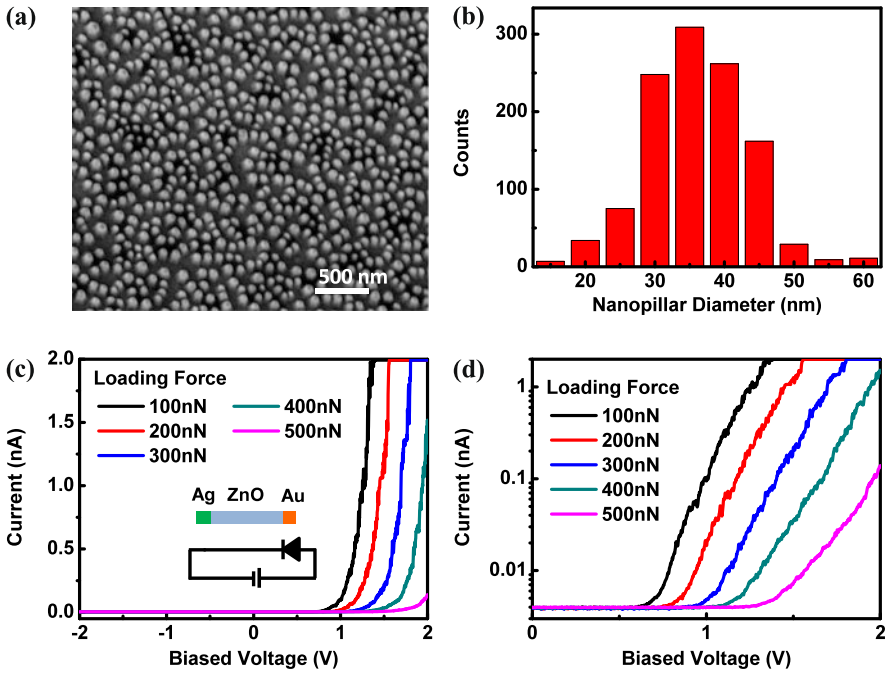

Fig. 4.12 (**a**) ZnO nanowires used for the single-Schottky sample; (**b**) diameter distribution of the nanowires; (**c**) *I–V* characteristics under various compressive forces of a sample with single-Schottky junctions; (**d**) current–voltage characteristics plotted on a semi-logarithmic scale

typical device. It is apparent that the NWs are short. The ZnO NWs used in this device are more like small nanopillars with a diameter around 35 nm. Figure 4.12(b) shows a distribution of the NW diameters as determined from a non-tilted SEM image.

The *I–V* characteristics of the device under various strains are shown in Fig. 4.12(c). Under negative voltage, only a small amount of current can go through. Under positive voltage, the current can reach several nano Ampères. When the external stress varies from 100 to 500 nN, there is a sharp increase in the current. The device performs like a single Schottky diode. This indicates that the Schottky barrier formed at the Au–ZnO junction is high and dominates the performance of the device. The insert in Fig. 4.12(c) shows the device structure and an equivalent circuit.

For an ideal Schottky diode, the *I–V* characteristics in the forward direction are described by [8]

$$I_f = AA^{**}T^2 \exp\left(-\frac{\phi_B}{k_B T}\right) \exp\left(\frac{qV_f}{nk_B T} - 1\right) \tag{4.9}$$

where V_f is the voltage dropped on the forward biased Schottky diode and n is the ideality factor [19]. Mathematically, the logarithm of the current $\ln I_f$ has a

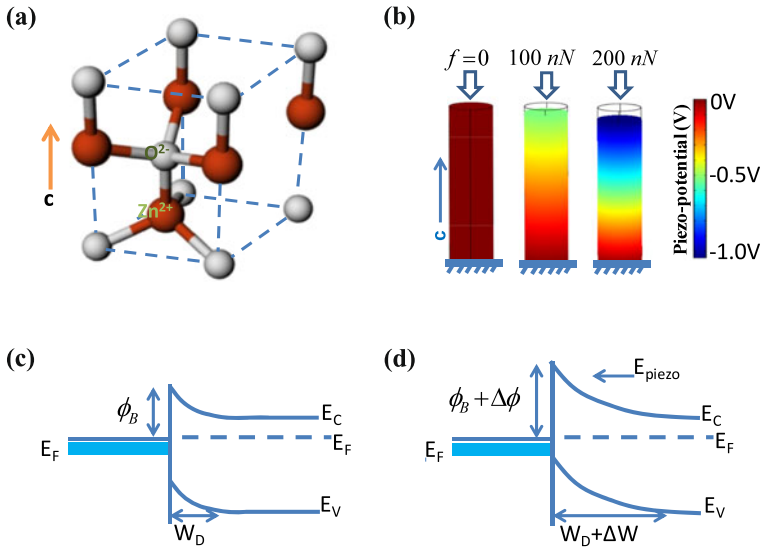

Fig. 4.13 (**a**) Stick-and-ball representation of the ZnO wurtzite crystal structure. Red and gray spheres denote Zn and O atoms, respectively; (**b**) finite element calculation of the piezopotential distribution in a ZnO nanowire 50 nm in width and 100 nm in length, under different uniaxial compressions of 0 nN (*left*), 100 nN (*middle*) and 200 nN (*right*); (**c**) Schottky barrier formed at the metal-semiconductor interface; (**d**) piezopotential influence on the Schottky-barrier height at the metal-semiconductor junction on (0001) plane

linear relationship to the voltage V_f dropped on the diode, and can be expressed as $\ln I_f \propto V_f$.

Figure 4.12(d) shows the forward *I*–*V* characteristics of this transistor on a semi-log scale. The good linear fit of the plots shows that the forward current has exponential relationship to the voltage. This indicates that the thermionic emission–diffusion model is the dominant process in our device.

4.3.3 Two-Leads Piezotronic Transistor

The stress-dependent *I*–*V* characteristics, both forward and reverse modes, can be explained by the piezotronic effect. Figures 4.13(a) and (b) show the mechanism of the piezotronic effect in ZnO NWs. ZnO has a non-central symmetric wurtzite crystal structure (Fig. 4.13(a)). For the sake of simplicity, we calculated the potential distribution using the finite element method by assuming the ZnO NW as an insulator. The color code plotted in Fig. 4.13(b) shows the calculated potential distribution along the *c*-axis oriented ZnO NW while various compressive strains are applied along the NW (0, 100 and 200 nN from left to right). The NW dimensions of the NW are 50 nm in diameter and 100 nm in length. The calculated piezopotentials are based on following parameters: piezo constant $d_{33} = -5.43 \times 10^{-12}$ C/N, relative

dielectric permittivity $\varepsilon_r = 10.204$ and the elasticity 210 GPa, which are the default parameters for piezoelectric ZnO materials in the COMSOL Multiphysics software (Version 4.2a), and there is no doping. The dependency rate of the piezopotential on the stress is about 5 mV/nN as shown in Fig. 4.13(b). In nanowires that are n-type doped or containing vacancies, the piezopotential will drive the free electrons to move from one side to the other side to "screen" the local piezopotential in the crystal and reach a new equilibrium. Due to the finite doping of the ZnO NWs, the piezopotential is partially screened but not completely, and the partially screened piezopotential will change the local Fermi level and conduction band near the surface. The piezopotential affects the SBH by changing the local Fermi level and conduction band at the semiconductor side of the Schottky junction. In our case, the ZnO NW is capped by an Au droplet and the bottom is connected to the as-grown ZnO conductive layer. The piezotronic effect mainly influences the Au–ZnO Schottky junction.

To illustrate the piezotronic effect simply, we can use the energy band diagrams shown in Figs. 4.13(c) and (d). The barrier height ϕ_B is quantitatively evaluated by the potential difference between the Fermi energy of the metal and the band edge of the n-type semiconductor where the electrons reside as shown in Fig. 4.13(c). If the semiconductor is a piezoelectric material, ZnO for example, and the crystallographic c-axis is directed towards the Au–ZnO junction, a piezopotential would be created in the crystal once a strain is applied as depicted in Fig. 4.13(d). The local contact characteristics are changed by the piezopotential due to the redistribution of the carriers. The c-axis of the vertical ZnO NWs grown on GaN-buffered c-plane sapphire is along the growth direction. When an external force is applied, there is a negative piezopotential generated at the Schottky junction between the Au droplet and the ZnO NW, which widens the depletion layer as shown in Fig. 4.13(d), thus enhancing the SBH. The strain dependent-piezopotential effectively changes the local contact characteristics and tunes/gates the carrier transport process at the metal-semiconductor interface.

4.4 Summary

In summary, a new type fully packaged strain sensor device based on the piezotronic effect has been demonstrated. The strain sensor was fabricated by bonding a ZnO PFW laterally on a flexible PS substrate and packaged by a PDMS thin film. The sensor devices have excellent stability, fast response and high gauge factor of up to 1250. The *I–V* characterization of the device is modulated by the change of SBH, which has a linear relationship with strain. The underlying mechanism for the change of SBH was attributed to the combination of piezoresistance and piezotronic effects, but the contribution made by the latter is dominant. The strain sensor developed here based on a flexible substrate has application in strain and stress measurements in cell biology, biomedical sciences, MEMS devices, structure monitoring, and even earthquake monitoring.

Using the strain induced change in the transport property of ZnO wire, we have demonstrated a piezoelectric diode-based switches with an on-to-off ratio ∼120. The wire was laterally bonded and fully packaged, and the design can be easily extended for nanowires, which are expected to have super-high sensitivity. The existence of the piezoelectric potential not only supports the mechanism proposed for nanogenerators and piezotronics, but also can be used to fabricate a new type of piezoelectric diodes and switches, which are highly sensitive, cost-effective, versatile and fully packaged for a wide range of applications.

In the strain-gated piezotronic transistor, demonstrated using the vertical NW array, the gate electrode of the transistor is replaced by the internal crystal potential generated by strain and the control over the transported current is at the interface between the nanowire and the top or bottom electrode. It gives the possibility of fabricating array of transistors using individual vertical nanowires that can be controlled independently by the applied mechanical force/pressure over the top. Such a piezotronic transistor array is a new design of transistors and is likely to have important application in high-resolution mapping of strain/force/pressure.

References

1. T. Toriyama, D. Funai, S.J. Sugiyama, Piezoresistance measurement on single crystal silicon nanowires. J. Appl. Phys. **93**(1), 561 (2003)
2. T.W. Tombler, C.W. Zhou, L. Alexseyev, J. Kong, H.J. Dai, L. Liu, C.S. Jayanthi, M.J. Tang, S.Y. Wu, Reversible electromechanical characteristics of carbon nanotubes under local-probe manipulation. Nature **405**, 769–772 (2000)
3. C. Stampfer, T. Helbling, D. Obergfell, B. Schöberle, M.K. Tripp, A. Jungen, S. Roth, V.M. Bright, C. Hierold, Fabrication of single-walled carbon-nanotube-based pressure sensors. Nano Lett. **6**(2), 233–237 (2006)
4. R.J. Grow, Q. Wang, J. Cao, D.W. Wang, H.J. Dai, Piezoresistance of carbon nanotubes on deformable thin-film membranes. Appl. Phys. Lett. **86**(9), 093104 (2005)
5. J. Zhou, Y.D. Gu, P. Fei, W.J. Mai, Y.F. Gao, R.S. Yang, G. Bao, Z.L. Wang, Flexible piezotronic strain sensor. Nano Lett. **8**(9), 3035–3040 (2008)
6. Z.Y. Zhang, C.H. Jin, X.L. Liang, Q. Chen, L.M. Peng, Current–voltage characteristics and parameter retrieval of semiconducting nanowires. Appl. Phys. Lett. **88**(7), 073102 (2006)
7. Z.Y. Zhang, K. Yao, Y. Liu, C.H. Jin, X.L. Liang, Q. Chen, L.M. Peng, Quantitative analysis of current–voltage characteristics of semiconducting nanowires: decoupling of contact effects. Adv. Funct. Mater. **17**(14), 2478–2489 (2007)
8. S.M. Sze, *Physics of Semiconductor Devices*, vol. 281 (Wiley, New York, 1981)
9. Z.Y. Fan, J.G. Lu, Electrical properties of ZnO nanowire field effect transistors characterized with scanning probes. Appl. Phys. Lett. **86**(3), 032111 (2005)
10. Y. Liu, Z. Kauser, P.P. Ruden, Z. Hassan, Y.C. Lee, S.S. Ng, F.K. Yam, Effect of hydrostatic pressure on the barrier height of Ni Schottky contacts on n-AlGaN. Appl. Phys. Lett. **88**(2), 022109 (2006)
11. W. Shan, M.F. Li, Y.P. Yu, W.L. Hansen, W. Walukiewicz, Pressure dependence of Schottky barrier height at the Pt/GaAs interface. Appl. Phys. Lett. **53**(11), 974–976 (1988)
12. Y. Liu, M.Z. Kauser, M.I. Nathan, P.P. Ruden, S. Dogan, H. Morkoc, S.S. Park, K.Y. Lee, Effects of hydrostatic and uniaxial stress on the Schottky barrier heights of Ga-polarity and N-polarity n-GaN. Appl. Phys. Lett. **84**(12), 2112–2114 (2004)
13. Z. Dridi, B. Bouhafs, P. Ruterana, Pressure dependence of energy band gaps for $Al_xGa_{1-x}N$, $In_xGa_{1-x}N$ and $In_xAl_{1-x}N$. New J. Phys. **4**, 94.1–94.15 (2002)

14. K.W. Chung, Z. Wang, J.C. Costa, P. Williamson, P.P. Ruden, M.I. Nathan, Barrier height change in GaAs Schottky diodes induced by piezoelectric effect. Appl. Phys. Lett. **59**(10), 1191–1193 (1991)
15. Y. Liu, M.Z. Kauser, D.D. Schroepfer, P.P. Ruden, J. Xie, Y.T. Moon, N. Onojima, H. Morkoc, K.A. Son, M.I. Nathan, Effect of hydrostatic pressure on the current–voltage characteristics of GaN/AlGaN/GaN heterostructure devices. J. Appl. Phys. **99**(11), 113706 (2006)
16. J. Zhou, P. Fei, Y.D. Gu, W.J. Mai, Y.F. Gao, R.S. Yang, G. Bao, Z.L. Wang, Piezoelectric-potential-controlled polarity-reversible Schottky diodes and switches of ZnO wires. Nano Lett. **8**(11), 3973–3977 (2008)
17. J.H. He, C.H. Hsin, L.J. Chen, Z.L. Wang, Piezoelectric gated diode of a single ZnO nanowire. Adv. Mater. **19**(6), 781–784 (2007)
18. J.F. Nye, *Physical Properties of Crystal* (Oxford University Press, London, 1955)
19. W.H. Han, Y.S. Zhou, Y. Zhang, C.Y. Chen, L. Lin, X. Wang, S.H. Wang, Z.L. Wang, Strain-gated piezotronic transistors based on vertical zinc oxide nanowires. ACS Nano **6**(5), 3760–3766 (2012)

Chapter 5
Piezotronic Logic Circuits and Operations

Abstract In this chapter, by utilizing the gating effect produced by the piezopotential in a nanowire under externally applied deformation, piezotronic transistors have been fabricated; one can use them for the universal logic operations such as NAND, NOR and XOR gates as has been demonstrated for performing piezotronic logic operations. The mechanical–electronic logic units are an important step toward the basic design of complex systems in human–CMOS interfacing, touch pad technology and active flexible, nanorobotics, active flexible electronics, microfluidics and MEMS.

A self-powered [1] autonomous intelligent nanoscale system should consist of ultrasensitive nanowire (NW)-based sensors [2–5], integrated high-performance memory and logic computing components for data storage and processing as well as decision making [6–12], and an energy scavenging unit for sustainable, self-sufficient and independent operation [1, 13–20]. The existing semiconductor NW logic devices are based on electrically gated field-effect transistors, which function as both the drivers and the active loads of the logic units by adjusting the conducting channel width [21, 22]. Moreover, the currently existing logic units are "static" and are almost completely triggered or agitated by electric signals, while the "dynamic" movable mechanical actuation is carried out by another unit possibly made of different materials.

In this chapter, we present the piezoelectric trigged mechanical–electronic logic operation using the piezotronic effect, through which the integrated mechanical electrical coupled and controlled logic computation is achieved using only ZnO NWs [23]. By utilizing the piezoelectric potential created in a ZnO NW under externally applied deformation, strain-gated transistors (SGTs) have been fabricated, using which universal logic components such as inverters, NAND, NOR, XOR gates have been demonstrated for performing piezotronic logic calculations, which have the potential to be integrated with the NEMS technology for achieving advanced and complex functional actions in applications of vital importance in portable electronics, medical sciences and defense technology, such as in nanorobotics for sensing and actuating, in microfluidics [24] for controlling the circuitry of the fluid flow, and in other micro/nanosystems for intelligent control and action.

Z.L. Wang, *Piezotronics and Piezo-Phototronics*, Microtechnology and MEMS,
DOI 10.1007/978-3-642-34237-0_5, © Springer-Verlag Berlin Heidelberg 2012

5.1 Strain-Gated Transistor

The piezopotential created inside a ZnO NW under strain can be effectively used as a gate voltage, which has been applied for fabricating a range of piezotronic nanodevices [25–28], and, therefore, the mechanic-electrical coupled and controlled actions can be performed in one structure unit made of a single material. Mechanical straining can create a piezopotential inside ZnO due to the polarization of the non-mobile ions, owing to the piezoelectric effect. In addition, the piezopotential can act as a "controller" for gating the transport behavior of the charge carriers, which is the fundamental principle for strain-gated electronic devices, based on which the ZnO-NW electromechanical switch has been fabricated [28].

5.1.1 Device Fabrication

A strain-gated transistor (SGT) is made of a single ZnO NW with its two ends, which are the source and drain electrodes, being fixed by metal contact on a polymer substrate (Fig. 5.1(a)). The SGI was fabricated by bonding two ZnO NWs laterally on a Dura–Lar film. The thickness of the Dura–Lar film is 0.5 mm. The ZnO NWs were synthesized via a physical vapor deposition method and typically have diameters of 300 nm and lengths of 400 μm (Fig. 5.1(a)). The films were first cleaned with acetone, isopropyl alcohol and DI water by sonication, after which the Dura–Lar films were dried by nitrogen gas blowing. One ZnO NW was placed flat on the top surface of the Dura–Lar film first using a probe station (Cascade Microtech, Inc.) under an optical microscope (Leica Microsystems, Inc.). Silver paint (Ted Pella, Inc.) was applied at both ends of the ZnO NW for electrical contacts. The second ZnO NW was placed on the bottom surface of the Dura–Lar film in the same way.

Once the substrate is bent, a tensile/compressive strain is created in the NW since the mechanical behavior of the entire structure is determined by the substrate. Utilizing the piezopotential created inside the NW, the gate input for a NW SGT is an externally applied strain rather than an electrical signal. I_{DS}–V_{DS} characteristic for each single ZnO-NW SGT is obtained as a function of the strain created in the SGT (Fig. 5.1(a)) before further assembly into logic devices. A NW SGT is defined as forward biased if the applied bias is connected to the drain electrode (Fig. 5.1(a)).

For a SGT, the external mechanical perturbation induced strain (ε_g) acts as the gate input for controlling the "on"/"off" state of the NW SGT. The positive/negative strain is created when the NW is stretched/compressed (see SI for the calculation of the strain in the NW SGT). The I_{DS}–ε_g curves at a fixed V_{DS} show that I_{DS} increases as the gate strain ε_g increases and the threshold gate strain ε_T is around 0.08 % (Fig. 5.1(b)), which show that the SGT behaves in a similar way to a n-channel enhancement-mode MOSFET. The threshold gate strain ε_T is determined from the intercept (on the ε_g axis) of the tangent of the maximum slope region (shown as the black dashed line in Fig. 5.1(b)) of the I_{DS}–ε_g curve. The I_{DS}–ε_g transfer curve obtained for drain bias voltage $V_{DS} = 1$ V (Fig. 5.2) demonstrates that

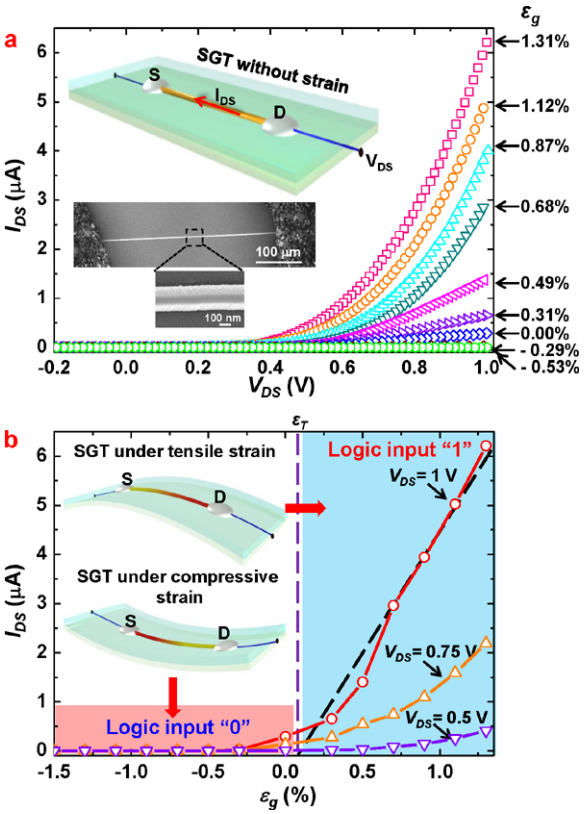

Fig. 5.1 Single ZnO NW strain-gated transistor (SGT). (**a**) I_{DS}–V_{DS} output characteristic for a ZnO SGT device with strain sweeping from $\varepsilon_g = -0.53$ % to 1.31 % at a step of 0.2 %. (*Insets*) *Top*: schematic of a single ZnO NW SGT under bias without strain. Current flows from drain to source electrode with external bias applied at the drain side. *Bottom*: top-view SEM image of the active part of a ZnO SGT ($L = 70$ μm, diameter = 300 nm), with both ends of the ZnO NW fixed by silver paste. (**b**) I_{DS}–ε_g transfer characteristic for the same ZnO SGT device under three different V_{DS} bias values: 1, 0.75 and 0.5 V, respectively. The threshold gate strain ε_T is determined as around 0.08 % from the intercept (on the ε_g axis) of the tangent of the maximum slope region (shown as the *black dashed line*) of the I_{DS}–ε_g curve. (*Insets*) *Top*, schematic of a ZnO SGT under tensile strain and the corresponding I_{DS}–ε_g characteristic curve (*blueish region*), which is the logic "1" strain input region for the SGT. *Bottom*, schematic of a ZnO SGT under compressive strain and the corresponding $I_{DS} - \varepsilon_g$ characteristic curve (*red region*), which is the logic "0" strain input region of the SGT. As in the NW, the piezopotential created by strain is negative in the red color region and positive in the yellow color region [23]

the NW SGT has a peak pseudo transconductance, $g_m = dI_{DS}(V_{DS})/d\varepsilon_g$, which is 6 μA for a strain change of $\Delta\varepsilon_g = 1$ %. The on and off currents I_{on} and I_{off} for the NW SGT can be determined as the values obtained at $\varepsilon_{g(on)} = \varepsilon_g - 0.3$ % and $\varepsilon_{g(off)} = \varepsilon_g + 0.7$ %, so that 70 % of the ε_g swing above the threshold strain ε_g turns the ZnO NW SGT on, while the remaining 30 % defines the "off" operation range,

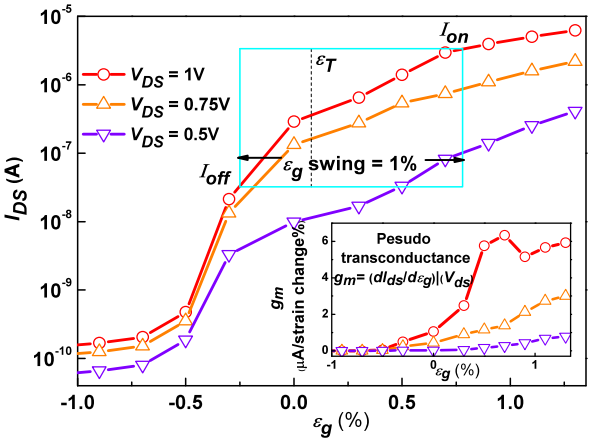

Fig. 5.2 I_{DS}–ε_g transfer characteristic for ZnO NW SGT. I_{DS}–ε_g transfer characteristic for the ZnO SGT device under three different V_{DS} bias values: 1, 0.75 and 0.5 V, respectively. The *blue square* defines the 1 % gate strain window. On and off currents are defined as the values obtained at $\varepsilon_{g(on)} = \varepsilon_g - 0.3$ % and $\varepsilon_{g(off)} = \varepsilon_g + 0.7$ %, so that 70 % of the ε_g swing above the threshold strain ε_g turns the ZnO NW SGT on, while the remaining 30 % defines the "off" operation range. (*Inset*) Pseudo transconductance for this ZnO NW SGT with V_{DS} bias values of 1, 0.75 and 0.5 V, respectively, from top to bottom [23]

which is demonstrated in Fig. 5.3. $I_{on} = 3.38$ μA and $I_{off} = 0.03$ μA are hence obtained with I_{on}/I_{off} ratio of 112 for $V_{DS} = 1$ V; this ratio is comparable to the reported value for the Ge/Si NW-based device that was electrically driven [22]. It can also be foreseen from the I_{DS}–εg transfer curves (Fig. 5.3) that the ZnO-NW SGT-based electromechanical amplifier can be realized by integrating with nanoscale electromechanical transducing units [6].

5.1.2 Fundamental Principle

The working principle of a SGT is illustrated by the band structure of the device. A strain–free ZnO NW has Schottky contacts at the two ends with the source and drain electrodes but with different barrier heights of Φ_S and Φ_D, respectively (Fig. 5.3(a)). The Fermi level inside the ZnO NW is considered flat here for illustration purpose, which is valid in our devices since the most of the bias falls at the reversed biased junction [28]. When the drain is forward biased, the quasi-Fermi levels at the source ($E_{F,S}$) and drain ($E_{F,D}$) are different by the value of eV_{bias}, where V_{bias} is the applied bias (Fig. 5.3(b)). An externally applied mechanical strain (ε_g) results in both the band structure change and piezoelectric potential field inside a ZnO NW [28]. The change in band structure leads to the piezoresistance effect, which is a non-polar and symmetric effect at both the source and drain contacts. Since ZnO is a polar structure along c-axis, straining in axial direction (c-axis) creates a polarization of cations and anions in the NW growth direction, resulting in

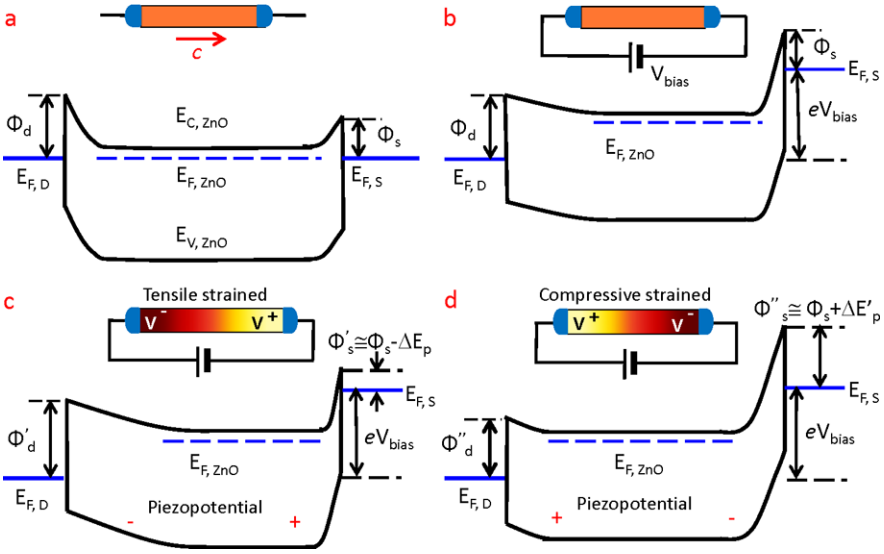

Fig. 5.3 The band structures of the ZnO NW SGT under different conditions for illustrating the mechanism of the strain-gated transistor (SGT). The crystallographic c-axis of the nanowire directs from drain to source. (**a**) The band structure of a strain–free ZnO NW SGT at equilibrium with different barrier heights of Φ_S and Φ_D at the source and drain electrodes, respectively. (**b**) The quasi-Fermi levels at the source ($E_{F,S}$) and drain ($E_{F,D}$) of the ZnO SGT are split by the applied bias voltage V_{bias}. (**c**) With tensile strain applied, the SBH at the source side is reduced from Φ_S to $\Phi'_S \cong \Phi_S - \Delta E_P$. (**d**) With compressive strain applied, the SBH at the source side is raised from Φ_S to $\Phi''_S \cong \Phi_S + \Delta E'_P$ [23]

a piezopotential drop from V^+ to V^- inside the NW (Fig. 5.3), which produces an asymmetric effect on the changes in the Schottky barrier heights (SBHs) at the drain and source electrodes. Under tensile strain, the SBH at the source side reduces from Φ_S to $\Phi'_S \cong \Phi_S - \Delta E_P$ (Fig. 5.3(c)), where ΔE_P denotes the change from the locally created piezopotential, and it is a function of the applied strain, resulting in increased I_{DS}. For the compressively strained SGT, the sign of the piezopotential is reversed, and thus the SBH at the source side is raised from Φ_S to $\Phi''_S \cong \Phi_S + \Delta E'_P$ (Fig. 5.3(d)), where $\Delta E'_P$ denotes the piezopotential effect on the SBH at source side, resulting in a large decrease in I_{DS}. Therefore, as the strain ε_g is swept from compressive to tensile regions, the I_{DS} current can be effectively turned from "off" to "on" while V_{DS} remains constant. This is the fundamental operating principle of the SGT.

5.2 Strain-Gated Invertor

The piezotronic strain-gated complementary logic gates are built using back-to-back packaged n-type ZnO NW SGTs on the top and bottom surfaces of a flexible substrate. Our first example is to illustrate the ZnO-NW strain-gated inverter (SGI)

(Fig. 5.4). When the substrate is bent downward (Fig. 5.4(a1)), a tensile strain of 0.05–1.5 % is created in SGT 1, while a compressive strain with the same magnitude is simultaneously produced in SGT 2, which results in a complementary "on" and "off" status in the two SGTs, respectively. Alternatively, if the substrate is bent upward (Figs. 5.4(a3)), the two SGTs have a complementary "off" and "on" status, respectively. Therefore, these two SGTs behave in a similar way to the operation of the NMOS and PMOS transistors in the conventional complementary-metal-oxide-semiconductor (CMOS) inverters [29].

The strain–voltage transfer characteristic (SVTC) and noise margins of the NW SGI are obtained by plotting the measured output voltages versus corresponding gate strains (Fig. 5.4(b)). V_{OH} and V_{OL} represent the high and low output voltages of the SGI, with ideal values of $V_{OH} = V_{DS} = 1$ V and $V_{OL} = 0$ V. The experimental values for V_{OH} and V_{OL} are 0.98 V and 0.0001 V, respectively. The measured value for V_{OH}, smaller than the applied 1 V, is due to the voltage drop across the SGT that is at "on" status. The logic swing of the SGI defined by $(V_{OH} - V_{OL})$ is 0.98 V. The switching threshold strain of the SGI, ε_I, at which the output of the SGI switches between logic high and low status, is obtained at point C with a strain value of -0.6 % in Fig. 5.4(b). The slope value of the dashed line connecting the point of the origin and point C in Fig. 5.4(b) is 1. In order to characterize the effect of the input gate strain on the SGI output, the largest input strain for generating output logic "1", ε_{IL}, and the smallest input strain for inducing output logic "0", ε_{IH}, are determined at the pseudo unit gain points A and B (see Fig. 5.4(b) and SI) with strain values of -0.8 % and -0.38 %, respectively. The slopes of the SVTC curve (red line) at points A and B are both -1. The input strain zone with $\varepsilon < \varepsilon_{IL}$ $(= -0.8$ %) (purple color zone in Fig. 5.4(b)) induces the logic output of "1" for the SGI, while input strain zone with $\varepsilon > \varepsilon_{IH}$ $(= -0.38$ %) (the bluish color zone in Fig. 5.4(b)) induces logic output "0" for the SGI. The negative values for ε_{IL} and ε_{IH} may be due to the fact that some initial strains were unpurposeful introduced in the SGTs during the fabrication process [30]. In the logic low input region (purple color region in Fig. 5.4(b)), SGT 1 is on and SGT 2 is off; while in the logic high input region (bluish color region in Fig. 5.4(b)), SGT 1 is off and SGT 2 is on. The response time of the SGI is dictated by the straining rate, which is an application-dependent factor and the transient property can be investigated for ZnO NW SGI. The strain-gated logic devices are designed to interface with the ambient environment, which is associated with low-frequency mechanical actions, and the aim and targeting applications are different from those of conventional silicon devices which aim at speed. Switching frequency is not the critical issue as long as the strain-gated logic devices can respond to and process the mechanical signals in a timely manner, such as in applications of nanorobotics, transducers and micro-machine. The applications of SGTs are complementary to those of the CMOS technology. Unlike the conventional CMOS inverter, there is no electrical gate in the ZnO-NW SGT and hence the gate leakage current can be ignored in the ZnO-NW SGI.

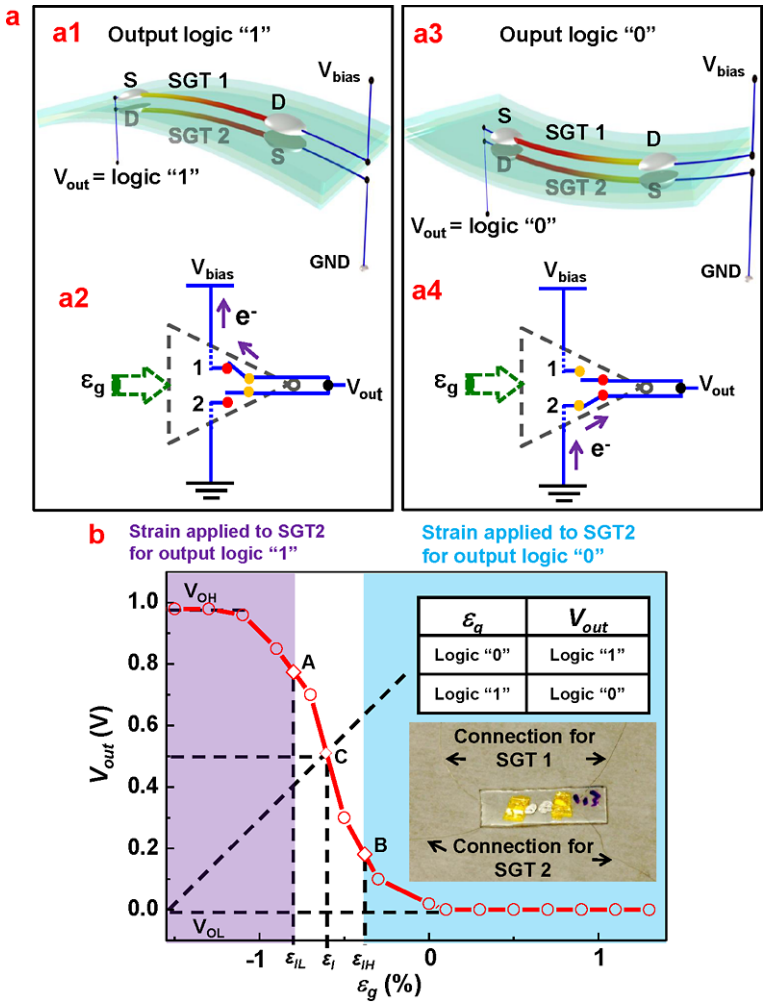

Fig. 5.4 ZnO NW strain-gated inverter (SGI). (**a1**)–(**a4**) Schematics and corresponding symbols of a ZnO NW SGI performing logic operations in responding input strain. The strain input for the SGI is defined in reference to the strain acting to SGT 2. When the strain input for the SGI is logic "0", SGT 1 is on and SGT 2 is off. Therefore the electrical output is logic "1" for the SGI. GND is the grounded end. When the strain input for the SGI is logic "1", SGT 1 is off and SGT 2 is on. Therefore the electrical output is logic "0" for the ZnO SGI. The *c*-axis direction and the polarity of the piezopotential field for each SGT under strains are defined in Fig. 5.1. (**b**) The strain–voltage transfer characteristic (SVTC) and noise margins of the ZnO NW SGI with $V_{DS} = 1$ V. The slope of the dashed line connecting the point of the origin and point C is 1. The slopes of points A and B on the SVTC curve (*red line*) are both -1. *Inset*, optical picture of a ZnO NW SGI, with two SGTs and four connecting wires [23]

Table 5.1 Two kinds of transition occur during the switching of a ZnO NW strain-gated NAND gate. One kind of transition changes the on/off status for all four SGTs, such as the case happening in the first two columns of the table (with purple color). The other kind of transition changes the on/off status for only two SGTs, like the cases happening in the last four columns of the table (with bluish color). The two numbers in the quotation marks represent the logic levels for strain input on the SGIs in a ZnO NW strain-gated NAND gate

	"0 0" → "1 1"		"0 1" → "1 1"		"1 0" → "1 1"	
SGT 1	On	Off	On	Off	Off	Off
SGT 2	Off	On	Off	On	On	On
SGT 3	Off	On	On	On	Off	On
SGT 4	On	Off	Off	Off	On	Off

Table 5.2 Two kinds of transition occur during the switching of a ZnO NW strain-gated NOR gate. One kind of transition changes the on/off status for all four SGTs, such as the case happening in the first two columns of the table (with purple color). The other kind of transition changes the on/off status for only two SGTs, like the cases happening in the last four columns of the table (with blueish color). The two numbers in the quotation marks represent the logic levels for strain input on the SGIs in a ZnO NW strain-gated NOR gate

	"0 0" → "1 1"		"0 0" → "1 0"		"0 0" → "0 1"	
SGT 5	Off	On	Off	On	Off	Off
SGT 6	On	Off	On	Off	On	On
SGT 7	On	Off	On	On	On	Off
SGT 8	Off	On	Off	Off	Off	On

5.3 Piezotronic Logic Operations

5.3.1 NAND and NOR

Logic operations of NW strain-gated NAND and NOR gates were realized by integrating two NW SGIs, which are gated individually by the applied strains, according to corresponding connection rules (Figs. 5.5A(a1) and (a2) for the NAND gate and Figs. 5.5A(b1) and (b2) for the NOR gate). The output voltages of NAND and NOR gates versus the input gate strains are shown in Fig. 5.5A(a3) for the NAND gate and Fig. 5.5A(b3) for the NOR gate. Two types of transition occur during the switching operation of both the ZnO NW strain-gated NAND and NOR gates, which have been tabulated (Tables 5.1 and 5.2). It can also be seen that NW strain-gated NAND

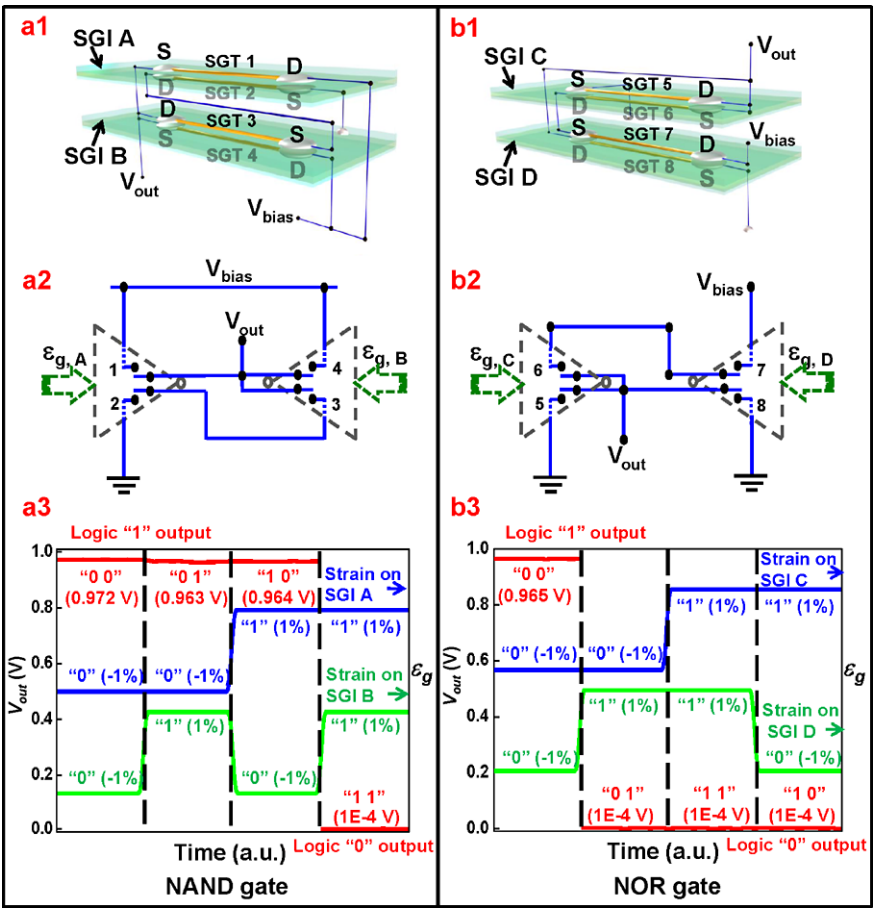

Fig. 5.5A (**a**), (**b**). ZnO NW strain-gated NAND and NOR logic gates. (**a1**)–(**a3**) ZnO NW strain–gated NAND gate. (**a1**) Schematic of the ZnO NW strain-gated NAND logic gate, which is composed of two SGIs, SGI A, and SGI B. The strain input A for SGI A is defined in reference to the strain applied to SGT 2 and the strain input B for SGI B is defined in reference to the strain applied to SGT 3. (**a2**) Layout for ZnO NW strain-gated NAND logic gate by connecting two ZnO NW SGIs. (**a3**) Logic operations and experimental truth table of the ZnO NW strain-gated NAND logic gate. The red line is the electrical output of the NAND gate. *Blue* and *green lines* represent the strain input applied on SGI A and SGI B, respectively. "1" and "0" in the quotation marks along the input curves represent the logic levels of the input. For the output, the first number in the quotation marks represents the logic level for strain input on SGI A and the second number represents the logic level for strain input on SGI B. The values in the parentheses are the corresponding physical values for the input and output. The same denominations apply for NOR and XOR logic gates. (**b1**)–(**b3**) ZnO NW strain-gated NOR gate. (**b1**) Schematic of the ZnO NW strain-gated NOR logic gate, which is composed of two SGIs, SGI C and SGI D. The strain input C for SGI C is defined in reference to the strain applied to SGT 5 and the strain input D for SGI D is defined in reference to the strain applied to SGT 8. (**b2**) Layout for ZnO NW strain-gated NOR logic gate connecting two ZnO NW SGIs. (**b3**) Logic operations and experimental truth table of the ZnO NW strain-gated NOR logic gate. The *red line* is the electrical output of the NOR gate. *Blue* and *green lines* represent the strain input applied on SGI C and SGI D, respectively. The abbreviation a.u. is for arbitrary units

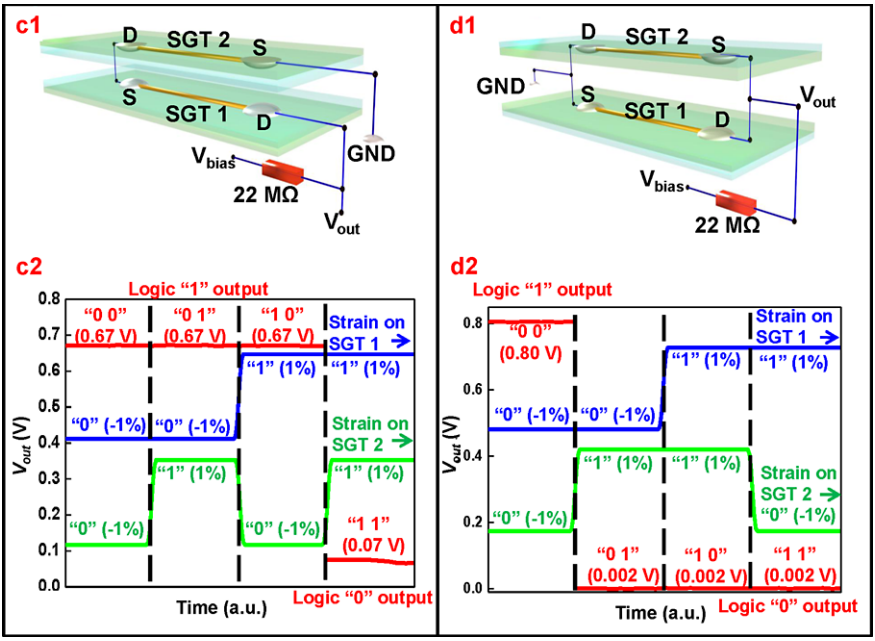

Fig. 5.5B (**c**), (**d**). (**c1**) Schematic of a resistive-load ZnO NW NAND gate constructed from serial connection of two ZnO NWs. A 22 MΩ resistor is used as the pull-up load. (**c2**) Logic operations and experimental truth table of the resistive-load ZnO NW NAND logic gate. *Blue curve* and *green curve* represent the strain input applied on SGT 1 and SGT 2, respectively. (**d1**) Schematic of a resistive-load ZnO NW NOR gate constructed from parallel connection of two ZnO NWs. A 22 MΩ resistor is used as the pull-up load. (**d2**) Logic operations and experimental truth table of the resistive-load ZnO NW NOR logic gate. *Blue curve* and *green curve* represent the strain input applied on SGT 1 and SGT 2, respectively [23]

and NOR gates with active loads (Figs. 5.5A(a3) and (b3)) exhibit better overall performance, such as larger logic swing, compared to passive-load NAND and NOR gates (Figs. 5.5B(c) and (d)).

5.3.2 XOR

The strain-gated ZnO NW XOR logic was also realized by connecting two SGTs in parallel (Fig. 5.6(a)). The drain electrode of SGT 1 in Fig. 5.6(a) is connected to the electrical input V_A while the drain electrode of SGT 2 is connected to $V_{\bar{A}}$, which is the logically complement electrical input to V_A. If the strain-gated input logic for SGT 2 is B, then the strain input logic for SGT 1 is $\bar{B}$. The change in the connections of the electrodes from those demonstrated in the NW SGI results in different logic functions. When the substrate is bent downward or upward, the electric output would be either V_A or $V_{\bar{A}}$, with the overall output of the device

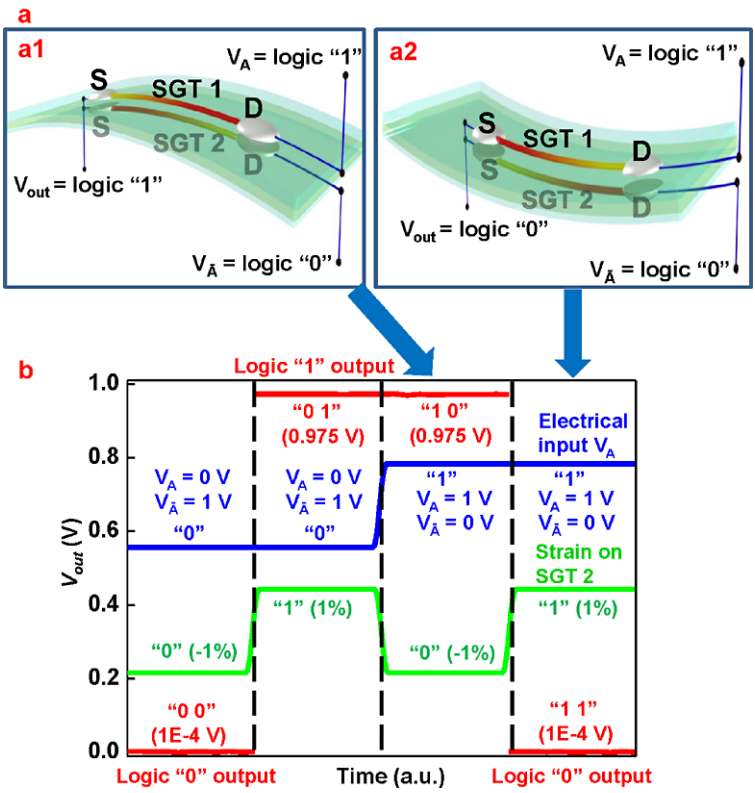

Fig. 5.6 ZnO NW strain-gated XOR logic gate. (**a1**)–(**a2**) Schematics of a ZnO NW XOR logic gate performing logic operations on strain and electrical input. (**a1**) When the strain input applied on SGT 2 is logic "0" and the electrical input V_A applied on SGT 1 is logic "1", SGT 1 is on and SGT 2 is off. Therefore the electrical output is logic "1" for the XOR gate. (**a2**) When the strain input applied on SGT 2 is logic "1" and the electrical input $V_{\bar{A}}$ applied on SGT 2 is logic "0", SGT 1 is off and SGT 2 is on. Therefore the electrical output is logic "0" for the XOR gate. (**b**) Logic operations and experimental truth table of the ZnO NW strain-gated XOR logic gate. The *red line* is the electrical output of the XOR gate. *Blue* and *green lines* represent the electrical and strain input applied on SGT 1 and SGT 2, respectively. We use the abbreviation a.u., arbitrary units [23]

logically expressed as $V_{\text{out}} = \bar{B}V_A + BV_{\bar{A}}$, which is the XOR logic. The output voltages of the XOR gate versus the input gate strains are shown in Fig. 5.6(b).

If drain electrodes of SGT 1 and SGT 2 in Fig. 5.6(a) are connected independently to arbitrary electrical input signals D_1 and D_0 rather than logically complements (V_A and $V_{\bar{A}}$), the XOR gate demonstrated above is essentially a 2:1 multiplexer (MUX), with a control bit B that is the input strain logic applied on SGT 2. Analogously, an n:1 MUX enables us to pick one of the n inputs and direct it to the output. When B is logic "1", SGT 1 is off and the output is determined by the input connected to the drain electrode of SGT 2. Conversely, when B is logic "0", SGT 2 is off and the output is determined by the input connected to the drain elec-

trode of SGT 1. Reversely, if the input D_1 and D_0 act as the output ports and the output for MUX as the input side, the device acts as a demultiplexer (DEMUX). The circuit can be expanded easily to create larger MUXs based on the above basic structures. The NW strain-gated MUXs and DEMUXs are critical logic components for processing mechanic-electrical signals.

5.4 Summary

By utilizing the gating effect produced by piezoelectric potential in a ZnO NW under externally applied deformation, SGTs have been fabricated, using which the universal logic operations such as NAND, NOR and XOR gates have been demonstrated for the first time for performing piezotronic logic operations [23]. In contrast to the conventional CMOS logic units, the SGT-based logic units are driven by mechanical agitation and relies only on n-type ZnO NWs without the presence of p-type semiconductor components. The mechanical–electronic logic units can be integrated with NEMS technology to achieve advanced and complex functionalities in nanorobotics, microfluidics and micro/nanosystems. Recently, the integration of the other two important components in a self-powered autonomous intelligent nanoscale system, the energy harvesting and the sensing/detecting parts, has been demonstrated [31] and ZnO piezotronic logic devices can be further integrated with the ultrasensitive ZnO NW sensors and ZnO NW-based nanogenerators to achieve a self-sustainable, all nanowire based, multifunctional self-powered autonomous intelligent nanoscale system.

References

1. Z.L. Wang, J.H. Song, Piezoelectric nanogenerators based on zinc oxide nanowire arrays. Science **312**, 242–246 (2006)
2. F. Patolsky, G.F. Zheng, C.M. Lieber, Fabrication of silicon nanowire devices for ultrasensitive, label-free, real-time detection of biological and chemical species. Nat. Protoc. **1**, 1711–1724 (2006)
3. Y. Cui, Q.Q. Wei, H.K. Park, C.M. Lieber, Nanowire nanosensors for highly sensitive and selective detection of biological and chemical species. Science **293**, 1289–1292 (2001)
4. E. Stern, J.F. Klemic, D.A. Routenberg, P.N. Wyrembak, D.B. Turner-Evans, A.D. Hamilton, D.A. LaVan, T.M. Fahmy, M.A. Reed, Label-free immunodetection with CMOS-compatible semiconducting nanowires. Nature **445**, 519–522 (2007)
5. P.H. Yeh, Z. Li, Z.L. Wang, Schottky-gated probe-free ZnO nanowire biosensor. Adv. Mater. **21**(48), 4975–4978 (2009)
6. S.C. Masmanidis, R.B. Karabalin, I. De Vlaminck, G. Borghs, M.R. Freeman, M.L. Roukes, Multifunctional nanomechanical systems via tunably coupled piezoelectric actuation. Science **317**, 780–783 (2007)
7. A. Bachtold, P. Hadley, T. Nakanishi, C. Dekker, Logic circuits with carbon nanotube transistors. Science **294**, 1317–1320 (2001)
8. Y. Huang, X.F. Duan, Y. Cui, L.J. Lauhon, K.H. Kim, C.M. Lieber, Logic gates and computation from assembled nanowire building blocks. Science **294**, 1313–1317 (2001)

9. Z.H. Chen, J. Appenzeller, Y.M. Lin, J. Sippel-Oakley, A.G. Rinzler, J.Y. Tang, S.J. Wind, P.M. Solomon, P. Avouris, An integrated logic circuit assembled on a single carbon nanotube. Science **311**, 1735 (2006)
10. C. Thelander, H.A. Nilsson, L.E. Jensen, L. Samuelson, Nanowire single-electron memory. Nano Lett. **5**(4), 635–638 (2005)
11. T. Rueckes, K. Kim, E. Joselevich, G.Y. Tseng, C.L. Cheung, C.M. Lieber, Carbon nanotube-based nonvolatile random access memory for molecular computing. Science **289**, 94–97 (2000)
12. S.H. Lee, Y. Jung, R. Agarwal, Highly scalable non-volatile and ultra-low-power phase-change nanowire memory. Nat. Nanotechnol. **2**, 626–630 (2007)
13. M.S. Dresselhaus, G. Chen, M.Y. Tang, R.G. Yang, H. Lee, D.Z. Wang, Z.F. Ren, J.P. Fleurial, P. Gogna, New directions for low-dimensional thermoelectric materials. Adv. Mater. **19**(8), 1043–1053 (2007)
14. B.Z. Tian, X.L. Zheng, T.J. Kempa, Y. Fang, N.F. Yu, G.H. Yu, J.L. Huang, C.M. Lieber, Coaxial silicon nanowires as solar cells and nanoelectronic power sources. Nature **449**, 885–889 (2007)
15. M. Law, L.E. Greene, J.C. Johnson, R. Saykally, P.D. Yang, Nanowire dye-sensitized solar cells. Nat. Mater. **4**, 455–459 (2005)
16. X.D. Wang, J.H. Song, J. Liu, Z.L. Wang, Direct-current nanogenerator driven by ultrasonic waves. Science **316**, 102–105 (2007)
17. Y. Qin, X.D. Wang, Z.L. Wang, Microfibre–nanowire hybrid structure for energy scavenging. Nature **451**, 809–813 (2008)
18. R.S. Yang, Y. Qin, L.M. Dai, Z.L. Wang, Power generation with laterally packaged piezoelectric fine wires. Nat. Nanotechnol. **4**, 34–39 (2009)
19. C.E. Chang, V.H. Tran, J.B. Wang, Y.K. Fuh, L.W. Lin, Direct-write piezoelectric polymeric nanogenerator with high energy conversion efficiency. Nano Lett. **10**(2), 726–731 (2010)
20. C.F. Pan, H. Wu, C. Wang, B. Wang, L. Zhang, Z.D. Cheng, P. Hu, W. Pan, Z.Y. Zhou, X. Yang, J. Zhu, Nanowire-based high-performance "micro fuel cells": one nanowire, one fuel cell. Adv. Mater. **20**(9), 1644–1648 (2008)
21. K.L. Ekinci, M.L. Roukes, Nanoelectromechanical systems. Rev. Sci. Instrum. **76**(6), 061101 (2005)
22. J. Xiang, W. Lu, Y.J. Hu, Y. Wu, H. Yan, C.M. Lieber, Ge/Si nanowire heterostructures as high-performance field-effect transistors. Nature **441**, 489–493 (2006)
23. W.Z. Wu, Y.G. Wei, Z.L. Wang, Strain-gated piezotronic logic nanodevices. Adv. Mater. **22**(42), 4711–4715 (2010)
24. T. Thorsen, S.J. Maerkl, S.R. Quake, Microfluidic large-scale integration. Science **298**, 580–584 (2002)
25. Z.L. Wang, Towards self-powered nanosystems: from nanogenerators to nanopiezotronics. Adv. Funct. Mater. **18**(22), 3553–3567 (2008)
26. Z.L. Wang, ZnO nanowire and nanobelt platform for nanotechnology. Mater. Sci. Eng. Rep. **64**(3–4), 33–71 (2009)
27. Nanopiezotronics was elected to be the top 10 emerging technologies by MIT Technology Review T10 in 2009. http://www.technologyreview.com/read_article.aspx?ch=specialsections&sc=tr10&id= 22118
28. J. Zhou, P. Fei, Y.D. Gu, W.J. Mai, Y.F. Gao, R.S. Yang, G. Bao, Z.L. Wang, Piezoelectric-potential-controlled polarity-reversible Schottky diodes and switches of ZnO wires. Nano Lett. **8**(11), 3973–3977 (2008)
29. P.E. Allen, D.R. Holberg, *CMOS Analog Circuit Design*, 2nd edn. (Oxford University Press, Oxford, 2002)
30. Z.Y. Gao, J. Zhou, Y.D. Gu, P. Fei, Y. Hao, G. Bao, Z.L. Wang, Effects of piezoelectric potential on the transport characteristics of metal–ZnO nanowire–metal field effect transistor. J. Appl. Phys. **105**(11), 113707 (2009)
31. S. Xu, Y. Qin, C. Xu, Y.G. Wei, R.S. Yang, Z.L. Wang, Self-powered nanowire devices. Nat. Nanotechnol. **5**, 366–373 (2010)

Chapter 6
Piezotronic Electromechanical Memories

Abstract In this chapter, we treat the piezoelectrically modulated resistive switching device based on a piezotronic nanowire, through which the write/read access of the memory cell is programmed via electromechanical modulation. Adjusted by the strain-induced polarization charges created at the semiconductor/metal interface under externally applied deformation by the piezoelectric effect, the resistive switching characteristics of the cell can be modulated in a controlled manner, and the logic levels of the strain stored in the cell can be recorded and read out, which has the potential for integrating with NEMS technology to achieve micro/nanosystems capable for intelligent and self-sufficient multidimensional operations.

The concept of complementing field effect transistors (FETs) with two-terminal hysteretic resistive switches has recently attracted great interest in implementing and scaling novel non-volatile resistive memories [1–5] for ultrahigh-density memory storage [6, 7] and logic applications [8, 9] with characteristics such as high density, low cost, fast write/read accessing speed and long endurance/retention time [10]. Notably, previously existing non-volatile resistive memories are all based on electrically switchable resistance change [10] by means of formation of conductive filaments [5, 11], charge-transfer-induced conformational change [12], electrochemical processes [13], or field-assisted drift/diffusion of charged ions [3, 4, 6, 14] in various oxides and ionic conductors [15, 16]. These devices are electrically programmed and they are not suitable for direct interfacing with actuation/triggering other than electrical input.

For applications such as human–computer interfacing, sensing/actuating in nanorobotics, and smart MEMS/NEMS [18], a direct interfacing of electronics with mechanical actions is required. In this chapter, we present the first piezoelectrically modulated resistive switching device based on piezotronic ZnO nanowire (NW), through which the write/read access of the memory cell is programmed via electromechanical modulation [17]. Adjusted by the strain-induced polarization charges created at the semiconductor/metal interface under externally applied deformation by the piezoelectric effect, the resistive switching characteristics of the cell can be modulated in a controlled manner, and the logic levels of the strain stored in the cell can be recorded and read out, which has the potential for integrating with NEMS

Z.L. Wang, *Piezotronics and Piezo-Phototronics*, Microtechnology and MEMS,
DOI 10.1007/978-3-642-34237-0_6, © Springer-Verlag Berlin Heidelberg 2012

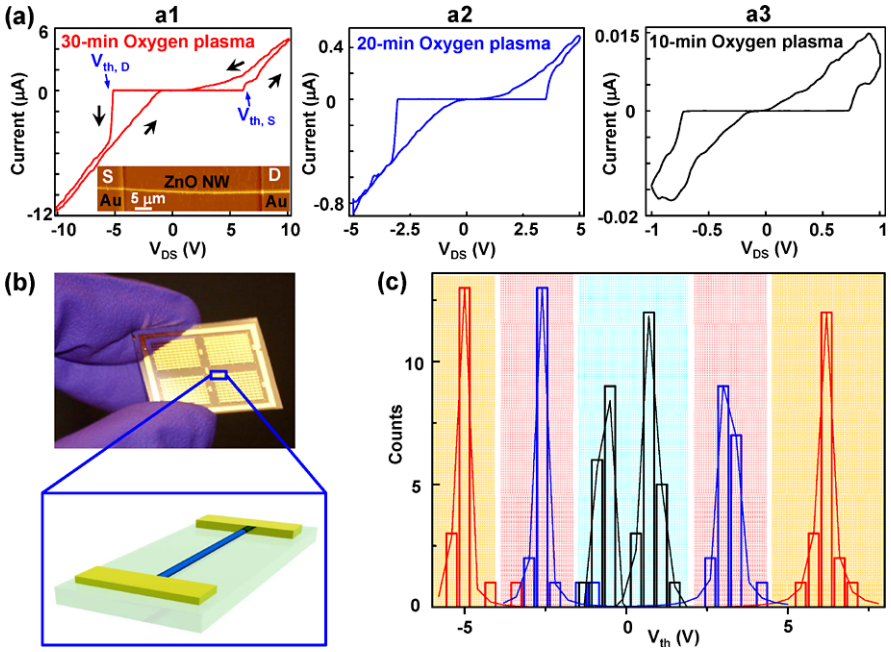

Fig. 6.1 Effects of oxygen–plasma treatment on electrical properties of ZnO PRM cells. (**a1**)–(**a3**) *I*–*V* characteristics of ZnO PRM cells after 30, 20 and 10 minutes oxygen–plasma treatment. The sweeping frequency is 0.1 Hz. (**a1**) *Inset*: Atomic force microscopy (AFM) image of one ZnO PRM cell. (**b**) Optical image of the large-scale as-fabricated PRM cells after printing transfer of ZnO NWs and lithography patterning of metal electrodes. (**c**) Statistical distributions of the $V_{th,S}$ and $V_{th,D}$ peaks for PRM cells with different periods of oxygen–plasma treatment. *Red*, *blue*, and *black lines* are for PRM cells with 30, 20, and 10 minutes oxygen–plasma treatment, respectively [17]

technology to achieve micro/nanosystems capable for intelligent and self-sufficient multidimensional operations [18, 20].

6.1 Device Fabrication

The basic structure of the piezoelectrically modulated resistive memory (PRM) is shown in Fig. 6.1(a1) (Inset), which consists of a ZnO piezotronic NW that is in contact with Au electrodes fabricated by lithography on a flexible PET substrate (from DuPont, thickness ~ 1.25 mm). The two electrodes are labeled as the drain (D) and source (S) electrodes of the PRM cell. The single-crystalline ZnO NWs used in PRM devices were synthesized via a physical vapor deposition process [21] with diameters of 500 nm and lengths of 50 μm (Fig. 6.1(a1) (Inset)). ZnO NWs grown on alumina plates were transferred to the PET receiving substrate by sweeping the PET substrate across the NWs. Electrode patterns over the transferred ZnO NWs were

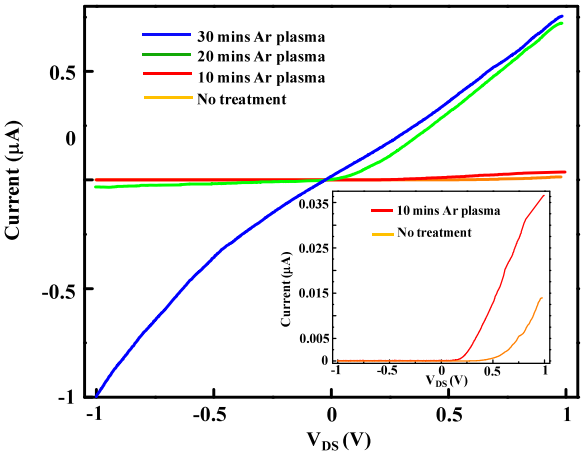

Fig. 6.2 I–V curves of PRM cells with argon–plasma treatment. For PRM cells treated with argon plasma, the threshold voltages decreased and the conductance increased with respect to the pristine one, as the treatment time increased. The rectification disappeared in the I–V curve for PRM cell treated with 30 minute argon plasma. *Inset*: magnified plot for pristine PRM cell and cell with 10-minute argon–plasma treatment [17]

defined using photolithography and then followed by evaporating 350 nm thick Au film (E-beam evaporation). After lift-off step, a substantial amount of the ZnO NWs was patterned with ordered Au electrodes (Fig. 6.2). Au electrodes form Schottky contacts with the ZnO NWs, which are critical for a working piezotronic device. Finally, the entire substrate can be further packaged with a thin layer of PDMS to enhance mechanical robustness.

The PRM cells were then treated in oxygen plasma for 30 minutes before further characterization. Plasma treatment using argon or oxygen gas was performed on a plasma cleaning system (South Bay Technology, Inc., PC-150) in order to investigate the effect of pre-treatment on the performance and consequently the underlying working mechanism of the PRM cell. For both the argon– and oxygen–plasma treatment, the chamber pressure was maintained at 170 mTorr during the process. The forward power used was 30 W with the reflected power of 0 W. The duration time of plasma treatment was programmed to be from 10 to 30 minutes for different groups of PRM cells investigated.

6.2 Principle of Electromechanical Memory

Once the substrate is deformed, a pure tensile/compressive strain is created in the NW since the mechanical behavior of the entire cell structure is determined by the substrate (Fig. 6.1(b)). All of the I–V curves presented were measured at a sweeping frequency of 0.1 Hz at room temperature unless otherwise noted. Several key features can be observed from the representative hysteretic I–V curve obtained (Methods) for a single ZnO PRM cell (treated with 30-minute oxygen plasma) without applying an external strain (Fig. 6.1(a1)). First, as the bias voltage increased from 0 to 10 V, the output current of the PRM cell increased abruptly at 5.73 V, which is defined as the threshold point $V_{\mathrm{th,S}}$. An abrupt transition and switching from high-resistance state (HRS) to low-resistance state (LRS) occurred at $V_{\mathrm{th,S}}$. Secondly,

as the voltage was subsequently decreased towards negative values, the PRM cell switched back to the high-resistance OFF state. Thirdly, when the bias voltage exceeded certain negative values ($V_{\mathrm{th,D}} = -5$ V in Fig. 6.1(a1), the PRM cell was turned to the ON state again and subsequent decrease in magnitude of the negative bias voltage switched the PRM cell back to the OFF state. This hysteretic sweeping sequence is indicated by arrowheads in Fig. 6.1(a1). The overall resistive switching observed for a single PRM cell is unipolar since the switching sequence is independent of the polarity of the bias voltage [10] (Fig. 6.1(a1)), which can be understood by the symmetry in structures of the PRM cells. Current rectification, which can minimize cross talk between individual memory cells and solve the sneak path problem in potential large-scale ultrahigh-density applications [22, 23], was also observed, suggesting that the PRM cell can be modeled as two back-to-back Schottky barriers connected in series with the NW in the metal–semiconductor–metal (M–S–M) configuration and the LRS state of the cell is dictated by Schottky-like transport at one of the Au/ZnO interfaces, which will be discussed in detail later.

Noticeably, the I–V characteristic of the PRM cell is significantly different from those observed in previous single ZnO NW-based piezotronic devices [17, 18] (orange line in Fig. 6.2), which is proposed to result from the oxygen–plasma treatment prior to the measurement, as elaborated in the following. In order to investigate the effect of pre-treatment on the performance of the PRM cell, six groups of PRM cells were electrically characterized after different plasma pre-treatments (Methods). The first three groups were treated with oxygen plasma for 30, 20 and 10 minutes, respectively and the typical I–V curves are shown in Figs. 6.1(a1)–(a3). The rest three groups of PRM cells were treated with argon plasma for 30, 20, and 10 minutes and their individual typical I–V curves are shown in Fig. 6.2, respectively. The I–V curve of the PRM cell directly assembled without pre-treatment (pristine PRM cell) is also plotted in Fig. 6.2 for comparison. It can be seen clearly that significant changes occur in the shape, threshold voltage, and current range of the I–V curves for these samples. With increasing the period of time of treatment with oxygen plasma, the threshold voltage of the PRM cell increased accordingly, and increased hysteresis was also observed in the I–V curve (Figs. 6.1(a1)–(a3)). If the PRM cell was treated with argon plasma, the threshold voltage decreased and the conductance increased with respect to the pristine one, and finally the rectification disappeared in the I–V curve. The observed variations in the I–V curves of the PRM cells, which were fabricated using the ZnO NWs synthesized under the same experimental condition, are due to the fact that oxygen vacancies are capable of influencing the Schottky contacts between ZnO and metal electrodes [24]. The synthesis condition (argon atmosphere at high temperature [21]) for ZnO NWs used in the reported piezotronic devices [26, 32] and pristine PRM cells tended to create a large amount of oxygen vacancies in the ZnO NWs, which possibly induced the observed lower threshold voltages of 0.5–0.7 V due to the high density of oxygen vacancies near the metal-ZnO interface and pinning of the ZnO Fermi level close to the $V_O^{\bullet\bullet}$ defect level [24]. If, however, the pristine ZnO NWs were treated with additional oxygen plasma for a prolonged period of time, the concentration of oxygen vacancies could be largely reduced, which contributed to the observed increase

in threshold voltages as well as the hysteresis loop of the I–V curves, as shown in Figs. 6.1(a1)–(a3).

The mechanical deformations were applied onto the PRM cells using a 3-axis linear stage (Newport, Inc., 460P-XYZ-05). Electrical measurements were carried out with a computer-controlled data acquisition system, which consists of a function generator (Stanford Research Systems, Inc., DS345), a low-noise current preamplifier (Stanford Research Systems, Inc., SR570) and a shielded connector block with signal-labeled BNC connectors (NI BNC2120). For each strain state of the PRM cell, the output current was obtained by sweeping the DC bias across the device at a fixed frequency of 0.1 Hz.

The capability in designing the switching characteristics of the PRM cell in a controllable manner is further confirmed by the sharp and distinct statistical distributions of the $V_{\mathrm{th,S}}$ and $V_{\mathrm{th,D}}$ peaks for PRM cells with different periods of oxygen–plasma treatment, with $V_{\mathrm{th,S}} = 6.15 \pm 0.39$ V and $V_{\mathrm{th,D}} = -5.12 \pm 0.03$ V, $V_{\mathrm{th,S}} = 3.18 \pm 0.20$ V and $V_{\mathrm{th,D}} = -2.67 \pm 0.22$ V as well as $V_{\mathrm{th,S}} = 0.74 \pm 0.51$ V and $V_{\mathrm{th,D}} = -0.68 \pm 0.20$ V for PRM cells with treatment for 30, 20 and 10 minutes, respectively, by oxygen plasma (Fig. 6.1(c)). The predictable electrical properties of these ZnO NWs with controlled treatment process enable the reproducible assembly of NW structures at large quantity for further applications. The slight difference and asymmetry observed between $V_{\mathrm{th,S}}$ and $V_{\mathrm{th,D}}$ within each group of PRM cells is possibly induced by the non-uniform geometry of the ZnO NW, as indicated by the AFM image inset in Fig. 6.1(a1). It is well known that the Schottky barrier height (SBH) induced at a metal/semiconductor interface can be affected by factors such as the geometry and effective areas of the contact [25]. Moreover, the interface/surface states can also shift the SBH [25]. Notably, as can be seen from the semi-logarithmic plots of the data presented in Figs. 6.1(a1)–(a3) (Fig. 6.3), the PRM cells gradually lose their non-volatility as the period of oxygen–plasma treatment increases. The non-volatility of PRM cells with 10-minute oxygen–plasma treatment can be observed by sweeping only at positive voltages (0–1 V) and the high-conductance state is not lost at small bias in subsequent sweeps (for 20 cycles), which indicates that this kind of cell has the memory effect. The PRM cells with 30-minute oxygen plasma, however, did not show the same non-volatility in the current experiment.

6.3 Effect of Temperature on Memory Performance

Temperature-dependent I–V measurements (Methods) were performed to obtain further insight into the switching mechanism of the PRM cell without applying external deformations. The representative result acquired from an Au/ZnO-NW/Au PRM cell clearly demonstrates the variations with temperature in the hysteretic I–V switching characteristics (Fig. 6.4(a)). The threshold turn-on voltage for the reversely biased Schottky barrier of the PRM cell increased almost linearly with decreasing temperature (Fig. 6.4(b)), and the hysteresis loop increased with the decreasing temperature (Fig. 6.4(a)). The magnitudes of the current for PRM cell at

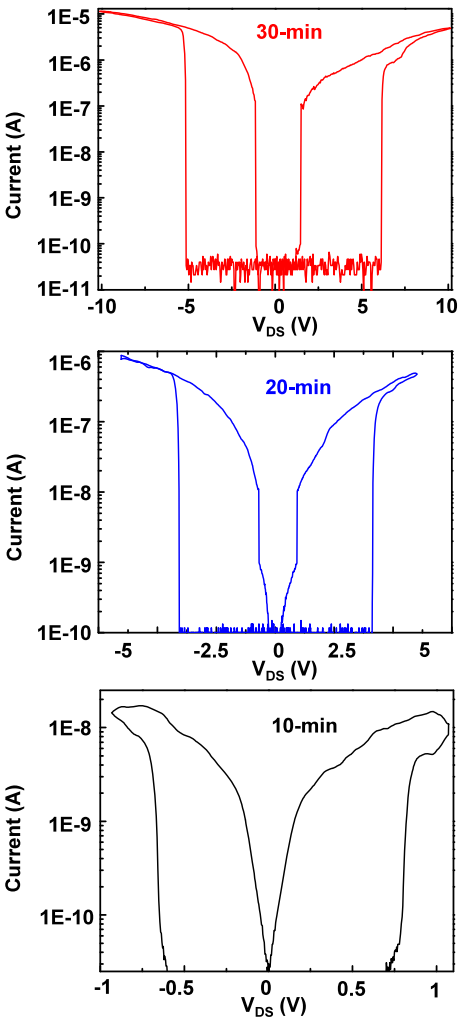

Fig. 6.3 I–V characteristics of ZnO PRM cells after 30, 20, and 10 minutes of oxygen plasma treatment [17]

very large bias ($V = \pm 10$ V) were almost constant and independent of temperature (Fig. 6.4(a)).

Although the nature of resistive switching and related charge transport process at microscale in M–S–M structures is still under debate [1–5], the movement of charged species that modulates the current flow seems to be a dominant mechanism [3]. Drift/diffusion of defects such as positively charged oxygen vacancies under applied electrical field has been suggested to change the electronic barrier at the metal/semiconductor interface, which possibly results in the observed resistive switching [4]. Oxygen vacancies are known to belong to the predominant ionic defects in ZnO [26] and can influence the Schottky contacts between ZnO and metal electrodes [24]. On the basis of the experimental results, a general model based on the coupled transport of charged dopants and electrons under applied electric

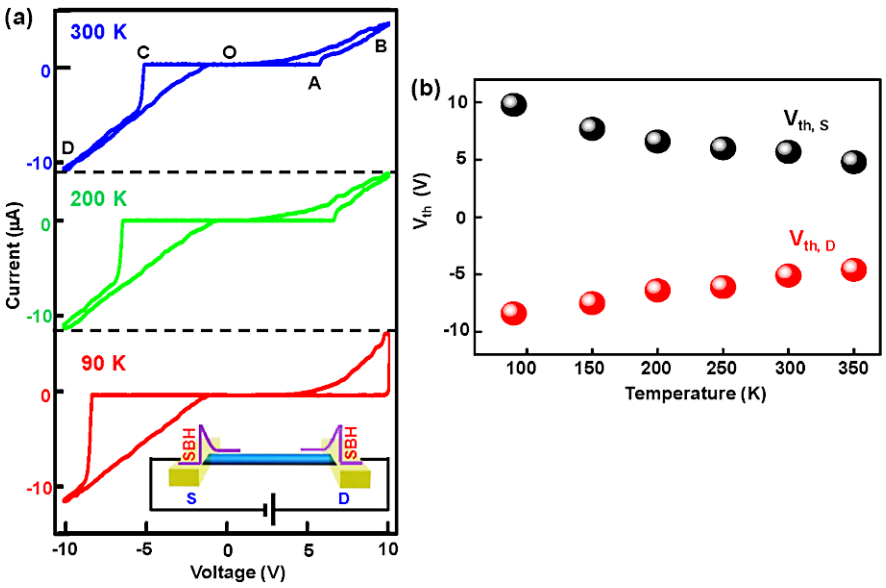

Fig. 6.4 Temperature-dependent I–V measurements of PRM cells at strain-free condition. (**a**) I–V characteristics of ZnO PRM cells at 300, 200, and 90 K, respectively. The sweeping frequency is 0.1 Hz. *Inset*: schematic showing the bias condition of the PRM cell when Schottky barrier at source side is reversely biased. (**b**) Dependence of threshold voltages on temperature. Both $V_{th,S}$ (in *black*) and $V_{th,D}$ (in *red*) increased in magnitudes almost linearly with the decreasing temperature. The hysteresis loop increased with the decreasing temperature [17]

field [4] is adopted and modified to explain the hysteretic switching behavior of the PRM cell without external deformation applied. The drift/diffusion of the oxygen vacancies towards the interface effectively reduces the local SBH, while the drift/diffusion of vacancies away from the interface increases the SBH.

The hysteretic switching sequences obtained at different temperatures can be characterized by four typical regions: (1) O–A, (2) A–B–O, (3) O–C, and (4) C–D–O, as labeled in Fig. 6.4(a) as an example. For easy discussion, the bias is set to be applied on the drain (D) electrode with respect to the source (S) side (Inset sketch in Fig. 6.4(a)). The overall macroscopic resistance of the PRM cell is $R_{PRM} = R_S + R_{NW} + R_D$, where R_S and R_D are the electrical resistances contributed by Schottky barriers at source and drain sides that may vary during the experiment and R_{NW} is the intrinsic resistance of the ZnO NW. It has previously been demonstrated that for semiconductor NW-based M–S–M structure, the I–V transport characteristic is normally dictated by the reversely biased Schottky barrier side [19, 27, 28]. As the bias voltage sweeps from O to A with the drain side forward-biased, the voltage drops mainly at the reversely biased source side. The total resistance of PRM cell is $R_{PRM} \sim R_S$ (with $R_S \gg R_{NW}, R_D$), which is the HRS state. The lower voltage at the source side attracts oxygen vacancies towards the interface to modify the contact barrier at the source. The switching from HRS to LRS state occurs at a larger bias beyond point A, in corresponding to a largely reduced

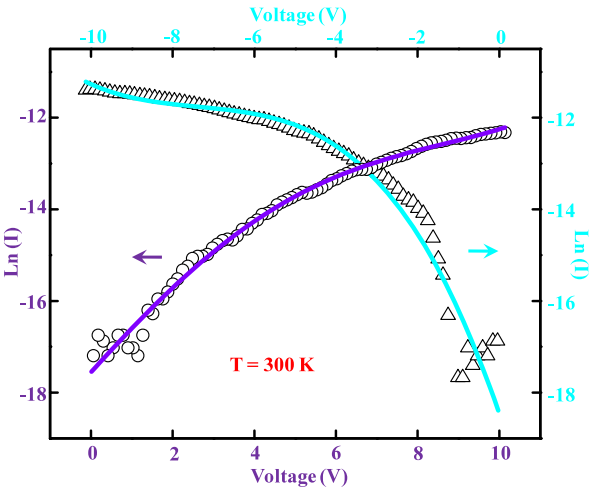

Fig. 6.5 I–V characteristic for PRM cell in region O–B and D–O in Fig. 6.4. The numerical fitting curves show that $\ln(I)$ linearly depends on $V^{1/4}$, which indicates that thermionic emission-diffusion dominates the transport at the reverse-biased barriers

SBH at the source side. When the bias voltage sweeps from point A to point O through point B, the $\ln(I)$–V curve for region B–O (empty circle in Fig. 6.5) shows that $\ln(I)$ relates to $V^{1/4}$, as confirmed by the numerical fitting curve (purple line in Fig. 6.5). This indicates that the thermionic emission-diffusion model dominates the transport at the reverse-biased source barrier [29]. An accelerated diffusion of the oxygen vacancies toward the source side at a large applied voltage and their accumulation are considered as the cause of the hysteresis observed in I–V curve.

As the applied bias switches the polarity from point O to point C, the source side is now forward-biased and the bias voltage drops mainly at the reversely biased drain side with the total resistance of PRM cell $R_{\mathrm{PRM}} \sim R_{\mathrm{D}}$, which is the new HRS state. Oxygen vacancies near the drain side are attracted towards and accumulated at the reversely biased drain barrier to modify the interface contact, while oxygen vacancies previously piled up at the source side are drifting away. Similar to the case in region O–A, the switch from HRS to LRS state occurs only after a larger bias beyond point C is applied. When the bias voltage sweeps from point C to point O through point D, the $\ln(I)$–V curve for region D–O (empty triangle in Fig. 6.5) can again be numerically fitted using the $\ln(I) \sim V^{1/4}$ relationship (blue line in Fig. 6.5), indicating that the thermionic emission-diffusion model also dominates the transport at the reverse-biased drain barrier.

It can also be observed that both $V_{\mathrm{th,S}}$ and $V_{\mathrm{th,D}}$ and hence the width of the HRS window increased as the temperature decreased from 350 to 90 K (Fig. 6.4(b)). Qualitatively, this can be understood since the drift/diffusion of the charged ions/dopants and electrons are thermally activated processes. Employing the rigid point ion model derived by Mott and Gurney [30], the diffusion coefficient of oxygen vacancy is given by $D = D_0 \cdot \exp(-E_a/kT)$ and the drift velocity is $v = a \cdot f \cdot \exp(-E_a/kT) \cdot \sinh(qE_a/2kT)$, where E_a is the activation energy, k is the Boltzmann constant, a is the effective hopping distance for the ion to hop between potential wells, f is the attempt-to-escape frequency. At decreased temperatures, larger bias is required to attract sufficient oxygen vacancies towards the

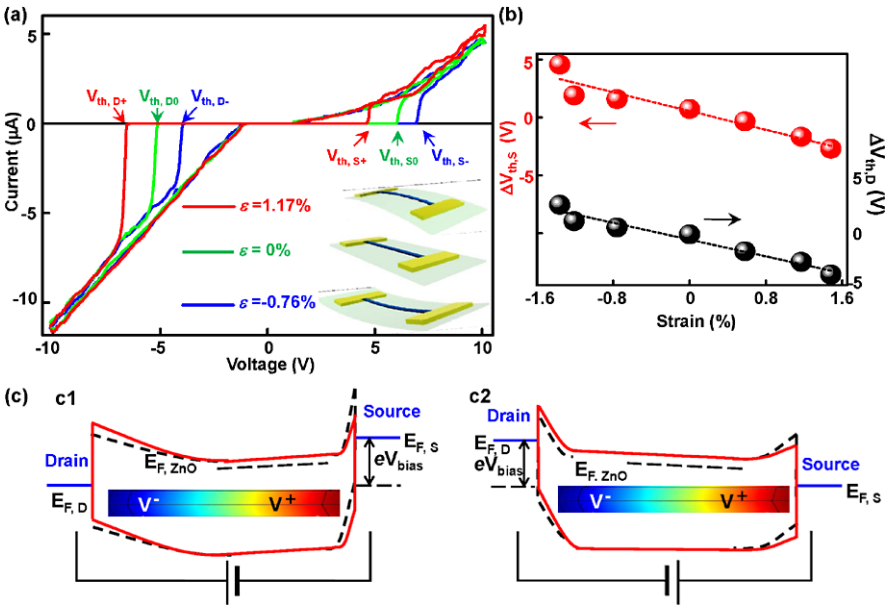

Fig. 6.6 Stain-modulated hysteretic switching of PRM cell. (**a**) I–V characteristics of ZnO PRM cells under tensile, zero and compressive strains, respectively. (**b**) Dependence of threshold voltages on applied strains. Both $V_{th,S}$ (in *red*) and $V_{th,D}$ (in *black*) almost linearly depends on strain applied to the PRM cell, while the width of the HRS window remains almost constant for different strain values. (**c**) Schematic of band-diagram of PRM cell under tensile strain. (**c1**) Schottky barrier at drain side is forward-biased. (**c2**) Schottky barrier at drain side is reversely biased. *Red solid lines* represent band-diagrams after tensile strain is applied. *Black dashed lines* represent band-diagrams under strain-free condition. The color gradient represents the distribution of piezopotential field [17]

respective reversely biased barrier to switch the PRM cell from HRS to LRS state within the timescale in the experimental setup (the sweeping frequency of the bias signal was 0.1 Hz).

6.4 Piezotronic Effect on Electromechanical Memory

The external mechanical perturbation induced strain (ε_g) acts as the programming input for modulating the hysteretic I–V characteristics of the PRM cell. A positive/negative strain is created when the ZnO NW is stretched/compressed (see Supporting Information for calculation of the strain in the PRM cell). Interesting phenomena were observed when a PRM cell experienced straining (Fig. 6.6(a)). When the PRM cell was tensile stretched ($\varepsilon = 1.17$ %), the hysteretic switching curve shifted towards lower voltage side by 1.49 V (red line in Fig. 6.6(a)); when the cell was compressively deformed ($\varepsilon = -0.76$ %), the hysteretic switching curve shifted towards higher voltage side by 1.18 V (blue line in Fig. 6.4(a)). $V_{th,S+}$,

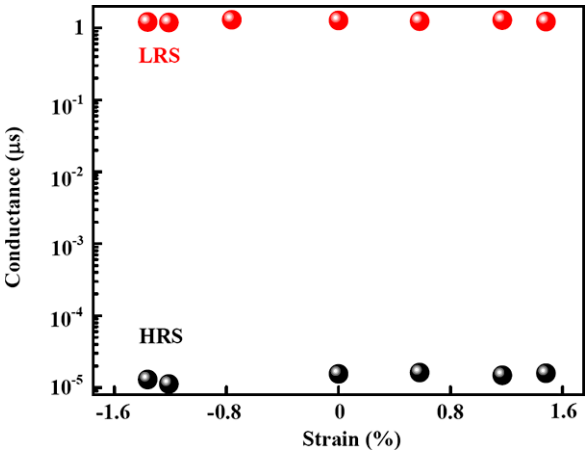

Fig. 6.7 Ratio of conductance at LRS and HRS for the PRM cell under different strains. The ratio of conductance at LRS and HRS remains steady at high values ($\sim 10^5$) under different strains, demonstrating the stable performance of the PRM cell [17]

$V_{\mathrm{th,S0}}$, $V_{\mathrm{th,S-}}$, and $V_{\mathrm{th,D+}}$, $V_{\mathrm{th,D0}}$, $V_{\mathrm{th,D-}}$ are the threshold switching voltages for the PRM cell with tensile, zero and compressive strains, respectively. The same hysteretic switching curves can then be plotted in a semi-logarithmic current scale to illustrate and highlight the characteristics of the curves (Fig. 6.8). The ratios of conductance between LRS and HRS for the PRM cell remain steady at high values ($\sim 10^5$) under different strains (Fig. 6.7), demonstrating the stable performance of the cell and its potential feasibility for applications in flexible memory and logic operations [19]. The intrinsic rectifying behavior of the PRM cell may solve the sneak path problem as well as reduce the static power consumption [23], which allows for construction of large passive resistive-switching device arrays. The changes in threshold switching voltages of the PRM cell with different strains have been plotted in Fig. 6.6(b). It can be seen that the change in both $V_{\mathrm{th,S}}$ and $V_{\mathrm{th,D}}$ almost linearly depends on strain applied to the PRM cell, while the width of the HRS window ($V_{\mathrm{th,S}i} - V_{\mathrm{th,D}i}$, where $i = +, 0, -$) remains almost constant for different strain values. This strain-modulated change in the threshold switching voltages was also observed for other PRM cells with oxygen–plasma treatment.

It is well known that ionic polarization in ZnO can be induced by strain owing to the lacking of center symmetry in ZnO, which can strongly affect the charge transport [18]. Novel effects [31] and applications [17, 27, 32] have been observed and implemented utilizing the piezotronic effect in ZnO [18]. The fundamental concept of the piezotronic effect is that the SBH at the metal–semiconductor contact can be effectively tuned by the strain-induced piezoelectric polarization charges at the interface. The local conduction band profile can then be modified by shifting the local Fermi level. The change in SBH induced by piezoelectric polarization is given approximately by $\Delta\phi_B = \sigma_{\mathrm{pol}} \cdot D^{-1} \cdot (1 + 1/(2q_s w_d))^{-1}$, where σ_{pol} is the volume density of the polarization charge and directly related to the piezoelectric polarization P vector, D is the two-dimensional density of interface states at the Fermi level at the Schottky barrier, q_s is the two-dimensional screening parameter, and w_d is the width of the depletion layer [33]. Thus the mechanical strain can effectively change the local contact characteristics as well as the charge carrier

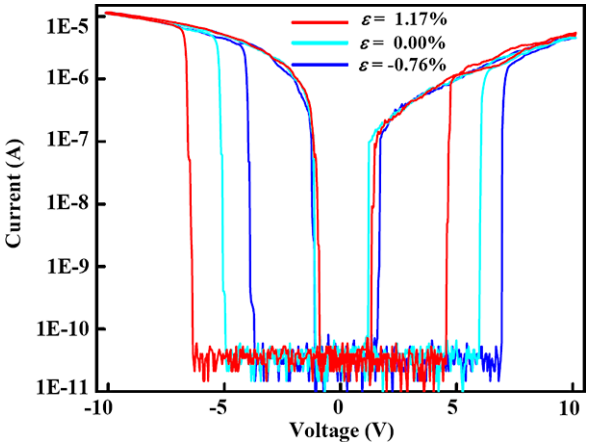

Fig. 6.8 Stain-modulated hysteretic switching curves of PRM cell in a semi-logarithmic current scale. The upper and lower branches of the hysteretic I–V characteristics correspond to the LRS and HRS states for PRM cell with different strains. Abrupt transitions between LRS and HRS branches of the hysteretic I–V curves occur at the respective threshold switching voltages, which are indicated by series of lines between the LRS and HRS branches

transport process. Based on the above discussions, the modulation effect of strain on the hysteretic switching behavior of the PRM cell, as shown in Figs. 6.6(a)–(b), can then be understood and explained using the band-diagram of the working device (Fig. 6.6(c)). If the PRM cell is under tensile strain with the Schottky barrier at drain side being forward-biased ($V > 0$ in Fig. 6.6(a)), the positive piezoelectric potential resulting from the positive strain-induced polarization charges reduced the SBH at the reverse-biased source barrier, while the negative piezoelectric potential resulting from the negative strain-induced polarization charges increased the SBH at the forward-biased drain barrier (red line in Fig. 6.6(c1)). Since the I–V characteristic in this situation is dictated by the reversely biased source barrier, the existence of strain-induced piezoelectric potential results in the shift of switching threshold voltage from $V_{\mathrm{th,S0}}$ to $V_{\mathrm{th,S+}}$, indicating only a smaller bias is required to switch the PRM cell from HRS to LRS state. Alternatively, if the Schottky barrier at drain side is reverse-biased ($V < 0$ in Fig. 6.6(a)), the SBH is still reduced at the source barrier while it is increased at the drain barrier (Fig. 6.6(b2)) since the polarity of the strain did not change, and hence the piezoelectric potential remained negative and positive at source and drain barriers, respectively. The I–V characteristic is now dictated by the reversely biased drain side in this case, and a shift of switching threshold voltage from $V_{\mathrm{th,D0}}$ to $V_{\mathrm{th,D+}}$ was observed, indicating that a larger bias has to be applied in order to switch the PRM cell from HRS to LRS state. By the same token, in the case of applying a compressive strain to the PRM cell, the shift of switching threshold voltage from $V_{\mathrm{th,S0}}$ to $V_{\mathrm{th,S}}$ and $V_{\mathrm{th,D0}}$ to $V_{\mathrm{th,D}}$ can be explained.

Under the strain-free condition and if the applied external bias exceeds the threshold voltage, the device is in LRS, and the concentration of oxygen vacancies in the

NW can significantly influence the total conductance of the NW as well as the SBHs at the source/drain (see Figs. 6.1(a1)–(a3) and 6.2). Now we consider the case that a strain is applied to the PRM cell. The effect of the piezopotential can be equivalently taken as applying a positive voltage at the barrier interface if the local piezoelectric polarization charges are positive, which in effect decreases the value of the external bias required to overcome the SBH at the interface. Alternatively, a negative voltage is created to act on the interface if the polarization charges are negative, which increases the value of the external bias required to overcome the barrier at the interface. From the data shown in Fig. 6.6, the HRS window remains almost constant regardless of the magnitude and sign of the applied strain, indicating that the shifts in the observed threshold voltages under different strains are dictated by the piezoelectric polarization charges at the interfaces and the contribution from the diffusion of the oxygen vacancies has negligible effect. This is because the oxygen vacancies are distributed in the entire NW, while the piezoelectric charges are accumulated right at the very near barrier interface in a region of less than a sub-nanometer. The diffusion force contributed by the piezoelectric charges on the oxygen vacancies is a long-range interaction force, thus the variation of the vacancy concentration at the interface owing to piezoelectric effect is rather small. Furthermore, the entire I–V curves are "translated" for a constant voltage, that is, the change of threshold switch voltage caused by the piezoelectric charges. For the samples pre-treated in oxygen plasma, the concentration of the oxygen vacancies was largely reduced in the NW, thus, the screening effect of the free charge carriers to the piezoelectric charges was significantly reduced, and the effect of the piezoelectric charges is enhanced [34]. Therefore, the shifts in threshold switch voltages due to piezoelectric polarization at both drain and source sides for a fixed strain have the same magnitude but opposite polarities, provided that the doping level is low. This indicates that the magnitude of the piezopotential at the interface is as large as 1.2 V at $0.5 \sim 0.76$ % of strain. The oxygen–plasma pre-treatment to the ZnO NWs may also improve the output of the nanogenerator [34].

6.5 Rewritable Electromechanical Memory

The fabricated PRM can function as an electromechanical memory, in which the write/read access can be programmed via mechanical actuation. A pulse train consisting of several write/read/erase pulses is applied to the PRM cell to record and read out the polarity/logic levels of the "stored" strain in the cell, by monitoring the characteristic patterns in the output current (Fig. 6.9). The data shown in Fig. 6.9 were obtained for the same PRM cell under different strain status, which is equivalent to the cases of three identical PRM cells under tensile strain (A cell), zero strain (B cell) and compressive strain (C cell), for easy description. First, a positive write pulse (10 ms) with $V_{\mathrm{th,S0}} < V_{\mathrm{write1}} < V_{\mathrm{th,S}}$ is applied to these three cells. This short pulse sets the A and B cells to switch from the HRS to the LRS state, while the C cell remains in the HRS state. The status of the three cells is then read out by a read

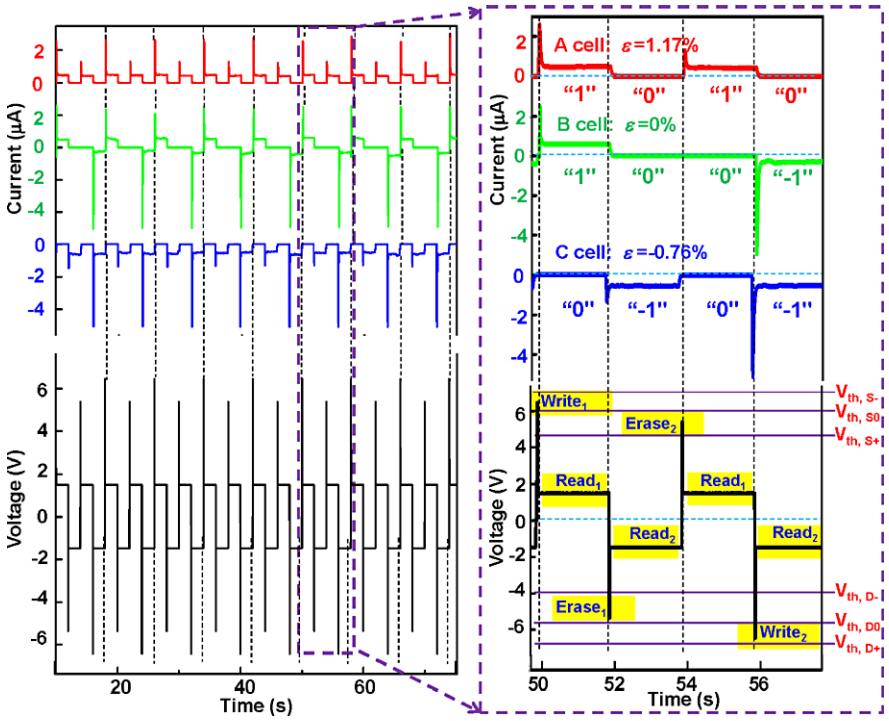

Fig. 6.9 Write/read access of PRM cell as an electromechanical memory. A pulse train consisting of several write/read/erase pulses was applied to the PRM cell to record and read out the logic levels of the "stored" strain in the cell. Each write/erase pulse was followed by a read pulse with positive or negative polarity, respectively. The following voltage amplitudes were applied: 6.44 V (write 1), 1.5 V (read 1), −5.35 V (erase 1), −1.5 V (read 2), 5.37 V (erase 2) and −6.42 V (write 2). Short current spikes occur in the output reading current with the write/erase pulses, if the resistance states (HRS to LRS) change in the PRM cell [17]

pulse (2 s) with a small magnitude ($V_{\text{read1}} < V_{\text{th,S+}}$). Subsequently, a negative erase pulse (10 ms) with $V_{\text{th,D0}} < V_{\text{erase1}} < V_{\text{th,D}}$ resets the A and B cells from the LRS to the HRS state, while it sets the C cell into the LRS state. A follow-up read pulse (2 s) with a small negative value ($V_{\text{read1}} > V_{\text{th,D}}$) is applied to read the new states of the cells. In the third step, a positive erase pulse (10 ms) with $V_{\text{th,S+}} < V_{\text{erase2}} < V_{\text{th,S0}}$ sets the A cell from the HRS to the LRS state again, while it keeps the B and C cells in the HRS state. The same V_{read1} pulse is then applied to read the new states of the cells. Finally, a negative write pulse (10 ms) with $V_{\text{th,D+}} < V_{\text{write2}} < V_{\text{th,D0}}$ resets the A cell into the HRS state, while it sets the B and C cells into the LRS state. The same V_{read2} pulse is then applied to read the new states of the cells. After the above series of the pulse train is applied, the waveform of the output currents of the cells is monitored and analyzed (Fig. 6.9). If the logic levels of the output currents with positive, almost zero and negative values are labeled as "1", "0" and "−1", the logic pattern of "1 0 1 0" indicates the positive nature of the "stored" strain in A cell. The

logic patterns of "1 0 0 −1" and "0 −1 0 −1" represent the zero and negative strain status of the B and C cells, respectively. A quantitative analysis of the magnitudes of the output currents can give the absolute values of the strains stored in the PRM cells. Although there have been numerous research and commercial products on strain detection and measurements such as semiconductor MEMS/NEMS piezoresistive strain gauges [35, 36], the PRM cells demonstrated here are fundamentally different from the these devices. Piezoresistance effect is a non-polar and symmetric effect resulting from the band structure change, while the PRM cells are based on the asymmetric piezotronic effect. ZnO is a polar structure along *c*-axis, straining in axial direction (*c*-axis) creates a polarization of cations and anions in the NW growth direction, resulting in a piezopotential drop from V^+ to V^- along the NW, which produces an asymmetric effect on the changes in the Schottky barrier heights (SBHs) at the drain and source electrodes. The strain sensor based on the piezotronic effect has been reported to possess much higher sensitivity than previously reported devices [27].

6.6 Summary

By utilizing the strain-induced polarization charges created at the semiconductor/metal interface under externally applied deformation as a result of the piezotronic effect, the switching characteristics of the ZnO NW resistive switching devices can be modulated and controlled. We further demonstrated that the logic levels of the strain applied on the memory cell can be recorded and read out for the first time utilizing the piezotronic effect [17, 18], which has the potential for implementing novel nanoelectromechanical memories and integrating with NEMS technology to achieve micro/nanosystems capable of intelligent and self-sufficient multidimensional operations [18, 20]. Taking advantage of the recently developed large-scale fabrication technique of ZnO NW arrays [37], non-volatile resistive switching memories using ZnO NW array as the storage medium may be readily engineered and implemented for applications such in flexible electronics and force/pressure imaging. Non-Boolean neuromorphic computing might also be realized by integrating arrays of high-density resistive memory cells [38, 39] on flexible substrates.

References

1. R. Waser, M. Aono, Nanoionics-based resistive switching memories. Nat. Mater. **6**(11), 833–840 (2007)
2. A. Sawa, Resistive switching in transition metal oxides. Mater. Today **11**(6), 28–36 (2008)
3. D.B. Strukov, G.S. Snider, D.R. Stewart, R.S. Williams, The missing memristor found. Nature **453**(7191), 80–83 (2008)
4. J.J. Yang, M.D. Pickett, X.M. Li, D.A.A. Ohlberg, D.R. Stewart, R.S. Williams, Memristive switching mechanism for metal/oxide/metal nanodevices. Nat. Nanotechnol. **3**(7), 429–433 (2008)

5. B.J. Choi, D.S. Jeong, S.K. Kim, C. Rohde, S. Choi, J.H. Oh, H.J. Kim, C.S. Hwang, K. Szot, R. Waser, B. Reichenberg, S. Tiedke, Resistive switching mechanism of TiO_2 thin films grown by atomic-layer deposition. J. Appl. Phys. **98**(3), 033715 (2005)
6. S.H. Jo, K.H. Kim, W. Lu, High-density crossbar arrays based on a Si memristive system. Nano Lett. **9**(2), 870–874 (2009)
7. D.B. Strukov, K.K. Likharev, Prospects for terabit-scale nanoelectronic memories. Nanotechnology **16**(1), 137–148 (2005)
8. Q.F. Xia, W. Robinett, M.W. Cumbie, N. Banerjee, T.J. Cardinali, J.J. Yang, W. Wu, X.M. Li, W.M. Tong, D.B. Strukov, G.S. Snider, G. Medeiros-Ribeiro, R.S. Williams, Memristor—CMOS hybrid integrated circuits for reconfigurable logic. Nano Lett. **9**(10), 3640–3645 (2009)
9. J. Borghetti, G.S. Snider, P.J. Kuekes, J.J. Yang, D.R. Stewart, R.S. Williams, 'Memristive' switches enable 'stateful' logic operations via material implication. Nature **464**(7290), 873–876 (2010)
10. R. Waser, R. Dittmann, G. Staikov, K. Szot, Redox-based resistive switching memories—nanoionic mechanisms, prospects, and challenges. Adv. Mater. **21**(25–26), 2632–2663 (2009)
11. D.H. Kwon, K.M. Kim, J.H. Jang, J.M. Jeon, M.H. Lee, G.H. Kim, X.S. Li, G.S. Park, B. Lee, S. Han, M. Kim, C.S. Hwang, Atomic structure of conducting nanofilaments in TiO_2 resistive switching memory. Nat. Nanotechnol. **5**(2), 148–153 (2010)
12. J. Chen, W. Wang, M.A. Reed, A.M. Rawlett, D.W. Price, J.M. Tour, Room-temperature negative differential resistance in nanoscale molecular junctions. Appl. Phys. Lett. **77**(8), 1224–1226 (2000)
13. A. Baikalov, Y.Q. Wang, B. Shen, B. Lorenz, S. Tsui, Y.Y. Sun, Y.Y. Xue, C.W. Chu, Field-driven hysteretic and reversible resistive switch at the $AgPr_{0.7}Ca_{0.3}MnO_3$ interface. Appl. Phys. Lett. **83**(5), 957–959 (2003)
14. Y.J. Dong, G.H. Yu, M.C. McAlpine, W. Lu, C.M. Lieber, Si/a-Si core/shell nanowires as nonvolatile crossbar switches. Nano Lett. **8**(2), 386–391 (2008)
15. S. Seo, M.J. Lee, D.H. Seo, E.J. Jeoung, D.S. Suh, Y.S. Joung, I.K. Yoo, I.R. Hwang, S.H. Kim, I.S. Byun, J.S. Kim, J.S. Choi, B.H. Park, Reproducible resistance switching in polycrystalline NiO films. Appl. Phys. Lett. **85**(23), 5655–5657 (2004)
16. K. Szot, W. Speier, G. Bihlmayer, R. Waser, Switching the electrical resistance of individual dislocations in single-crystalline $SrTiO_3$. Nat. Mater. **5**(4), 312–320 (2006)
17. Z.L. Wang, Piezopotential gated nanowire devices: piezotronics and piezo-phototronics. Nano Today **5**, 540–552 (2010)
18. W.Z. Wu, Z.L. Wang, Piezotronic nanowire-based resistive switches as programmable electromechanical memories. Nano Lett. **11**(7), 2779–2785 (2011)
19. Z.W. Pan, Z.R. Dai, Z.L. Wang, Nanobelts of semiconducting oxides. Science **291**, 1947–1949 (2001)
20. Z.L. Wang, Toward self-powered sensor networks. Nano Today **5**(6), 512–514 (2010)
21. W.Z. Wu, Y.G. Wei, Z.L. Wang, Strain-gated piezotronic logic nanodevices. Adv. Mater. **22**(42), 4711–4715 (2010)
22. J.C. Scott, Is there an immortal memory? Science **304**(5667), 62–63 (2004)
23. E. Linn, R. Rosezin, C. Kugeler, R. Waser, Complementary resistive switches for passive nanocrossbar memories. Nat. Mater. **9**(5), 403–406 (2010)
24. M.W. Allen, S.M. Durbin, Influence of oxygen vacancies on Schottky contacts to ZnO. Appl. Phys. Lett. **92**(12), 12210 (2008)
25. E.H. Rhoderick, R.H. Williams, *Metal–Semiconductor Contacts* (Clarendon, Oxford, 1988)
26. L. Schmidt-Mendem, J.L. MacManus-Driscoll, ZnO-nanostructures, defects, and devices. Mater. Today **10**(5), 40–48 (2007)
27. J. Zhou, P. Fei, Y.D. Gu, W.J. Mai, Y.F. Gao, R.S. Yang, G. Bao, Z.L. Wang, Piezoelectric-potential-controlled polarity-reversible Schottky diodes and switches of ZnO wires. Nano Lett. **8**(11), 3973–3977 (2008)
28. Z.Y. Zhang, K. Yao, Y. Liu, C.H. Jin, X.L. Liang, Q. Chen, L.M. Peng, Quantitative analysis of current–voltage characteristics of semiconducting nanowires: decoupling of contact effects.

Adv. Funct. Mater. **17**(14), 2478–2489 (2007)
29. S.M. Sze, *Physics of Semiconductor Devices* (Wiley, New York, 1981)
30. N.F. Mott, R.W. Gurney, *Electronic Processes in Ionic Crystals*, 2nd edn. (Clarendon, Oxford, 1948)
31. K.W. Chung, Z. Wang, J.C. Costa, F. Williamsion, P.P. Ruden, M.I. Nathan, Barrier height change in GaAs Schottky diodes induced by piezoelectric effect. Appl. Phys. Lett. **59**(10), 1191 (1991)
32. W.H. Liu, M.B. Lee, L. Ding, J. Liu, Z.L. Wang, Piezopotential gated nanowire–nanotube hybrid field-effect transistor. Nano Lett. **10**(8), 3084–3089 (2010)
33. Y. Zhang, Y.F. Hu, S. Xiang, Z.L. Wang, Effects of piezopotential spatial distribution on local contact dictated transport property of ZnO micro/nanowires. Appl. Phys. Lett. **97**(3), 033509 (2010)
34. Y.F. Gao, Z.L. Wang, Equilibrium potential of free charge carriers in a bent piezoelectric semiconductive nanowire. Nano Lett. **9**(3), 1103–1110 (2009)
35. L. Cao, T.S. Kim, S.C. Mantell, D.L. Polla, Simulation and fabrication of piezoresistive membrane type MEMS strain sensors. Sens. Actuators A, Phys. **80**(3), 273–279 (2000)
36. E. Mile, G. Jourdan, L. Duraffourg, S. Labarthe, C. Marcoux, D. Mercier, P. Robert, P. Andreucci, Sensitive in plane motion detection of NEMS through semiconducting (p+) piezoresistive gauge transducers. IEEE Sens. J. **1**(3), 1286–1289 (2009)
37. Y.G. Wei, W.Z. Wu, R. Guo, D.J. Yuan, S.M. Das, Z.L. Wang, Wafer-scale high-throughput ordered growth of vertically aligned ZnO nanowire arrays. Nano Lett. **10**(9), 3414–3419 (2010)
38. K. Boahen, Neuromorphic microchips. Sci. Am. **292**(5), 56–63 (2005)
39. S.H. Jo, T. Chang, I. Ebong, B.B. Bhadviya, P. Mazumder, W. Lu, Nanoscale memristor device as synapse in neuromorphic systems. Nano Lett. **10**(4), 1297–1301 (2010)

Chapter 7
Theory of Piezo-Phototronics

Abstract Devices fabricated by using the inner-crystal piezopotential as a "gate" voltage to tune/control the carrier generation, transport, and recombination processes at the vicinity of a p–n junction are named *piezo-phototronics*. The presence of piezoelectric charges at the interface/junction can significantly affect the charge carrier separation and transport. This chapter focuses on the basic theory for the piezo-phototronic effect on LED, photon detector, and solar cell. Both analytical equations and numerical simulations are given to present the basic physics for understanding the general phenomena.

For piezoelectric semiconductors, such as ZnO, GaN, InN and CdS, a piezoelectric potential (piezopotential) is created in the crystal by applying a stress. Devices fabricated by using the inner-crystal piezopotential as a "gate" voltage to tune/control the carrier generation, transport, and recombination processes at the vicinity of a p–n junction are named *piezo-phototronics*. The presence of piezoelectric charges at the interface/junction can significantly affect the performance of light emitting diode (LED), photodetector and solar cell fabricated using these materials. In this chapter, we introduce the theory of the piezo-phototronics. Besides deriving some simplified equations for describing the effect, numerical calculations are given for predicting the quantitative behavior of the piezo-phototronic devices [1].

7.1 Theoretical Frame of the Piezo-Phototronic Effect

Semiconductor physics and piezoelectric theories are used for describing the process involved in a piezo-phototronic device that is fabricated by piezoelectric semiconductor. The static and dynamic transport behavior of the charge carriers and the interaction of a photon and an electron in semiconductors are described by semiconductor physics [2]. The behavior of the piezoelectric material under dynamic straining is described by piezoelectric theories [3]. Therefore, electrostatic equations, current-density equations, continuity equations, and piezoelectric equations are applied as basic governing equations for characterizing piezo-phototronics devices.

Z.L. Wang, *Piezotronics and Piezo-Phototronics*, Microtechnology and MEMS,
DOI 10.1007/978-3-642-34237-0_7, © Springer-Verlag Berlin Heidelberg 2012

The electrostatic behavior of charges in piezoelectric semiconductor is described by the Poisson equation [2]:

$$\nabla^2 \psi_i = -\frac{\rho(\mathbf{r})}{\varepsilon_s} \tag{7.1}$$

where ψ_i, $\rho(\mathbf{r})$ and ε_s are the electric potential distribution, the charge density distribution, and the permittivity of the material.

The drift and diffusion current-density equations that correlate the local fields, charge densities, and local currents are [2]

$$\begin{cases} \mathbf{J}_n = q\mu_n n\mathbf{E} + qD_n \nabla n, \\ \mathbf{J}_p = q\mu_p p\mathbf{E} - qD_p \nabla p, \\ \mathbf{J} = \mathbf{J}_n + \mathbf{J}_p \end{cases} \tag{7.2}$$

where $\mathbf{J}_n$ and $\mathbf{J}_p$ are the electron and hole current densities, q is the absolute value of unit electronic charge, μ_n and μ_p are electron and hole mobilities, n and p are concentrations of free electrons and free holes, D_n and D_p are diffusion coefficients for electrons and holes, respectively, $\mathbf{E}$ is electric field, and $\mathbf{J}$ is the total current density.

The charge transport under the driving of a field is described by the continuity equations [2]

$$\begin{cases} \dfrac{\partial n}{\partial t} = G_n - U_n + \dfrac{1}{q}\nabla \cdot \mathbf{J}_n, \\ \dfrac{\partial p}{\partial t} = G_p - U_p - \dfrac{1}{q}\nabla \cdot \mathbf{J}_p \end{cases} \tag{7.3}$$

where G_n and G_p are the electron and hole generation rates, U_n and U_p are the recombination rates, respectively.

The relationship between polarization $\mathbf{P}$ vector and a small uniform mechanical strain $\mathbf{S}$ is given by [3]

$$(\mathbf{P})_i = (\mathbf{e})_{ijk}(\mathbf{S})_{jk} \tag{7.4}$$

where the third order tensor $(\mathbf{e})_{ijk}$ is the piezoelectric tensor. The constituent equations can be written as [3]

$$\begin{cases} \boldsymbol{\sigma} = \mathbf{c}_E \mathbf{S} - \mathbf{e}^{\mathbf{T}}\mathbf{E}, \\ \mathbf{D} = \mathbf{e}\mathbf{S} + \mathbf{k}\mathbf{E} \end{cases} \tag{7.5}$$

where $\boldsymbol{\sigma}$ and $\mathbf{c}_E$ are the stress tensor and the elasticity tensor, respectively. $\mathbf{E}$, $\mathbf{D}$, and $\mathbf{k}$ are the electric field, the electric displacement, and the dielectric tensor, respectively.

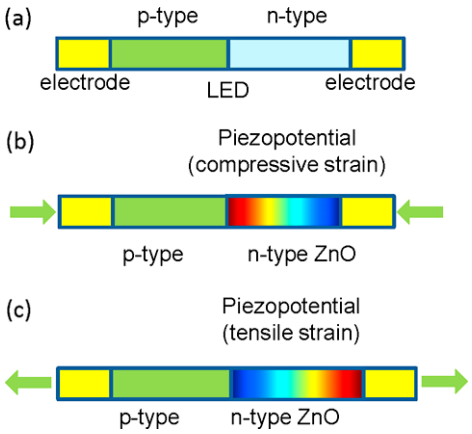

Fig. 7.1 Schematic of (**a**) a general n-type piezoelectric nanowire LED fabricated using p–n heterojunction structure. Schematic of a piezo-phototronic devices: piezo-LED under (**b**) compressive strain and (**c**) tensile, where the sign and magnitude of the piezopotential tunes/controls the photon emission, carrier generation and transport characteristics. The color code represents the distribution of the piezopotential at the n-type nanowire

7.2 Piezo-Phototronic Effect on LED

Taking a typical LED (Fig. 7.1(a)) as an example, the basic structure is a p–n junction. There are excessive carriers over their equilibrium values under forward bias. Thus, radiative recombination will take place by injecting minority carriers. The same concepts can apply to a single semiconductor nanowire (NW) LED. The working principle of the LED is to use a forward bias to obtain a radiative recombination between electrons and holes at the junction.

A piezo-phototronic LED is assumed to be a p-type non-piezoelectric and n-type piezoelectric heterostructure junction, as shown in Figs. 7.1(b) and (c). The fundamental principle of the piezo-phototronic device is that piezoelectric charges created at the junction area significantly modify the band structure at the interface, resulting in a control over the carrier generation, transport, and recombination at the p–n junction or M–S interface.

7.2.1 Analytical Solution for Simplified Piezoelectric LED

The interaction of a photon and an electron in a semiconductor device has three main optical processes: First, an electron excitation from valence band to the conduction band may be induced by a photon absorption. This process is the dominant process for photodetector and solar cell. Second, the reverse process of above absorption named recombination is photon emission induced by an electron return from the conduction band to the valence band, which is the main process for LED. Third,

an injected photon stimulates another similar photon by recombination process and give two coherent photons.

In this section, we take the LED as an example to present the piezo-phototronic effect. A vast literature exists on the experimental and theoretical study on the relationship between the LED light intensity and applied current density for general application in display and optical communication. The LED light intensity is a nonlinear relationship of the applied current density. The LED optical power density P_{optic} is a nonlinear function of the current density J. Therefore, the linear relationship can be considered as the first order approximation. For simplicity, the LED optical power density P_{optic} with current density J can be generally considered as a power law relationship:

$$P_{\text{optic}} = \beta J^b \tag{7.6}$$

where β is constant depending on device materials and structures, b is the power law parameter, with $b = 1$ corresponding to a linear approximation and $b \neq 1$ to a nonlinear approximation. From our previous experimental work [4], $b = 1.6$.

According to classical semiconductor physics and our theoretical work on piezotronics effect [5], we take an ideal junction as an example to understand the piezo-phototronics effect. For an n-type single-side abrupt junction with donor concentration N_D, and locally $p_{n0} \gg n_{p0}$, the total current density had been received by solving above the basic equations (7.1)–(7.5) for the piezotronic p–n junction [5]:

$$J = J_{C0} \exp\left(\frac{q^2 \rho_{\text{piezo}} W_{\text{piezo}}^2}{2\varepsilon_s kT}\right)\left[\exp\left(\frac{qV}{kT}\right) - 1\right] \tag{7.7}$$

where the saturation current density and the Fermi level in the absence of piezopotential are defined by J_{C0} and E_{F0}:

$$J_{C0} = \frac{q D_p n_i}{L_p} \exp\left(\frac{E_i - E_{F0}}{kT}\right) \tag{7.8}$$

where E_i is the intrinsic Fermi level, and L_p is diffusion length of holes.

According to (7.6), (7.7), and (7.8), the piezo-LED optical power output can be obtained as

$$P_{\text{optic}} = \beta \left\{ J_{C0} \exp\left(\frac{q^2 \rho_{\text{piezo}} W_{\text{piezo}}^2}{2\varepsilon_s kT}\right)\left[\exp\left(\frac{qV}{kT}\right) - 1\right]\right\}^b. \tag{7.9}$$

The efficiency of an LED is determined by: (1) Internal Quantum Efficiency η_{in}, which is defined as the ratio of the number of photons emitted internally to the number of injected carriers passing the junction; (2) Optical Efficiency η_{op}; (3) External Quantum Efficiency η_{ex}; and (4) Power Efficiency η_{P}.

For easily comparing with data of the experiments, we calculate the External Quantum Efficiency for the simple cases described above:

$$\eta_{\text{ex}} = N_{\text{photons}} / N_{\text{elec}} \tag{7.10}$$

where N_{photons} and N_{elec} are the number of photons emitted externally and the number of carriers passing the junction, respectively. If P_{optic} is the optical power density received from the device per unit area, and J is the injection current density, the external quantum efficiency can be rewritten as

$$\eta_{\text{ex}} = \frac{q P_{\text{optic}}}{h v J} \tag{7.11}$$

where hv is the energy of the emitted photon. Thus, the external quantum efficiency can be rewritten as

$$\eta_{\text{ex}} = \alpha \eta_{\text{ex0}} \tag{7.12}$$

where η_{ex0} is defined as the External Quantum Efficiency without piezoelectric charges inside the p–n junction:

$$\eta_{\text{ex0}} = \frac{\beta q}{h v} \left\{ J_{C0} \left[\exp\left(\frac{qV}{kT} \right) - 1 \right] \right\}^{b-1} \tag{7.13}$$

and α is defined as the factor representing the piezo-phototronics effect:

$$\alpha = \left\{ \exp\left(\frac{q^2 \rho_{\text{piezo}} W_{\text{piezo}}^2}{2 \varepsilon_s k T} \right) \right\}^{b-1} \tag{7.14}$$

which describes the ability that the piezoelectric charges tune/control the carrier transport and photon recombination process.

According to (7.9), it is obvious that the relationship between LED optical power density P_{optic} and current density J is nonlinear. More importantly, (7.9) and (7.13) show that not only LED optical power output but also the external quantum efficiency of the piezoelectric p–n junction LED has a nonlinear relationship with local piezoelectric charges. Therefore, the photon emission process can be effectively tuned or controlled not only by the magnitude of the strain, but also by the sign of the strain (tensile vs. compressive). This is the mechanism of the piezo-phototronic devices for p–n junction LED.

For GaN or ZnO nanowire grown along c-axis, with a strain s_{33} along the c-axis, we choose a typical nonlinear approximation: $b = 2$, and the piezo-LED optical power output is given by

$$P_{\text{optic}} = \beta \left\{ J_{C0} \exp\left(-\frac{q e_{33} s_{33} W_{\text{piezo}}}{2 \varepsilon_s k T} \right) \left[\exp\left(\frac{qV}{kT} \right) - 1 \right] \right\}^2. \tag{7.15}$$

Therefore, the External Quantum Efficiency can be obtained as

$$\eta_{\text{ex}} = \exp\left(-\frac{q e_{33} s_{33} W_{\text{piezo}}}{2 \varepsilon_s k T} \right) \eta_{\text{ex0}}. \tag{7.16}$$

The piezo-phototronics effect factor in this case is given by

$$\alpha = \exp\left(-\frac{q e_{33} s_{33} W_{\text{piezo}}}{2 \varepsilon_s k T} \right). \tag{7.17}$$

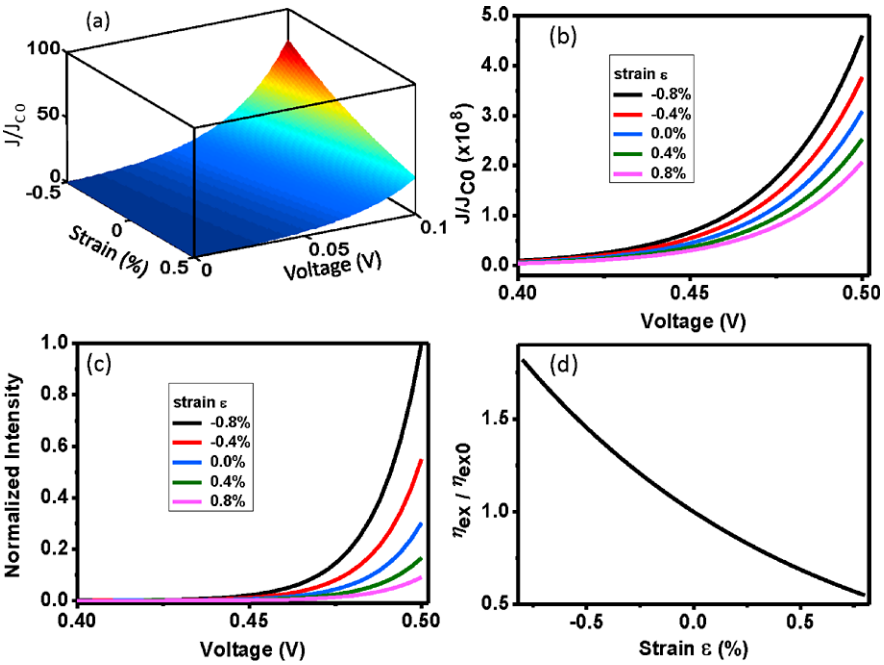

Fig. 7.2 (**a**) Calculated current–voltage characteristics of a piezo-LED with the presence of piezoelectric charges under various strain; (**b**) relative current density and (**c**) relative light intensity as a function of applied voltage at various applied strain (−0.08 % to 0.08 %); (**d**) relative external quantum efficiency as a function of applied strain

According to (7.15)–(7.17) [5], the current density, relative light intensity and the external quantum efficiency are calculated with typical material constants: piezoelectric constants $e_{33} = 1.22$ C/m^2 and relative dielectric constant $\varepsilon_S = 8.91$. The width of the piezo-charges is $W_{\text{piezo}} = 0.25$ nm. The temperature is $T = 300$ K. Figure 7.2(a) shows the calculated J/J_{C0} as a function of the externally applied voltage V and applied strain. The DC characteristics of the piezoelectric Schottky LED with applied strain varied from −0.8 % to 0.8 %, as shown in Fig. 7.2(b). When the strain changes from 0.8 % to −0.8 %, light intensity increases by 1095 % at $V = 0.5$ V in Fig. 7.2(c). Figure 7.2(d) shows the relative external quantum efficiency as a function of the externally applied strain, which clearly demonstrates piezoelectric tune/control on the photo emission process in the piezo-LED. This is the core physics of the piezo-phototronic effect.

7.2.2 *Numerical Simulation of Piezoelectric p–n Junctions LED Devices*

The simplified analyses for one-dimensional cases provide qualitative guidance for understanding the mechanism of how the piezopotential tunes/controls the photons

emission behavior. In the above simplified case, the nonradiative recombination is neglected for understanding the core of piezo-phototronics. According to our previous theoretical work on piezotronics [5, 6], the DC characteristics of the piezo p–n junction LED with strain can be numerically solved by (7.1)–(7.5). We assume that the relationship between LED optical power density P_{optic} and current density J is $P_{\text{optic}} = \beta J^b$.

Using the numerical model which developed for piezoelectric p–n junction, the piezoelectric equations, the electrostatic equation, the convection and diffusion equations are solved with the piezoelectric charge distribution provided.

There are two recombination processes: the band-to-band recombination process and the trap-assisted recombination process (named Shockley–Read–Hall recombination). A radiative process (photon emission) relates to band-to-band recombination, in which the energy transfers from conduction band to the valence band. The Shockley–Read–Hall recombination relates to the nonradiative process, which describes the recombination process by traps in the forbidden band gap of the semiconductor. For simplicity, we neglect another nonradiative process: the Auger process, which is about the energy transfer from injected electron or hole to another free electron or hole.

Following the piezoelectric diode model, the electron and hole generation rates have $G_n = G_p = 0$, which means no external optical excitation occurs in our model. In our simulation, we choose n-type ZnO as the piezoelectric semiconductor material. The length and radius of nanowire device are 100 and 10 nm, respectively. The length of the non-piezoelectric p-type is 20 nm and the length of n-type ZnO is 80 nm. The relative dielectric constants are $\kappa_{\perp}^r = 7.77$ and $\kappa_{//}^r = 8.91$. The intrinsic carrier density is $n_i = 1.0 \times 10^6$ cm^{-3}. The electron and hole mobilities are $\mu_n = 200$ cm^2/V s and $\mu_p = 180$ cm^2/V s. The carrier lifetimes are $\tau_p = 0.1$ μs and $\tau_n = 0.1$ μs. The n-type background doping concentration is $N_{Dn} = 1 \times 10^{15}$ cm^{-3}. The maximum donor doping concentration is $N_{Dn\,\max} = 1 \times 10^{17}$ cm^{-3} and the maximum acceptor doping concentration is $N_{Ap\,\max} = 1 \times 10^{17}$ cm^{-3}. The control constant $ch = 4.66$ nm. The temperature is $T = 300$ K. The piezoelectric charges are assumed to distribute uniformly at the two ends of the n-type segment within a region of 0.25 nm in Fig. 7.3(a). For easy of labeling, a z-axis is defined in Fig. 7.3(a), with $z = 0$ representing the end of the p-type. The p–n junction is located at $z = 20$ nm along the axis. The n-type ends at $z = 100$ nm.

The intensity–voltage curves are shown under various strains at $b = 2$ in Fig. 7.3(b). According to piezotronics theory, positive local piezoelectric charges are created by the negative strain (compressive strain) in our model, which reduces the built-in potential of the p–n junction. Thus, the corresponding saturation current density increases. As a result, current density increases at a fixed bias voltage, which results in an increase of the light intensity. Alternatively, negative piezoelectric charges induced by the positive strain (tensile strain) increase the built-in potential and reduce the saturation current. Thus, the corresponding current density and light intensity decrease at a fixed bias voltage. In Fig. 7.3(c), the intensity shows a clear trend of change at various strains from −0.08 % to 0.08 % at a fixed voltage $V = 0.9$ V, apparently displaying the effect of piezoelectric charges on the

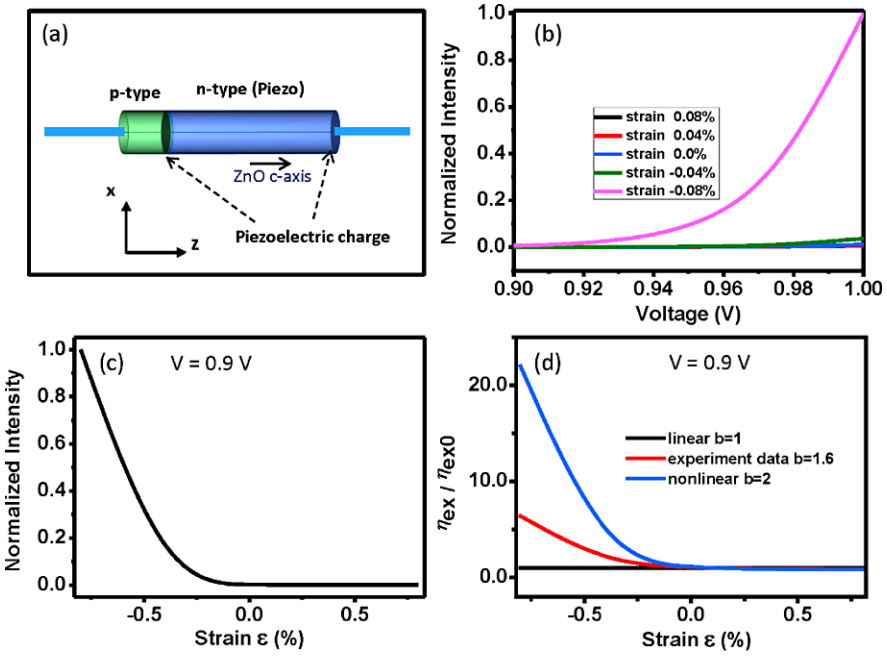

Fig. 7.3 (**a**) Schematic of a ZnO nanowire piezo-LED; (**b**) calculated relative intensity–voltage curves of the LED at various applied strain (−0.08 % to 0.08 %); (**c**) relative light intensity as a function of applied strain (−0.08 % to 0.08 %) at a fixed forward bias voltage of 0.9 V; (**d**) relative external quantum efficiency as a function of applied strain at a fixed forward bias voltage of 0.9 V with linear approximation, parabolic approximation and fitting parameter from our previous experiments data [1]

photon emission. Using our model, we also studied relative external quantum efficiency (piezo-phototronic factor α) at various strains at a fixed voltage $V = 0.9$ V. Figure 7.3(d) shows the relative external quantum efficiency (piezo-phototronic factor α) at various strains from −0.08 % to 0.08 %. By choosing the power law parameter $b = 1$, $b = 2$, and $b = 1.6$, the calculated piezo-phototronic factor and strain curves are corresponding to linear approximation, parabolic approximation (a typical nonlinear approximation) and experimental fitted data, respectively. Therefore, the piezoelectric charges at the p–n interface dominate the photon emission process, in agreement with our experimental results. The numerical results indicate that the piezo-phototronics effect is the result of tuning/controlling the light intensity and external quantum efficiency in the device by the generated piezoelectric charges inside p–n junction.

7.3 Piezo-Phototronic Effect on Photosensors

The piezo-phototronic effect is about the use of the inner-crystal piezoelectric potential to tune/control the charge carrier generation, separation, transport and/or re-

combination in optoelectronic devices. In this section, we have constructed a theoretical model for describing the characteristics of a metal–nanowire–metal structured piezo-phototronic photodetector. We discussed the influences of photoexcitation and piezoelectric charges on photocurrent and their coupling in dictating the performance of the photodetectors with a single Schottky contact and double Schottky contacts. Numerical simulations fit well to the experimental results of a ZnO nanowire-based UV detector. Such a study is extended to CdS nanowire-based photodetectors for visible light detection. We proposed three criteria for identifying the presence of piezo-phototronic effect in a general photodetector.

The theoretical model for two-way coupling in piezotronics has been developed in Chap. 3. Here we adopt the same assumptions and follow similar methods to elaborate the piezo-phototronic effect on photosensors [7]. The Schottky-contact current equation will be used as the basic starting point. The influence of photoexcitation and piezo-charges on material band structure will be discussed, and the final coupled term will be integrated into the current transport equation. To give a more intuitive perspective of the piezo-phototronic effect, we have also carried out numerical calculations. A one-dimensional model and other simplifications are adopted for easy understanding. The core equations and conclusions are shown as follows.

7.3.1 Current Density for a Forward Schottky Contact

For a piezo-phototronic photodetector, a measurement of the photon induced current is an indication of photon intensity. The coupling effect of piezoelectricity and photon excitation is also studied as a strain being applied. For an n-type Schottky contacted device between a metal and a semiconductor, under forward bias voltage, the thermionic emission (TE) theory should be adopted for the charge carrier transport, and the current density under forward bias J_F is

$$J_F = A^* T^2 e^{-\frac{q}{kT}\phi_n}\left(e^{\frac{q}{kT}V} - 1\right) \tag{7.18}$$

where A^* is the Richardson constant, T is temperature, ϕ_n is the effective Schottky barrier height, and V is the applied voltage across the contact.

7.3.2 Current Density for a Reversely Biased Schottky Contact

For a reversely biased n-type Schottky contact, the TE theory underestimates the current, and the thermionic field emission (TFE) theory with considering the tunneling effect better describes the behavior of heavily doped semiconductor materials [8, 9]. According to the TFE theory, the current density under reverse bias takes the form of

$$J_R = J_{sv} e^{-\frac{q}{E_0}\phi_n} e^{V_R\left(\frac{q}{kT} - \frac{q}{E_0}\right)} \tag{7.19}$$

where J_{sv} is the slowly varying term regarding applied voltage and Schottky barrier change, V_R is the reverse voltage, q is electron charge, k the Boltzmann constant, and E_0 is a tunneling parameter of the same order of but larger than kT. Usually E_0 is larger than kT, and is constant regarding barrier height and applied voltage, so it is reasonable to assume that $E_0 = akT$, with $a > 1$, so (7.19) now becomes

$$J_R = J_{sv} e^{-\frac{q}{akT}\phi_n} e^{V_R \frac{q}{kT}(1-\frac{1}{a})}. \tag{7.20}$$

7.3.3 Model for Photoexcitation

Photons with energy higher than the band gap (E_g) of the photodetector material will excite electron–hole pairs. Under steady light illumination, the excess free carrier concentration is constant. The excess carrier concentration is given by the continuity equation [10]

$$\Delta n = \Delta p = \tau_n G_L(I) \tag{7.21}$$

where Δn is the excess electron concentration and Δp the excess hole concentration under light illumination, τ_n is the carrier lifetime, and $G_L(I)$ is the rate of photon generation, which is a function of light intensity.

Without photoexcitation, the Fermi level of the semiconductor lines up with the Fermi level of the metal. When light is illuminated onto the nanowire, the existence of excess carriers will result in a split of the original Fermi level into two quasi-Fermi levels for electrons and holes accordingly, as shown in Fig. 7.4(b). As long as light illumination is uniform, the quasi Fermi level should also be uniform along the entire nanowire. The quasi Fermi level E_{F_n} for electrons and E_{F_p} for holes can be described by

$$E_{F_n} = E_F + kT \ln\left(\frac{n_0 + \Delta n}{n_0}\right), \tag{7.22a}$$

$$E_{Fp} = E_F - kT \ln\left(\frac{p_0 + \Delta p}{p_0}\right). \tag{7.22b}$$

7.3.4 Equations for Piezo-Charges and Piezopotential

As in previous theoretical frame work for piezotronics, the modification to the Schottky barrier height by piezo-charges is

$$\Delta\phi_{\text{piezo}} = -\frac{1}{2\varepsilon}\rho_{\text{piezo}} W_{\text{piezo}}^2 \tag{7.23}$$

where ρ_{piezo} is the density of the strain-induced piezo-charges at nanowire side of the metal–semiconductor junction, and W_{piezo} is the width of the piezo-polar charge distribution adjacent to the interface.

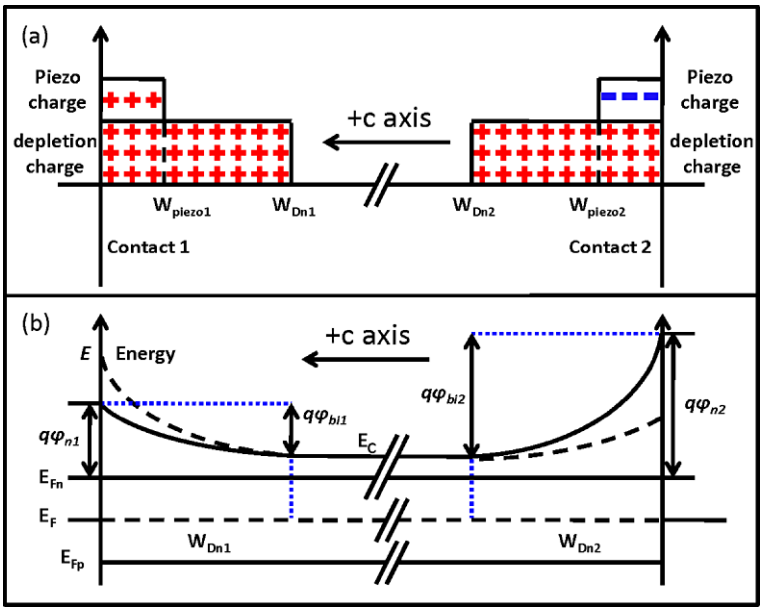

Fig. 7.4 Illustration of ideal metal–semiconductor–metal structures with the presence of piezo-charges and photon generated charges. (**a**) Space charge distribution and corresponding (**b**) energy band diagram in the presence of piezo charges and photo generated charges. *Dashed lines* stand for original barriers without strain nor photoexcitation. The *solid line* is the finally tuned band structure by the piezo-charges, with one end being lifted up and one side being lowered

As piezoelectricity originated from inner-crystal polarization of ions, the piezo-charges can be seen as fixed charges at the two ends of the nanowire with opposite signs, which is shown in Fig. 7.4(a). For a Wurtzite structured nanowire with strain along the c-axis, which is assumed to be the growth direction of the nanowire, the piezo polarization is

$$P = e_{33}s_{33} = \rho_{\text{piezo1}} W_{\text{piezo1}} = -\rho_{\text{piezo2}} W_{\text{piezo2}} \tag{7.24}$$

where e_{33} stands for the piezoelectric constant, and s_{33} stands for the strain along the c-axis, ρ_{piezo1} is the density of the strain-induced piezo-charges at contact 1, and ρ_{piezo2} is the density of the strain-induced piezo-charges at contact 2.

For a Schottky contact, photo excitation can effectively reduce the height of the Schottky barrier, while the introduction of local piezo-charges can change the barrier height, which can be quantitatively expressed as

$$\Delta\phi_n = -\frac{1}{2\varepsilon}\rho_{\text{piezo}} W_{\text{piezo}}^2 - \frac{kT}{q}\ln\left(\frac{n_0 + \Delta n}{n_0}\right). \tag{7.25}$$

Thus, the modified barrier height is

$$\phi_n = \phi_{n0} + \Delta\phi_n \tag{7.26}$$

where ϕ_{n0} is the original Schottky barrier height without strain or light illumination.

The electron current density transported through a forwardly biased Schottky contact is then

$$J_n = J_{n0}\left(\frac{n_0 + \Delta n}{n_0}\right)\exp\left(\frac{q}{kT}\frac{1}{2\varepsilon}\rho_{\text{piezo}}W_{\text{piezo}}^2\right) \tag{7.27}$$

where J_{n0} is the current density without applying light illumination or external strain, and

$$J_{n0} = A^* T^2 e^{-\frac{q}{kT}\phi_{n0}}\left(e^{\frac{q}{kT}V} - 1\right).$$

As the sign of ρ_{piezo} depends on the direction of c-axis and type of applied strain, the influence of the piezo-charges can either enhance photo excitation or reduce it.

7.3.5 *Piezo-Phototronics Effect for a Double-Schottky-Contact Structure*

In a device with double Schottky contacts, with certain bias voltage, one junction will be reversely biased and the other junction will be forwardly biased. The current across the double Schottky junction device should take the form

$$I = S_R J_R = V_{NW}/R_{NW} = S_F J_F \tag{7.28}$$

where S_R and S_F are cross section area for reverse junction and forward junction accordingly, R_{NW} is the resistance of the nanowire, and V_{NW} is the voltage across the nanowire. Thus we have

$$V_R + V_{NW} + V_F = V \tag{7.29}$$

where V_R and V_F are the voltage across the reverse and forward junction, V is the total applied voltage.

In (7.28), the R_{NW} term mainly influences the current behavior at applied voltage at 5 V or higher [9], and at working voltage range for photodetection, the dominating term should be mainly controlled by the reversely biased contact. To clearly see the effect of piezo-charges and photo excitation, we make the reasonable simplification that $V_R = cV$, where c is assumed constant and $c < 1$. Thus, (7.27) now becomes

$$J = J_{sv}\exp\left(-\frac{q}{akT}\phi_{n0}\right)\exp\left[V\frac{q}{kT}c\left(1 - \frac{1}{a}\right)\right]\left(\frac{n_0 + \Delta n}{n_0}\right)^{\frac{1}{a}} \times \exp\left(\frac{q}{akT}\frac{1}{2\varepsilon}\rho_{\text{piezo}}W_{\text{piezo}}^2\right). \tag{7.30}$$

Thus, the device current under different bias voltage takes the form

$$I = S_1 J_{C1} \left(\frac{n_0 + \Delta n}{n_0} \right)^{\frac{1}{a}} \exp\left(\frac{q}{akT} \frac{1}{2\varepsilon} \rho_{\text{piezo1}} W_{\text{piezo1}}^2 \right) \tag{7.31a}$$

when contact 1 is under reverse bias ($V > 0$)

$$I = -S_2 J_{C2} \left(\frac{n_0 + \Delta n}{n_0} \right)^{\frac{1}{a}} \exp\left(\frac{q}{akT} \frac{1}{2\varepsilon} \rho_{\text{piezo2}} W_{\text{piezo2}}^2 \right) \tag{7.31b}$$

when contact 2 is under reverse bias ($V < 0$) where

$$J_{C1} = J_{sv1} \exp\left(-\frac{q}{a_1 kT} \phi_{n10} \right) \exp\left[V \frac{q}{kT} c_1 \left(1 - \frac{1}{a_1} \right) \right]$$

and

$$J_{C2} = J_{sv2} \exp\left(-\frac{q}{a_2 kT} \phi_{n20} \right) \exp\left[V \frac{q}{kT} c_2 \left(1 - \frac{1}{a_2} \right) \right]$$

are the currents under reverse bias for contact 1 and 2 accordingly, and S_1 and S_2 are the areas for junction 1 and 2, respectively. As ρ_{piezo1} and ρ_{piezo2} have opposite signs, (7.31a), (7.31b) shows an asymmetric change in photocurrent under opposite bias by the same amount of applied strain.

7.3.6 Numerical Simulation of MSM Photodetector

We now apply our analytical result to numerical calculation for a Ag–ZnO–Ag structure. As the materials for piezo-phototronics are mainly wurtzite structured materials such as ZnO, CdS and GaN, which share the same crystal symmetry, their piezoelectric coefficient matrix takes the same form.

The parameters for ZnO are as follows: dielectric constant $\varepsilon = \varepsilon_s \varepsilon_0$, with $\varepsilon_s = 8.9$, piezoelectric coefficient $e_{33} = 1.22$ C/m^3. Notably, for CdS, the dielectric constant $\varepsilon_s = 9.3$ [11], piezoelectric coefficient $e_{33} = 0.385$ C/m^3, which means that the simulation results for CdS will only have a slight difference in magnitude, and will have the same trends of change with strain and light intensity. For photoexcitation, we suppose the external quantum efficiency $\eta_{\text{ext}} = 1$, the internal gain $\Gamma_G = 1.5 \times 10^5$ [12], carrier lifetime $\tau_n = 3$ ns [13]. For typical UV photodetection experiments the light wavelength $\lambda = 385$ nm. The diameter of the ZnO nanowire is assumed to be 100 nm. At dark condition, assume the electron concentration in ZnO nanowire is 1×10^{15} cm^{-3}.

For a Ag–ZnO–Ag structure with one Ohmic contact and one Schottky contact, when forward bias is applied on the Schottky contact, using (7.27), we are able to calculate the photocurrent under the same intensity of light illumination with applied strain varying from 0 to 1 %. Depending on the direction of c-axis, the photocurrent

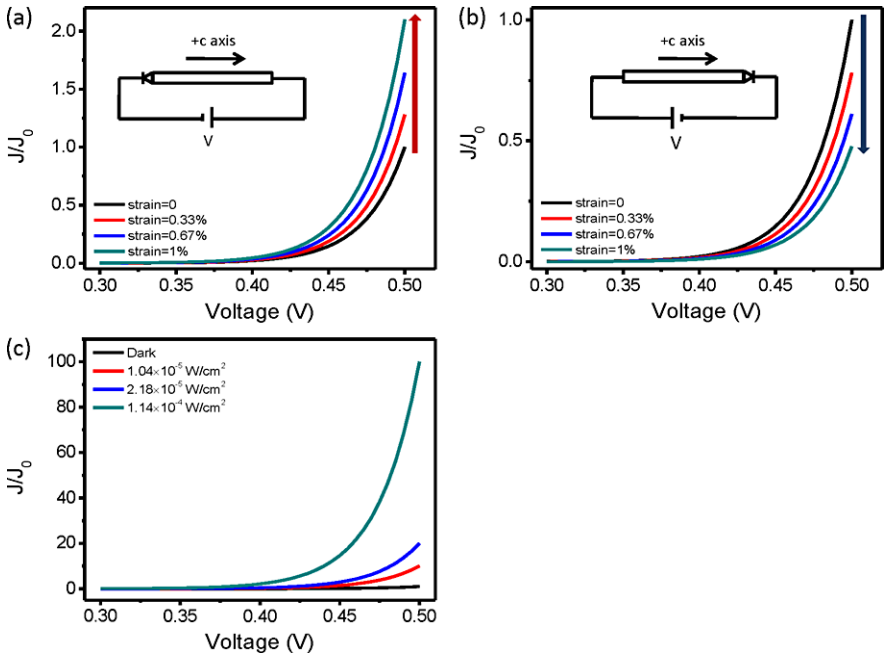

Fig. 7.5 Result for numerical simulation for a metal–ZnO–metal photodetector with Schottky contact on one end and Ohmic contact on the other based on our analytical solution. (**a**) and (**b**) are relative current density vs. voltage under different strains and the same illumination power, for two devices with different orientation of *c*-axis regarding the position of the Schottky contact. J_0 is set as the current of the device at zero strain and at applied voltage of 0.5 V. *Insets* are the configuration of device and direction of forward bias. (**c**) Current–voltage diagram under different illumination power. J_0 is set for the dark current at forward applied voltage of 0.5 V

can either increase or decrease with applied strain. Figures 7.5(a) and (b) shows the performance of two single-Schottky-contact devices, the configuration of which is shown in the inset of Figs. 7.5(a) and (b), accordingly. We are also able to calculate the photocurrent under strain free condition with different illumination power, as shown in Fig. 7.5(c).

For an Ag–ZnO–Ag structure with two Schottky contacts at both ends, we set $a = 1.3$ and $c = 0.8$ in (7.31a), which are reasonable values according to previous reports. The result of simulation according is shown in Fig. 7.6. In Fig. 7.6(a), the asymmetric characteristic of the piezo-phototronic effect is demonstrated very clearly: the change of current under the same amount of applied strain is opposite when the bias voltage is applied in opposite direction.

As will be presented in Chap. 8, the theoretically predicted results have been quantitatively verified by photodetectors based on CdS nanowires for visible light and ZnO nanowires for UV light. Our experimental results show that the piezo-phototronic effect dominates the performance of the photodetector rather than other experimental factors. It is shown that the piezo-phototronic effect is significantly pronounced at low light intensities, which is important for extending the sensitiv-

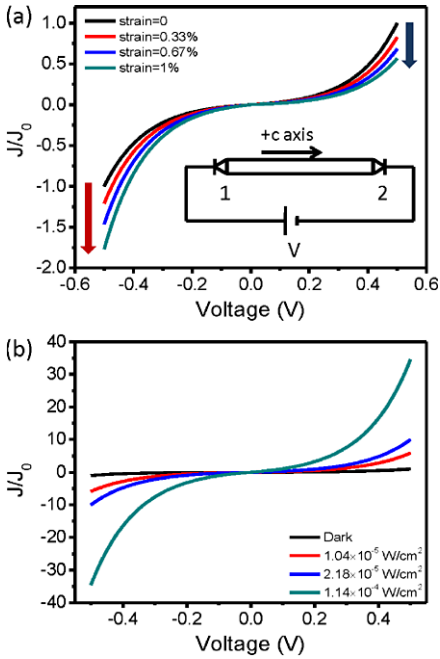

Fig. 7.6 Numerical simulation for a metal–ZnO–metal photodetector with Schottky contact on both ends based on our analytical solution. (**a**) Relative current density vs. voltage under different strains and the same illumination power. J_0 is set as the current of the device at zero strain and at reverse applied voltage of 0.5 V. The *inset* is the configuration of device and direction of forward bias. (**b**) Current–voltage diagram under different illumination power. J_0 is set for the dark current at forward applied voltage of 0.5 V

ity and application range of the photodetector. The conclusions drawn on Schottky contacts present the core properties of the effect and can be easily extrapolated to other structures like p–n junctions.

7.4 Piezo-Phototronic Effect on Solar Cell

There are several key parameters to evaluate the performance of a solar cell: photocurrent (short circuit current), open-circuit voltage, maximum output power, fill factor and ideal conversion efficiency. The fill factor is defined as the ratio of the maximum output power to the product of short circuit current and open-circuit voltage. The ideal conversion efficiency is defined as the ratio of the maximum power output to the incident solar power.

From the materials and device structural point of view, there are two approaches to optimize the solar cell performance: developing new energy efficiency materials and designing new structures. The metal–insulator–semiconductor (MIS) structure has been used to decrease the saturation current density in silicon solar cell [14]. The thickness dependence of p–n junction solar cells had been discussed theoretically for optimization of open-circuit voltages using the thermodynamic theory [15]. Polymer solar cells constructed based on the structure of a low-band gap polymer, PBDTTT4, to increase an open-circuit voltage as high as 0.76 V combined with a power conversion efficiency to as high as 6.77 % [16]. Theories and experiments have been

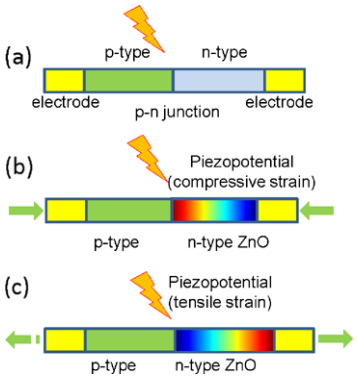

Fig. 7.7 Schematic diagram of (**a**) a general nanowire piezoelectric solar cell fabricated using a p–n junction structure. Schematics of the piezoelectric solar cells under (**b**) compressive strain and (**c**) tensile strain, where the polarity and magnitude of the piezopotential can effectively tune/control the carrier generation, separation and transport characteristics. The color code represents the distribution of the piezopotential at the n-type semiconductor nanowires

developed to understand the origin of the open-circuit voltage of polymer–fullerene solar cells [17]. Recently, a brand new method has been developed by using piezoelectric and ferroelectric materials for enhancing the performance of organic solar cells: piezoelectric solar cell (PSC), and ferroelectric polymer solar cell [18]. The core idea is to use the intrinsic potential provided by the material itself for enhancing charge separation. Developing the basic theory for understanding the experimental phenomena is needed.

Taking a typical nano/microwire solar cell (Fig. 7.7(a)) as an example, the basic structure is a p–n junction or metal–semiconductor (M–S) contact. The working principle of the solar cell is to use the high electric field in the depletion region to assist the separation of electron–hole pairs generated by incident photons. The piezoelectric charges created at the junction area under strain can effectively tune/control the solar cell performance. For example, ZnO nanowire solar cells are shown in Figs. 7.7(b) and (c), which is made of a p-type non-piezoelectric and n-type piezoelectric heterojunction. The piezopotential significantly modifies the band structure at the interface, resulting in a control over the carrier generation, separation and transport at the p–n junction or M–S interface, which is the fundamental piezo-phototronic effect.

The piezopotential distribution and the dynamic transport properties of the carriers have been discussed in the last few sections. In this section, we present a theoretical model for semi-quantitatively understanding the piezo-phototronic effect on the carrier generation and transport behavior [19]. The analytical results are obtained for a ZnO piezoelectric p–n junction solar cell under simplified conditions, which provides a basic physical picture for understanding the mechanism of the PSC. Furthermore, the maximum output of the PSC has been calculated numerically. Finally, the experimental results of organic solar cells support our theoretical model. Using

the piezoelectric effect created by external stress, our study not only provides the basic physics for understanding the characteristics of the solar cell, but also assists the design for higher performance solar cells.

7.4.1 Basic Equations

Piezoelectric theories and semiconductor physics are used for describing the properties of a PSC that is fabricated using piezoelectric semiconductors. The behavior of the piezoelectric material under dynamic straining is described by piezoelectric theories. The static and dynamic transport behavior of the charge carriers and the interaction of a photon and an electron in semiconductors are described by the basic equations of semiconductor physics.

The piezoelectric equation and constituent equations under a small uniform mechanical strain are given by

$$(\mathbf{P})_i = (\mathbf{e})_{ijk}(\mathbf{S})_{jk}, \tag{7.32a}$$

$$\begin{cases} \boldsymbol{\sigma} = \mathbf{c}_E\mathbf{S} - \mathbf{e}^{\mathbf{T}}\mathbf{E}, \\ \mathbf{D} = \mathbf{e}\mathbf{S} + \mathbf{k}\mathbf{E} \end{cases} \tag{7.32b}$$

where $\mathbf{P}$ is polarization vector, $\mathbf{S}$ is uniform mechanical strain, the third order tensor $(\mathbf{e})_{ijk}$ is the piezoelectric tensor, $\boldsymbol{\sigma}$ and $\mathbf{c}_E$ are the stress tensor and the elasticity tensor, respectively. $\mathbf{E}$, $\mathbf{D}$, and $\mathbf{k}$ are the electric field, the electric displacement, and the dielectric tensor, respectively.

The electrostatic behavior of charges in piezoelectric semiconductor is described by the Poisson equation:

$$\nabla^2\psi_i = -\frac{\rho(\mathbf{r})}{\varepsilon_s} \tag{7.33}$$

where ψ_i, $\rho(\mathbf{r})$, and ε_s are the electric potential distribution, the charge density distribution, and the permittivity of the material.

The drift and diffusion current-density equations that correlate the local fields, charge densities, and local currents are

$$\begin{cases} \mathbf{J}_n = q\mu_n n\mathbf{E} + qD_n\nabla n, \\ \mathbf{J}_p = q\mu_p p\mathbf{E} - qD_p\nabla p, \\ \mathbf{J} = \mathbf{J}_n + \mathbf{J}_p \end{cases} \tag{7.34}$$

where $\mathbf{J}_n$ and $\mathbf{J}_p$ are the electron and hole current densities, q is the absolute value of unit electronic charge, μ_n and μ_p are electron and hole mobilities, n and p are concentrations of free electrons and free holes, D_n and D_p are diffusion coefficients for electrons and holes, respectively, $\mathbf{E}$ is electric field, and $\mathbf{J}$ is the total current density.

The charge transport under the driving of a field is described by the continuity equations.

$$\begin{cases} \dfrac{\partial n}{\partial t} = G_n - U_n + \dfrac{1}{q}\nabla \cdot \mathbf{J}_n, \\ \dfrac{\partial p}{\partial t} = G_p - U_p - \dfrac{1}{q}\nabla \cdot \mathbf{J}_p \end{cases} \tag{7.35}$$

where G_n and G_p are the electron and hole generation rates; U_n and U_p are the recombination rates, respectively.

7.4.2 Piezoelectric Solar Cell Based on p–n Junction

According to our theoretical work on the piezotronic effect, an ideal p–n junction is taken as an example to understand the unique property of an PSC. There are two typical effects in a piezoelectric semiconductor material under applied external stress: the piezoresistance effect and piezotronic effect. Piezoresistance effect is about the strain-induced change in bandgap, density of states and/or mobility [20, 21]. Piezoresistance is mostly a volume effect and it is not sensitive to the reversal of the piezoelectric polarity in the semiconductor; thus, it can be truly considered as a change in resistance of the semiconductor bulk, and it has a little effect on the contact property. Although the change in bandgap can affect the saturation current density and the open-circuit voltage of a solar cell, the change of bandgap is independent of the sign of piezoelectric charges created at the contact of the device. The second effect is the piezotronic effect [22], which is about the polar direction dependence of an inner-crystal piezoelectric potential arising from the piezo-charges created at the contacts. Owing to the sign reversal of the piezo-charges at the two ends of the device, a non-symmetric effect is induced at the two ends. This means that the output of the solar cell depends on the polarity of the crystal.

Recent experiments of a P3HT/ZnO solar cell show a strong dependence of the open-circuit voltage on the orientation of the ZnO microwire once it is subjected to a strain [17], suggesting the key role played by the piezo-phototronic effect on solar cell output. The open-circuit voltage and maximum output power sensitively depend on the strain applied to ZnO, while the short circuit current density is not. Therefore, for a p–n junction nano/microwire solar cell to be used for following theoretical study, the photocurrent density (short circuit current density) is assumed independent of the external strain.

Theoretically, the short circuit current density results from the excitation of excess carriers by solar radiation. For simplify, we assume that the electron and hole generation rates (G_n and G_p) are constants:

$$G_n = G_p = \frac{J_{\text{solar}}}{q(L_n + L_p)} \tag{7.36}$$

where J_{solar} is the short circuit current density, L_n and L_p are the electron and hole diffusion lengths, respectively. We assume no radiative process (photon emission), which means no photon emission in our model $U_n = U_p = 0$. In our previous work, the piezoelectric p–n junction model was developed for understanding the physics of the piezoelectric semiconductor using the Shockley theory. The current density of the p–n junction has been obtained with the presence of piezoelectric polarization charges inside the p–n junction. Using the one-dimensional piezoelectric p–n junction model in the presence of photocurrent density J_{solar}, the total current density had been received by solving above basic equations (7.32a), (7.32b)–(7.36) under simplified conditions for an ideal p–n junction PSC:

$$J = J_{pn}\left[\exp\left(\frac{qV}{kT}\right) - 1\right] - J_{\text{solar}}, \tag{7.37a}$$

$$J_{pn} \equiv \frac{qD_p p_{no}}{L_p} + \frac{qD_n n_{po}}{L_n} \tag{7.37b}$$

where J_{pn} is the saturation current density, D_p and D_n are diffusion coefficients for electrons and holes, respectively, p_{no} and n_{po} are the thermal equilibrium hole concentration in n-type semiconductor and the thermal equilibrium electron concentration in p-type semiconductor, respectively. For organic solar cell based on the polymer as a p-type material and the ZnO micro/nanowires as the n-type material, the ZnO micro/nanowires have a high level n-type conductivity [23]. Thus, we assume the p-type side has an abrupt junction with donor concentration N_A, which means $n_{p0} \gg p_{n0}$ inside p–n junction, $J_{pn} \approx \frac{qD_n n_{po}}{L_n}$, where $n_{po} = n_i \exp(-\frac{E_i - E_F}{kT})$, n_i is the intrinsic carrier density and E_i is the intrinsic Fermi level. According to our previous theoretical work about piezotronics, the total current density is rewritten as

$$J = J_{pn0}\exp\left(-\frac{q^2\rho_{\text{piezo}}W_{\text{piezo}}^2}{2\varepsilon_s kT}\right)\left[\exp\left(\frac{qV}{kT}\right) - 1\right] - J_{\text{solar}}, \tag{7.38a}$$

$$J_{pn} = J_{pn0}\exp\left(-\frac{q^2\rho_{\text{piezo}}W_{\text{piezo}}^2}{2\varepsilon_s kT}\right) \tag{7.38b}$$

where the Fermi level and the saturation current density with the absence of piezopotential are defined by E_{F0} and $J_{pn0} = \frac{qD_n n_{po}}{L_n}\exp(-\frac{E_i - E_{F0}}{kT})$, respectively. Different from the original equation, the negative sign appearing in the exponential term in (7.38a), (7.38b) is to be elaborated as follows.

For PSC, (7.38a) and (7.38b) represent that the saturation current density J_{pn} decreases exponentially with the piezoelectric charges at the interface of the p–n junction. It must be mentioned that the term inside the exponential function of (7.38b) has a negative sign comparing to our previous piezoelectric p–n junction. The mechanism in terms of semiconductor physics is that the saturation current density J_{pn} depends on two parts: the thermal equilibrium hole concentration p_{no} in the n-type semiconductor and the thermal equilibrium electron concentration n_{po} in the p-type semiconductor. There are two approximate cases that can be obtained

directly from (7.37b): the first case is $n_{p0} \gg p_{n0}$, which means thermal equilibrium electron concentration n_{po} in p-type semiconductor dominates the current characteristic. This case corresponds to our PSC model. The second case is $p_{n0} \gg n_{p0}$, which means that the thermal equilibrium hole concentration p_{no} in n-type semiconductor dominates the current characteristic. This case had been presented in our previous study on piezoelectric p–n junction solar cell. As for the negative strain (compressive strain) case in our model, the positive piezoelectric charges attract the electrons and repel the holes. Alternatively, for the positive strain (tensile strain) case, negative piezoelectric charges attract the holes and repel the electrons. A distinction between positive and negative piezoelectric charges results in the opposite effects for the two cases, which is represented by the reversal in the sign of the term in the exponential function of (7.38b). According to (7.38a) and (7.38b), by setting $J = 0$, the open-circuit voltage of a PSC can be obtained as [19]

$$V_{\mathrm{OC}} = \frac{kT}{q} \ln\left(\frac{J_{\mathrm{solar}}}{J_{pn}} + 1\right). \tag{7.39a}$$

For typical solar cells with $J_{\mathrm{solar}} \gg J_{pn}$, the open-circuit voltage is approximately given by

$$V_{\mathrm{OC}} \approx \frac{kT}{q} \ln\left(\frac{J_{\mathrm{solar}}}{J_{pn}}\right) = \frac{kT}{q}\left\{\ln\left(\frac{J_{\mathrm{solar}}}{J_{pn0}}\right) + \frac{q^2 \rho_{\mathrm{piezo}} W_{\mathrm{piezo}}^2}{2\varepsilon_s kT}\right\}. \tag{7.39b}$$

Equation (7.39b) presents the open-circuit voltage as a function of the piezoelectric charges. The open-circuit voltage can be effectively tuned or controlled not only by the magnitude of the strain, but also by the sign of the strain (tensile vs. compressive). Though the above results are given by using a one-dimensional nano/microwire model, the mechanism of the piezo-phototronic effect can also be applied to bulk and thin film solar cells.

For GaN or ZnO nanowire grown along c-axis, with a strain s_{33} along the c-axis, solving piezoelectric equation (7.32a) gives $q\rho_{\mathrm{piezo}} W_{\mathrm{piezo}} = -e_{33}s_{33}$. Thus, the current density and open-circuit voltage of the solar cell are calculated using typical material constants: piezoelectric constants $e_{33} = 1.22$ C/m^2 and relative dielectric constant $\varepsilon_S = 8.91$. The width within which the piezo-charges are distributed uniformly is taken as $W_{\mathrm{piezo}} = 0.25$ nm, which is about one atomic layer in thickness. The temperature is $T = 300$ K. For all calculations, the lengths of the left-hand and right-hand side segments of the p–n structure are taken as 20 and 80 nm, respectively. The diameter of the nanowire is 20 nm. Figure 7.8(a) shows a schematic model for the calculation. A z-axis is defined along the c-axis of ZnO nanowire, with $z = 0$ representing the end of the p-type. The p–n junction is located at $z = 20$ nm along the axis and the n-type ends at $z = 100$ nm. Figure 7.8(b) presents the calculated current–voltage curve as a function of voltage and varied light intensity. The short circuit current density increases with light intensity. However, for a given J_{pn}, the open-circuit voltage increases logarithmically with the increase of photocurrent J_{solar}. Decreasing the saturation current density is likely to slightly increase the

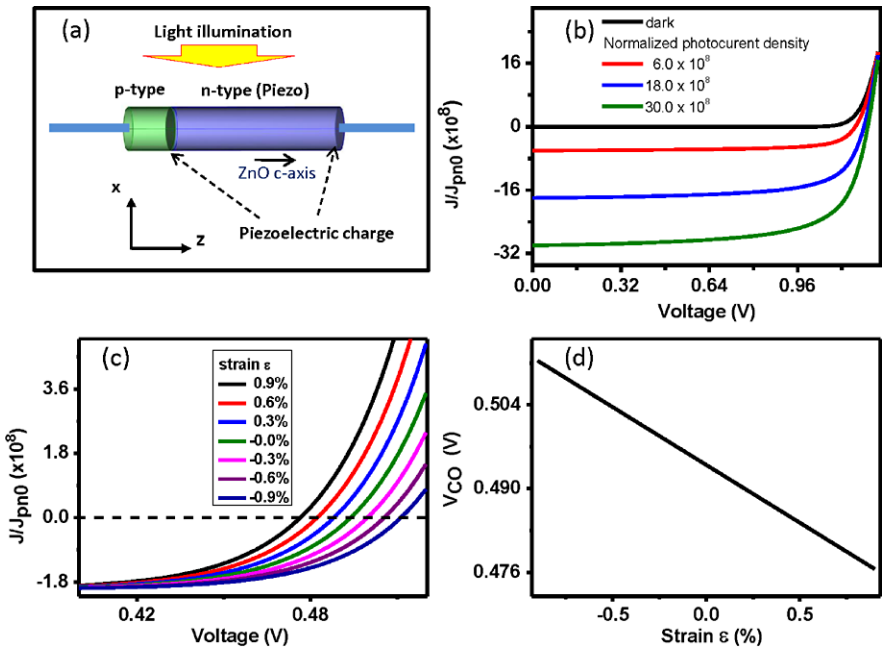

Fig. 7.8 (**a**) Schematic of a ZnO nanowire piezoelectric solar cell based on a p–n junction with the n-side being piezoelectric and the *c*-axis pointing away from the junction; (**b**) calculated current–voltage characteristics of the piezoelectric solar cell under various photocurrent density; (**c**) relative current density as a function of voltage at various applied strain (−0.9 % to 0.9 %); (**d**) open-circuit voltage as a function of the applied strain [19]

open-circuit voltage of the solar cell. At a fixed short circuit current density, the $J-V$ characteristic of the p–n junction solar cell is presented in Fig. 7.8(c) with applied strain varying from −0.9 % to 0.9 %. Figure 7.8(d) shows the open-circuit voltage as a function of the externally applied strain, which clearly demonstrates the piezo-phototronic effect on the performance of the solar cell. The open-circuit voltage drops from 0.48 to 0.51 V when the strain increases from −0.9 % to 0.9 %, as shown in Fig. 7.8(d).

Based the analytical results, the output power of the PSC can be obtained from (7.39a). Figure 7.9(a) shows the output power as a function of voltage at a fixed photocurrent density. The output power curve rises with the increase of strain, and each has its maximum at a specific voltage. By calculating the extreme-value using (7.39a), the maximum output power is shown as a function of applied strain in Fig. 7.9(b). It is obvious that the external strain can effectively tune the maximum output power of the solar cell.

For a comparison to the case shown in Fig. 7.8(a), we reverse the *c*-axis polarity of the n-type side (Fig. 7.10(a)), or exchange the n and p segments (Fig. 7.10(c)). The corresponding models are inset in the figures. The current–voltage curves and the open-circuit voltage of the two cases are plotted in Figs. 7.10(a) and (b), re-

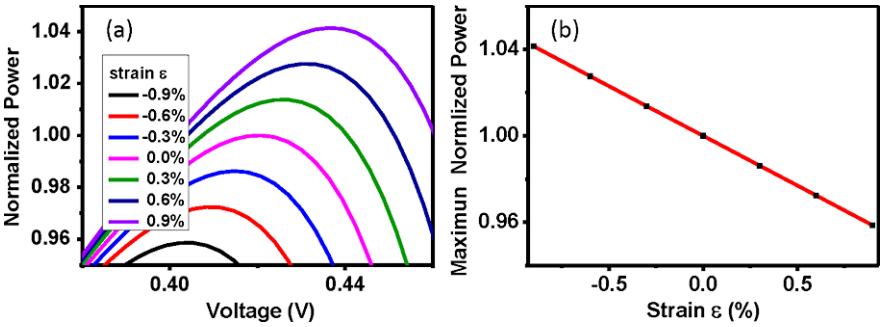

Fig. 7.9 (**a**) Output power of a ZnO nanowire p–n junction piezoelectric solar cell as a function of voltage and (**b**) relative maximum output power at various applied strain (−0.9 % to 0.9 %) [19]

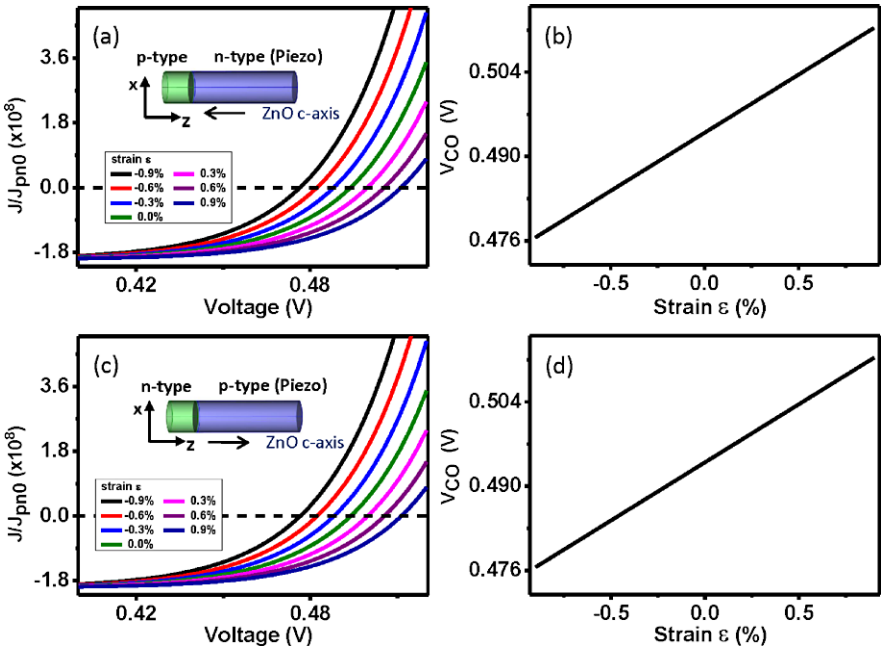

Fig. 7.10 (**a**) Current–voltage curves and (**b**) open-circuit voltage of a p–n-type solar cell, with the n-side (ZnO) being piezoelectric and the *c*-axis pointing toward the junction, under various applied strains (−0.9 % to 0.9 %). (**c**) Current–voltage curves and (**d**) open-circuit voltage of a p–n junction solar cell, with the p-side being piezoelectric and the *c*-axis pointing away from the junction, under various applied strains (−0.9 % to 0.9 %) [19]

spectively. In the case of Fig. 7.10(a), which has a reversal *c*-axis in comparison to that of Fig. 7.8(a), the trend of the current density depending on the strain as shown in Fig. 7.10(a) is opposite to that shown in Fig. 7.8(c), because the sign of the piezoelectric charges is reversed.

For non-piezoelectric n-type material and piezoelectric p-type semiconductor solar cell case, as shown in Figs. 7.10(c) and (d), the calculated $I-V$ curve and the open-circuit voltage show the same trend as for Figs. 7.10(a) and (b). The results indicate a choice of n- or p-type piezoelectric semiconductor materials and their corresponding piezoelectric polar directions may be used effectively for improving the solar cell performance.

7.4.3 Metal–Semiconductor Schottky Contacted Solar Cell

The metal–semiconductor (M–S) contact is an important component in solar cell devices. According to our theoretical work on the piezotronic effect [5], for n-type piezoelectric semiconductor nanowire, the total current density of an ideal M–S under simplified conditions is given by (7.40a), (7.40b) for a PSC [19]:

$$J = J_{\mathrm{MS}}\left[\exp\left(\frac{qV}{kT}\right) - 1\right] - J_{\mathrm{solar}}, \tag{7.40a}$$

$$J_{\mathrm{MS}} = J_{\mathrm{MS0}}\exp\left(\frac{q^2\rho_{\mathrm{piezo}}W_{\mathrm{piezo}}^2}{2\varepsilon_s kT}\right) \tag{7.40b}$$

where J_{MS} is the saturation current density and J_{MS0} is defined as the saturation current density in the absence of piezoelectric charges:

$$J_{\mathrm{MS0}} = \frac{q^2 D_n N_C}{kT}\sqrt{\frac{2qN_D(\psi_{bi0} - V)}{\varepsilon_s}}\exp\left(-\frac{q\phi_{Bn0}}{kT}\right) \tag{7.41}$$

where ψ_{bi0} and ϕ_{Bn0} are the built-in potential and Schottky barrier height with the absence of piezoelectric charges. In our case, the effect of piezoelectric charge can be considered as perturbation to the conduction-band edge E_C. Note that the sign of the exponential term in (7.40b) is reversed in comparison to that in (7.38a) for the reasons discussed in the last section.

Thus, the open-circuit voltage of an M–S contact PSC can be obtained as

$$V_{\mathrm{OC}} \approx \frac{kT}{q}\left\{\ln\left(\frac{J_{\mathrm{solar}}}{J_{\mathrm{MS0}}}\right) - \frac{q^2\rho_{\mathrm{piezo}}W_{\mathrm{piezo}}^2}{2\varepsilon_s kT}\right\}. \tag{7.42}$$

In the positive strain (tensile strain) case, the negative local piezoelectric charges increase the barrier height at the M–S contact, and thus result in a decrease in the saturation current density J_{MS} as shown in (7.40b); correspondingly, the open-circuit voltage of the M–S contact solar cell is increased according to (7.42). Alternatively, under a negative strain (compressive strain), the positive local piezoelectric charges decrease the barrier height at the M–S contact, resulting in an increase in the saturation current density J_{MS}, which reduces the open-circuit voltage of the M–S contacted solar cell. Therefore, the current density and the open-circuit voltage can

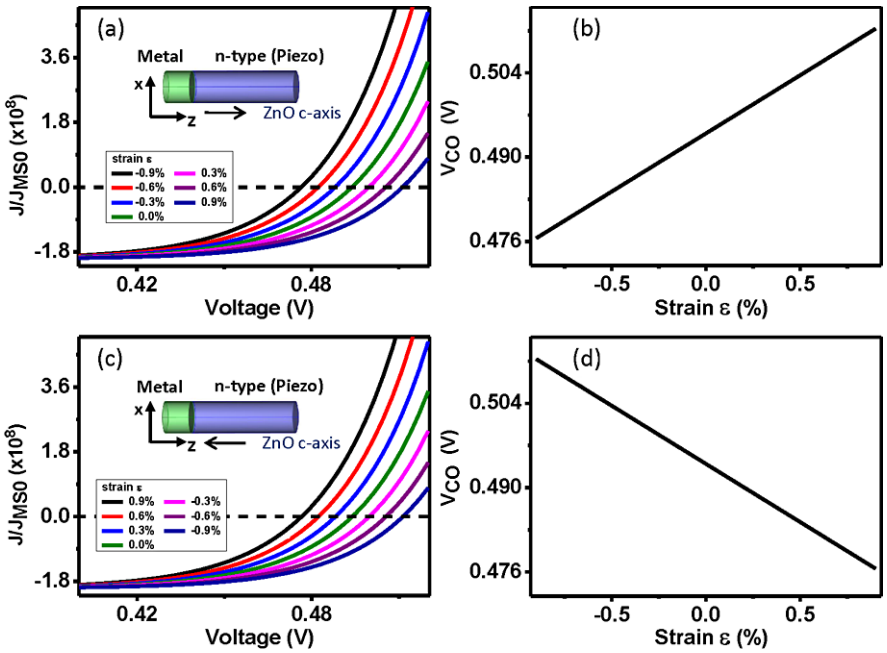

Fig. 7.11 (**a**) Schematic of a piezoelectric solar cell based on metal–semiconductor (ZnO) contact with the *c*-axis pointing away from the interface; and (**b**) the open-circuit voltage under various applied strain (−0.9 % to 0.9 %). (**c**) Schematic of a piezoelectric solar cell based on metal–semiconductor (ZnO) contact with the *c*-axis pointing toward the interface; and (**d**) open-circuit voltage under applied strain (−0.9 % to 0.9 %) [19]

be controlled not only by the magnitude of the strain, but also by the sign of the strain (tensile vs. compressive). For GaN or ZnO nanowire grown along the *c*-axis, with a strain s_{33} along the *c*-axis, the typical material constants for calculations are the same as for the p–n junction cases. The schematics of the calculated model are shown in Figs. 7.11(a) and (c). Figure 7.11(a) shows the calculated J/J_{MS0} as a function of voltage V at fixed light intensity. The current curves drop as the external applied strain changes from −0.9 % to 0.9 %. The open-circuit voltage increases as a function of the externally applied strain, as shown in Fig. 7.5(b). By switching the polar direction of the *c*-axis, the open-circuit voltage drops with the increase of strain (Figs. 7.11(c) and (d)). The theoretical result agrees qualitatively with our previous experiments.

7.5 Summary

In summary, we have presented the theoretical frame of piezo-phototronics for the cases of photon emission, photon detector and solar cell. Besides giving the governing equations, some analytical solutions are provided for easy understanding of

the physical pictures. Then, numerical calculated results by solving the full differential equations are presented. Although our model is based on semi-classical theory and the results could be semi-quantitative, it provides a clear understanding of the phenomena, which will be presented in future chapters. More sophisticated theories will be developed in the near future for quantifying the observed piezo-phototronic phenomena.

References

1. Y. Zhang, Z.L. Wang, Theory of piezo-phototronics for light-emitting diodes. Adv. Mater. **24**, 4712–4718 (2012)
2. S.M. Sze, *Physics of Semiconductor Devices*, 2nd edn. (Wiley, New York, 1981)
3. T. Ikeda, *Fundamentals of Piezoelectricity* (Oxford University Press, Oxford, 1996)
4. Q. Yang, W.H. Wang, S. Xu, Z.L. Wang, Enhancing light emission of ZnO microwire-based diodes by piezo-phototronic effect. Nano Lett. **11**(9), 4012–4017 (2011)
5. Y. Zhang, Y. Liu, Z.L. Wang, Fundamental theory of piezotronics. Adv. Mater. **23**(27), 3004–3013 (2011)
6. Comsol Model Gallery (Semiconductor Diode). http://www.comsol.com/showroom/gallery/114/, accessed October 2011
7. Y. Liu, Q. Yang, Y. Zhang, Y.Z. Yang, Z.L. Wang, Nanowire piezo-phototronic photodetector: theory and experimental design. Adv. Mater. **24**(11), 1410–1417 (2012)
8. E.H. Rhoderick, R.H. Williams, *Metal–Semiconductor Contact* (Clarendon, Oxford, 1988)
9. Z.Y. Zhang, K. Yao, Y. Liu, C.H. Jin, X.L. Liang, Q. Chen, L.M. Peng, Quantitative analysis of current–voltage characteristics of semiconducting nanowires: decoupling of contact effects. Adv. Funct. Mater. **17**(14), 2478–2489 (2007)
10. D.A. Neamen, *Semiconductor Physics and Devices*, 3rd edn. (McGraw-Hill, New York, 2002)
11. D.G. Thomas, J.J. Hopfield, Exciton spectrum of cadmium sulfide. Phys. Rev. **116**(3), 573–582 (1959)
12. Q. Yang, X. Guo, W.H. Wang, Y. Zhang, S. Xu, D.H. Lien, Z.L. Wang, Enhancing sensitivity of a single ZnO micro-/nanowire photodetector by piezo-phototronic effect. ACS Nano **4**(10), 6285–6291 (2010)
13. X.J. Zhang, W. Ji, S.H. Tang, Determination of optical nonlinearities and carrier lifetime in ZnO. J. Opt. Soc. Am. B **14**(8), 1951–1955 (1997)
14. R.B. Godfrey, M.A. Green, 655 mV open-circuit voltage, 17.6 % efficient silicon MIS solar cells. Appl. Phys. Lett. **34**(11), 790–793 (1979)
15. R. Brendel, H.J. Queisser, On the thickness dependence of open circuit voltages of p–n junction solar cells. Sol. Energy Mater. Sol. Cells **29**(4), 397–401 (1993)
16. H.Y. Chen, J.H. Hou, S.Q. Zhang, Y.Y. Liang, G.W. Yang, Y. Yang, L.P. Yu, Y. Wu, G. Li, Polymer solar cells with enhanced open-circuit voltage and efficiency. Nat. Photonics **3**, 649–654 (2009)
17. K. Vandewal, K. Tvingstedt, A. Gadisa, O. Inganas, J.V. Manca, On the origin of the open-circuit voltage of polymer-fullerene solar cells. Nat. Mater. **8**, 904–909 (2009)
18. Y.B. Yuan, T.J. Reece, P. Sharma, S. Poddar, S. Ducharme, A. Gruverman, Y. Yang, J.S. Huang, Efficiency enhancement in organic solar cells with ferroelectric polymers. Nat. Mater. **10**, 296–302 (2011)
19. Y. Zhang, Y. Yang, Z.L. Wang, Piezo-phototronics effect on nano/microwire solar cells. Energy Environ. Sci. **5**, 6850–6856 (2012)
20. A.D. Bykhovski, V.V. Kaminski, M.S. Shur, Q.C. Chen, M.A. Khan, Piezoresistive effect in wurtzite n-type GaN. Appl. Phys. Lett. **68**(6), 818–819 (1996)

21. R. Gaska, M.S. Shur, A.D. Bykhovski, J.W. Yang, M.A. Khan, V.V. Kaminski, S.M. Soloviov, Piezoresistive effect in metal–semiconductor–metal structures on p-type GaN. Appl. Phys. Lett. **76**(26), 3956–3958 (2000)
22. Z.L. Wang, Piezopotential gated nanowire devices: piezotronics and piezo-phototronics. Nano Today **5**, 540–552 (2010)
23. A. Janotti, C.G. Van de Walle, Fundamentals of zinc oxide as a semiconductor. Rep. Prog. Phys. **72**(12), 126501 (2009)

Chapter 8
Piezo-Phototronic Effect on Solar Cells

Abstract Effective electron–hole separation at a p–n junction is important for the efficiency of a solar cell. Band structure modification at the junction can be achieved by the piezo-phototronic effect, which is demonstrated in this chapter for tuning the solar cell output made using poly(3-hexylthiophene) (P3HT)-ZnO micro/nanowire and a n-CdS/p-Cu_2S coaxial nanowire. This effect offers a new concept for improving solar energy conversation efficiency by designing the orientation of the nanowires and the strain to be purposely introduced in the packaging of the solar cells.

Solar cell physics is one of the most important fields in optoelectronics. Using the barrier structure at a metal–semiconductor interface and the internal field formed at the charge depletion zone at a p–n junction, photon-generated electron–hole pairs in the semiconductor materials are separated, forming an output current. The presence of piezoelectric charges at the interface/junction can effectively change its performance in charge separation. This chapter is to study the piezo-phototronic effect on the solar cells.

8.1 Photocell of a Metal–Semiconductor Contact

At a metal–ZnO interface, a Schottky contact can be formed by choosing a proper metal type which can be modified during the engineering process [1]. A Schottky barrier is favorable to separate the electrons and holes created in the vicinity of the metal–ZnO interface under the excitation of a laser with energy higher than the band gap. If a strain is created in a ZnO nanowire (NW), a piezopotential drop is created along the NW, which may introduce non-symmetrical changes in the heights of the local Schottky barriers at the two ends of the NW. In this section, using a metal–semiconductor–metal back-to-back Schottky contacted ZnO microwire device, we demonstrate the piezoelectric effect on the output of a photocell [2]. An externally applied strain produces a piezopotential in the microwire, which tunes the effective height of the Schottky barrier (SB) at the local contact, consequently changing the transport characteristics of the device. Our study shows the possibility of maximizing the output of a photocell by controlling strain in the device.

Z.L. Wang, *Piezotronics and Piezo-Phototronics*, Microtechnology and MEMS,
DOI 10.1007/978-3-642-34237-0_8, © Springer-Verlag Berlin Heidelberg 2012

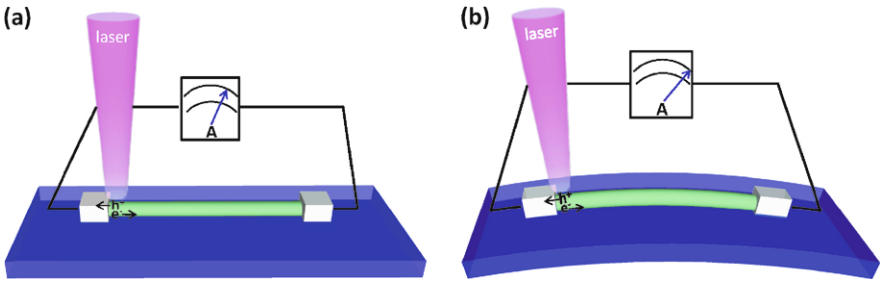

Fig. 8.1 Schematic of the experiment design. (**a**) Device without strain. (**b**) Device under strain [2]

8.1.1 Experimental Method

The ultra long ZnO microwires used in our study were grown by a high-temperature thermal evaporation process [3]. For fabricating a ZnO microwire photocell, a ZnO microwire was first laid down on a polystyrene (PS) substrate, and then each end of the wire was fixed to the substrate using silver paste. The dimension of the PS substrate was 3.5 mm in length, 5 mm in width and with a thickness of 1 mm. An additional very thin layer of polydimethylsiloxane (PDMS) was used to package the device, and it kept the device mechanically robust under repeated manipulation. Flexible and transparent microwire photocells were obtained after drying in air for 48 hours. The experimental design is sketched in Fig. 8.1. The strain was introduced via bending the substrate by a precisely controlled linear stage (MFA-CC, Newport Corp.) with a motion resolution of 0.0175 μm. A He–Cd laser beam (wavelength = 325 nm, diameter < 20 μm) was focused at the designed position on the device. We utilized a UV enhanced CCD to act as the monitor. A Keithley 4200 semiconductor characterization system was used to carry out electrical measurement.

8.1.2 Basic Principle

First, all of the devices were tested for the piezoelectric response. Because the microwire was laid on the surface of the substrate and fixed by the two ends, by considering the relative size of the microwire and the substrate, the mechanical behavior of the entire system was dominated by the substrate, and a bending of the flexible substrate produced purely a tensile or compressive strain in the microwire depending on its bending direction. The strain in the microwire can be quantified by the distance at which the substrate was deflected. A typical group of *I*–*V* curves representing the piezoelectric response is shown in Fig. 8.2(a). When a ZnO microwire was compressed or stretched along the *c*-axis, a piezopotential drop is created along the microwire. This piezoelectric field distribution around the metal–semiconductor contact area in the device will change the effective height of the SB in a different manner at each end and consequently the transport properties of the device, as

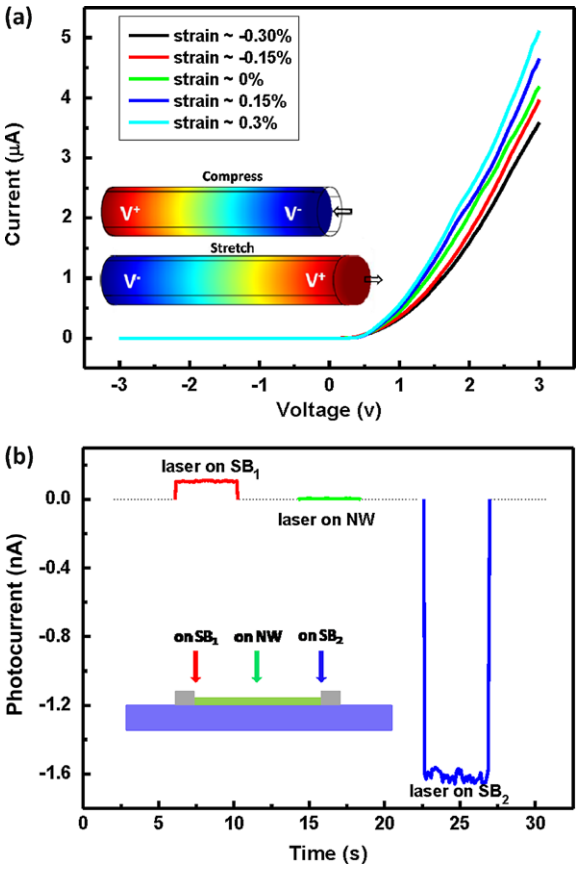

Fig. 8.2 (**a**) Piezoelectric response test of a device. *Inset*: Simulations of the piezopotential distribution in the wire under different straining conditions. (**b**) Measured output current when the laser spot was focused at different positions. The *inset* shows the sketched picture to indicate the related illuminating position of the laser on the device

shown in Fig. 8.2(a). It must be mentioned that the applied strain will also change the band structure slightly, which is the piezoresistance effect. This effect also introduces a change in the SB height, but it should be identical at the two ends of the device. While the piezopotential has polarity, it is a non-symmetric effect at the two ends and is likely to introduce a non-symmetric variation in the *I*–*V* characteristic.

For an M–S–M structure, the effectiveness of a SB for separating the photon excited electron–hole pairs strongly depend on the SB height. For a SB with a correct height (Fig. 8.3(a)), the electron excited by a photon at the vicinity of the M–S interface in the conduction band drifts toward the semiconductor side due to lower energy and finally reaches the metal side; the hole drifts toward the interface and recombines with an electron in the metal, forming a current loop. If the SB height is too high (Fig. 8.3(b)), the electron can drift into the semiconductor due to the steep band shape, but the hole is likely to be trapped at the band corner near the interface (Fig. 8.3(b)), which has a higher energy than the Fermi level, so that the electron in the metal cannot be effectively annihilate with the hole. Thus, the current loop is not formed. If the barrier height is too low (Fig. 8.3(c)), the flat shape of the band near the interface is not strong enough to drive the drift of electron and

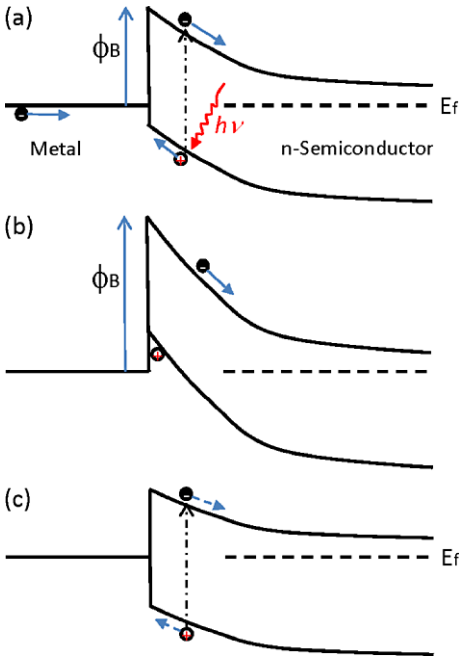

Fig. 8.3 Illustration of the height of a Schottky battier at a metal semiconductor interface and its effect on separating the phonon excited electron–hole pairs. (**a**) An optimized barrier height; (**b**) an interface with a too high barrier; and (**c**) an interface with a too low barrier [2]

hole toward opposite directions with considering the Coulomb interaction between the two, thus, they tend to recombine and there will be no charge separation. For a general fabricated device that has a barrier height not optimized for the solar cell, we can use the piezopotential to tune the height of the SB so that it has the maximized electron–hole separation but minimized electron–hole recombination, and a maximized photocurrent would be possible.

8.1.3 Optimization of Solar Cell Output

We now use the M–S–M contacted microwire to illustrate the effect of the piezopotential on the performance of a photocell. First, by shining a laser of wave length 325 nm, the output current was recorded from the device when the laser spot was focused at different positions on the device, as shown in Fig. 8.2(b). The entire device is constructed with two back-to-back SBs connected via the microwire. When the focal point of the laser beam changed from one SB to the other, the measured output current changed its sign. This is due to the opposite directions of the local electrical fields at the two SB areas, which enforce the separation of electrons and holes induced by the laser irradiation, and thus lead them to flow in opposite directions. If we fixed the laser beam at one SB area, and bend the substrate of the device step by step, strain will be introduced into the device step by step. Depending on the deformation direction, the sign of the strain is changed from negative to positive or

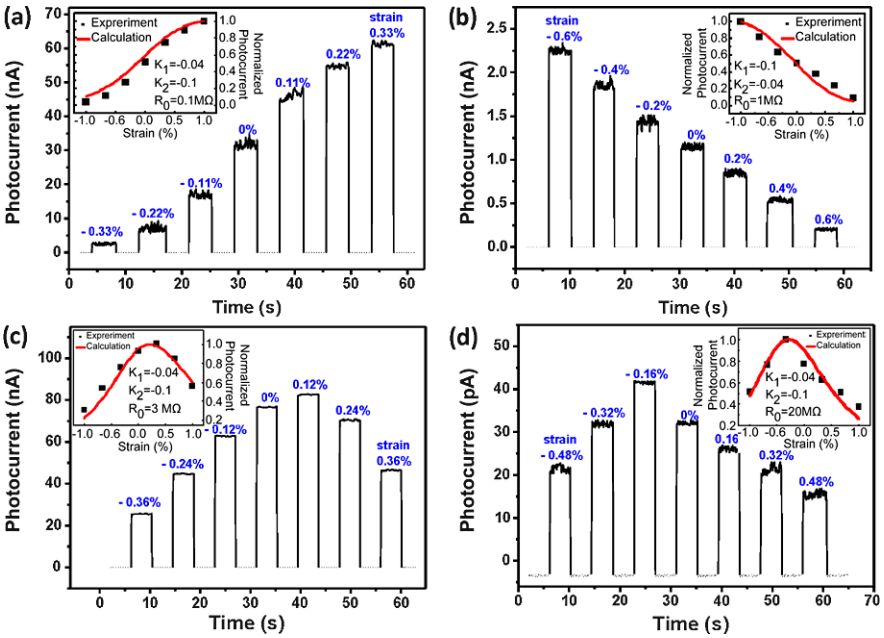

Fig. 8.4 Output current responses to the strain applied on the device, which can be divided into four categories: (**a**) increasing, (**b**) decreasing, and with a maximum under (**c**) applying positive strain or (**d**) negative strain. The *inset* is the calculated results to indicate the output current behavior based on the related parameters, showing a similar changing trend compared with the experimental data after normalization [2]

vice versa. Meanwhile the corresponding piezopotential distribution in the wire will also be adjusted step by step. This will alter the effective heights of the two SBs and thus the characteristic of the microwire photocell.

Four kinds of characteristic relationship between the output current and the applied strain have been observed. The first one is that the output current increases with applied strain, as shown in Fig. 8.4(a). We have tested 26 devices, 14 of them exhibited this type of behavior. The second kind is just opposite to the first one: the output current decreases when the applied strain is increased (Fig. 8.4(b)). Only two devices out of the 26 had this type of output current characteristic. The third kind and the fourth are similar. They both have a maximum output current responding to the applied strain. But for the former one, the maximum point occurred in the tensile strain range (Fig. 8.4(c)), while the latter is in the compressive strain range (Fig. 8.4(d)). Among the 26 devices, six devices were in the third case and four in the fourth one. These different behaviors indicated some intrinsic difference in these photocells.

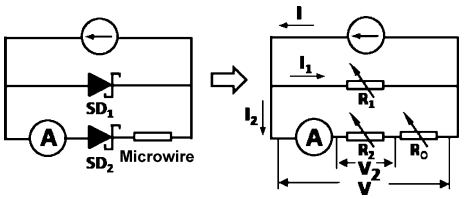

Fig. 8.5 The structure of a microwire photocell circuit and its corresponding equivalent circuit for theoretical calculation

8.1.4 Theoretical Modeling

The coupling among the optical, mechanical, and electrical properties in these ZnO devices provides a new method to distinguish and probe their intrinsic characteristics. Their behavior can be quantitatively understood based on an equivalent circuit simulation together with thermionic-emission theory for the photocell. When a laser beam with a fixed power is focused at the SB area, this part worked as a constant photocurrent source, which is connected in parallel with a forward biased Schottky diode (referred to as SD_1) that characterizes the role played by the SB. The output current we measured is the current that passes through the rest of the circuit, which is the other forward biased Schottky diode at the opposite end of the device (referred to as SD_2) and the microwire. When a strain is introduced into the device via bending, the SB height and the resistance of the microwire are all changed correspondingly. These three parts will serve as three rheostats (R_1, R_2, and R_0) that are a function of the strain. The coupling among these variable electronic parameters and their matching with the load produces various output configurations, as elaborated in what follows [2].

Based on the characteristics of the equivalent circuit (Fig. 8.5(b)), we have

$$I = I_1 + I_2, \tag{8.1}$$

$$V = I_2 R_0 + V_2 \tag{8.2}$$

in which, I is the constant photocurrent induced by the laser irradiation, I_1 and I_2 are the currents passing through the corresponding circuit branch where SD_1 and SD_2 are contained, V and V_2 are the voltage drops on the constant photocurrent source and SD_2. For a forward biased Schottky diode, the current passing through can be described by thermionic-emission theory [2]:

$$I_1 = I_{1s}\left[\exp\left(\frac{qV}{kT}\right) - 1\right], \tag{8.3}$$

$$I_2 = I_{2s}\left[\exp\left(\frac{qV_2}{kT}\right) - 1\right] \tag{8.4}$$

where

$$I_{1s} = S_1 A^* T^2 \exp\left(-\frac{q\phi_1}{kT}\right), \tag{8.5}$$

$$I_{2s} = S_2 A^* T^2 \exp\left(-\frac{q\phi_2}{kT}\right) \tag{8.6}$$

in which S_1 and S_2 are the Schottky contact areas and ϕ_1 and ϕ_2 are the SB heights for SD_1 and SD_2, respectively, A^* is the Richardson constant for thermionic emission, T is the temperature, q is the electron charge, k is the Boltzmann constant.

If $qV/kT \ll 1$, we can get the analytical solution of the measured output current I_2 from (8.1)–(8.4) as

$$I_2 = \frac{\alpha I}{\alpha(\frac{I_{1s}}{I_{2s}} + 1) + R_0 I_{1s}} \tag{8.7}$$

where $\alpha = kT/q$. If this condition cannot be met, we also checked the numerical solutions for I_2. We found that for the same parameters, the analytical and numerical solutions showed the same variation trend, and there were only some small differences in the current magnitude for the final simulation data. So, in order to get a more intuitive analysis, we assume that (8.7) always holds.

We can define a function $f(\varepsilon)$ as [2]

$$f(\varepsilon) = \alpha\left(\frac{I_{1s}}{I_{2s}} + 1\right) + R_0 I_{1s} \tag{8.8}$$

in which ε is the applied strain. According to the experimental results, the variation of R_0 in responding to the strain can be ignored. Our previous experimental results showed that, for a small strain range, we can introduce an empirical expression:

$$\begin{cases} \phi_1 = K_1\varepsilon + \phi_{10}, \\ \phi_2 = K_2\varepsilon + \phi_{20}, \end{cases} \quad \text{and} \quad \begin{cases} K_1 < 0, \\ K_2 < 0. \end{cases} \tag{8.9}$$

Thus, based on (8.5), (8.6), and (8.8), we get

$$\frac{df(\varepsilon)}{d\varepsilon} = \left(-\frac{1}{kT}\right) I_{1s} K_1 \left[R' + R_0\right] \tag{8.10}$$

in which

$$R' = \frac{\alpha}{I_{2s}}\left(1 - \frac{K_2}{K_1}\right). \tag{8.11}$$

Case 1: If $|K_1| > |K_2|$, $df(\varepsilon)/d\varepsilon > 0$, I_2 will be a decreasing function of ε, in corresponding to the case observed in Fig. 8.4(b).

Case 2: If $|K_1| < |K_2|$, the sign of $df(\varepsilon)/d\varepsilon$ depends on the relative magnitude between $|R'|$ and R_0. Because I_{2s} is a function of ϕ_2, R' it will change its magnitude when strain is applied. Thus, under a proper straining condition, we have the following subcases:

Case 2a: when $|R'| > R_0$, $df(\varepsilon)/d\varepsilon < 0$, I_2 is an increasing function of ε.

Case 2b: when $|R'| = R_0$, $df(\varepsilon)/d\varepsilon = 0$, I_2 will reach its maximum at this point.
Case 2c: when $|R'| < R_0$, $df(\varepsilon)/d\varepsilon > 0$, I_2 is a decreasing function of ε.

Because the strain we applied was of a limited extent, the variation range of $|R'|$ is restricted. If $|R'| \gg R_0$ is the initial state of the device, the change of $|R'|$ will be for the strain range of Case 2a, which corresponds to the result presented in Fig. 8.4(a). Similarly, if the initial states of the device is $|R'| \ll R_0$, the change of $|R'|$ will be a for Case 2c, the corresponding result is shown in Fig. 8.4(b). Finally, if $|R'|R$ is comparable with the value of R_0, I_2 reaches its maximum in the positive (Fig. 8.4(c)) or negative (Fig. 8.4(d)) strain range depending on the initial relative magnitude of the two values.

From the statistical point of view, the probability for having $|K_1| > |K_2|$ and $|K_1| < |K_2|$ should be equal. Thus, the monotonic decreasing case should be observed more than half the time in fabricated devices. This is not the case observed in our experiments. As we have shown previously, the free electrons in the n-type ZnO will partially screen the piezoelectric field. Since the laser beam was focused on the SD_1 area, the free carrier density at this local region was increased drastically under laser irradiation. In such a case, the effect introduced by the piezopotential was much reduced at this local region. Therefore, in most cases, $|K_1| < |K_2|$. In reference to the distribution of device characteristics as elaborated in Fig. 8.4, most of the devices met the criterion of $|R'| > R_0$ (Case 2a). Therefore, the four different photocurrent behaviors presented in Fig. 8.4 represent the different intrinsic characteristics of microwire photocells.

In order to examine the intrinsic role played by $|K_1/K_2|$ and $|R'/R_0|$ as stated above, we calculated the output current from (8.7) as a function of these two parameters. The related experimental data were plotted comparing with these calculated results after normalization. We fixed $\phi_{10} = \phi_{20} = 0.4$ eV, and $I = 10^{-8}$ A for all of the cases. We chose $K_1 = -0.04$, $K_2 = -0.1$, which is the typical value obtained from the experiments, when R_0 is changed from 0.1 to 3 MΩ and then to 20 MΩ, the photocurrent behaviors changed from increasing to a maximum point at the positive strain range, and then to a maximum point at the negative strain range, as shown in the inserts of Figs. 8.4(a), (c) and (d), respectively. When we chose $K_1 = -0.1$, $K_2 = -0.04$ and $R = 1$ MΩ, a decreasing behavior of the photocurrent is obtained, as shown in the insert of Fig. 8.4(b). These simulated results quantitatively agree with the experimental data in the overall trend.

8.2 p–n Heterojunction Solar Cells

In this section, we use a p–n heterojunction-based solar cell made of poly(3-hexylthiophene) (P3HT) and ZnO micro/nanowire to demonstrate the effect of piezopotential on the solar efficiency. The experimental data were understood based on the modification of the band structure at the p–n junction by the piezopotential, which is referred to as a result of the piezotronic effect.

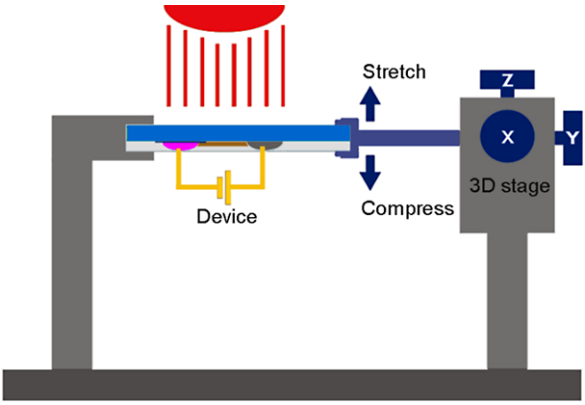

Fig. 8.6 The measuring system of the device. The tensile and compressive strains were produced by using a three-dimensional mechanical stage (the displacement resolution of 1 μm) to bend the free end of the device. Under AM 1.5 illumination with 100 mW/cm^2 light intensity, the performances of the device with the different strains were measured by a computer-controlled measurement system

The measuring system of the device is shown in Fig. 8.6. One end of the device was fixed tightly on a sample holder with the other end free to be mechanically bent. The tensile and compressive strains were produced by using a three-dimensional mechanical stage (the displacement resolution of 1 μm) to bend the free end of the device. Under AM 1.5 illumination with 100 mW/cm^2 light intensity, the performances of the device with the different strains were measured by a computer-controlled measurement system. To obtain a constant area of light illumination under the different strains, the applied strain was lower than 0.4 % to minimize the degree of deformations of the device. The device was illuminated by sunlight through the PS substrate, ZnO wire, P3HT and PDMS film. Figure 8.7(d) shows a photovoltaic performance of the device at different strains under the light illumination. The V_{oc} of the device without strains is 0.198 V, which is consistent with literature value of P3HT/ZnO solar cells (0.2 V) [4]. The V_{oc} decreases and increases with increasing tensile and compressive strains, respectively.

8.2.1 Piezopotential on the Solar Output

A schematic of the device is shown in Fig. 8.6(a) [5]. The PS substrate has a length of 4 cm, width of 8 mm, and thickness of 0.5 mm. The ZnO micro/nanowires were synthesized by a high-temperature thermal evaporation process, following the procedure described by Pan et al. [3]. The long ZnO microwires were chosen because they are easy to manipulate, but the same process applies to nanowires. To avoid the movement of ZnO wire in the electromechanical measurement process, the bottom at one end of the ZnO wire was fixed by a thin epoxy paint film on the PS substrate

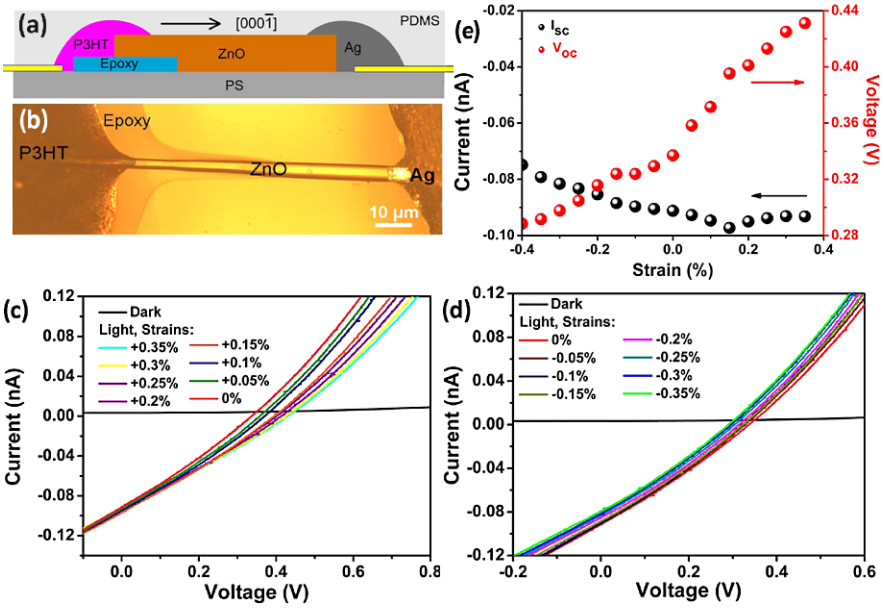

Fig. 8.7 (**a**) Schematic of a fabricated device of the [000$\bar{1}$] type. (**b**) Optical image of the fabricated device. (**c**), (**d**) *I*–*V* characteristics of the device under the tensile and compressive strain. (**e**) Dependence of I_{sc} and V_{oc} on applied strain [5]

under optical microscopy. The P3HT in C6H5Cl solution was then dropped on the fixed end of the ZnO wire to produce the p–n heterojunction. The other end of the ZnO wire was fixed by silver paste, serving as an electrode. The device was then packaged by a thin layer of PDMS to prevent the ZnO wire from contamination. Figure 8.6(b) shows an optical image of a fabricated device, showing that a smooth ZnO wire was connected by P3HT and silver paste on the substrate. The used ZnO micro/nanowires have a wurtzite structure and grow along the [0001] direction by the TEM analysis, as shown in Fig. 8.6(c).

Since the thickness and the length of the ZnO wire are much smaller than those of PS substrate, the bending of the PS substrate can produce solely a tensile or compressive strain in the ZnO wire, depending on its bending directions. The strains induced in the ZnO wire can be obtained by using the deformation of the substrate. The short-circuit current I_{sc} and V_{oc} under the different strains are shown in Fig. 8.6(e). The V_{oc} increases and decreases with increasing the compressive and tensile strains, respectively. However, the I_{sc} almost shows a constant value of 0.035 nA under the different strains.

Since ZnO has a non-central symmetric crystal structure with a polar direction along its *c*-axis, there are two ways to contact the P3HT with ZnO wire growing along [0001]. The first way is shown in Fig. 8.6(a), where the direction from P3HT to ZnO is along [0001]. The other way is shown in Fig. 8.6(a), where the direction from P3HT to ZnO is along [000$\bar{1}$]. Figure 8.7(b) shows an optical image of the

Table 8.1 The I_{sc}, V_{oc} at the different strains, and the corresponding $\Delta V_{oc}/V_{oc}$ of the fabricated 11 devices of [0001] and [000$\bar{1}$] types

Type	Sample	I_{sc} (nA) [0 strain]	V_{oc} (V) [0 strain]	V_{oc} (V) [**Compressive(-0.35%)** /tensile(0.35%) strain]	$\Delta V_{oc}/V_{oc}$ (max) [**Compressive(-0.35%)** /tensile(0.35%) strain]
[0001]	1	-0.035	0.198	**0.241**/0.178	**22%**/-10%
	2	-0.049	0.282	**0.332**/0.256	**18%**/-9%
	3	-0.050	0.262	**0.362**/0.236	**38%**/-10%
	4	-0.010	0.154	**0.195**/0.142	**21%**/-8%
	5	-0.093	0.363	**0.372**/0.353	**2%**/-3%
[000-1]	6	-0.090	0.337	0.292/**0.431**	-13%/**28%**
	7	-0.200	0.495	0.435/**0.559**	-12%/**25%**
	8	-0.246	0.268	0.257/**0.306**	-4%/**14%**
	9	-0.090	0.331	0.273/**0.383**	-18%/**16%**
	10	-0.151	0.378	0.313/**0.417**	-17%/**10%**
	11	-0.149	0.377	0.325/**0.423**	-14%/**12%**

fabricated device of the [000$\bar{1}$] type. As shown in Figs. 8.7(c) and (d), the *I*–*V* characteristics of the devices show an opposite changing trend with the applied strains as compared with those in Fig. 8.6(d). Figure 8.7(e) shows that the V_{oc} increases and decreases with increasing tensile and compressive strains, respectively. The I_{sc} shows almost a constant value of 0.09 nA under the tensile strain and a slight decrease under the compressive strain. We listed the measured results for a total of 11 fabricated devices in Table 8.1 for presenting the consistency of the measured data. The output power of the solar cells can be maximized by applying a proper strain in the device. When a -0.35 % strain is applied on the device, the V_{oc} can be enhanced by 38 % as compared with that without strain (Table 8.1). There are five devices of the [0001] case and six devices of the [000$\bar{1}$] case. It can be clearly seen that the tendencies of the change of V_{oc} with the strains are opposite for the two types of contact orientation.

8.2.2 Piezotronic Model

As a p–n heterojunction solar cell, the fabricated device can be described by a Shockley equivalent circuit [5]. The open-circuit voltage V_{oc} and the reverse saturation current I_0 can then be expressed as

$$V_{oc} = n\frac{kT}{e}\ln\left(\frac{I_{sc}}{I_0}\right), \tag{8.12}$$

$$I_0 = I_{00}\exp\left(\frac{-\Delta E}{rkT}\right) \tag{8.13}$$

where I_{sc} is the short-circuit current, I_{00} is a prefactor, r is an ideality factor, ΔE is the energy band difference between the conduction band of a n-type inorganic

material and the lowest unoccupied molecular orbit (LUMO) of a p-type organic material. By combining (8.12) and (8.13), the open-circuit voltage V_{oc} can be given by

$$eV_{oc} = \frac{n}{r}\Delta E + nkT \ln\left(\frac{I_{sc}}{I_{00}}\right). \tag{8.14}$$

Equation (8.14) indicates that the open-circuit voltage V_{oc} is associated with both the energy band difference ΔE and the short-circuit current I_{sc}. In our experiment, the I_{sc} is almost constant, and the change of V_{oc} suggests that ΔE may change at the junction area under different strains, in agreement with the result expected from the piezotronic model, to be presented in follows.

Usually, when the ZnO semiconductor material is subjected to strain, the change of the energy band at the interface is associated with the piezoresistance effect and piezoelectric effect. For the piezoresistance effect, it has been reported that the tensile strain in single ZnO wire along the direction of [0001] can decrease the band gap of ZnO, which could increase the ΔE and the V_{oc}. However, since the piezoresistance effect is a nonpolar and symmetric effect, it can only result in a similar trend of change of V_{oc} for the fabricated devices of [0001] and [000$\bar{1}$] types, which cannot explain the experimental results presented in Figs. 8.6 and 8.7. For the piezoelectric effect, it has been extensively reported that the strained ZnO micro/nanowire can change the local energy band profile, resulting in a modulation of *I*–*V* characteristics [6–8]. According to the fundamental theory of piezotronics [9], the energy band profile of p–n junction at the interface can be effectively tuned by the strain-induced piezoelectric polarization charges. The piezoelectric polarization charges modify the potential profile at the junction area, resulting in a change of energy band at the p–n junction [10].

We calculated the distribution of piezopotential in a single ZnO wire with a growth direction of [0001]/[000$\bar{1}$] by using the Lippman theory [11, 12], as shown in Fig. 8.8. For simplicity of the calculation, we ignore the doping in ZnO so that it is assumed to be an insulator. The diameter and length of ZnO wire are 1 μm and 10 μm, respectively. The tensile and compressive strains are 0.1 % and −0.1 %, respectively. Although the calculated piezopotential at the end of ZnO wire is up to 150 V, the actual piezopotential in ZnO is much lower due to the screening effect of the free charge carriers. When the ZnO wire was stretched along the *c*-axial direction, it can create a polarization of cations and anions along the *c*-axial direction and result in a piezopotential change from V_- to V_+ along the ZnO wire, as shown in Fig. 8.8(a). On the basis of the above discussions and calculation of the piezopotential, the modulation effect of the strain on the V_{oc} of the fabricated device, as shown in Figs. 8.6 and 8.7, can then be understood and explained by using the band diagram of the P3HT/ZnO heterojunction at the interface (Figs. 8.7(c) and (f)). Considering the result, shown in Fig. 8.8(a–e), that the P3HT is in contact only with the top side of the wire, we can build the following model for understanding our measured results. When the device of the [0001] type is under the tensile strain (Fig. 8.8(a)) or the device of the [000$\bar{1}$] type is under the compressive strains (Fig. 8.8(b)), the negative piezopotential is in contact with the P3HT. The negative piezoelectric polarization charges at the interface lift the local conduction band level of ZnO, which

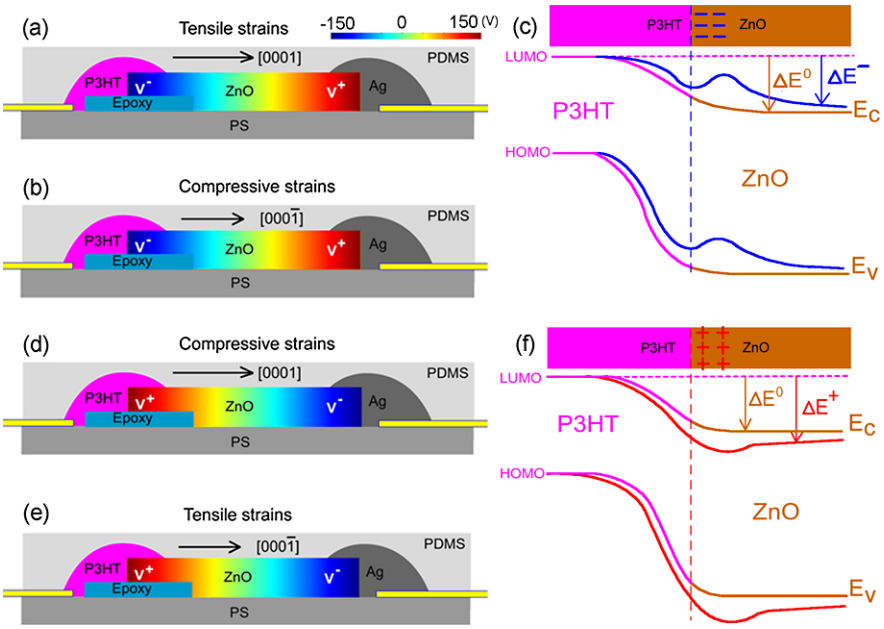

Fig. 8.8 (**a**), (**b**) The piezopotential distributions in the stretched device of [0001] type and compressed device of [000$\bar{1}$] type. (**c**) Schematic energy band diagram of P3HT/ZnO in the presence of negative piezoelectric charges. The *blue line* indicates the modified energy band diagram by the piezoelectric potential in ZnO. (**d**), (**e**) Calculated piezopotential distributions in the compressed device of [0001] type and stretched device of [000$\bar{1}$] type. (**d**) Schematic energy band diagram of P3HT/ZnO in the presence of positive piezoelectric charges. The *red line* represents the modified energy band diagram of ZnO under the compressive strain [5]

can result in a decrease of ΔE and V_{oc} according to (8.14) (as shown in Fig. 8.8(c)). Moreover, for the cases in Fig. 8.8, the positive piezoelectric polarization charges at the interface can lower the local conduction band level of ZnO, resulting in an increase of ΔE and V_{oc} (as shown in Fig. 8.8(f)).

8.3 Enhanced Cu_2S/CdS Coaxial Nanowire Solar Cells

The core-shell geometry of NWs is proposed to be able to enhance the efficiency of charge collection by shortening the paths traveled by minority carriers [13–15], increasing the optical quality of the material [16], or strain engineering of the bandgap [16]. However, the strain in the NW is a critical issue for such core-shell NW PV devices. First, for decreasing electron–hole interface recombination and increasing charge collection efficiency, a single crystal epitaxial p–n structure is highly desirable, but these epitaxial heterojunction NWs introduce static strain as a result of a misfit between the inherent crystal lattices between the core and shell materials.

Second, flexible PV devices have been the subject of research for powering flexible electronics and devices, which inevitably introduce strain during the operation. Thus, our goal here is to study the piezo-phototronic effect on the performance of piezoelectric PV devices made using single crystal epitaxial coaxial structures.

Our PV device is based on epitaxial coaxial NWs with p-Cu_2S as shell and n-CdS as core. CdS is a piezoelectric material with wurzite structure that has non-central symmetry. Due to the polarization of ions in CdS NW, a piezopotential is created by applying a stress. Owing to the simultaneous possession of piezoelectricity and semiconductor properties, the piezopotential created in the core has a strong effect on the carrier transport at the interface/junction, known as piezo-phototronic effect, which is to use the piezopotential created in the wurzite structure crystal to control the carrier generation, transport, separation, and/or recombination for improving the performance of optoelectronic devices. In this section, we tune the performance of the n-CdS/p-Cu_2S coaxial NW PV devices by the piezo-phototronic effect when the devices are subjected to strain, which offers a new concept for improving solar energy conversation efficiency [16].

8.3.1 Design of the Photovoltaic Device

The n-CdS NW is synthesized via a vapor–liquid–solid (VLS) method, which gives high-quality and long NWs. The morphology of the as-fabricated CdS NWs is presented in Fig. 8.9(a), with lengths of several hundreds of micrometers and diameters varying from tens of nanometers to several micrometers. Figure 8.9(b) is a low-magnification transmission electron microscopy (TEM) image of an individual as-fabricated n-CdS NW, showing a uniform shape of the NW. The epitaxial shell layer is obtained using a solution-based cation exchange reaction that creates a hetero-junction between the single-crystalline CdS core and single-crystalline Cu_2S shell. A high-resolution TEM (HRTEM) image and the selected area diffraction (SAD) pattern of a CdS/Cu_2S coaxial NW are presented in Figs. 8.9(c) and (d), respectively. It indicates that the growth direction of the coaxial NW is [0001] (c-axis), and the thickness of the shell layer is 10–15 nm. The enlarged image clearly shows high-quality epitaxial crystallinity at the interface of the coaxial NWs. Figure 8.9(e) is an in-situ energy-dispersive X-ray (EDX) line scan across the entire NW, which clearly shows that the Cu is located at the shell, while the Cd located at the core. Both the moiré fringes in the HRTEM image, the splitting of the diffraction spots (marked by the white arrows in Fig. 8.9(d)) and the EDX line scale profile confirm the core/shell hetero-epitaxial junction between the CdS core and Cu_2S shell.

The fabrication process of the coaxial CdS/Cu_2S NW PV devices is demonstrated in Fig. 8.10(a). First, we carefully chose a long CdS NW and dispersed it onto a polyethylene terephthalate (PET) or a polystyrene (PS) substrate; one end of the CdS NW was fixed by silver paste, serving as an electrode. After that a layer of epoxy was used to cover the silver-fixed side of the CdS, preventing Cu^+ from exchange in the following steps. Cation conversion was performed by dipping the

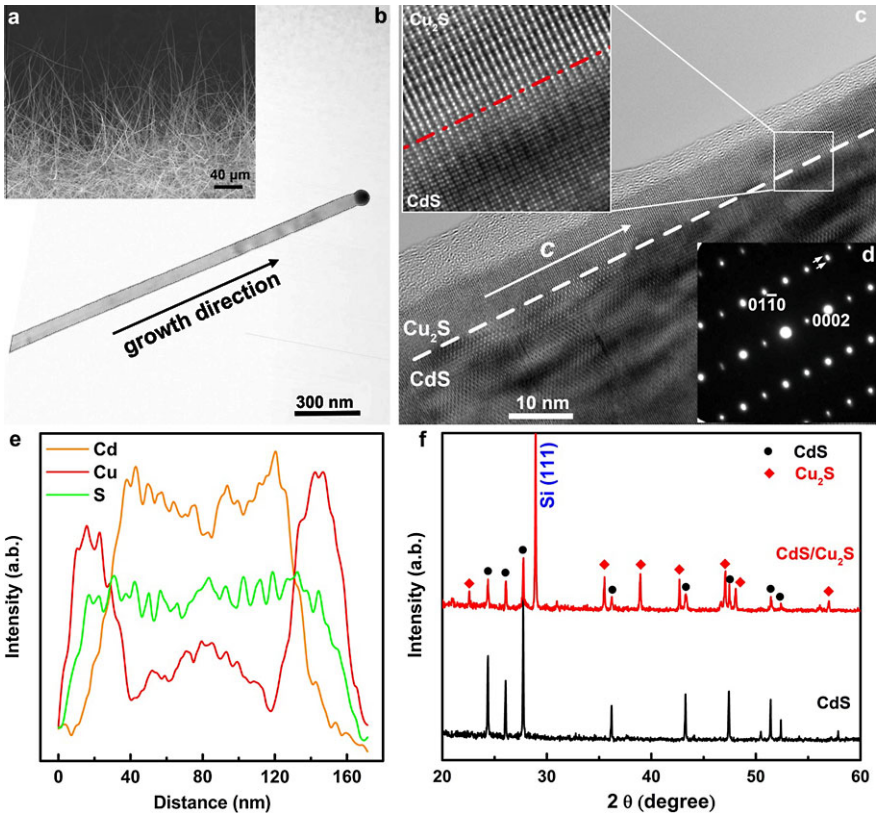

Fig. 8.9 Synthesis and characterization of the coaxial Cu_2S/CdS NWs. (**a**) SEM image of the morphology of the as-synthesized CdS NWs. (**b**) A low-magnification TEM image of an individual as-fabricated CdS NW, which is proved to be synthesized via a VLS method by the remaining gold catalyst on the tip of the NW. (**c**), (**d**), Representative high-resolution TEM image and electron diffraction pattern of the Cu^+ treated Cu_2S/CdS coaxial NWs. The *dashed line* indicates the interface between CdS and Cu_2S. The enlarged image clearly shows high-quality epitaxial crystalline at the interface of the coaxial NWs. (**e**) Line scan chemical profile across the NW acquired using the energy-dispersive X-ray spectroscopy (EDS), (**f**), X-ray diffraction spectra of CdS (the *black trace*) and Cu_2S/CdS coaxial NWs (the *red trace*). The peaks in the *red trace* marked with *black dots* belong to CdS core, and the peaks marked with *red dots* belong to Cu_2S shell. From [17]

CdS NW into CuCl solution at 50 °C for 10 s. It was then thoroughly rinsed with deionized water, ethanol and isopropanol (IPA) and blown dry with nitrogen. Subsequently, the other end of the coaxial NW was also fixed with silver paste, contacting with the p-Cu_2S layer. An oxygen plasma was carried out for improving the contact between CdS/Ag and Cu_2S/Ag before each step. Finally, the entire fabricated device is packaged with polydimethylsiloxane (PDMS), preventing the device from contamination and damage. An optical microscope image of an as-fabricated device is shown in Fig. 8.10(b).

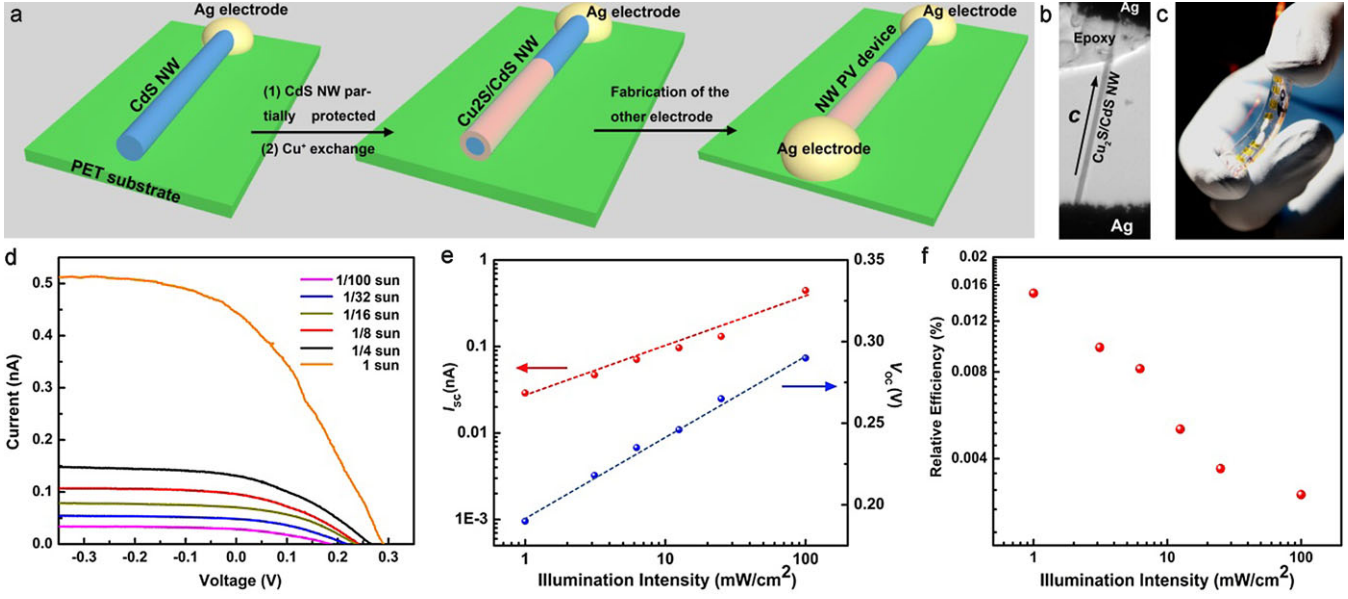

Fig. 8.10 Fabrication and characterization of CdS-Cu_2S core-shell nanowire PV devices. (**a**) Schematic of the fabrication process. From left to right, a CdS (*blue*) NW with metal contact at one end is partially immersed into CuCl solution to form a layer of Cu_2S (*pink*) shell, and then metal contact at the other end was fabricated on the Cu_2S shell. The polymer masking step is not shown. (**b**), (**c**) Optical microscopy and digital image of a typical PV device. (**d**) *I–V* characteristic of a core-shell nanowire PV device under an illumination from 1 percent sun to a full sun (AM 1.5). (**e**) Light intensity dependence of the photocurrent (I_{sc}) and open-circuit voltage (V_{oc}). (**f**) Light intensity dependence of the conversion efficiency (η). From [17]

The as-measured *I–V* characteristic of the coaxial NW PV devices under different illumination intensities is presented in Fig. 8.10(c). This nanowire PV devices were 225 μm long and 5.8 μm in diameter, and yielded a short-circuit current I_{sc} of 0.44 nA under a full-sun intensity. The performance of the PV device dropped with the illumination intensity decreasing from a full sun to 1 percent of a sun: the short-circuit current I_{sc} dropped from 0.44 to 0.03 nA, while the open-circuit voltage (V_{oc}) dropped from 0.29 to 0.19 V, with a rate ($\Delta V_{oc}/\Delta \ln(I_{illum}) =$ 50 mV, where I_{illum} is the relative illumination intensity), comparable to that of the silicon nanowire[2] ($\Delta V_{oc}/\Delta \ln(I_{illum}) = 56$ mV) and Cu_2S thin film PVs[24] ($\Delta V_{oc}/\Delta \ln(I_{illum}) = 39$ mV). The corresponding relative conversion efficiency (conversion efficiency/illumination intensity) under different illumination intensities is plotted in Fig. 8.10(e). The higher relative convention efficiency under low illumination conditions implies that our PV devices may be suitable for some special working conditions, such as in indoor applications. The main reason is that the charge collection efficiency is higher for the PV devices under low light intensity. When the light intensity is low, the amount of the light-generated electron–hole pairs is small, it can be sufficiently separated with low carrier recombination at the interface; but at a high light intensity, there are a large numbers of light-generated electron–hole pairs, which cannot be sufficiently separated, and this results in a high recombination at the interface. The performance of such coaxial CdS/Cu_2S NW PV devices can be increased by optimizing the design, structure, doping, semiconductor/metal contacts, working condition, and so on. Tang et al. reported a very high FF PV device with the output performance of: $V_{oc} = 0.61$ V, $I_{sc} = 147$ pA, $FF = 80.8$ % and $\eta = 5.4$ %, this will let such kind of PV devices have bright future in the practical application.

8.3.2 Piezo-Phototronic Effect on the Output

To investigate the piezo-phototronics effect on the PV devices, the PV devices were subjected to compressive strain, and the results are presented in Figs. 8.11 and 8.12. The schematic of the measurement set-up for studying the piezo-phototronic effect PV devices is demonstrated as in the insert upper-right in Fig. 8.11(a). One end of the PS substrate was fixed tightly on a manipulation holder, with the other end free to be bent. A three-dimensional (3D) mechanical stage with movement resolution of 1 μm was used to apply the strain on the free end of the PS substrate, to introduce a compressive or tensile strain.

Due to the asymmetric polarity of the CdS NW, there are two different configurations of our CdS/Cu_2S NW PV devices when the *c*-axis of the CdS NW pointing upward: one is Cu_2S shell only located at the upper part of the CdS NW, denoted as configuration I (Fig. 8.13(d)); the other is Cu_2S shell only located at the lower part of the CdS NW, denoted as configuration II (Fig. 8.13(g)). The piezo-phototronic effect on a PV device with configuration I is illustrated in Fig. 8.11: these nanowire PV devices were 220 μm long and 4.95 μm in diameter, and yielded a I_{sc} of 0.25 nA

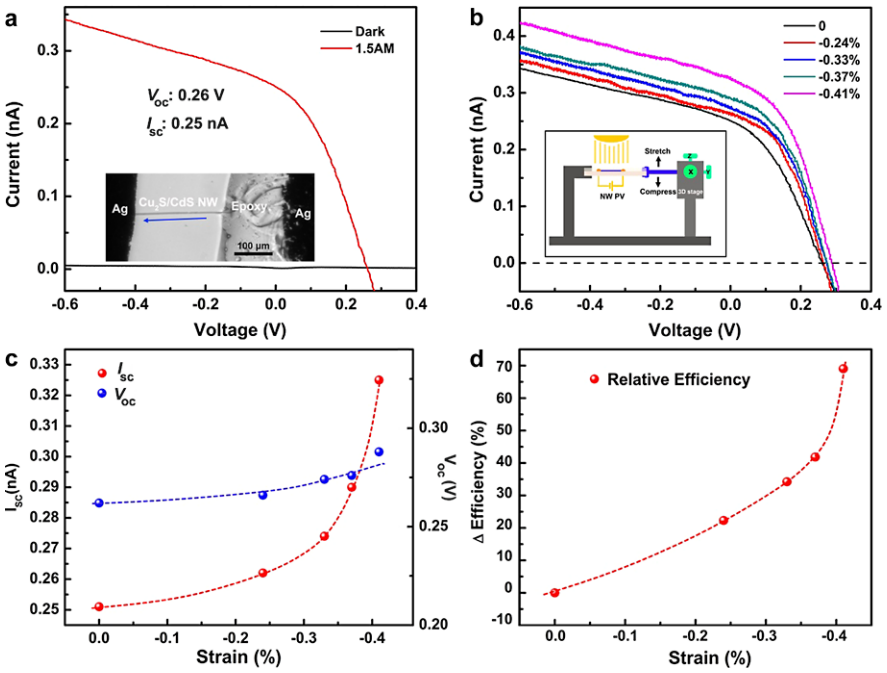

Fig. 8.11 The performance of the Cu_2S/CdS coaxial NW solar cell under compressive strains. (**a**) The dark and 1.5 AM illuminated *I–V* curve of the NW solar cell. The short-circuit current is 0.25 nA, the open-circuit voltage is 0.26 V without applied strain. The *inset* is an optical microscopy image of the Cu_2S/CdS coaxial NW solar cell. (**b**) The *I–V* curve of the same NW solar cell under different compressive strain, clearly indicating the current increase with increasing external compressive strain. The schematic of the measurement set-up for studying the piezo-phototronic effect PV devices is demonstrated as *inset*. (**c**), (**d**), Dependence of the open-circuit voltage (**c**), the short-circuit current (**c**) and relative efficiency change (**d**) on the strain. The data plotted in (**c**) and (**d**) are extracted from (**b**). From [17]

and V_{oc} of 0.26 V under a full-sun intensity (Fig. 8.11(a)). The *I–V* curves of the PV device subjected to strains were presented in Fig. 8.11(b). The performance of this PV device was enhanced when the PV device was subjected to a compressive strain up to −0.41 %, and the I_{sc} and the V_{oc} under different strains were extracted and plotted in Fig. 8.11(c). It can be found that the I_{sc} increased from 0.25 to 0.33 nA, about 32 % incensement; while the V_{oc} varying between 0.26 and 0.29 V, about 10 % fluctuation. As dominated by the enhancement of the output current, the relative convention efficiency change of this PV device increased about 70 % when a −0.41 % compressive strain was applied (Fig. 8.11(d)).

The piezo-phototronics effect on another PV device with configuration II is illustrated in Fig. 8.12, which is 328 μm long and 6.7 μm in diameter, and yielded a I_{sc} of 3.47 nA and V_{oc} of 0.54 V under a full-sun intensity (Fig. 8.12(a)). Different from the previous one, the performance of this device dropped when the applied compressive strain was increased, as shown in Fig. 8.12(b). The I_{sc} and the V_{oc}

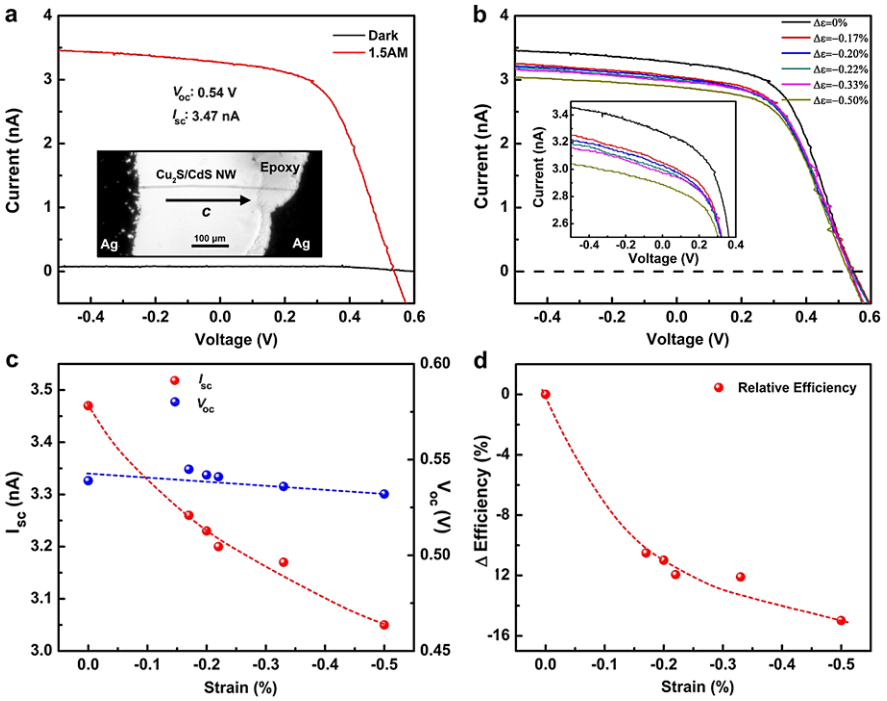

Fig. 8.12 The performance of the Cu_2S/CdS coaxial NW solar cell under compressive strains. (**a**) The dark and 1.5 AM illuminated *I–V* curve of the NW solar cell. The short-circuit current is about 3.47 nA, the open-circuit voltage is 0.54 V without applied strain. The *inset* is an optical microscopy image of the Cu_2S/CdS coaxial NW solar cell. (**b**) The *I–V* curve of the same NW solar cell under different compressive strain. The *inset* is an enlarged plot of the *I–V* curve, clearly indicating the current decrease with increasing external compressive strain. (**c**), (**d**) Dependence of the open-circuit voltage (**c**), the short-circuit current (**c**) and relative efficiency change (**d**) on the strain. The data plotted in (**c**) and (**d**) are extracted from (**b**). From [17]

under different strains were extracted and plotted in Fig. 8.11(c). It can be found that the I_{sc} dropped from 3.47 to 3.05 nA for nearly 14 %; while the V_{oc} varying between 532 and 545 mV, only 2 % fluctuation. As a result of the decreasing of the output current, the energy convention efficiency decreased about 15 % when a 0.5 % compressive strain was applied. By comparing the two NW PVs shown in Figs. 8.11 and 8.12, we found that such a piezo-phototronics effect has larger impact/enhancement on a PV of lower FF and lower efficiency. For example, the performance increases about 70 % for the PV shown in Fig. 8.11, which has a lower output performance, while the performance only changes 15 % for the PV shown in Fig. 8.12, which has a higher output performance. Such enhanced performance of the PV devices under a compressive strain is suggested arising from the effective decrease of the barrier height between Cu_2S and CdS at the heterojunction interface [17] as a result of the band modification caused by piezoelectric polarization charges, as discussed in what follows.

8.3.3 Theoretical Model

A theoretical model is proposed to explain the piezo-phototronic effect on the performance of the PV devices using energy band diagrams, as shown in Fig. 8.13. CdS has a non-central symmetric wurzite structure, in which the cations and anions are tetrahedrally coordinated. A straining on the basic unit results in a polarization of the cations and anions, which is the cause of the piezopotential inside the crystal. For a coaxial n-CdS/p-Cu_2S NW PV device, schematic structure, numerically calculated piezopotential distribution and the corresponding energy band diagram (with a barrier at the interface [16]) of a strain-free coaxial piezoelectric NW PV device are presented in Fig. 8.13(a)–(c), respectively. For a typical PV device, there are three key processes for dictating its performance as shown in Fig. 8.13(c): (I) generation rate of the electron–hole pairs under the illumination; (II) separation efficiency of the generated electron–hole pairs, with electrons traveling toward the CdS side, and the holes toward the Cu_2S side; and (III) recombination rate between electrons and holes. For a certain PV device, the output voltage is nearly a constant, which depends on illumination intensity and temperature ($V_{oc} = (E_{fn} - E_{fp})/q$), where E_{fn} and E_{fp} are the quasi-Fermi level of the electrons and holes under illumination, and q is the electron charge, if the illumination intensity, working temperature, and the doping level of the p–n junction are fixed. In such case, the number of the light-generated electron–hole pairs is a constant. Thus, the performance of the PV device is mainly determined by the carrier separation, transport, and recombination processes.

Since the p-Cu_2S shell is non-piezoelectric and its size is only 10–15 nm, heavily doped, much thinner than the diameter of the CdS core (up to tens of micrometers, such as 5.8 μm of the device in Fig. 8.10(d)), our discussions mainly focus on the piezoelectric effect from the CdS core. With the assumption of low doping in CdS for simplicity, numerically calculated piezopotential distribution in the CdS/Cu_2S core-shell NWs shows that a potential drop is created along its length when the CdS NW is under c-axis strain (Fig. 8.13(e) and (h)). For a PV device with configuration I as shown in Figs. 8.11 and 8.13(d), the local positive piezoelectric charges at the Cu_2S/CdS interface (Fig. 8.13(e)) will lower the conduction and valence bands of CdS, as labeled in Fig. 8.13(f), resulting in a decrease of the barrier height at the heterojunction interface. This is equivalent to increase of the depletion width and internal field, which will accelerate the electron–hole pair separation process and reduce the possibility of recombination, thus enhancing the performance of the PV with the increase of the applied compressive strain. For a PV device with configuration II as shown in Figs. 8.12 and 8.13(g), the effect of the local negative piezopotential at the Cu_2S/CdS interface (Fig. 8.13(h)) will lift up the conduction and valence bands of CdS, as labeled in Fig. 8.13(i), resulting in an increase of the barrier height at the heterojunction interface. This is equivalent to decrease the depletion width and internal field, which will make the electron–hole pair more difficult to separate and thus increase the possibility of recombination. Subsequently, the output current and the convention efficiency are decreased when the device is compressively strained. This is the basic mechanism of how does the piezo-phototronic effect tunes the output efficiency of a solar cell.

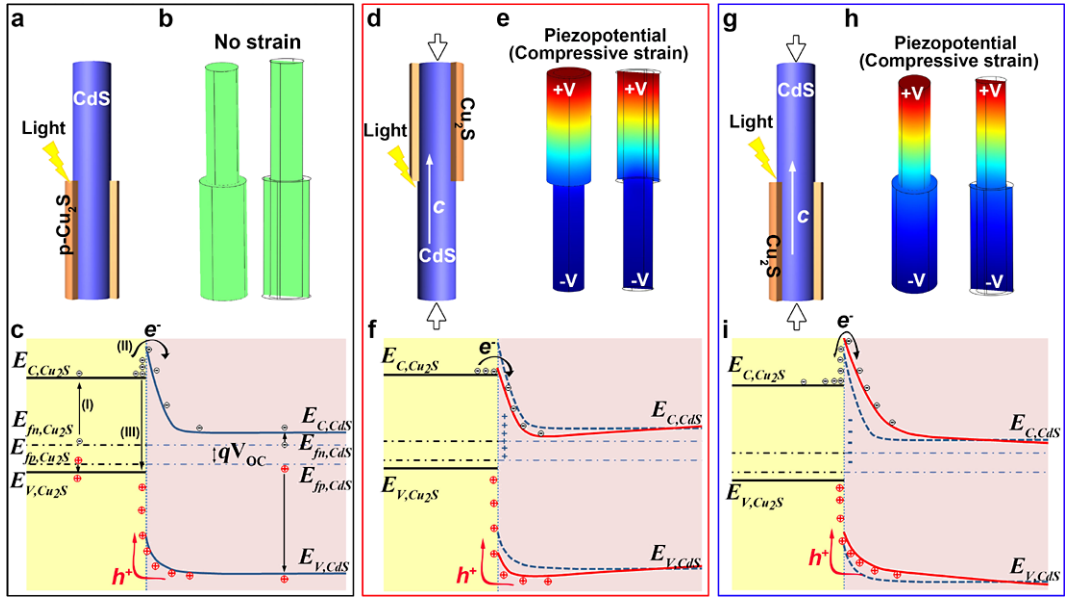

Fig. 8.13 Schematics and energy band diagrams demonstrate the piezo-phototronic effect on coaxial piezoelectric nanowire solar cells. (**a**)–(**c**) Schematics (**a**), numerically calculated piezopotential distribution ((**b**), both the tilt-view (*left*) and cross section-view (*right*)) and the corresponding energy band diagram (**c**) of a strain-free coaxial piezoelectric NW solar cell. (**d**), (**f**) Schematics (**g**), numerically calculated piezopotential distribution (**h**) and the corresponding energy band diagram (**i**) of a coaxial piezoelectric NW solar cell under compressive strain for a PV device with configuration (**i**). The upper part of the CdS NW is positively charged, while the lower part is negatively charged due to the piezoelectric potential under compressive strain. The positive charges at CdS side lower the conduction and valence bands of CdS at the interface of the p–n junction, which decrease the barrier height at the interface of the heterojunction, resulting in an enhancement of the PV performance. (**g**)–(**i**) Schematics (**d**), numerically calculated piezopotential distribution (**e**) and the corresponding energy band diagram (**f**) of a coaxial piezoelectric NW solar cell under compressive strain for a PV device with configuration II. The negative charges at the CdS/Cu_2S interface lift up the conduction and valence band of CdS at the interface of the p–n junction, thus resulting in a drop of the PV device. The *dashed line* in (**f**) and (**i**) represents the original conduction and valence band of the piezopotential along the coaxial nanowires. From [17]

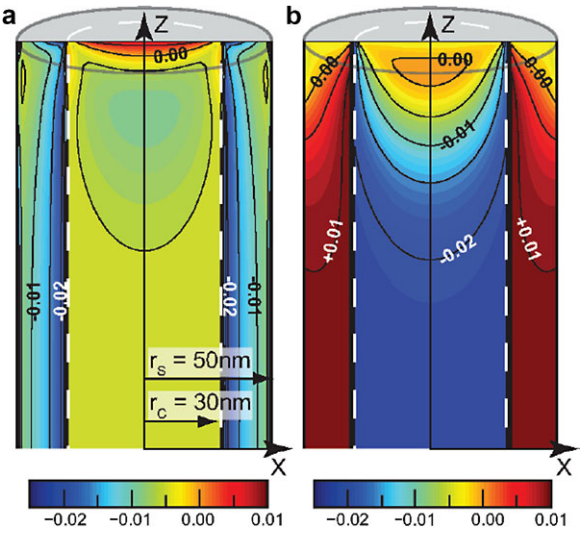

Fig. 8.14 Elastic strain components (**a**) ε_{xx} and (**b**) ε_{zz} at an x–z cross section of a core-shell NW. The NW is oriented along the [111] crystallographic direction and consists of a cylindrical InAs core and a surrounding InP shell. The length of the core-shell NW is $L_z = 350$ nm, the radius of the core is $r_c = 30$ nm, and the outer radius of the shell is $r_s = 50$ nm. Due to the symmetry, the strain components only in half of the core-shell NW are shown (Figure courtesy of Boxberg et al. [18])

8.4 Solar Efficiency of Heterostructured Core-Shell Nanowires

Epitaxial core-shell NWs grown with different materials acquire in general elastic strain as a result of a misfit between the inherent crystal lattices of the core and shell materials. Such a static and internally built strain can create piezoelectric polarization in the NW. Xu's group has theoretically investigated the piezopotential created in a core-shell NWand its possibility for solar cell application [18]. A model system is a III–V zinc blende (ZB) with NWs grown along the [111] direction and III–V wurtzite (WZ) NWs grown along the [0001] direction. Thus, the z-axis in is equal to the [111] direction of the ZB structure or the [0001] direction of the WZ structure. The [101-1] direction of the ZB structure or the a-axis of the WZ structure as the x axis of the coordinate system.

Figure 8.14 shows the numerically computed ε_{xx} and ε_{zz} in a ZB core-shell (InP) NW oriented core (InAs) along the [111] crystallographic direction. The considered NW consists of a cylindrical InAs core and a surrounding InP shell, with the length L_z of 350 nm, the radius of the core r_c of 30 nm, and the outer radius of the shell r_s of 50 nm. Figures 8.14(a) and (b) show the strain distributions at an x–z cross section of the NW. The strain components ε_{xx} and ε_{yy} are very similar except for a rotation of $\pi/2$ around the z axis. The strain is reduced considerably via surface bulging at an end of the NW. The strain components, ε_{xx} and ε_{yy}, are constant deep inside the NW only within the core, whereas ε_{zz} becomes stepwise constant far from the NW ends.

The lattice-mismatch-induced strain in an epitaxial core-shell nanowire gives rise to an internal electric field along the axis of the nanowire. This piezoelectric field results predominantly from atomic layer displacements along the nanowire axis within both the core and shell materials and can appear in both zinc blende and wurtzite crystalline core-shell nanowires. The effect can be employed to separate photon-

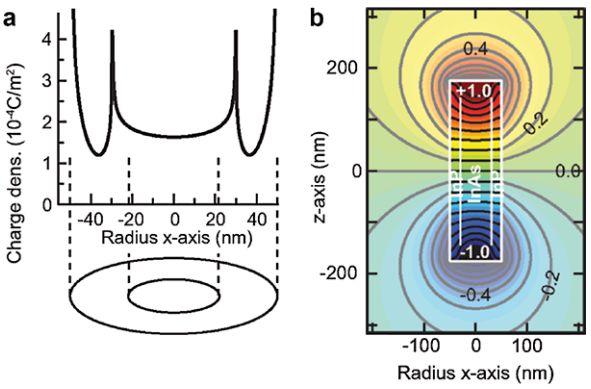

Fig. 8.15 (**a**) Effective surface charge density and (**b**) piezoelectric potential in a cylindrical InAs/InP WZ core-shell NW in vacuum. The surface charge density in (**a**) is evaluated at the In-terminated end of the NW (the upper end of the NW shown in (**b**)). The labels of the potential isosurfaces in (**b**) are given in volts (Figure courtesy of Boxberg et al. [18])

generated electron–hole pairs in the core-shell nanowires and thus offers a new device concept for solar energy conversion [18].

Figure 8.15(a) shows the numerically computed effective piezoelectric surface charge density at an end surface of a WZ core-shell NW. The effective charge is positive at the A end surface and negative at the B end surface of the InAs/InP core-shell NW. The effective surface charge density diverges at the material interface where the relative permittivity is discontinuous. However, the integrated effective charge remains finite. Figure 8.15(b) shows the piezoelectric potential at an x–z cross section of a core-shell NW in vacuum. Figure 8.15(b) shows a clear dipole-like potential landscape. The internal piezoelectric field becomes practically constant in this sufficiently long NW. This is consistent with the charge densities presented in Fig. 8.15(a) and supports the analytical model of the piezoelectric field. The axial piezoelectric field present in strained compound semiconductor core-shell nanowires can be exploited for efficient solar energy conversion.

Figure 8.16(a) depicts the photovoltaic mechanism in a strained core-shell NW. Here, the piezoelectric field is employed for generating a photocurrent from one end of the NW to the other. The magnitude of the field (i.e., the slope of the band edge energies in the middle section of the NW shown in Fig. 8.16(a)) can be comparable to that of a typical built-in field in a p–n junction diode and is widely tunable, not only by combining different core and shell materials, but also by varying the thickness of the shell with respect to the diameter of the core. However, we note that the maximum effective built-in potential in a strained, piezoelectric semiconductor NW is limited by the band gap energy E_g of the materials (as in traditional p–n junction diodes). The conduction band and valence band edges will be flattened by charge accumulations or pinned to the Fermi energy of the contacts at the two ends of a core-shell NW. The maximum length of the active region of a piezoelectric core-shell NW diode is, consequently, a function of the piezoelectric field strength E_z and the band gap energy E_g and is given by $L_m = E_g/(eE_z)$, where e is the electron charge. Figure 8.16(b) shows an example of how arrays of piezoelectric core-shell NWs could be electrically contacted and deployed for large area solar cells. Here, it is assumed that the array of piezoelectric core-shell NWs is grown on a heavily doped semiconductor substrate. After a suitable transparent material is

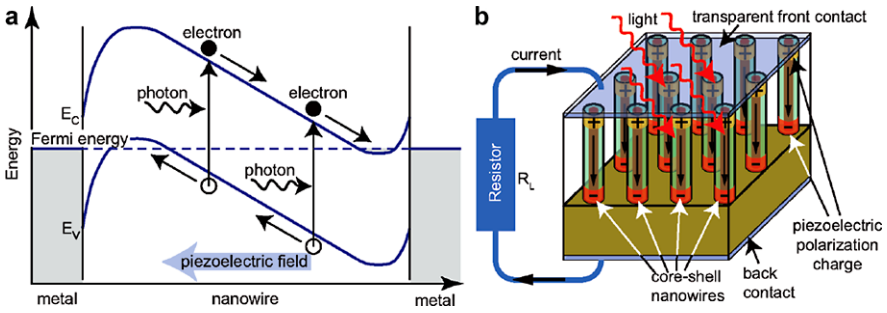

Fig. 8.16 (**a**) Schematic description of the band diagram within an electrically contacted n-type NW core and photovoltaic operation principle of a strained piezoelectric core-shell NW. The slope of the conduction (E_c) and valence (E_v) band edges in the middle segment of the NW is caused by the piezoelectric field. The band bendings at the ends of the NW represent typical effects of charge exchanges at metal–semiconductor interfaces. (**b**) Schematic diagram for a core-shell NW solar cell device, where piezoelectrically polarized NWs are grown vertically on a conductive substrate. For a further description of the device operation, see the main text (Figure courtesy of Boxberg et al. [18])

added, a transparent conducting film is deposited on top as a front contact. When the sunlight is incident on the device, electron–hole pairs will be generated in the NWs. These photon-generated electron–hole pairs may be separated by the piezoelectric fields present in the NWs, and thus a photovoltage between the front and back contacts, or a photocurrent in the circuit as shown in Fig. 8.16(b) will be created. In comparison with previously proposed NW photovoltaic devices, this design does not require the fabrication of a p–n junction in the NWs, which leads to a technology advantage in the device fabrication. Nevertheless, the axial p–n junctions could be integrated into the core-shell NWs to achieve enhancement of solar energy conversion. Such a theoretical prediction remains to be verified by experiments.

8.5 Summary

In summary, we have elaborated of how to use the inner crystal generated piezopotential by strain to enhance the photon to electricity conversion process. We have presented new approaches for fabricating high-efficiency solar cells using piezophototronic effect. The first example is a metal–semiconductor–metal back-to-back Schottky contacted ZnO microwire device. An externally applied strain produces a piezopotential in the microwire, which tunes the effective Schottky barrier (SB) height of the microwire at the local contact, consequently changing the electrical parameter of the device. By properly tuning the strain in a device, it is possible to maximize the output power of a photocell, light emitting diode and solar cells.

In the second example, using P3HT/ZnO micro/nanowire p–n heterojunction on a PS substrate as a model system, we have demonstrated the effect of piezopotential on the output voltage of the flexible solar cells. The strain-induced piezopotential is

created under an externally applied strain as a result of the piezotronic effect, which tunes the energy band profile at the interface of p–n heterojunction, consequently modulating the performance of the device. The output power of solar cells could be enhanced by tuning the strains in the devices. Our study not only adds further understanding about piezotronic devices, but also shows that it can be applied to enhance their performance of solar cells fabricated by using wurtzite structured materials.

In the last example, we demonstrated largely enhanced performance of n-CdS/p-Cu_2S coaxial NW PV devices using the *piezo-phototronics effect* when the PV device is subjected to an external strain. The piezo-phototronic effect could control the electron–hole pair generation, transport, separation, and/or recombination, thus tuning the performance of the PV devices: when the p–n junction is parallel to the *c*-axis of the NW (configure I), the PV performance enhances with increasing the compressive strain, but decreases with increasing the tensile strain. This effect offers a new concept for improving solar energy conversation efficiency by designing the orientation of the nanowires and the strain to be purposely introduced in the packaging of the solar cells. This study shed light on the enhanced flexible solar cells for applications in self-powered technology, environmental monitoring, and even defensive technology.

References

1. Z.Y. Gao, J. Zhou, Y.D. Gu, P. Fei, Y. Hao, G. Bao, Z.L. Wang, Effects of piezoelectric potential on the transport characteristics of metal–ZnO nanowire–metal field effect transistor. J. Appl. Phys. **105**(11), 113707 (2009)
2. Y.F. Hu, Y. Zhang, Y.L. Chang, R.L. Snyder, Z.L. Wang, Optimizing the power output of a ZnO photocell by piezopotential. ACS Nano **4**(8), 4962 (2010)
3. Z.W. Pan, Z.R. Dai, Z.L. Wang, Nanobelts of semiconducting oxides. Science **291**, 1947–1949 (2001)
4. Y. Vaynzof, D. Kabra, L. Zhao, P.K.H. Ho, A.T.S. Wee, R.H. Friend, Improved photoinduced charge carriers separation in organic–inorganic hybrid photovoltaic devices. Appl. Phys. Lett. **97**(3), 033309 (2010)
5. Y. Yang, W.X. Guo, Y. Zhang, Y. Ding, X. Wang, Z.L. Wang, Piezotronic effect on the output voltage of P3HT/ZnO micro/nanowire heterojunction solar cells. Nano Lett. **11**(11), 4812–4817 (2011)
6. J. Zhou, Y.D. Gu, P. Fei, W.J. Mai, Y.F. Gao, R.S. Yang, G. Bao, Z.L. Wang, Flexible piezotronic strain sensor. Nano Lett. **8**(9), 3035–3040 (2008)
7. Q. Yang, X. Guo, W.H. Wang, Y. Zhang, S. Xu, D.H. Lien, Z.L. Wang, Enhancing sensitivity of a single ZnO micro-/nanowire photodetector by piezo-phototronic effect. ACS Nano **4**(10), 6285–6291 (2010)
8. J. Zhou, P. Fei, Y.D. Gu, W.J. Mai, Y.F. Gao, R.S. Yang, G. Bao, Z.L. Wang, Piezoelectric-potential-controlled polarity-reversible Schottky diodes and switches of ZnO wires. Nano Lett. **8**(11), 3973–3977 (2008)
9. Y. Zhang, Y. Liu, Z.L. Wang, Fundamental theory of piezotronics. Adv. Mater. **23**(27), 3004–3013 (2011)
10. Z.L. Wang, Piezopotential gated nanowire devices: piezotronics and piezo-phototronics. Nano Today **5**, 540–552 (2010)
11. Y.F. Gao, Z.L. Wang, Electrostatic potential in a bent piezoelectric nanowire. The fundamental theory of nanogenerator and nanopiezotronics. Nano Lett. **7**(8), 2499–2505 (2007)

12. Z.Y. Gao, J. Zhou, Y.D. Gu, P. Fei, Y. Hao, G. Bao, Z.L. Wang, Effects of piezoelectric potential on the transport characteristics of metal–ZnO nanowire–metal field effect transistor. J. Appl. Phys. **105**(11), 113707 (2009)
13. D.R. Kim, C.H. Lee, P.M. Rao, I.S. Cho, X.L. Zheng, Hybrid Si microwire and planar solar cells: passivation and characterization. Nano Lett. **11**(7), 2704–2708 (2011)
14. C.F. Pan, Z.X. Luo, C. Xu, J. Luo, R.R. Liang, G. Zhu, W.Z. Wu, W.X. Guo, X.X. Yan, J. Xu, Z.L. Wang, J. Zhu, Wafer-scale high-throughput ordered arrays of Si and coaxial $Si/Si_{1-x}Ge_x$ wires: fabrication, characterization, and photovoltaic application. ACS Nano **5**(8), 6629–6636 (2011)
15. J.A. Czaban, D.A. Thompson, R.R. LaPierre, GaAs core–shell nanowires for photovoltaic applications. Nano Lett. **9**(1), 148–154 (2009)
16. C.F. Pan, S.M. Niu, Y. Ding, L. Dong, R.M. Yu, Y. Liu, G. Zhu, Z.L. Wang, Enhanced Cu2S/CdS coaxial nanowire solar cells by piezo-phototronic effect. Nano Lett. **12**(6), 3302–3307 (2012)
17. T.S. Tevelde, Mathematical analysis of a heterojunction, applied to the copper sulphide–cadmium sulphide solar cell. Solid-State Electron. **16**(12), 1305–1314 (1973)
18. F. Boxberg, N. Søndergaard, H.Q. Xu, Photovoltaics with piezoelectric core–shell nanowires. Nano Lett. **10**(4), 1108–1112 (2010)

Chapter 9
Piezo-Phototronic Effect on Photodetector

Abstract An effective electron–hole separation at a Schottky contact or p–n junction is important for the efficiency of a photon detector. In this chapter, we demonstrate how the piezo-phototronic effect can be used to largely improve the responsivity of a photon detector in a whole range from visible to UV. After a systematic study on the Schottky barrier height change with tuning the strain and the excitation light intensity, an in-depth understanding is provided about the physical mechanism of the coupling of piezoelectric, optical and semiconducting properties. Our results show that the piezo-phototronic effect can enhance the detection sensitivity more than fivefold for pW levels light detection.

The core of the piezo-phototronic devices are to use the internal piezoelectric field to tune the charge generation, separation, transport and/or recombination process at the interface for enhancing optoelectronic processes. In this chapter, we demonstrate the piezo-phototronic effect on the sensitivity of nanowire-based photodetector [1]. The responsivity of a ZnO-based photodetector is, respectively, enhanced by 530 %, 190 %, 9 % and 15 % upon 4.1 pW, 120.0 pW, 4.1 nW, 180.4 nW UV light illumination onto the wire by introducing a −0.36 % compressive strain in the wire. After a systematic study on the Schottky barrier height change with tuning the strain and the excitation light intensity, an in-depth understanding is provided about the physical mechanism of the coupling of piezoelectric, optical and semiconducting properties. Later, this idea is also extended to visible light detection using CdS nanowires. Our results show that the piezo-phototronic effect can enhance the detection sensitivity more than fivefold for pW levels light detection.

9.1 Design of Measurement System

Our device is a metal–semiconductor–metal structure (MSM). The contacts at the two ends of the semiconductor wire are two back-to-back Schottky contacts. The device was fabricated by bonding a ZnO micro/nanowire laterally on a polystyrene (PS) substrate, which has a thickness much larger than the diameter of the ZnO micro/nanowire (see Experimental for details). The experimental setup is shown

Z.L. Wang, *Piezotronics and Piezo-Phototronics*, Microtechnology and MEMS,
DOI 10.1007/978-3-642-34237-0_9, © Springer-Verlag Berlin Heidelberg 2012

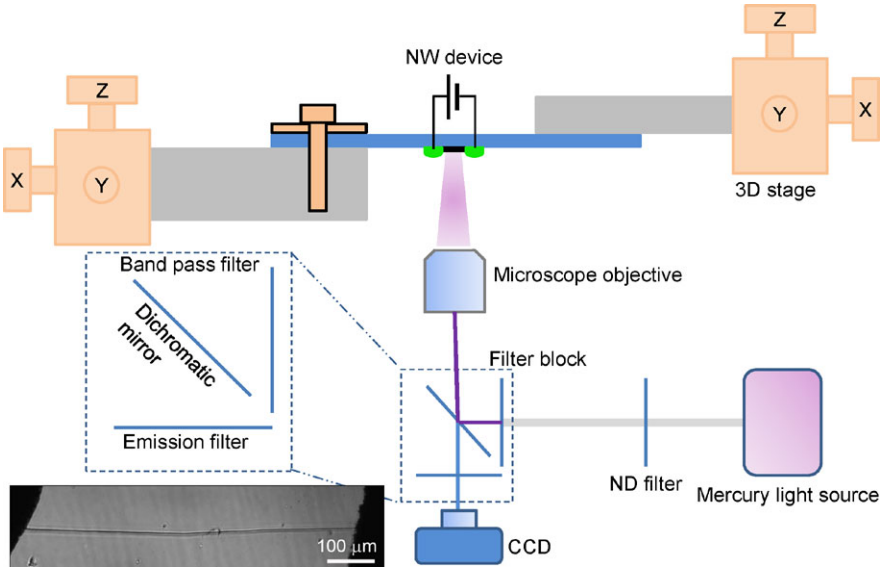

Fig. 9.1 Schematic diagram of the measurement system to characterize the performance of the piezopotential tuned photodetector. An optical microscopy image of a ZnO wire device is shown [1]

schematically in Fig. 9.1. The mechanical behavior of the device was dominated by the substrate by considering the relative size of the wire and the substrate. The strain in the wire was mainly axial compressive or tensile strain depending on the bending direction of the PS substrate, and it was quantified by the maximum deflection of the free end of the substrate. The optical image of the photodetector shown in Fig. 9.1 indicates that a smooth ZnO wire was placed on the substrate with two-end fixed. Monochromatic UV, blue or green light was illuminated on the ZnO wire to test the performance of the device.

The ZnO micro/nanowires used in our study were synthesized by a high-temperature thermal evaporation process [2]. The detailed device fabrication process was introduced elsewhere [3]. Briefly, single ZnO wire was bonded on PS substrate (typical length of ~7 cm, width of ~15 mm and thickness of 0.5 mm) by silver pastes. A very thin layer of polydimethylsiloxane (PDMS) was used to package the device, which kept the device mechanically robust under repeated manipulation and prevented the semiconductor wire from contamination or corrosion. A 3D stage with movement resolution of 1 μm was used to bend the free end of the device to produce a compressive and tensile strain. Another 3D stage was used to fix the sample under microscope and to keep the device in focus during the substrate bending process.

Nikon Eclipse Ti inverted microscope system was used to monitor the sample and excite the photodetector. A Nikon Intensilight C-HGFIE lamp with a remote controller was used as the excitation source. Monochromatic UV (centered at 372 nm), blue (centered at 486 nm) or green light (centered at 548 nm) was illuminated on the ZnO wire to test the performance of the device, which was focused by a 10X micro-

scope objective with a 17.5 mm work distance. Monochromatic light was obtained by a filter block between the source and microscope objective (Fig. 9.1). There were three sets of filter blocks which were used to obtain monochromatic UV, blue, and green light. The optical power density impinging on the nanowire photodetector was varied by means of neutral density filters. The illumination density was determined by a thermopile power meter (Newport 818P-001-12). I–V measurement was done by applying an external bias to the wire and recording using a Keithley 487 picoammeter/voltage source in conjunction with a GPIB controller (National Instruments GPIB-USB-HS, NI 488.2). In order to compare and analyze the results, time dependent photocurrent, light intensity dependent photocurrent and photocurrent used for analyzing responsivity and strain effects were measured at a fixed applied bias of −5 V.

9.2 Characterization of the Fabricated UV Sensor

Before the electromechanical and optical measurements, we first measured the original I–V characteristics of the device in the dark condition. Various I–V characteristics were found in the experiments. In this study, we only focused on the devices that have symmetric Schottky contacts at the two ends of the ZnO wire and have very low dark-current characteristics, which ensures low noise and ultrasensitivity of the photodetector. The results of photocurrent measurements performed on a single ZnO wire device (Device #1) in standard ambient conditions are summarized in Fig. 9.2. Figure 9.2(a) shows some typical I–V characteristics of the ZnO wires in the dark and under UV illumination ($\lambda = 372$ nm) at various light intensities. The symmetric rectifying I–V curves indicated that there were two back-to-back Schottky contacts at the two ends of the ZnO wire. As for the UV responsivity measurements in this paper, the bias was set at a fixed value of −5 V (reverse bias) for all of the measurements unless specifically indicated. The measured absolute current increased significantly with light illumination: the dark current was about 14 pA, the current increased to 260 nA under 22 μW/cm^2 light illumination, further increased to 1.9 μA under 33 mW/cm^2 light illumination. The sensitivity defined as $(I_{\text{light}} - I_{\text{dark}})/I_{\text{dark}}$ was found to be 1.8×10^6 % and 1.4×10^7 % at 22 μW/cm^2 and 33 mW/cm^2 illumination, respectively. The sensitivity here is one or two orders of magnitude higher than that in a single Schottky contact device [4, 5], because of the very low dark current due to the depletion layer formed at the two Schottky contacts and oxygen-related hole-trapping states at the ZnO wire surface. The spectral photoresponse of a ZnO wire photodetector showed a large UV-to-visible rejection ratio, which is defined as the sensitivity measured at UV divided by that at blue, and it was about 10^4 for the photodetector. The high spectral selectivity combined with high sensitivity suggests the possibility of using the ZnO wire photodetector as 'visible–blind' UV photodetector for environmental, space-based, defense and industrial applications. The photodetector was also measured with light on and off for many cycles with different light intensities, showing an excellent reversibility and

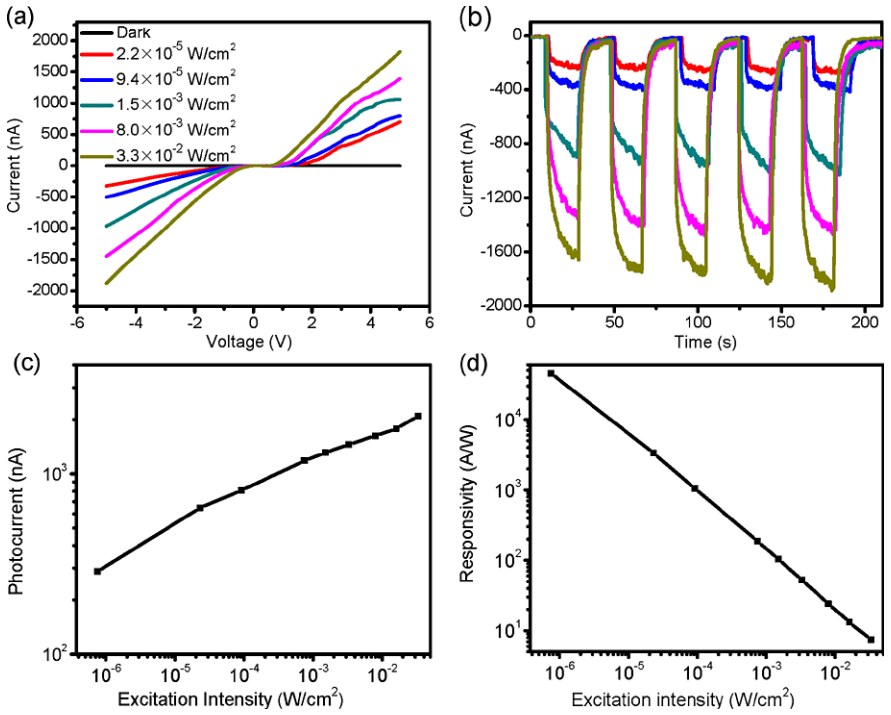

Fig. 9.2 (**a**) I–V characteristics of a single ZnO wire photodetector (device #1) as a function of light intensity. (**b**) Repeatable response with different excitation light intensity, plotted in the same color code with (**a**). (**c**) Absolute photocurrent of a single ZnO wire device measured as a function of the excitation intensity. (**d**) Derived photon responsivity relative to excitation intensity on the ZnO NW [1]

stability with decay time about 1 s (Fig. 9.2(b)). The relative long reset time may be caused by the ultra-long length of the wire which is used for easy and precise controlling the strain in the wire.

The intensity dependences of the photocurrents ($I_{\text{ph}} = |I_{\text{light}} - I_{\text{dark}}|$) are plotted in Fig. 9.2(c). The photocurrent increased linearly with the optical power and showed no saturation at high power levels, offering a large dynamic range from sub-μW/cm^2 to mW/cm^2. The total responsivity of the photodetector, $\Re$, is defined as

$$\Re = \frac{I_{\text{ph}}}{P_{\text{ill}}} = \frac{\eta_{\text{ext}} q}{h\nu} \cdot \Gamma_G, \tag{9.1}$$

$$P_{\text{ill}} = I_{\text{ill}} \times d \times l \tag{9.2}$$

where $\Re$ is the responsivity, I_{ph} photocurrent, P_{ill} the illumination power on the photodetector, η_{ext} the external quantum efficiency, q the electronic charge, h Planck's constant, ν the frequency of the light, Γ_G the internal gain, I_{ill} the excitation power, d the diameter of the ZnO wire, l is the spacing between two electrodes. Remarkably, the calculated responsivity of the device is super high, approximately

4.5×10^4 A/W at an intensity of 0.75 μW/cm^2 of UV light illumination. The internal gain can be estimated to be 1.5×10^5 by assuming $\eta_{ext} = 1$ for simplicity. The high internal gain and high responsivity are attributed to the oxygen-related hole-trapping states [14] and the shrinking of the Schottky barrier upon illumination [6]. The decrease of the responsivity at relatively high light intensities is due to hole-trapping saturation and Schottky barrier transparent at large light intensity (Fig. 9.2(d)).

9.3 Piezo-Phototronic Effect on UV Sensitivity

9.3.1 Experimental Observations

We now use the MSM structure to illustrate the effects of the piezopotential on the performance of the photodetector (device #2). First, we investigated the effects of piezopotential on the dark current of the photodetector. Without strain, the dark current versus voltage curve of the device in semi-logarithmic scale was very flat (Fig. 9.3 inset), even out to high bias, and it remained <50 pA at a reverse bias of −20 V. We did not observe any evidence of breakdown due to the low level defects in the ZnO wire and good Schottky contact. I–V curves in the dark remained with no change under different tensile and compressive strains (Fig. 9.2(a)), which means that the piezopotential has a very small effect on the dark current. Then we measured I–V curve under various compressive and tensile strain upon UV illumination (Figs. 9.2(b) and (c)). The absolute current at a negative bias increased step-by-step when applied a variable strain from 0.36 % tensile to −0.36 % compressing. Because the dark current did not change under strain, the sensitivity, responsivity, and detectivity of the photodetector increased under compressive strain. The responsivity of the photodetector under −0.36 % compressive strain was enhanced by 530 %, 190 %, 9 % and 15 % upon 0.75 μW/cm^2, 22 μW/cm^2, 0.75 mW/cm^2 and 33 mW/cm^2 illumination, respectively. The corresponding light power illuminated onto the ZnO wire was about 4.1 pW, 120.0 pW, 4.1 nW, 180.4 nW, respectively. Figure 9.2(d) shows absolute photocurrent relative to excitation intensity under different strain with a natural logarithmic scale. It can be seen that the photocurrent is greatly enhanced for pW level light detection by using the piezoelectric effect. It is pointed out that the effect of strain is much larger for weak light detection than for strong light detection.

In our experiments, some of the devices show opposite change when applying the same strain, as shown in Fig. 9.4 (device #1), and the absolute current decreased step-by-step when applying a variable strain from 0.26 % tensile to −0.26 % compressing. This phenomenon is attributed to the switching in signs of the piezopotential, which depends on the orientation of the c-axis of the ZnO wire. We have 50 % chance in experiments to have the ZnO wire oriented along the c or $-c$ direction (the axial direction of the wires).

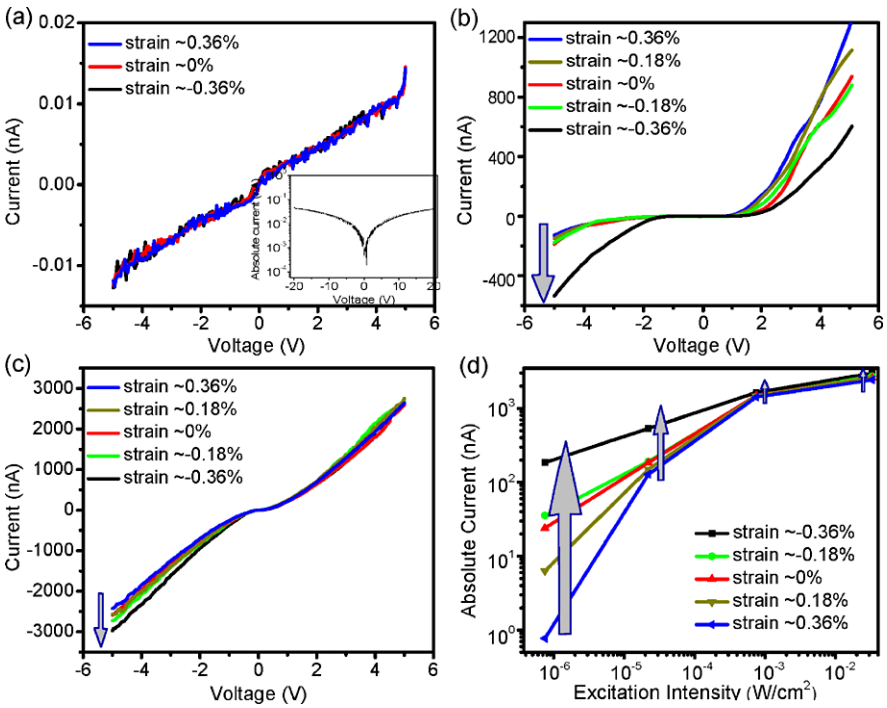

Fig. 9.3 (**a**) Typical dark I–V characteristics of a ZnO wire device (device #2) under different strain. (**b**) I–V curves of the device under different strain with excitation light intensity of 2.2×10^{-5} W/cm^2; the power illuminated on the nanowire was 120 pW, responsivity was increased by 190 % under −0.36 % compressive strain. (**c**) I–V curves of the device under different strain with excitation light intensity of 3.3×10^{-2} W/cm^2; the power illuminated on the nanowire was 180.4 nW, responsivity was increased by 15 % under compressive −0.36 % strain. (**d**) Absolute photocurrent relative to excitation intensity of device #2 under different strain [1]

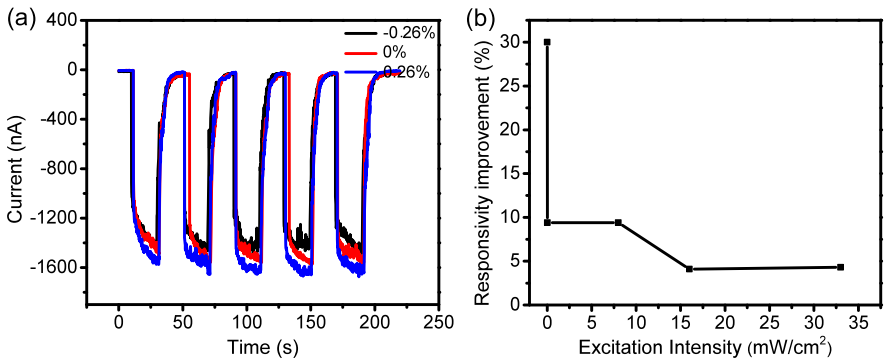

Fig. 9.4 (**a**) Reversible response under different strain with illumination light intensity of 3.3×10^{-3} W/cm^2 (device #1). (**b**) Responsivity improvement ratio as a function of illumination light intensity under 0.26 % tensile strain [1]

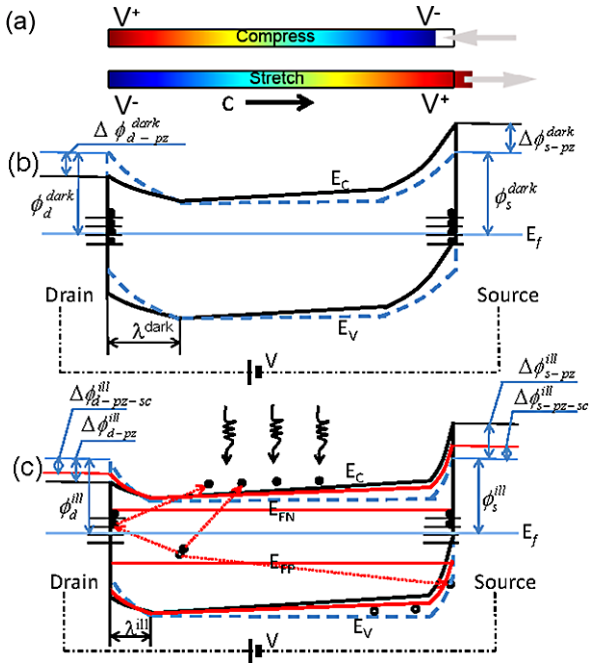

Fig. 9.5 Schematic energy band diagram illustration for tuning the barrier height by piezopotential. (**a**) Simulation of the piezopotential distribution in the wire under compressive and tensile strain, the diameter and length used for calculation is about 1 μm and 20 μm, respectively. The pressure on *c*-plane is about ±1 MPa. (**b**) Barrier height tuned by piezopotential under compressive strain in the dark. (**c**) Barrier height tuned by piezopotential under compressive strain with light illumination [1]

9.3.2 Physics Model

Our device can be considered as a single ZnO wire sandwiched between two back-to-back Schottky diodes, as shown in Fig. 9.5. In our case, when a relatively large negative voltage was applied, the voltage drop occurred mainly at the reversely biased Schottky barrier ϕ_d at the drain side, which is denoted as $V_d \approx V$. Under reverse bias and in the dark condition, thermionic emission with barrier lowering is usually the dominant current transport mechanism at a Schottky barrier, which can be described by the thermionic-emission-diffusion theory (for $V \gg 3kT/q \sim 77$ mV) as [7]

$$I_{\mathrm{TED}}^{\mathrm{dark}} = SA^{**}T^2 \exp\left[-\frac{1}{kT}\cdot\left(q\phi_d^{\mathrm{dark}}\right)\right] \times \exp\left(\frac{1}{kT}\cdot\xi^{1/4}\right), \tag{9.3}$$

$$\xi = q^7 N_D (V + V_{bi} - kT/q)/8\pi^2\varepsilon_s^3, \tag{9.4}$$

$$V_{bi} = \phi_d^{\mathrm{dark}} - (E_C - E_f) \tag{9.5}$$

in which S the area of the Schottky contact, A^{**} the effective Richardson constant, T the temperature, q the unit electronic charge, k the Boltzmann constant, N_D the donor impurity density, V the applied voltage, V_{bi} the built-in potential, and ε_s the permittivity of ZnO.

The effect of photo illumination on semiconductor thermionic emission is to lower the energy barrier by the difference between the quasi-Fermi level with photoexcitation and the Fermi level without photoexcitation [8] and to reduce the

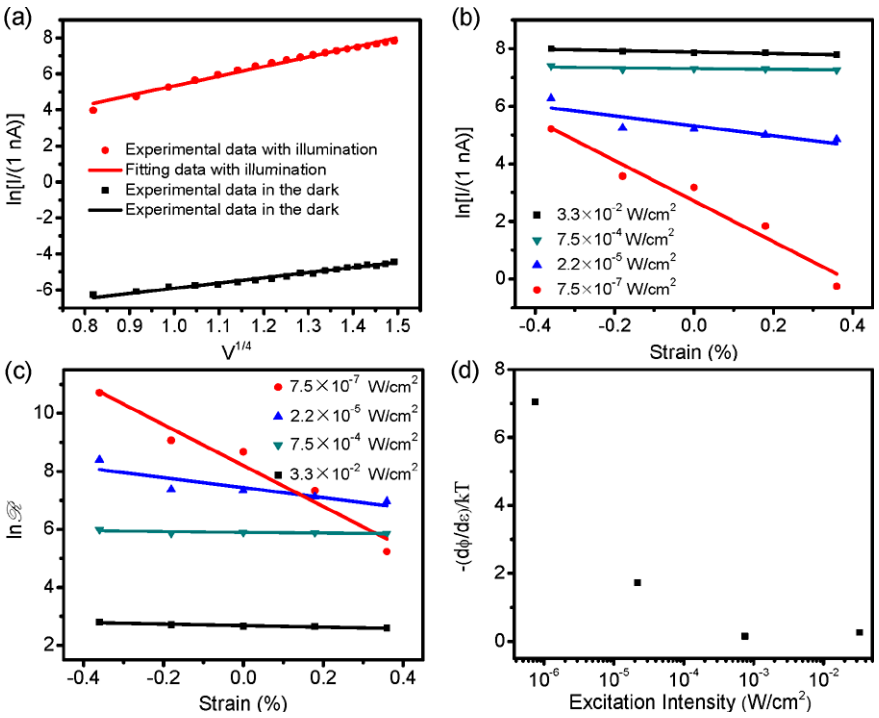

Fig. 9.6 (**a**) Plot of $\ln[I/(1\text{ nA})]$ as a function of $V^{1/4}$, by using the data from Figs. 9.3(a) and (c) for the case of without strain. The *red circles* and *line* represent the experimental data and fitting curve with 3.3×10^{-2} W/cm^2 light illumination. The *black squares* and *line* represent the experimental data and fitting curve in the dark condition. (**b**) Plot of $\ln[I/(1\text{ nA})]$ as a function of strain under different excitation light intensity. (**c**) Responsivity (units A/W) as a function of strain under different excitation light intensity on a natural logarithmic scale. (**d**) The derived change of the Schottky barrier height with strain as a function of excitation light intensity [1]

width of depletion layer by photon-generated holes trapping in the depletion layer (Fig. 9.5(c)). The current transport mechanism with illumination can be described as

$$\begin{aligned} I_{\text{TED}}^{\text{ill}} &= SA^{**}T^2 \exp\left\{-\frac{1}{kT}\cdot\left[q\phi_d^{\text{dark}} - (E_{FN} - E_f)\right]\right\} \times \exp\left(\frac{1}{kT}\cdot\xi^{1/4}\right) \\ &= SA^{**}T^2 \exp\left[-\frac{1}{kT}\cdot\left(q\phi_d^{\text{ill}}\right)\right] \times \exp\left(\frac{1}{kT}\cdot\xi^{1/4}\right) \end{aligned} \tag{9.6}$$

where E_{FN} is quasi Fermi level with illumination.

The $\ln[I/(1\text{ nA})]$–V curve shown in Fig. 9.6(a) qualitatively indicates that the variation of $\ln[I/(1\text{ nA})]$ can be described by the power law of $V^{1/4}$ for reversely biased Schottky barrier. However, the slope and extended zero voltage point for the fitting data with light illumination is larger than those in the dark. According to (9.3) and (9.6), the difference may be attributed to an effective lowering of the Schottky barrier, and the change of N_D due to the holes trapped in the depletion region.

By assuming that S, A^{**}, T, N_D are independent of strain at small deformation, the change of Schottky barrier height (SBH) with strain upon illumination can be determined by

$$\ln\left[\frac{I(\varepsilon_{xx})}{I(0)}\right] = -\frac{\Delta\phi_d^{\text{ill}}}{kT} \tag{9.7}$$

where $I(\varepsilon_{xx})$ and $I(0)$ are the current measured through the ZnO wire at a fixed bias with and without strain applied, respectively. $\Delta\phi_d^{\text{ill}}$ is the change of SBH under light illumination. Figure 9.6(b) shows the $\ln[I/(1\text{ nA})]$ as a function of strain with different excitation light intensity on a natural logarithmic scale. The results indicate that the change of SBH has an approximately linear relationship with strain. Furthermore, the slope of the change of SBH varies with the excitation light intensity. It means that the derived change of barrier height with strain depends on excitation light intensity, the SBH changes faster at low light intensity than that at high light intensity (Fig. 9.6(d)). The change of the total responsivity of the photodetector with strain is similar to the change of current; the difference is that the current increases when increasing light intensity, but the responsivity decreases.

It is known that the change of Schottky barrier height under strain is a combined effect from both strain induced band structure change (e.g., piezoresistance) and piezoelectric polarization [9, 10]. The contributions from band structure effect to SBH in source and drain contacts are denoted as $\Delta\phi_{d-bs}$ and $\Delta\phi_{s-bs}$, respectively. Assuming the axial strain is uniform in the ZnO wire along its entire length, $\Delta\phi_{d-bs} = \Delta\phi_{s-bs}$ if the two contacts are identical. This is the piezoresistance effect, which is symmetric and has equal effects regardless the polarity of the voltage. The asymmetric change of I–V curve at negative and positive bias in our case is dominated by piezoelectric effect rather than piezoresistance effect. The effect of piezopotential to the SBH can be qualitatively described as follows. For a constant strain of ε_{xx} along the length of the wire, an axial polarization $P_x = \varepsilon_{xx} e_{33}$ occurs, where e_{33} is the piezoelectric tensor. A potential drop of approximately $V_p^+ - V_p^- = \varepsilon_{xx} L e_{33}$ is along the length of the wire, where L is the length of the wire. Therefore, the modulations to the SBH at the source and drain sides are of the same magnitude but opposite sign ($V_p^+ = -V_p^-$), which are denoted by $\Delta\phi_{d-pz}$ and $\Delta\phi_{s-pz}(\Delta\phi_{d-pz} = -\Delta\phi_{s-pz})$.

In the experiments, we fixed the light intensity and bent the substrate step-by-step, thus strain was introduced into the device step-by-step. Depending on the deformation direction, the sign of the strain was changed from positive to negative or vice versa. Meanwhile, the corresponding piezopotential distribution in the wire was also adjusted step-by-step, which changed the effective heights of the two Schottky barriers and thus the photocurrent and responsivity of the device. Figure 9.5(a) shows a numerically calculated piezopotential distribution in the wire using the finite element method without considering the natural doping. If the nanowire is positioned along c-axis direction from drain to source side, a positive potential drop will be induced along the length of the wire under compressive strain. Therefore the SBH at the drain contacts was decreased with increasing compressive strain, simultaneously the photocurrent and responsivity were increased under compressive strain.

The effect of piezopotential decreases with increasing light intensity (Fig. 9.6(d)), which may be caused by the screening effect of the newly generated charge carriers to the piezopotential. When ZnO wire is under high light intensity, large amounts of free electrons and holes are generated. They will accumulate and make the piezoelectrical potential partially screened, and $\Delta\phi_{d-pz}$ will be decreased to $\Delta\phi_{d-pz-sc}$ (Fig. 9.5(c)).

It is interesting that the piezoelectric effect on I–V curve in the dark is not obvious either (Fig. 9.3(a)). In the dark, the surface of the ZnO wire is depleted by absorbed oxygen molecules and the dark current is very low (about 14 pA at −5 V applied bias). In this case, the device can be considered as an insulator wire sandwiched between two back-to-back Schottky diodes, and the current is controlled by the bulk of the sample, not by the Schottky contact. Thus although piezopotential tunes the SBH, it cannot have a dominant effect on the dark current. Therefore, piezopotential dramatically increases the responsivity for pW level light detection while keeping the low dark current characteristics of the devices, which is very useful for applications.

9.4 Piezo-Phototronic Effect on Visible Photodetector

Our CdS nanowires were synthesized using high-temperature thermal evaporation process. The photodetectors are fabricated in a similar way as reported previously [1]: a single CdS nanowire is placed on an elastic Kapton (polyimide) substrate with the size around 20 mm × 8 mm × 0.5 mm, with both ends bonded to the substrate and copper wires using silver paste. The device is placed upside-down onto a Nikon Eclipse Ti inverted microscope system, which can monitor and excite the photon detection.

9.4.1 Experimental Results and Comparison with Calculation

Our experimental results show two kinds of typical MSM photodetector, single Schottky contact photodetector and double Schottky contact photodetector. Figure 9.7 is the result for a single Schottky contact photodetector. As shown in Fig. 9.7, under increasing strain, the current decreases. Thus, the device configuration and direction of the c-axis is as shown in the inset of Fig. 9.7(b). In Fig. 9.7(d), the illumination power is kept at 6.4×10^{-6} W/cm^2, the change of responsivity R with applied strain for the photodetector is calculated. Responsivity is the measurement of degree of sensitivity, and we have $R = \frac{I_{\text{ph}}}{P_{\text{ill}}}$, where I_{ph} is the photo current, P_{ill} is the illumination power, which is the measurement of light intensity. We see that the responsivity in this case decreases with positive strain. As the piezo-phototronic effect is asymmetric and direction sensitive, to get enhancement rather than decrease in device performance, the direction of c-axis should be taken into consideration in

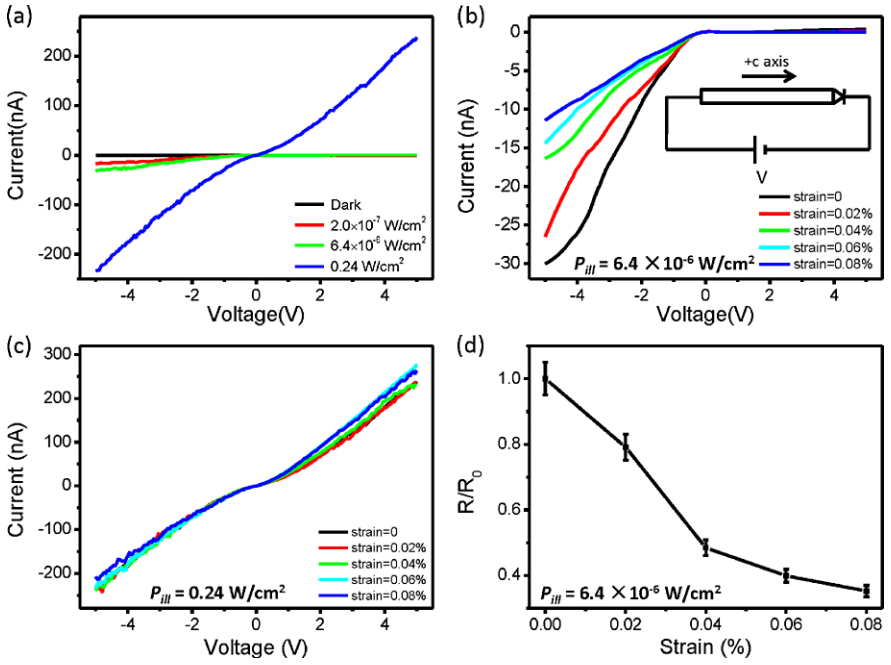

Fig. 9.7 Experimental results for a CdS nanowire MSM photodetector with a single Schottky contact [11]. Light illumination with monochromic blue light centered at 486 nm. (**a**) Current–voltage characteristic under different illumination power. The *inset* it for a dark current without strain. (**b**) Current–voltage characteristic under different strain when illumination power is 6.4×10^{-6} W/cm^2. The *inset* is the configuration of device and direction of forward bias. (**c**) Current–voltage characteristic under different strains when illumination power is 0.24 W/cm^2. (**d**) Calculated relative responsivity under various applied strain when illumination power is 6.4×10^{-6} W/cm^2. R_0 is set as the responsivity under zero strain for this illumination power [11]

device fabrication with a single Schottky contact. In Fig. 9.8(c), when illumination power increases to as high as 0.24 W/cm^2, the rectifying current–voltage behavior has changed to a nearly symmetric behavior. This can be explained by the increase of quasi-Fermi level, which leads to a quick breakdown of the Schottky contact under reversely biasing voltage.

Figure 9.8 is the result for a double Schottky contact photodetector. As shown in Fig. 9.8(b), the change in I–V characteristic with applied strain is in the way exactly as predicted by the theoretical model: while the current under forward bias increases with applied strain, under reverse bias the current decreases.

In both Figs. 9.7(c) and 9.8(c), we see that, with an increase in illumination power, the strain effects are not as significant as that at lower illumination power. The piezo-charges are independent of illumination power, and change in Fermi level at higher illumination power can dictate the change in Schottky barrier height. With

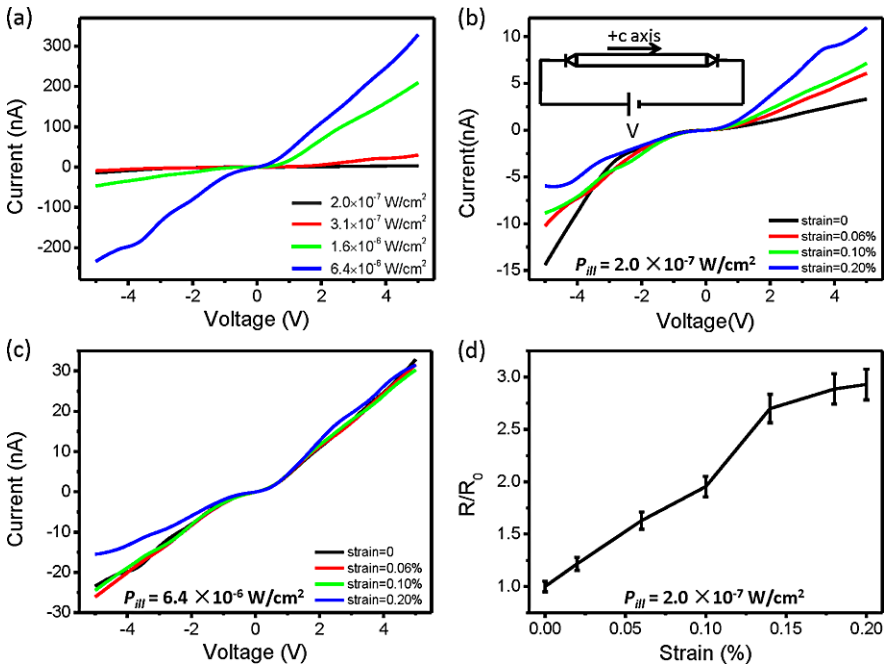

Fig. 9.8 Experimental results for a CdS nanowire MSM photodetector with double Schottky contacts. Light illumination with monochromic blue light centered at 486 nm. (**a**) Current–voltage characteristic under different illumination power. (**b**) Current–voltage characteristic under different strain when illumination power is 2.0×10^{-7} W/cm^2. The *inset* is the configuration of device and direction of forward bias. *Inset* is the configuration of device and direction of forward bias. (**c**) Current–voltage characteristic under different strains when illumination power is 6.4×10^{-6} W/cm^2. (**d**) Calculated relative responsivity under various applied strain when illumination power is 2.0×10^{-7} W/cm^2. R_0 is set as responsivity under zero strain for this illumination power [11]

higher light density, the I–V characteristic of the photodetector gets closer to a linear behavior, because the photo excited excess charge carrier density Δn can be significantly larger than the intrinsic charge carrier due to doping, and the quasi-Fermi level for electrons gets much higher than the Fermi level of the metal, whereas charge redistribution also takes place, which can reduce the depletion region and lower the effective Schottky barrier height. Thus, the Schottky barrier height gets so low that their behavior is very close to the linear behavior of an Ohmic contact, and the influence of the piezo-charges are not as significant as lower illumination power conditions. Therefore, the piezo-phototronic effect can help enhance the sensitivity of the detection at low light intensity, but does not necessarily have a significant effect for strong light intensity. In practice, the detection of low intensity light is practically desired.

9.4.2 Effect from Piezoresistance

When a crystal lattice is deformed under strain, the band gap width shall have a minor change, and can finally result in conductance change of the semiconductor. This is called the piezoresistance effect [12, 13]. The piezoresistance effect is present in semiconductors either with or without piezoelectricity. In piezotronics and piezo-phototronics, piezoresistance is always accompanied by the piezoelectric effect.

In the piezoresistance effect, the change of resistance is given by

$$\frac{\delta\rho}{\rho} = \pi \frac{\delta l}{l}$$

where ρ is the resistance of the semiconductor, l is the original length of the nanowire, $\delta\rho$ is the resistance change due to piezoresistance effect, δl is the change in nanowire length, and π is the piezoresistance coefficient. We can see that the piezoresistance is a resistance effect that is a uniform and symmetric effect, regardless of the biasing of the applied voltage.

9.4.3 Effect from Series Resistance

There are a lot of factors that result in deviation of I–V characteristic from the ideal current–voltage equation, and one of the most important factors should be the effect of the series resistance. The series resistance is the equivalent resistance of various factors in the electric circuit, including outer circuit resistance, capacitors and inductors. Methods to solve the influence of series resistance have been extensively developed [14, 15]. According to these solutions, when the applied voltage is small, the device behavior is dominated by current equations for contact junction; when the applied voltage is large, the device behavior is mostly linear. Other factors also include the surface trapped charges on the contact areas, and change in contact areas due to externally applied strain. These factors either have similar behavior to the piezoresistance effect or should be too small to affect the results.

9.5 Judging Criteria for Piezo-Phototronic Photodetection

In our model and experiments, we successfully demonstrate the difference between the piezo-phototronics effect and other non-piezoelectric effects in highly sensitive photodetection. Here we propose three criteria for characterizing piezo-phototronic photodetection [11].

(1) Piezo-phototronic photodetection requires the presence of a Schottky junction or p–n junction. The piezo-charges originate from the dipole nature of piezoelectricity, and they accumulate at the ends of the piezoelectric semiconductor nanowire as fixed charges. With the existence of a charge barrier, the small

amount of piezo-charges can effectively tune the current transport properties of the photodetector.

(2) Photoexcitation influences the current–voltage characteristic through generating excess free charges. Provided that the entire device is under uniform illumination, photon generation of electrons and holes effectively tunes quasi Fermi level, and this change is applied along the entire wire, resulting in a decrease of the barrier height.

(3) Piezoelectric effect influences photodetection by strain induced polar charges at the ends of the nanowires. The effect of piezo-charges in a double Schottky contact photodetector shall result in asymmetric change in barrier heights at the two sides. Other factors induced by external strain such as piezoresistance or contact area change will induce symmetric change in both ends of the nanowire. In this way, we can easily tell whether the change is caused by genuine piezo-phototronics effect.

These three criteria give a better understanding of our piezo-phototronics experiments, and work as guidance for our future work in related areas. It is also possible to extrapolate our assumption onto other piezo-phototronics phenomena, such as the piezo-phototronic LED or photocell cases, and a similar conclusion should be reached.

9.6 Summary

In summary, we have demonstrated a piezopotential tuned low dark-current ultrasensitive ZnO wire UV photosensor and CdS visible photosensor. The device retains low dark-current characteristics while increasing the responsivity dramatically for pW level light detection by piezopotential. The derived change of barrier height with strain depends on the excitation light intensity, the SBH changes faster at low light intensity than that at high light intensity. The physical mechanism is explained by considering both piezopotential effect and photon-generated free charges screening effect. Three-way coupling of semiconducting, photonic and piezoelectric properties of semiconductor nanowires will allow tuning and controlling of electro-optical process by strain induced piezopotential, which is the piezo-phototronic effect, and it will also lead to further integration between piezoelectric devices with microelectronic and optomechanical systems.

We have then discussed other factors in the experiments and concluded three criteria based on the physics of piezo-phototronic photodetectors, to differentiate the piezo-phototronic effect from other effects. These criteria support our previous experimental results, and can give guidance to future experiments.

References

1. Q. Yang, X. Guo, W.H. Wang, Y. Zhang, S. Xu, D.H. Lien, Z.L. Wang, Enhancing sensitivity of a single ZnO micro-/nanowire photodetector by piezo-phototronic effect. ACS Nano **4**(10), 6285–6291 (2010)
2. Z.W. Pan, Z.R. Dai, Z.L. Wang, Nanobelts of semiconducting oxides. Science **291**, 1947–1949 (2001)
3. J. Zhou, P. Fei, Y.D. Gu, W.J. Mai, Y.F. Gao, R.S. Yang, G. Bao, Z.L. Wang, Piezoelectric-potential-controlled polarity-reversible Schottky diodes and switches of ZnO wires. Nano Lett. **8**(11), 3973–3977 (2008)
4. J. Zhou, Y.D. Gu, Y.F. Hu, W.J. Mai, P.H. Yeh, G. Bao, A.K. Sood, D.L. Polla, Z.L. Wang, Gigantic enhancement in response and reset time of ZnO UV nanosensor by utilizing Schottky contact and surface functionalization. Appl. Phys. Lett. **94**(19), 191103 (2009)
5. T.Y. Wei, C.T. Huang, B.J. Hansen, Y.F. Lin, L.J. Chen, S.Y. Lu, Z.L. Wang, Large enhancement in photon detection sensitivity via Schottky-gated CdS nanowire nanosensors. Appl. Phys. Lett. **96**(1), 013508 (2010)
6. R.R. Mehta, B.S. Sharma, Photoconductive gain greater than unity in CdSe films with Schottky barriers at the contacts. J. Appl. Phys. **44**(1), 325–328 (1973)
7. S.M. Sze, *Physics of Semiconductor Devices* (Wiley, New York, 1981)
8. J.W. Schwede, I. Bargatin, D.C. Riley, B.E. Hardinm, S.J. Rosenthal, Y. Sun, F. Schmitt, P. Pianetta, R.T. Howe, Z. Shen, N.A. Melosh, Photon-enhanced thermionic emission for solar concentrator systems. Nat. Mater. **9**, 762–767 (2010)
9. K.W. Chung, Z. Wang, J.C. Costa, F. Williamson, P.P. Ruden, M.I. Nathan, Barrier height change in GaAs Schottky diodes induced by piezoelectric effect. Appl. Phys. Lett. **59**(10), 1191–1193 (1991)
10. W. Shan, M.F. Li, P.Y. Yu, W.L. Hansen, W. Walukiewicz, Pressure dependence of Schottky barrier height at the Pt/GaAs interface. Appl. Phys. Lett. **53**(11), 974–976 (1988)
11. Y. Liu, Q. Yang, Y. Zhang, Y.Z. Yang, Z.L. Wang, Nanowire piezo-phototronic photodetector: theory and experimental design. Adv. Mater. **24**(11), 1410–1417 (2012)
12. P.W. Bridgman, The effect of homogeneous mechanical stress on the electrical resistance of crystals. Phys. Rev. **42**(6), 858–863 (1932)
13. C.S. Smith, Piezoresistance effect in germanium and silicon. Phys. Rev. **94**(1), 42–49 (1954)
14. H. Norde, A modified forward $I-V$ plot for Schottky diodes with high series resistance. J. Appl. Phys. **50**(7), 5052–5053 (1979)
15. C.D. Lien, F.C.T. So, M.A. Nicolet, An improved forward $I-V$ method for nonideal Schottky diodes with high series resistance. IEEE Trans. Electron Devices **31**, 1502–1503 (1984)

Chapter 10
Piezo-Phototronic Effect on Light-Emitting Diode

Abstract As a classical device, the performance of an LED is dictated by the structure of the p–n junction and the characteristics of the semiconductor materials. Once an LED is made, its efficiency is determined largely by the local charge carrier densities and the time at which the charges can remain at the vicinity of the junction. The latter is traditionally controlled by growing a quantum well or using a built-in electronic polarization for "trapping" electrons and holes in the conduction and valence bands, respectively. This is a rather complex and expensive process involving MBE and MOCVD, and more importantly, the width and potential well depth of the quantum well are fixed once the growth is complete. In this chapter, we describe the piezo-phototronic effect on the light emitting of a n-ZnO–p-GaN structure for illustrating its general impact to LED. The emission intensity and injection current at a fixed applied voltage have been enhanced by a factor of 17 and 4 after applying a 0.093 % compressive strain, respectively, and the corresponding conversion efficiency has been improved by a factor of 4.25 in reference to that without applying strain! The absolute external efficiency has reached 7.82 %. This hugely improved performance is suggested to arise from an effective increase in the local "biased voltage" as a result of the band shift caused by piezopotential and the trapping of holes/electrons at the interface region in a channel created by the piezopotential near the interface. The study shows that the piezo-phototronic effect can be very effectively used for enhancing the efficiency of energy conversion in today's green and renewable energy technology without using the sophisticated nanofabrication procedures that are of high cost and complex. The physical model presented can be expanded to many other materials.

Highly efficient ultraviolet (UV) emitters are required for applications in chemical, biological, aerospace, military and medical technologies. Although the internal quantum efficiency of the UV LED is as high as 80 %, the external efficiency for a conventional single p–n junction thin-film-based LED is only about 3 % due to the low extraction efficiency (about $1/4n^2$, where n is the refraction index) as a result of total internal reflection [1]. The usage of ZnO nanowires (NWs) as active layers to fabricate nanosized heterojunction LED is expected to be an effective approach for improving extraction efficiency [2–4], but the reported data so far show low exter-

Z.L. Wang, *Piezotronics and Piezo-Phototronics*, Microtechnology and MEMS,
DOI 10.1007/978-3-642-34237-0_10, © Springer-Verlag Berlin Heidelberg 2012

nal efficiency (∼2 %), possibly due to the very low internal efficiency of NW-based LED.

Light emission from semiconductors depends not only on the efficiency of carrier injection and recombination but also extraction efficiency. For ultraviolet emission from high band gap materials such as ZnO, nanowires have higher extraction efficiencies than thin films, but conventional approaches for creating a p–n diode result in low efficiency. In this chapter, we demonstrate how the piezo-phototronic effect can be effectively utilized to enhance the external efficiency of an LED fabricated using a single ZnO micro-/nanowire on a GaN substrate [5]. The emission light intensity and injection current at a fixed applied voltage has been enhanced by a factor of 17 and 4 after applying a 0.093 % compressive strain, respectively, and the corresponding conversion efficiency was improved by a factor of 4.25. This is suggested to arise from an effective increase in the local "biased voltage" as a result of the band modification caused by piezopotential and the trapping of free carriers at the interface region in a channel created by the piezopotential near the interface. Furthermore, the piezoresistance and piezooptic (photoelastic) effects have been utilized to simultaneously tune the light-emitting intensity, spectra, and polarization. Our study shows that the piezo-phototronic effect can be effectively used for enhancing the efficiency of energy conversion in today's safe, green, and renewable energy technologies.

10.1 LED Fabrication and Measurement Method

Our experiments were carried out based on the following design. A single ZnO micro-/nanowire LED was fabricated by manipulating a wire on a trenched substrate. The Mg acceptor doping concentration was about $5 \times 10^{17}/\text{cm}^3$. The ZnO micro/nanowires were synthesized by a high-temperature thermal evaporation process. Before fabricating a n-ZnO wire/p-GaN film LED, a 20-nm layer of Ni and 50-nm layer of Au were deposited by thermal evaporation on the p-GaN as the anode electrode; and a 100-nm layer of ITO was sputtered on the sapphire substrate as the cathode electrode, both followed by rapid thermal annealing in air at 500 °C for 5 min. Then, the GaN covered sapphire substrate was attached closely to an ITO coated sapphire substrate (a small trench was formed between the two substrates). A single ZnO micro-/nanowire was picked up from the glass substrate and transferred to the trenched substrates across the gap by micromanipulation (as shown in Fig. 10.1(b), inset, and Fig. 10.2). A transparent PS film with thickness of 500 μm and width less than the length of ZnO wire was used to cover the NW, and an external stress was applied onto the PS film by an alumina rod connected to a piezo nanopositioning stage that was fixed on a 3D micromanipulation stage. The entire device was packaged using narrow transparent adhesive tapes to obtain a tight contact between ZnO wire and GaN substrate (Fig. 10.1(b), inset).

A normal force was applied on the PS film by an alumina rod connected to a piezo nanopositioning stage. In this case, a compressive stress was applied uniformly normal to the interface between the side surface of the ZnO wire and the GaN substrate

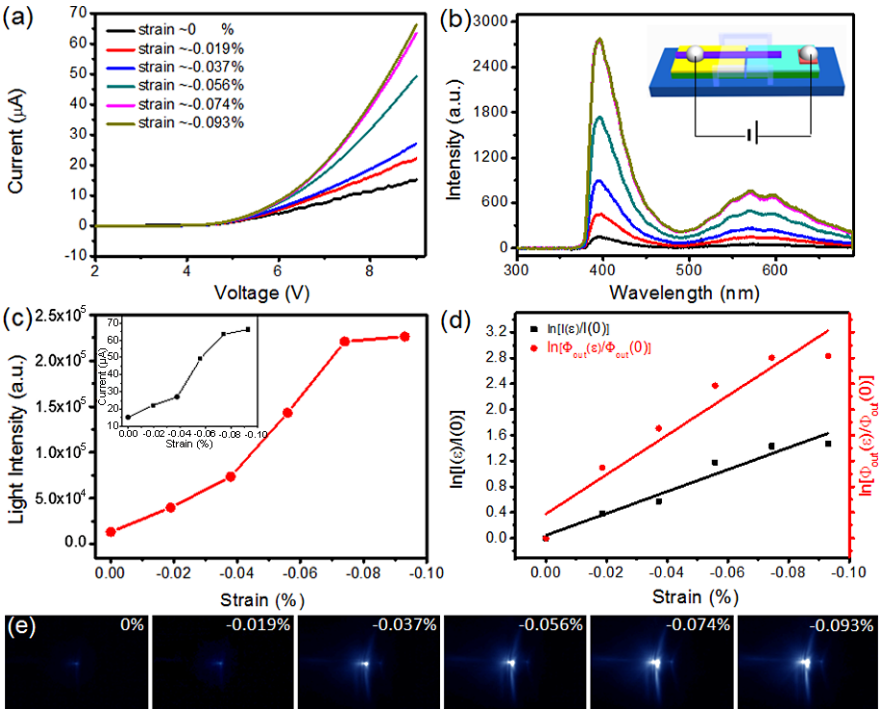

Fig. 10.1 Enhancement of emission light intensity and conversion efficiency of a (n-ZnO wire)–(p-GaN film) LED under applied strain. A schematic diagram of the fabricated device is inset in (**b**). (**a**) I–V characteristics of the device at forward bias with the variation of the applied strain; and (**b**) the corresponding optical spectra of the emitted light at a bias of 9 V. (**c**) Integrated emission light intensities from the data shown in (**b**), showing a huge increase in the emission intensity with the increase of the applied compressive strain. The inset is the injection current of the LED at 9 V biasing voltage with the increase of the strain. (**d**) Change in relative injection current $\ln[I(\varepsilon)/I(0)]$ and relative emission light intensity $\ln[\Phi_{\text{out}}(\varepsilon)/\Phi_{\text{out}}(0)]$ under different strain. The LED efficiency has been increased by a factor of 4.25 at the maximum applied strain in comparison to the zero strain case. (**e**) CCD images recorded from the emitting end of a packaged single wire LED under different applied strain [5]

surface; such a compressive force along the a-axis of the ZnO wire resulted in a tensile strain along the c-axis, the growth direction of the wire. In this design, there was no transverse bending or twist on the wire to ensure the stability of the p–n junction interface between the ZnO wire and GaN substrate.

The measurement system is built based on an inverted microscope and 3D micromanipulation stages (Fig. 10.3). A normal force was applied on the PS film by an alumina rod connected to a piezo nanopositioning stage with closed loop resolution 0.2 nm (Fig. 10.3). To calculate the strain on the wire, we need to know the stress added on the PS tape. The recorded deformation on the piezo nanopositioning stage is determined by the deformation of PS film and Kapton film, considering the dimension (Fig. 10.2) and Young's modulus of each element in the device.

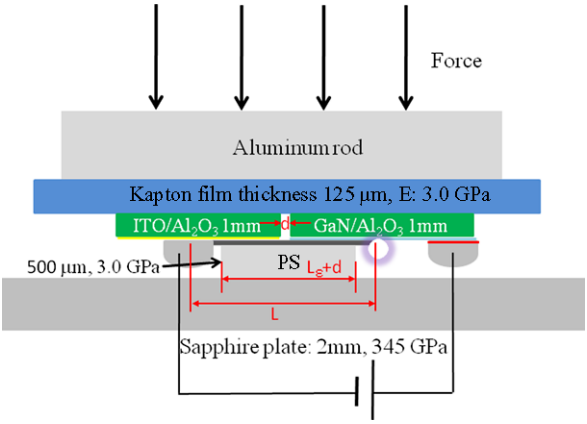

Fig. 10.2 Detailed side view of the device structure. GaN covered sapphire substrate is attached closely to an ITO coated sapphire substrate on a Kapton film. A single ZnO micro-/nanowire is placed across the two substrates. A transparent PS film with thickness of 500 μm is used to cover the wire and force is added on the PS film by an alumina rod connecting to a piezo nanopositioning stage (closed loop resolution 0.2 nm) fixed on a 3D micromanipulation stage [5]

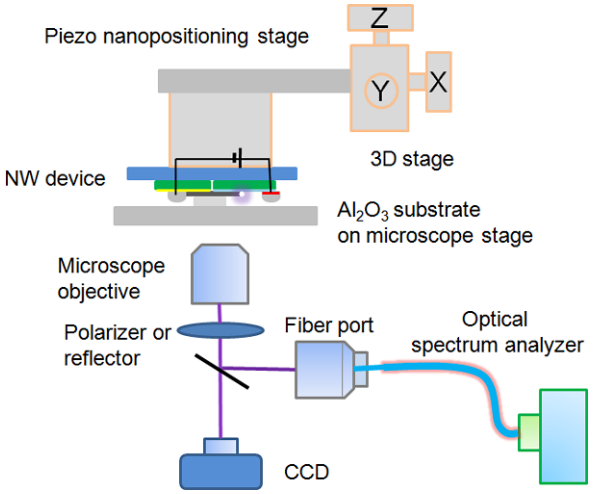

Fig. 10.3 Schematic diagram of the measurement system for characterizing the performance of a ZnO wire LED under applied compressive strain

In the experiment, we measured the output light intensity by spectrometer or CCD, which characterizes the optical power in a relative manner. We mainly focus on the relative change of the output light intensity as well as the quantum efficiency under different strain. We derive the change of quantum efficiency by analyzing the output light intensity and current under the applied strain. The data for investigating the influence of strain on light intensity and spectrum are recorded using a fiber optical spectrometer. The integration of peak spectrum is considered as the relative emission light intensity. The data for studying the strain effect on the polarization are

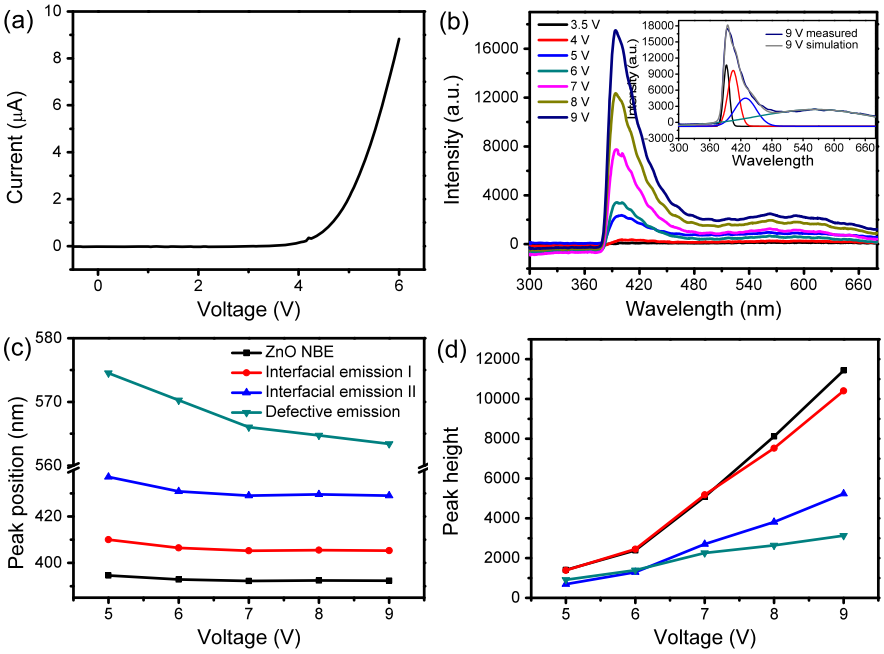

Fig. 10.4 Characteristics of a single wire LED without applying strain. (**a**) I–V characteristics of the LED. (**b**) EL spectrum as a function of the forward biased voltage. The *inset* image shows the Gaussian deconvolution analysis of the EL emission. (**c**) Four emission bands peak position as a function of the biased voltage. (**d**) Peak height as a function of the biased voltage [5]

recorded using a CCD. The relative light output intensity is extracted by analyzing the brightness of the image.

10.2 Characterization of LED

Before the electromechanical and optical measurements, we first measured the original optoelectronic performance of the device without strain. The current–voltage (I–V) characteristic of a single n-ZnO wire/p-GaN substrate LED device is shown in Fig. 10.4(a). The I–V curve clearly shows a nonlinear increase of current under the forward bias, which indicates reasonable p–n junction characteristics and the possibility of light emission. The turn-on voltage of the hybrid heterojunction of ZnO/GaN (wire/film) is around 3 V. The emission spectrum of the as-fabricated LED was monitored at different biased voltages/injection-currents at room temperature. Peak-deconvolution of the emission spectra using Gaussian functions (inset picture in Fig. 10.4(b)) shows that the blue/near-UV emission spectrum consists of a distinct peak centered at 390–395 nm and a long red tail until 460 nm. In order to analysis the peak position shift under biased voltage and strain, we use two emission

bands centered at 405–415 nm and 420–440 nm in the deconvolution to represent the long red tail in blue/near-UV emission spectrum considering two interface states at GaN side and ZnO side of the heterojunction, respectively.

10.3 Piezoelectric Effect on LED Efficiency

The I–V characteristics, dependence of emission intensity on the applied voltage and the features of the characteristic peaks of an as-fabricated LED without applying additional strain are presented in the SI. The external efficiency of an as-fabricated single wire LED was measured conservatively to be ~1.84 % before applying a strain, which is as high as that for a single p–n junction-based UV LED [2–4]. To test the strain effect on a single ZnO wire LED, we systematically investigated its output light intensity, electroluminescence spectra and polarization as the strain being applied. At a fixed applied bias above the turn-on voltage (3 V), the current and light emission intensity increased obviously with increase of the compressive strain (Figs. 10.1(a) and (b)). The significantly enhanced light intensity can also be directly observed in optical images recorded by a CCD (Fig. 10.1(e)). The $\ln[I(\varepsilon)/I(0)]$ and $\ln[\Phi_{\text{out}}(\varepsilon)/\Phi_{\text{out}}(0)]$ dependence on strain ε is shown in Fig. 10.1(d), where $\Phi_{\text{out}}(\varepsilon)$ and $I(\varepsilon)$ are the light intensity and injection current of the LED under strain, respectively; $\Phi_{\text{out}}(0)$ and $I(0)$ are the corresponding quantities of the as-fabricated LED without applying an external strain; both curves have a linear relationship with external strain, and the slope of $\ln[\Phi_{\text{out}}(\varepsilon)/\Phi_{\text{out}}(0)] - \varepsilon$ is larger than that of $\ln[I(\varepsilon)/I(0)] - \varepsilon$, indicating a clear increase in light conversion efficiency. The injection current and output light intensity were largely enhanced by a factor of 4 and 17, respectively, after applying a 0.093 % a-axis compressive strain, indicating that the conversion efficiency was improved by a factor of 4.25 in reference to that without applying strain. This means that the external true efficiency of the LED can reach ~7.82 % after applying a strain, which is comparable to that of the LED structures based on nanorods enhanced hybrid quantum wells LED.

To confirm the validity of the observed data, the stability of the contact between ZnO wire and GaN was carefully examined by repeating the applied strain. Once the strain was retracted, the light emission intensity dropped back to the value observed at strain free case (Fig. 10.5(b)). A linear relationship observed in the enhancement factor with strain (Fig. 10.1(d)) proved that a possible change in contact area between n- and p-side of the device was not responsible to the observed increase in efficiency.

10.4 Effect of Piezo-Polar Directions

ZnO has a polar direction that is along its c-axis, which is the growth direction of the wires. During the fabrication of the devices, there is a 50 % chance for the wires to be oriented with c-axis pointing from ITO side to the GaN side, while the other

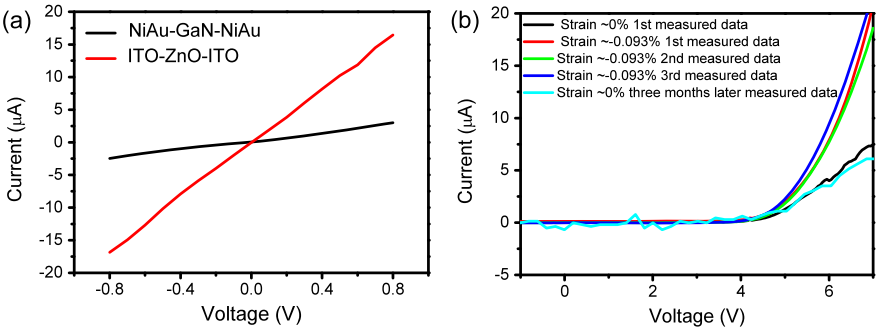

Fig. 10.5 (**a**) I–V curves of Ni/Au–GaN–Ni/Au contacts and ITO-ZnO-ITO contacts. The nearly Ohmic contacts and large current at small bias voltage (0.8 V) confirm that the rectifying I–V curves of our devices come from the p–n diode. (**b**) I–V curve of a single wire LED under the same strain measured at different time and I–V curve of the device after keeping it in dry cabinet for three months, showing its great stability

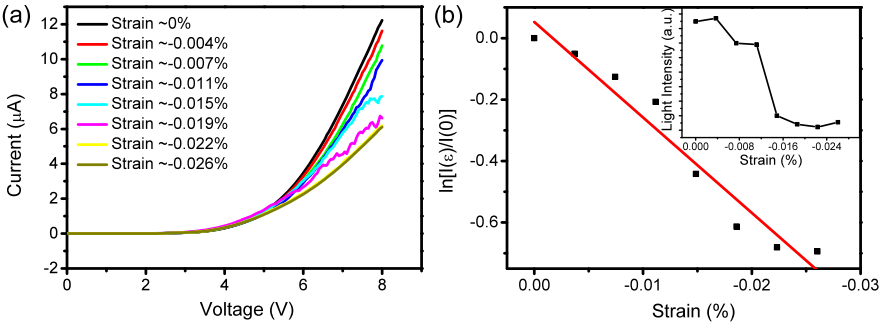

Fig. 10.6 Electronic and optical characteristics of a ZnO wire LED whose injection current and emission light intensity decreases with the increase of a-axis compressive strain. (**a**) I–V curve of the LED under different strain. (**b**) Plot of $\ln[I(\varepsilon)/I(0)]$ at 8 V biased voltage under different strain, the inset shows the change of light intensity at 8 V biased voltage under different strain. Such result is possible if the c-axis of the wire is oriented pointing away of the GaN side (see main text)

50 % are oriented in reverse direction. In the main text, we have presented the data for the former case (see Figs. 10.1). Here we present the latter case in Fig. 10.6.

The data shown in Fig. 10.6 indicate that the improved contact between the wire and the GaN substrate may not be responsible to the change of emission intensity, rather it is likely due to the piezoelectric effect as described in the text.

10.5 Relationship Between the Injection Current and the Applied Strain

From the theory, a linear relationship is expected between the logarithm of the injection current and the applied strain. This is consistent with the data presented in

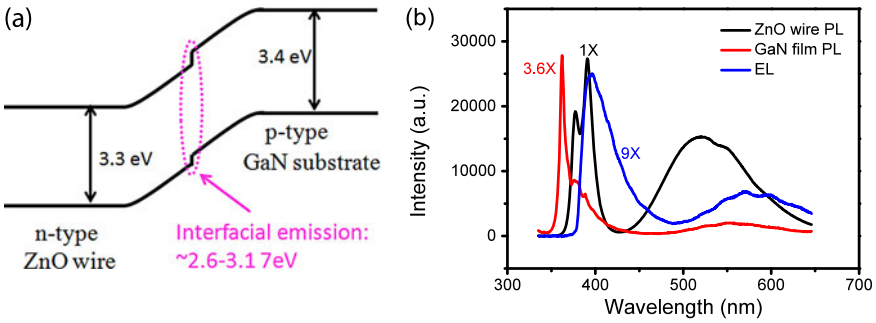

Fig. 10.7 (**a**) Schematic energy band diagram of a p–n junction without strain. (**b**) Photoluminescence and spectra of a single ZnO wire and GaN film and electroluminescence spectrum of a single wire LED

Figs. 10.1(d) and 10.6. This is other evidence proving that a possible change in contact area between n- and p-side of the device was not responsible for the observed increase in efficiency.

10.6 Emission Spectra and Excitation Processes

10.6.1 Band Diagram of the Heterojunction

Band-line-up data for the ZnO/GaN heterostructure are needed for analyzing the emission characteristics of the LED [5]. ZnO and GaN have a type-II band offset. The ideal heterojunction band diagram for n-ZnO/p-GaN is constructed by following the Anderson model [1]. To construct the diagram, the band gap energies of ZnO and GaN are assumed to be 3.3 and 3.4 eV, respectively. The electron affinities of ZnO and GaN are assumed to be 4.5 and 4.1 eV. The valence band offset here is about 0.3 eV, which is in the range of valance band offset values reported for ZnO/GaN heterojunction from 0.13 to 1.6 eV. The origin of light emission could be analyzed based on the schematic band diagram and through comparison of photoluminescence (PL) and EL spectra (Fig. 10.7). Two UV peaks in the PL spectra of ZnO wire centered at 376 nm (3.30 eV) and 391 nm (3.17 eV), correspond to the bandgap recombination and phonon assisted exciton emission, respectively [2]. Three UV peaks in the PL spectra of GaN film centered at 362 nm (3.40 eV), 377 nm (3.29 eV), and 390 nm (3.18 eV) correspond to the bandgap recombinations and Mg acceptor related emission [6] (the acceptor activation energy for Mg in GaN is about 0.14–0.21 eV), respectively.

There has been a controversy about the emission origination in ZnO/GaN heterojunction LED [2, 6]. It is shown in Fig. 10.7(b) the EL emission overlaps with 390 nm peak in ZnO PL and has a long red tail until 460 nm. Peak-deconvolution of the EL spectra using Gaussian functions (inset picture in Fig. 10.4(b)) shows that

the spectrum consists of a distinct peak centered at 390–395 nm, a long red tail until 460 nm and a weak yellow emission at around 570 nm. According to the PL spectra, the band centered in the range of 390–395 nm could be attributed to the phonon assisted excitonic emission in ZnO wire. Shorter wavelength emission from GaN film and ZnO wire may be reabsorbed by ZnO wire, therefore, there is no peak shorter than 390 nm. However, the tail emission (ranged from UV peak to 460 nm) has no corresponding band in individual PL spectra of ZnO or GaN. Referring to the band diagram, the tail emission may be attributed to interfacial emission that comes from the radiative interfacial recombination of the electrons from n-ZnO and holes from p-GaN [6, 7]. There is a discontinuity at the interface, and this abrupt discontinuity may influence the EL spectra. The energy of the electrons and holes at this discontinuity interface is not a fixed value as shown in Fig. 10.7(a), but has a range of variation. Therefore, the interfacial emission should be a red broad tail emission in UV range. The interface states are like incorporating of one compound into the other in some respects. The incorporation of one compound into the other would lead to a reduced bandgap as compared to that of either ZnO or GaN. Density functional theory calculation reveals that incorporation GaN cluster in a ZnO host results in a more effective bandgap reduction than incorporating ZnO in a GaN host. In order to analyze the peak position shift under biased voltage and strain, we use two emission bands centered at 405–415 nm and 420–440 nm in the deconvolution to represent the long red tail in blue/near-UV emission spectrum considering two interface states at GaN side and ZnO side of the heterojunction, respectively.

10.6.2 Emission Spectra of a Strained LED

The enhancements of the distinct emission bands are analyzed as a function of the applied strain using the peak-deconvolution method (Fig. 10.8(a)). The analysis of the emission origin is presented in the section D of SI. The emission coming from the ZnO-GaN interface grew fastest among four emission bands, due to the trapping of free carriers in the channel near the interface. The ratio of the UV-to-visible emission increased with the increase of the in-plane compressive strain (Fig. 10.8(d)), since the UV/blue near band edge emission is more sensitive to the band structure change than the defect centers. The peak positions of the four emission bands did not exhibit any appreciable shift under straining (Fig. 10.8(c)), but they did have obvious blue shift as the applied bias voltage was increased (Fig. 10.4(c)). These results indicated that the effect of strain on the LED is different from the effect of increase of applied bias voltage on it.

It is known that the bandgap of ZnO decreases under compressive a-axis strain [8, 9], while the bandgap of GaN also decreases under compressive c-axis strain [10, 11]. In this case, the peak position should have a red shift under compressive strain. On the other hand, the emission centers of the n-ZnO/p-GaN LED have blue shift with the increase of injection current due to the band renormalization, band filling at high current and/or the increased kinetic energies of electrons and

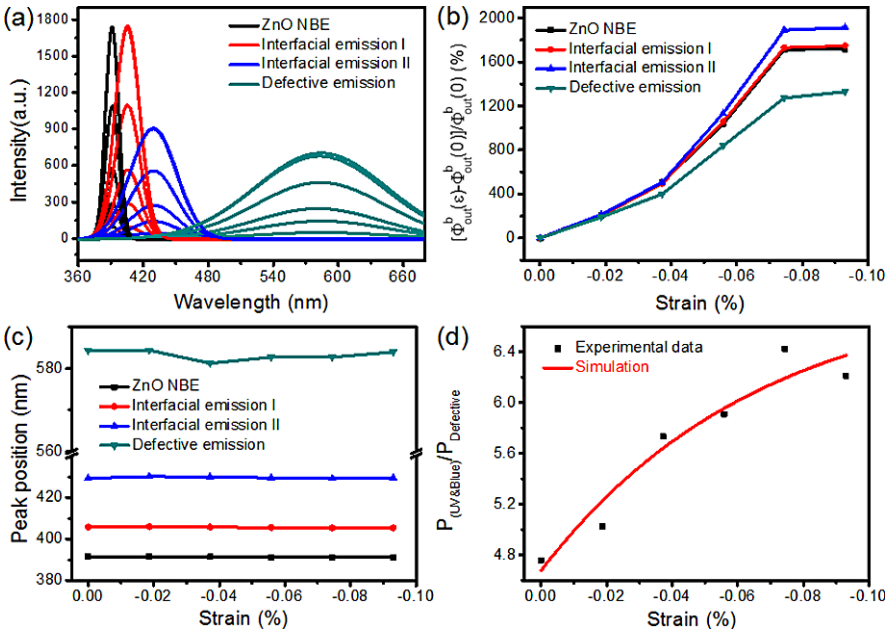

Fig. 10.8 Quantifying the spectra of the emitted light from a (n-ZnO wire)–(p-GaN film) LED under different applied strain. (**a**) The four emission bands derived using deconvolution from the data shown in Fig. 10.1(b). (**b**) Change in relative peak height as a function of the external strain. (**c**) Dependence of the peak position on the applied strain. (**d**) The ratio of the emitted UV-to-visible intensities as a function of the strain [5]

holes. When these two complementary effects co-exist, one may balance the other, resulting in negligible shift in emission peaks.

10.7 Piezo-Phototronic Effect on LED

10.7.1 Fundamental Physical Process

When the n-ZnO wire/p-GaN substrate LED is under axial straining, two typical effects influence the output light intensity and spectra. One is the piezoresistance effect, which is caused by the change in bandgap and possibly density of states in the conduction band. This effect acts as adding a series resistance to the LED. The second effect is the piezo-phototronic effect [12], which concerns the tuning of the optoelectronic process at the interface using the piezopotential created along the ZnO wire. ZnO has a non-central symmetric crystal structure, in which the cations and anions are tetrahedrally coordinated. A straining on the basic unit results in a polarization of the cations and anions, which is the cause of the piezopotential inside the crystal. As for the ZnO (n-type)–GaN (p-type) LED, a schematic diagram of its

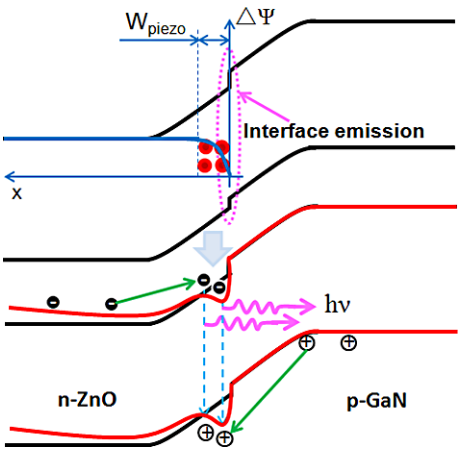

Fig. 10.9 Proposed mechanism of the enhanced light emission under strain for a (n-ZnO wire)–(p-GaN film) LED. Schematic energy band diagram of the p–n junction without (*upper*) and with (*lower*, *red line*) applied compressive strain, where the channel created at the interface inside ZnO is due to the piezopotential created by strain. The *blue line* presents the potential profile along the x-axis (the $-c$-axis of ZnO wire) assuming positive piezo-charges distribute within a width of W_{piezo} adjacent to the interface. The *red dots* represent the local piezo-charges near the interface, which produces a carrier trapping channel. The slope of the *red line* in the lower image at the ZnO side represents the driving effect of piezopotential to the movement of the charge carriers [5]

band structure is presented in Fig. 10.9. The finite doping in the wire may partially screen the piezoelectric charges, but it cannot totally eliminate the piezoelectric potential if the doping level is low, thus a dip in the band is possible. This is proved by the numerous studies we have carried out for nanogenerators and piezotronics. The low-doping in ZnO wire here is consistent with our experiment results because the ZnO wire is fabricated by a high-temperature thermal evaporation process using pure ZnO powders as the source [13]. If the c-axis of the ZnO wire is pointing from the ITO side to the GaN side, as labeled in Fig. 10.9(b), the effect of the local negative piezopotential at the ITO side is equivalent to applying an extra forward biased voltage on the device. Thus, the depletion width and internal field are reduced under this additional component of forward biased voltage. Subsequently, the injection current and emitting light intensity under the same externally applied forward voltage increase when the device is strained. Alternatively, if the c-axis of the ZnO wire is reversed and pointing away from the GaN side, the GaN side has a lower piezopotential, which is equivalent to applying an extra reversely biased voltage on the device. The depletion width and internal field are thus increased, resulting in a reduction of the injection current and emitting light intensity with the increase of the applied strain. Experimentally, when manipulating the wires for fabricating devices, about 50 % of them have the c-axis of the wires pointing from the ITO side to the GaN side, while the other 50 % pointing in the reverse direction. For the 20 devices we have measured, about 50 % of the devices showed enhanced light emitting when

strained, while the remaining had reduced light-emitting intensity, consistent with the expected results. This fact also indicates that the observed enhancement in light emission is dominated by the polar piezopotential effect rather than any non-polar effects such as change in contact area and/or piezoresistance.

10.7.2 Effect of Strain on Band Profile of the Heterojunction

In LED, the output photon intensity in an unstrained and a strained LED could be given by [14]

$$\Phi_{\text{out}}(0) = \eta_{\text{ex}}(0)\frac{I(0)}{e} = mh\nu\eta_e(0)\eta_i(0)\frac{I(0)}{e}, \tag{10.1}$$

$$\Phi_{\text{out}}(\varepsilon) = \eta_{\text{ex}}(\varepsilon)\frac{I(\varepsilon)}{e} = mh\nu\eta_e(\varepsilon)\eta_i(\varepsilon)\frac{I(\varepsilon)}{e} \tag{10.2}$$

where m represents the percentage of the light being probed by the spectrometer or CCD, Φ_{out} is the recorded output light intensity, η_{ex} is the external efficiency, which describes the ratio of externally produced photon flux to the inject electron flux; η_e is the overall extraction efficiency that is related to the absorption and reflection of the light in the device; η_i is therefore simply the ratio of the generated photon flux to the electron injection flux. Strain will affect the output light intensity of LED through the effect on external efficiency and the amount of injection current.

A negative piezopotential along c-axis will be induced in the wire under in-plane a-axis compressive strain (Fig. 10.9(b)). The local band structure and internal field near the p–n junction will be changed/modified (Fig. 10.9(a)) including barrier height modification and band bending. In order to simplify the problem, we investigate the barrier height modification and band bending effects separately.

For barrier height modification, according to the Schokley equation, the p–n junction I–V characteristics without strain can be described as [15]

$$I(0) = I_0\left(e^{qV_A/nkT} - 1\right) \sim I_0 e^{qV_A/kT} \quad \text{if } V_A \gg kT/q, \tag{10.3}$$

$$I_0 = qA\left(\frac{D_N}{L_N}\frac{n_i^2}{N_A} + \frac{D_P}{L_P}\frac{n_i^2}{N_D}\right) \tag{10.4}$$

where q the unit electron charge, V_A is the external voltage on the p–n junction, T the temperature, n_i intrinsic carrier density. D_N, L_N, and N_A are referred to as diffusion coefficient and diffusion length of minority carrier holes, and the total number of acceptor density in a p-type material, respectively. D_P, L_P, and N_D are referred to as diffusion coefficient and diffusion length of the minority carrier electrons, and the total number of donor density in an n-type material, respectively. Assuming that the piezopotential drop across the junction is $\Delta\Psi$, the current flow through the p–n junction under strain can be described as

$$I(\varepsilon) = I_0\left(e^{(qV_A+\Delta\Psi)/kT} - 1\right) \sim I_0 e^{\frac{qV_A+\Delta\Psi}{kT}} \quad \text{if } (V_A + \Delta\Psi) \gg kT/q. \tag{10.5}$$

The change of current with strain can be determined by [20]

$$\ln\left(\frac{I(\varepsilon)}{I(0)}\right) = \Delta\Psi/kT. \tag{10.6}$$

When an in-plane stress σ_{xx} is added on the wire, the y-direction and z direction of the NW is free. The finite-element analysis method (COMSOL) is used to calculate the stress and piezopotential in the wire [21]. Generally speaking, according to the conventional theory of piezoelectricity and elasticity, the mechanical equilibrium and the direct piezoelectric effect can be described by the coupled constitutive equation:

$$\begin{cases} \sigma_p = c_{pq}\varepsilon_q - e_{kp}E_k, \\ D_i = e_{iq}\varepsilon_q + \kappa_{ik}E_k \end{cases} \tag{10.7}$$

where σ is the stress tensor, ε is the strain, E is the electric field, and D is the electric displacement. κ_{ik} is the dielectric constant, e_{iq} is the piezoelectric constant, and c_{pq} is the mechanical stiffness tensor. By considering the C_{6v} symmetry of a ZnO crystal (with wurtzite structure), c_{pq}, e_{kp}, and κ_{ik} can be written as

$$c_{pq} = \begin{vmatrix} c_{11} & c_{12} & c_{13} & 0 & 0 & 0 \\ c_{12} & c_{11} & c_{13} & 0 & 0 & 0 \\ c_{13} & c_{13} & c_{33} & 0 & 0 & 0 \\ 0 & 0 & 0 & c_{44} & 0 & 0 \\ 0 & 0 & 0 & 0 & c_{44} & 0 \\ 0 & 0 & 0 & 0 & 0 & \frac{(c_{11}-c_{12})}{2} \end{vmatrix}, \tag{10.8a}$$

$$e_{kp} = \begin{vmatrix} 0 & 0 & 0 & 0 & e_{15} & 0 \\ 0 & 0 & 0 & e_{15} & 0 & 0 \\ e_{31} & e_{31} & e_{33} & 0 & 0 & 0 \end{vmatrix}, \tag{10.8b}$$

$$\kappa_{ik} = \begin{vmatrix} \kappa_{11} & 0 & 0 \\ 0 & \kappa_{11} & 0 \\ 0 & 0 & \kappa_{33} \end{vmatrix}. \tag{10.8c}$$

For ZnO, we have $c_{11} = 207$ GPa, $c_{12} = 117.7$ GPa, $c_{13} = 106.1$ GPa, $c_{33} = 209.5$ GPa, $c_{44} = 44.8$ GPa, and $c_{55} = 44.6$ GPa. The relative dielectric constants are $\kappa_{11} = 7.77$ and $\kappa_{33} = 8.91$, and the piezoelectric constants are $e_{31} = -0.51$ C/m^2, $e_{33} = 1.22$ C/m^2, and $e_{15} = -0.45$ C/m^2 [21].

The electrostatic behavior of charges can be described by the Poisson equation:

$$\nabla \cdot D = \rho(x, y, z) \tag{10.9}$$

where D is the electric displacement, ρ is the charge density. For a one-dimensional problem, this reduces to a more useful form of:

$$\kappa_{ik}\frac{d^2\Delta\psi_i}{dx^2} = -\kappa_{ik}\frac{d\Delta E}{dx} = -\rho \tag{10.10a}$$

where ψ_i is electrical potential. The conductivity of the ZnO is ignored in the simulation for simplicity, which is valid if the density of doping/vacancy is low, which means that

$$\nabla \cdot D = \rho(x, y, z) = 0. \tag{10.10b}$$

In order to solve the problem, we also need the mechanical equilibrium condition assuming there is no body force on the wire:

$$\nabla \cdot \sigma = 0. \tag{10.11}$$

The compatibility equation is a geometrical constraint that must be satisfied by strain ε:

$$e_{ilm} e_{jpq} \frac{\partial^2 \varepsilon_{mp}}{\partial x_l \partial x_q} = 0. \tag{10.12}$$

The fully coupled equations (10.9)–(10.12) along with appropriate boundary conditions give a complete description of a static piezoelectric system [5].

The maximum potential along the c-axis can also be estimated assuming there is a uniform stress along a-axis of the wire ($\sigma_{xx} \neq 0$, other $\sigma = 0$) and only considering the direct piezoelectric effect:

$$|\Delta\Psi| \sim (e_{31}\varepsilon_{xx} + e_{31}\varepsilon_{yy} + e_{33}\varepsilon_{zz}) L_\varepsilon / \kappa \tag{10.13}$$

where e_{31} and e_{33} are the linear piezoelectric coefficients, ε_{xx}, ε_{yy}, and ε_{zz} the strain tensors along a-, b-, and c-axis of the wire, L_ε the effective length of the wire under strain. Equation (10.13) shows that the piezopotential has a linear relationship with the external strain. Generally, we can expect that $\ln(\frac{I(\varepsilon)}{I(0)})$ of the p–n junction have a linear relationship with the external strain (Fig. 10.1(d)).

The localized positive piezopotential of ZnO near the interface will induce band bending to form electron and hole channels (Fig. 10.9(a)) near the ZnO/GaN interface which can be predicted from the Poisson equation. The piezopotential is solved by the Poisson equation by assuming that the piezoelectric charge distribute near the interface of a p–n junction within a width of W_{piezo} as shown in Fig. 10.9(a):

$$\kappa_{ik} \frac{d^2 \Delta\psi_i}{dx^2} = -\Delta\rho(x) = -\rho_{\text{piezo}}(x). \tag{10.14}$$

We got the solution when assuming $\rho = 0$ outside the piezo-charge area as the boundary conditions:

$$\Delta\psi(x) = \frac{1}{\kappa}\rho_{\text{piezo}}\left(W_{\text{piezo}} - \frac{x}{2}\right)x \quad \text{for } 0 \leq x \leq W_p, \tag{10.15a}$$

$$\Delta\psi(x) = \frac{1}{2\kappa}\rho_{\text{piezo}} W_{\text{piezo}}^2 \quad \text{for } x > W_p. \tag{10.15b}$$

The potential profile is depicted in Fig. 10.10. The band profile under strain is the coupling of piezopotential and strain free band profile of p–n junction (the red line

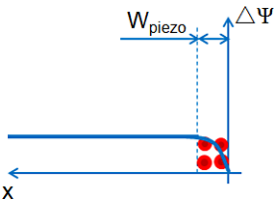

Fig. 10.10 Potential profile along the x-axis (the $-c$-axis of ZnO wire) assuming positive piezo-charges (*red dots*) distribute within a width of W_{piezo} adjacent to the interface

in the lower image of Fig. 10.9). Thus, a negative drop will form near the interface. If the drop is large enough in a small distance, electron and hole channels will be created near the interface. Electrons and holes are to be trapped in the electron and hole channels, respectively. The trapped holes increase the holes injection from p-GaN to n-ZnO, which will increase the recombination efficiency between electrons and holes near the interface. Combining (10.1), (10.2) and (10.6), the output light intensity of the LED under strain is related to the injection current and external efficiency under strain by

$$\ln\left(\frac{\Phi_{\text{out}}(\varepsilon)}{\Phi_{\text{out}}(0)}\right) = \ln\left(\frac{I(\varepsilon)}{I(0)}\right) + \ln\frac{\eta_{\text{ex}}(\varepsilon)}{\eta_{\text{ex}}(0)} = \frac{\Delta\Psi}{kT} + f(\varepsilon) \tag{10.16}$$

where $\eta_{\text{ex}}(\varepsilon)$ and $\eta_{\text{ex}}(0)$ represent the output external efficiency of LED with and without applying a strain, respectively, k is the Boltzmann constant, T is temperature, and $f(\varepsilon)$ represents the effect of strain on external efficiency. It is expected that the $\ln[\Phi_{\text{out}}(\varepsilon)/\Phi_{\text{out}}(0)] - \varepsilon$ and $\ln[I(\varepsilon)/I(0)] - \varepsilon$ have a linear relationship with the external strain, as shown by the experimental data in Fig. 10.1(d). If the recombination efficiency can be increased by strain, it is expected that the rate at which the light output increases is larger than that the current increases.

The enhancement factor for light emission was larger than that for the injection current (Fig. 10.1(d)), which means that the quantum efficiency was enhanced with the increase of strain (see Fig. 10.1). The enhancement of external efficiency may be caused by the localized positive piezopotential near GaN/ZnO interface, which produces carrier trapping channels (see Fig. 10.9(a)). Electrons and holes can be temporarily trapped and accumulated in the channels in the conduction and valance band, respectively. Since abundant electrons are available in ZnO, for instance, the efficiency of the LED is largely dominated by the local concentration of holes because of the high activation energy of the most commonly used acceptor dopants (Mg) in GaN (~200 meV). The trapped holes may increase the hole injection from p-GaN into n-ZnO, which increases the recombination efficiency of electrons and holes near the junction, resulting in a large increase in emission intensity.

It must be pointed out that the model presented in Fig. 10.10 assumes that the polarization charges are at the interface of p–n junction. As for the case presented here, GaN is also a polar structure oriented with the polar direction parallel to the normal of the film. In such a case, the strain induced piezoelectric charges are at the interface regardless the orientation of ZnO microwire. Thus the above model can be used qualitatively understand the experimental results.

10.8 Strain Effect on Photon Polarization

The photoelastic effect can be investigated by studying the light polarization under different strain. Electroluminescence light propagates along the wire and oscillates in the wire due to interfere as a result of the end-surface reflection. The transmittance obeys the Airy equation [16]:

$$\Phi_T = \Phi_0 \frac{1}{1 + F \sin^2(\theta/2)}, \tag{10.17}$$

$$\theta = 2\pi s/\lambda, \tag{10.18}$$

$$F = 4R/(1-R)^2, \tag{10.19}$$

$$s = 2nL \tag{10.20}$$

where Φ_T is the intensity of the transmitted light detected by CCD camera, and Φ_0 is the total propagating light intensity including the reflected and transmitted light, R is reflectivity, n is the refractive index, L is the length of the wire, s is the optical path, λ is the light wavelength.

It is known that the refractive index n of ZnO is changed under strain, which will change the optical path and the phase of the transmitted light reaching the end of the wire [18]

$$s = s_0 + \Delta s = 2n_0 L + 2\Delta n L_\varepsilon = 2n_0 L + 2 \times \frac{1}{2} n^3 \beta \sigma L_\varepsilon, \tag{10.21}$$

$$\sigma = E\varepsilon \tag{10.22}$$

where n_0 is the native refractive index without strain, L is the total length of the wire, L_ε is the effective length of the wire under strain, β is the photoelastic coefficient, σ is the applied stress on the wire, ε is the applied strain on the wire, E is Young's modulus of ZnO. LED is a result of spontaneous emission polarized at various angles, but the guiding mode propagating along the ZnO wire is dominated by the $P_\perp$ modes whose polarization direction is perpendicular to the wire. Therefore, the Airy equation for the $P_\perp$ mode light of ZnO wire under strain could be written as

$$\Phi_{\text{out}}^{\perp} \sim \Phi_0^{\perp} \frac{1}{1 + F \sin^2[(2\pi n_0 L + \pi n_0^3 \beta E\ \varepsilon L_\varepsilon)/\lambda]} \tag{10.23}$$

where $\Phi_T^{\perp}$ is the transmitted light intensity in the $P_\perp$ modes detected by CCD camera, and $\Phi_0^{\perp}$ is the total propagating light intensity including the reflected and transmitted light. Since the large aspect ratio of the wire, the effect of strain on the optical path of the $P_\parallel$ modes, is much smaller than that on $P_\perp$ modes, the ratio of $\Phi_{\text{out}}^{//}/\Phi_{\text{out}}^{\perp}$ can be described by the equation

$$\Phi_{\text{out}}^{//}/\Phi_{\text{out}}^{\perp}(\varepsilon) \sim \left\{1 + \frac{4R}{(1-R)^2} \sin^2\left[\frac{\pi 2\pi n_0 L + \pi n_0^3 \beta E\ \varepsilon L_\varepsilon}{\lambda}\right]\right\}. \tag{10.24}$$

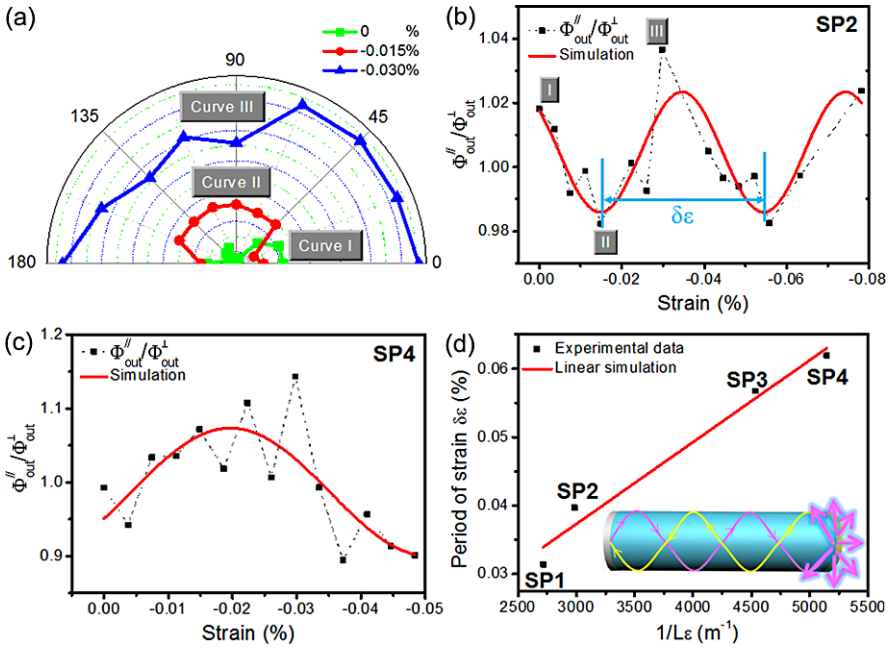

Fig. 10.11 Effects of strain on the polarization of the (n-ZnO wire)–(p-GaN film) emitted light. (**a**) Beam profile for the LED output under different strain as a function of the polarization angle. (**b**) The $\Phi^{//}_{out}/\Phi^{\perp}_{out}$ ratio of the device used for (**a**) under different strain, where the points corresponding to the curves *I*–*III* are labeled *I*–*III* marked. The period at which the intensity ratio varies is defined as $\delta\varepsilon$. (**c**) The $\Phi^{//}_{out}/\Phi^{\perp}_{out}$ ratio of device SP4 under different strain. (**d**) Plot of the measured strain varying period $\delta\varepsilon$ vs. the inverse of the effective length of the ZnO wire under strain. The *inset* shows a schematic standing wave within a Fabry–Pérot cavity (ZnO wire) for the $P_{\perp}$ modes [5]

According to the equation, when the change of optical path equals one wavelength λ,

$$\delta s = n^3 \beta E(\delta\varepsilon) L_\varepsilon = \lambda \tag{10.25}$$

the phase will have a change of 2π, corresponding to a period of $\Phi^{//}_{out}/\Phi^{\perp}_{out}$ modulation by changing strain (see Fig. 10.11(b)).

Thus,

$$\delta\varepsilon = \frac{\lambda}{n^3 \beta E} \frac{1}{L_\varepsilon} = b \frac{1}{L_\varepsilon} \tag{10.26}$$

where b the slope of the line curve in Fig. 10.11(d). The photoelastic coefficient could be derived by

$$\beta = \frac{\lambda}{b n^3 E}. \tag{10.27}$$

Figure 10.11(d) shows the strain periods $\delta\varepsilon$ versus the inverse of the length of the wire under strain $(1/L_\varepsilon)$. The strain period $\delta\varepsilon$ can be derived from the data simula-

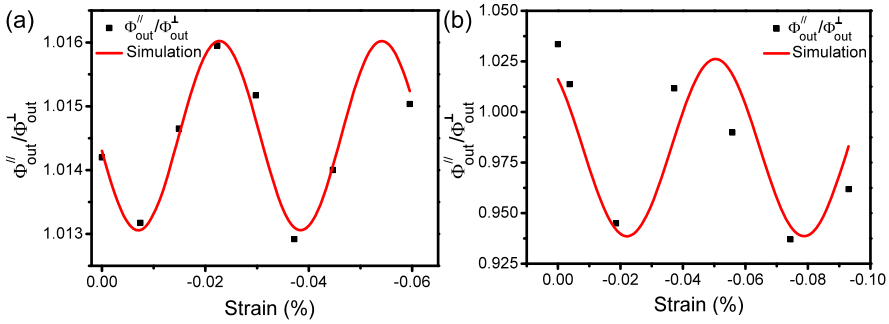

Fig. 10.12 $\Phi^{//}_{out}/\Phi^{\perp}_{out}$ as a function of strain of devices for devices SP1 and SP3, which are plotted in Fig. 10.11(d)

tion (Fig. 10.11(b)). Four periods of strain $\delta\varepsilon$ are 0.031 %, 0.040 %, 0.057 %, and 0.062 %, and the measured effective lengths are 368.0, 335.1, 220.6, and 194.4 μm, respectively. The Young modulus of ZnO and polystyrene is about 129 and 3 GPa, respectively. It can be seen that there is a linear relationship between $\delta\varepsilon$ and $1/L_{\varepsilon}$. From the slope of the curve, we can calculate the photoelastic coefficient, which is 3.20×10^{-12} m^2/N (395 nm wavelength).

The change in refraction index of ZnO is also possible under strain, which is the photoelastic effect. We investigated the photoelastic effect by studying the polarization behavior of the emission under applied strain. Figure 10.11(a) shows the electroluminescence intensity of a single wire LED as a function of the rotation angle of the polarizer in reference to the orientation of the wire. If $\Phi^{//}_{out}$ and $\Phi^{\perp}_{out}$ represent the intensities of the emission light when the polarization direction parallel ($P_{||}$ modes) and perpendicular ($P_{\perp}$ modes) to the wire, respectively, the dependence of $\Phi^{//}_{out}/\Phi^{\perp}_{out}$ on strain can be fit using a function of sine square (Figs. 10.11(b), (c), and 10.12), which may correspond to the resonance phenomenon of the Fabry–Pérot cavity inside the wire, as described in follows.

Spontaneous emission from LED is polarized at various angles, but the guiding modes propagating along the ZnO wire are dominated by the $P_{\perp}$ modes [5]. The propagating light along the wire may oscillate in the wire and interfere with each other due to end-surface reflection (Fig. 10.11(d), inset). The change of refractive index under strain affects the optical path length of the propagating light, resulting in a modulation in the interference pattern inside the wire and in light emission. On the other hand, since the large aspect ratio of the wire (typically more than 100), the effect of strain on the optical path of the $P_{||}$ modes is much smaller than that on $P_{\perp}$ modes. A simulation using (10.24) in reference to the data presented in Figs. 10.11 and 10.12 derives the photoelastic coefficient $\beta \sim 3.2 \times 10^{-12}$ m^2/N (at a wavelength of 395 nm) from the slope of the $\delta\varepsilon$ versus $1/L_{\varepsilon}$ curve, where $\delta\varepsilon$ is the strain period at which the $\Phi^{//}_{out}/\Phi^{\perp}_{out}$ oscillates. The β value is consistent with that reported for ZnO [17]. This study shows that it is possible to manipulate the polarization of a single wire LED through a proper externally applied strain.

Although our study has been focused on a single wire LED, an array of NWs with polarity control can be fabricated using a sweeping-printing-method [18] so that all of the NWs have the same *c*-axis orientation, and the nanowire array-based LEDs can be fabricated on a polymer substrate for flexible LEDs, through which a mechanical strain can be applied in a synchronized manner to uniformly enhance the output intensities of all NWs. Furthermore, electric driven polarized laser emission may also be possible by improving the reflectivity, increasing the driven current, improving the recombination efficiency, and solving the heating problem.

10.9 Electroluminescence Properties of p-Type GaN Thin Films

In this section, we present the electroluminescence (EL) properties of Mg-doped p-type GaN thin films: they can be tuned by piezo-phototronic effect via adjusting minority carrier injection efficiency at the metal-semiconductor (M–S) interface by strain induced polarization charges [19]. The device is a metal-semiconductor-metal structure of indium tin oxide (ITO)–GaN–ITO. Under different straining conditions, the changing trend of the transport properties of GaN films can be divided into two types in corresponding to the different *c*-axis orientations of the films. An extreme value was observed for the integral EL intensity under certain applied strain due to the adjusted minority carrier injection efficiency by piezoelectric charges introduced at the M–S interface. The external quantum efficiency of the blue EL at 430 nm was changed by 5.84 % under different straining conditions, which is one order of magnitude larger than the change of the green peak at 540 nm. The results indicate that the piezo-phototronic effect has a larger impact on the shallow acceptor states related EL process than the one related to the deep acceptor states in p-type GaN films. This study has great significance for the practical applications of GaN in optoelectronic devices under working environment where mechanical deformation is unavoidable such as for flexible/printable light-emitting diodes.

10.9.1 Piezo-Phototronic Effect on LED

Transparent ITO electrodes were fabricated on Mg-doped p-type GaN thin films to form a metal–semiconductor-metal (M–S–M) structure. When a constant voltage was applied, under different straining status, the current passing through the GaN film was increased or decreased step by step depending on the orientation of the *c*-axis of the film. Such a result is due to the tuning of the Schottky barrier height at the M–S contacts by the local piezoelectric charges introduced by strain. The intensity of the EL emitting from the M–S interface under the electrode was also modulated by the piezoelectric charges around this area under strain via adjusting minority carrier injection efficiency. An extreme value for the integral EL intensity was observed. The EL at 430 nm owing to the shallow acceptor states was more

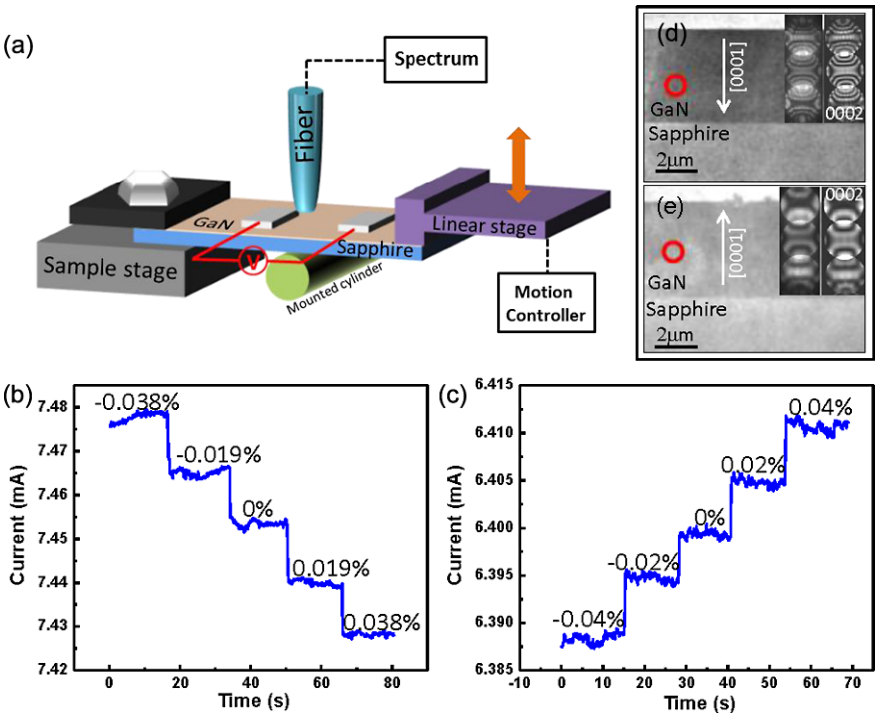

Fig. 10.13 (**a**) Schematic diagram of the experiment setup. Under a constant applied voltage, the current passing through the GaN film was (**b**) decreased or (**c**) increased step by step as the applied strain was increased. Devices with the former behavior are assigned to the first group, while devices with the latter behavior are assigned to the second group. (**d**) and (**e**) Corresponding TEM results for the GaN film structures in the devices belong to the first and the second group, respectively. The *left-hand parts of the inserts* are the CBED patterns taken from the *red circled areas*. The *right-hand parts* are the corresponding simulated patterns. From [19]

significantly affected by this piezo-phototronic effect than the emission at 540 nm that is related to the deep acceptor states. This study is significantly important for the GaN thin film's applications in optoelectronic devices.

The Mg-doped p-type GaN films used in this work were grown on sapphire (0001) substrates by low-pressure metal organic chemical vapor deposition (MOCVD). The samples were annealed for acceptor activation. The estimated concentration of Mg is around $3 \times 10^{19}/\text{cm}^3$, and the free hole concentration is around $8 \times 10^{17}/\text{cm}^3$. ITO electrodes were deposited on the surface of GaN film with a dimension of 2×2 mm. The distance between the two electrodes was around 1–2 mm. The experiment setup is shown in Fig. 10.13(a). One end of the substrate was fixed on a sample stage. A mounted cylinder was put underneath the substrate to support it with an adjusted position between two electrodes. A three-dimensional (3D) DC-motor linear stage with digital motion controller was used to push the free end of the substrate to introduce strain in the GaN film. The film can be stretched or compressed in parallel to the film plane by putting the substrate facing up or

facing down. The electrical measurement was carried out by using a Keithley 4200 semiconductor characterization system. A fiber coupled with a grating spectrometer (Acton SP-2356 Imaging Spectrograph, Princeton Instruments) was put near the electrode area just above the mounted cylinder to collect the EL spectrum. Such a setup can ensure the distance between the fiber and the GaN film to be consistent when the strain was applied. Current passing through the GaN film and the corresponding EL spectrum was recorded simultaneously under different straining conditions.

The experiment results show that when a constant voltage was applied between the two ITO electrodes, the measured current passing through the GaN film was changed step by step under different straining conditions. A linear relationship between the measured current and applied strain was obtained for all of the devices, but it can be divided into two groups with opposite trends. For the first group, as shown in Fig. 10.13(b), the current was decreased as the strain was increased. While for the second group, as indicated in Fig. 10.13(c), the current was increased as the strain was increased. In order to correlate the measured data with the crystallographic polar directions of the films, transmission electron microscopy (TEM) investigations were carried out using a Hitachi HF2000 operated at 200 kV. Cross-sectional samples were prepared for the thin films so that the GaN films and the sapphire substrates can be simultaneously captured. By using the convergent beam electron diffraction (CBED) technique, which is unique in determining the polar direction of the thin film in reference to the simulated CBED patterns, the results show that the two different behaviors as presented in Figs. 10.13(b) and (c) correspond to GaN films with opposite *c*-axis orientations in reference to the sapphire substrates, as shown in Figs. 10.13(d) and (e), respectively. The structures of both films are single crystals with a thickness around 4 μm. The interface between the GaN film and the sapphire is clear. The only difference is that for the first group, the *c*-axis of the GaN film points downward to the substrate, while it points upward from the substrate for the second group.

10.9.2 Theoretical Model

We take the case of the first group as an example to explain how the orientation of the *c*-axis plays a key role in the experimentally observed current dependence on the strain applied to the film. As shown in Fig. 10.14(a), the two ITO electrodes and the GaN film form an M–S–M structure. Due to the difference in work functions between ITO and GaN, two Schottky barriers (ϕ_o) were formed at the two M–S contacts. When a voltage is applied between the two electrodes, the path of the current going through the device is schematically indicated by a green dashed line in Fig. 10.14(a) (or going through in the opposite direction depending on the polarity of the applied voltage). When the substrate is bent in a curve so that the film is under tensile strain in parallel to the film plane (Fig. 10.14(b)), net piezoelectric charges are generated at the top and bottom surfaces of the GaN film. According to

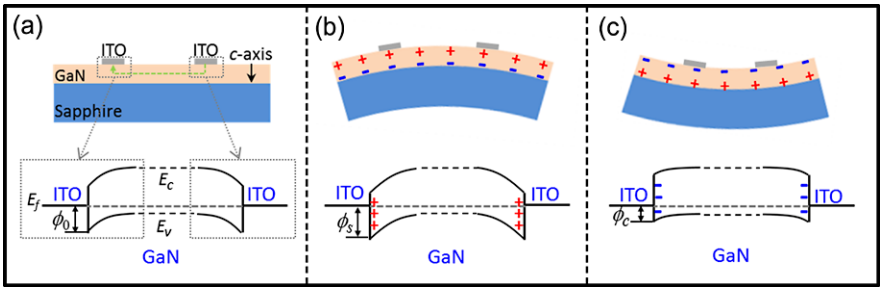

Fig. 10.14 (**a**) Device construction and corresponding energy band diagram. Two Schottky barriers (ϕ_o) were formed at the M–S contacts. Here we take the case of the p-GaN film with c-axis pointing downward to the substrate as an example. (**b**) When the GaN film is stretched in parallel to the film plane, positive piezoelectric charges are introduced at the top surface of the GaN film, resulting in an increased Schottky barrier height (ϕ_s). (**c**) When GaN film is compressed in parallel to the film plane, negative piezoelectric charges are introduced at the top surface of the GaN film, resulting in decreased Schottky barrier height (ϕ_c). From [19]

the orientation of the c-axis in this case, positive piezoelectric charges present at the top surface of the GaN film, which is the two ITO-GaN contact areas, as shown in Fig. 10.14(b). As a result, the Schottky barrier heights are increased at both contacts (ϕ_s, where $\phi_s > \phi_o$) (note that GaN is p-type). So, under a constant applied voltage, the measured current passing through the GaN film would be reduced. Alternatively, when the substrate is bent in a curve so that the film is under compressive strain in parallel to the film plane (Fig. 10.14(c)), negative piezoelectric charges are generated at the top surface of the GaN film, and the Schottky barrier heights at the two contacts are reduced (ϕ_c, where $\phi_c < \phi_o$). Thus, the measured current would be increased.

While for the devices in the second group with the c-axis orientation of the GaN film points upward from the substrate, when the film is under tensile strain in parallel to the film plan, negative piezoelectric charges are generated at the top surface of the GaN film. Thus, the Schottky barrier heights at the two contacts are reduced simultaneously, and the measured current passing through the GaN film is increased with the increase of strain. This is the result observed experimentally in Fig. 10.13(d). By the same token, the experimental data for the case when the film is under compressive strain in parallel to the film plane can be explained as well.

10.9.3 Analysis of Emission Characteristics

Under different straining conditions, the EL spectra were recorded from the electrode area that was under forward bias, e.g., with the GaN film having a higher potential than the ITO. Two dominant peaks were observed. One is located at 430 nm, which is related to the emission between conduction band or shallow donors to Mg shallow acceptors [20, 21], as shown in Fig. 10.15(a). The other one is located at

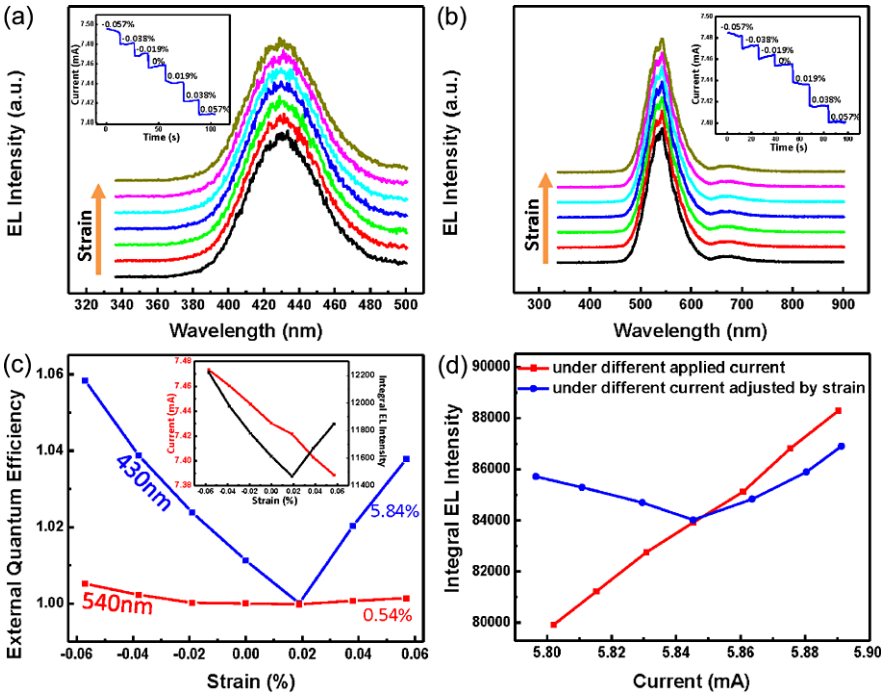

Fig. 10.15 Recorded EL spectra at (**a**) 430 nm and (**b**) 540 nm when different strain was applied to the GaN film under constant applied voltage. The vertical axes are shifted for clarity. The *insets* are the corresponding measured current response. (**c**) External quantum efficiency of EL emission at 430 nm and 540 nm when different strain was applied. The *inset* is the change of current and integral EL intensity under different strain condition corresponding to the data in (**a**). (**d**) The change of integral EL intensity due to the current change introduced by two different approaches. From [19]

540 nm, for which deep Mg acceptors are involved in the emission process [22, 23], as shown in Fig. 10.15(b). The inserts of these figures show corresponding current changes under different applied strain with a constant applied voltage. We can see that the current decreased as the applied strain increased, which indicates that the *c*-axis of the GaN film pointed downward to the sapphire substrate in this case, as we have discussed in the previous section. For both wavelength emissions, no shift in emission energy was observed when strain was applied or when the current passing through the GaN film was changed. The measured current has a linear relationship with the applied strain, but the integral EL intensity has a "V" shape, as shown in the insert of Fig. 10.15(c). When the applied strain was increased, first, the integral EL intensity was decreased as the measured current was decreased. But then it reached a minimal value and then went up while the current kept decreasing when strain was further increased. We can define the external quantum efficiency as the ratio of the integral EL intensity to the measured current, and normalize it using the minimum value for comparison purpose, which is plotted in Fig. 10.15(c). In addition to the

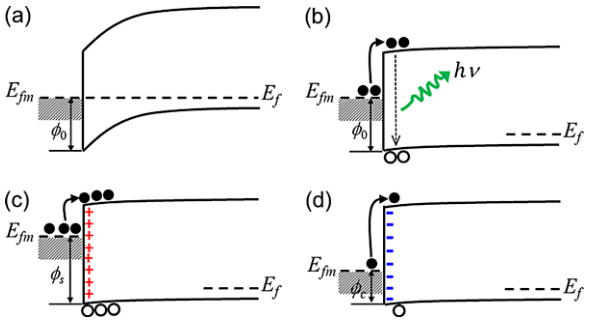

Fig. 10.16 Proposed working mechanism: (**a**) A Schottky barrier is formed at the ITO/GaN interface. (**b**) Under forward bias, electrons as the minority carriers inject from ITO to GaN, and recombine with holes in GaN accompanying with radiative emission. (**c**) When the GaN film is stretched in parallel to the film plane, positive piezoelectric charges are created at the interface. The injection efficiency of electrons from ITO to GaN is promoted, and thus the emission efficiency. (**d**) When the GaN film is compressed in parallel to the film plane, negative piezoelectric charges present at the interface. The injection efficiency of electrons from ITO to GaN is suppressed, and thus the emission efficiency. From [19]

observed minimal value, another very interesting thing is that the external quantum efficiency of blue EL emission at 430 nm was changed by 5.84 % under different applied strain, while for the emission at 540 nm, it was only changed by 0.54 %, which is one order of magnitude smaller. It seems that the shallow acceptor state related emission process is more sensitive to the M–S interface environment than the deep acceptor states related one. The mechanism of this phenomenon is still under investigation.

As we know that the magnitude of current passing through the GaN film plays a very important role on the EL emission intensity, but it is not the only determining factor. To elaborate on this, we compared the integral EL intensity change due to current change introduced by using two different approaches, as shown in Fig. 10.15(d). For the first approach, different current was applied directly to the device. A linear relationship was observed between the integral EL intensity and the applied current. For the second approach, the applied voltage was fixed. Then, by introducing different strain in the GaN film, the transport current can be tuned. In this case, a minimal value was observed for the integral EL intensity. When comparing these two cases, it is very interesting that, even under the same current condition, the integral EL intensity is obviously different for the two approaches. It means that, when strain is present in the film, there should be some factors that can change the ratio between the currents that contribute to the emission and non-emission processes. The strain induced piezoelectric charges at the ITO/GaN interface are suggested to be dominant.

As shown in Fig. 10.16(a), a Schottky barrier is formed at the ITO/GaN interface. To stimulate EL emission, the Schottky barrier is forward biased. In our experiments, normally the device is operated at a high voltage (larger than 20 V), so that a flat band condition is used here, as shown in Fig. 10.16(b). The current pass-

ing through the ITO/GaN interface is contributed from two parts: the flow of holes from GaN to ITO and the flow of electrons from ITO to GaN. For the EL emission process, we are more interested in the latter process, which it is the injection of minority carriers into the p-type GaN. The injected minority carriers can then recombine with holes radiatively in the GaN, as shown in Fig. 10.16(b). Thus, the injection efficiency of minority carriers at the interface plays a very important role on the luminescence efficiency [24]. When the GaN film was under tensile strain in parallel to the film plane (applied strain > 0), positive piezoelectric charges showed up at the ITO/GaN interface, and the Schottky barrier height for holes was increased (ϕ_s), while the barrier for electron injection from ITO to GaN was decreased, as shown in Fig. 10.16(c). Also the positive piezoelectric charges at the interface in GaN will attract more electrons diffusing from the ITO side. Both of them will enhance the injection efficiency of minority carriers, and therefore the luminescence efficiency. This is the reason for the observed phenomenon that, although the total current passing through the GaN film was reduced step by step, the obtained integral EL intensity started to increase under certain straining conditions, as in the results shown in Fig. 10.16(c). Starting from this point, although the total current is reduced, the part of the current contributing to the EL emission process is increasing due to the enhanced injection efficiency of electrons at the ITO/GaN interface, which is the result of introduced positive piezoelectric charges around this area, or the piezo-phototronic effect. When the GaN film was compressed in parallel to the film plane (applied strain < 0), negative piezoelectric charges showed up at the ITO/GaN interface, as shown in Fig. 10.16(d). The barrier for electron injection at the interface was increased, and the negative piezoelectric charges in the GaN would also resist the injection of electrons. So, the injection efficiency of minority carriers was decreased and therefore the luminescence efficiency. This is why the integral EL intensity for the same device is lower when the GaN film was compressed than when it was in a non-straining status even under the same current condition, as the right part of the plot shown in Fig. 10.15(d). Our former theoretical simulations have predicted that the strain induced piezoelectric charges can adjust the minority carrier injection at the interface of a p–n junction [25]. Here, our experiment results demonstrated that this can also work on the Schottky barrier at the metal–semiconductor interface.

To further verify our proposed mechanism, we applied a constant current passing through the GaN film, and checked the change of the integral EL intensity under different straining conditions. The results are shown in Fig. 10.17. In such a situation, the change in EL intensity induced by current change is eliminated. The dominant factor here is the injection efficiency of the minority carriers. A linear relationship was obtained between integral EL efficiency and the applied strain. It means that, when the GaN film was stretched in parallel to the film plane, the positive piezoelectric charges at the interface of ITO/GaN will increase the contribution of the minority carrier injection in the total current, and thus the luminescence efficiency. While when the GaN film was compressed in parallel to the film plane, the negative piezoelectric charges at the interface will reduce the current contributed by the minority carrier injection, and thus the luminescence efficiency. It is consistent

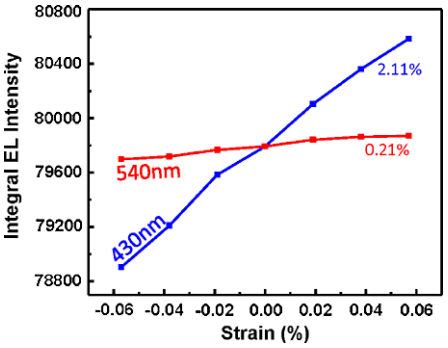

Fig. 10.17 When a constant current was applied on the device, a linear relationship was obtained between the integral EL intensity and the applied strain, consistent with our proposed working mechanism. From [19]

with our proposed mechanism. In this case, eliminating the current change effect, the integral EL intensity was modulated by 2.11 % for the emission at 430 nm, and 0.21 % for the emission at 540 nm due to the piezo-phototronic effect under different straining conditions. Because the current is constant here, it is equal to the changes of the external quantum efficiency.

10.10 Summary

As a classical device, the performance of an LED is dictated by the structure of the p–n junction and the characteristics of the semiconductor materials. Once an LED is made, its efficiency is determined largely by the local charge carrier densities and the time at which the charges can remain at the vicinity of the junction. The latter is traditionally controlled by growing a quantum well or using a built-in electronic polarization for "trapping" electrons and holes in the conduction and valance bands, respectively. Instead of using this pre-fabricated structure, we have introduced the piezopotential created in ZnO by strain to control the charge transport process at the ZnO–GaN interface, demonstrating the first LED whose performance is controlled by piezoelectric effect [5]. The emission intensity and injection current at a fixed applied voltage have been enhanced by a factor of 17 and 4 after applying a 0.093 % compressive strain, respectively, and the corresponding conversion efficiency has been improved by a factor of 4.25 in reference to that without applying strain! An external efficiency of 7.82 % has been achieved. This hugely improved performance is not only attributed to the increase of injection current by the modification of the band profile, but also to the more elegant effect of the creation of a trapping channel for holes near the heterojunction interface, which greatly enhances the external efficiency. An increase in UV-to-visible ratio and stabilization of the peak position show that the spectrum quality is improved by external straining. In addition, the polarization of the output light has been modulated by the piezooptic effect. Our discovery is important not only for exploring the piezo-phototronic effect through a three-way coupling among mechanical, electronical, and optical properties, but also can largely improve the efficiency and performance of LEDs and the design of a

large range of optoelectronic devices based on ZnO and GaN with the use of their piezoelectric property.

Lastly, piezo-phototronic effect on EL of GaN thin films was investigated. By depositing transparent ITO electrodes on the film, a metal-semiconductor-metal structure was formed. When strain was applied to the GaN film, the induced piezoelectric charges at the ITO/GaN interface modified the Schottky barrier height and two kinds of changing trend of the transport properties were obtained depending on the *c*-axis orientations of the GaN films. Also these piezoelectric charges changed the minority carrier injection efficiency at the M–S interface, which resulted in a modification of the EL emission intensity. The piezo-phototronic effect has a more pronounced effect on the EL emission process involving the shallow acceptor states than the one involving the deep acceptor states in the p-type GaN thin films. As a dominant material for the optoelectronic devices, this study provides a further understanding of the GaN, and may be significant for its future applications in flexible optoelectronics.

References

1. T. Fujii, Y. Gao, R. Sharma, E.L. Hu, S.P. DenBaars, S. Nakamura, Increase in the extraction efficiency of GaN-based light-emitting diodes via surface roughening. Appl. Phys. Lett. **84**(6), 855–857 (2004)
2. X. Duan, Y. Huang, R. Agarwal, C.M. Lieber, Single-nanowire electrically driven lasers. Nature **421**, 241–245 (2003)
3. M.A. Zimmler, D. Stichtenoth, C. Ronning, W. Yi, V. Narayanamurti, T. Voss, F. Capasso, Scalable fabrication of nanowire photonic and electronic circuits using spin-on glass. Nano Lett. **8**(6), 1695–1699 (2008)
4. S. Xu, C. Xu, Y. Liu, Y.F. Hu, R.S. Yang, Q. Yang, J.H. Ryou, H.J. Kim, Z. Lochner, S. Choi, R. Dupuis, Z.L. Wang, Ordered nanowire array blue/near-UV light emitting diodes. Adv. Mater. **22**(42), 4749–4753 (2010)
5. Q. Yang, W.H. Wang, S. Xu, Z.L. Wang, Enhancing light emission of ZnO microwire-based diodes by piezo-phototronic effect. Nano Lett. **11**(9), 4012–4017 (2011)
6. J.M. Bao, M.A. Zimmler, F. Capasso, X.W. Wang, Z.F. Ren, Broadband ZnO single-nanowire light-emitting diode. Nano Lett. **6**(8), 1719–1722 (2006)
7. B. Weintraub, Y.G. Wei, Z.L. Wang, Optical fiber/nanowire hybrid structures for efficient three-dimensional dye-sensitized solar cells. Angew. Chem., Int. Ed. Engl. **48**(47), 8981–8985 (2009)
8. L.B. Shi, S. Cheng, R.B. Li, L. Kang, J.W. Jin, M.B. Li, C.Y. Xu, A study on strain affecting electronic structure of wurtzite ZnO by first principles. Mod. Phys. Lett. B **23**(19), 2339–2352 (2009)
9. W. Shan, W. Walukiewicz, J.W. Ager, K.M. Yu, Y. Zhang, S.S. Mao, R. Kling, C. Kirchner, A. Waag, Pressure-dependent photoluminescence study of ZnO nanowires. Appl. Phys. Lett. **86**(15), 153117 (2005)
10. V.Y. Davydov, N.S. Averkiev, I.N. Goncharuk, D.K. Nelson, I.P. Nikitina, A.S. Polkovnikov, A.N. Smirnov, M.A. Jacobsen, O.K. Semchinova, Raman and photoluminescence studies of biaxial strain in GaN epitaxial layers grown on 6H-SiC. J. Appl. Phys. **82**(10), 5097–5102 (1997)
11. M. Suzuki, T. Uenoyama, Strain effect on electronic and optical properties of GaN/AlGaN quantum-well lasers. J. Appl. Phys. **80**(12), 6868–6874 (1996)
12. Z.L. Wang, Piezopotential gated nanowire devices: piezotronics and piezo-phototronics. Nano Today **5**, 540–552 (2010)

13. Z.W. Pan, Z.R. Dai, Z.L. Wang, Nanobelts of semiconducting oxides. Science **291**, 1947–1949 (2001)
14. S.N. Cha, J.S. Seo, S.M. Kim, H.J. Kim, Y.J. Park, S.W. Kim, J.M. Kim, Sound-driven piezoelectric nanowire-based nanogenerators. Adv. Mater. **22**(42), 4726–4730 (2010)
15. X.D. Wang, J. Zhou, J.H. Song, J. Liu, N.S. Xu, Z.L. Wang, Piezoelectric field effect transistor and nanoforce sensor based on a single ZnO nanowire. Nano Lett. **6**(12), 2768–2772 (2006)
16. Y. Yang, J.J. Qi, Q.L. Liao, H.F. Li, Y.S. Wang, L.D. Tang, Y. Zhang, High-performance piezoelectric gate diode of a single polar-surface dominated ZnO nanobelt. Nanotechnology **20**, 125201 (2009)
17. J. Ebothe, W. Gruhn, A. Elhichou, I.V. Kityk, R. Dounia, A. Addou, Giant piezooptics effect in the ZnO-Er^{3+} crystalline films deposited on the glasses. Opt. Laser Technol. **36**(3), 173–180 (2004)
18. G.A. Zhu, R.S. Yang, S.H. Wang, Z.L. Wang, Flexible high-output nanogenerator based on lateral ZnO nanowire array. Nano Lett. **10**(8), 3151–3155 (2010)
19. Y.F. Hu, Y. Zhang, S.H. Wang, L. Lin, Y. Ding, G. Zhu, Z.L. Wang, Piezo-phototronic effect on electroluminescence properties of p-type GaN thin films. Nano Lett. **12**(7), 3851–3856 (2012)
20. U. Kaufmann, M. Kunzer, M. Maier, H. Obloh, A. Ramakrishnan, B. Santic, P. Schlotter, Nature of the 2.8 eV photoluminescence band in Mg doped GaN. Appl. Phys. Lett. **72**(11), 1326–1328 (1998)
21. B.Z. Qu, Q.S. Zhu, X.H. Sun, S.K. Wan, Z.G. Wang, H. Nagai, Y. Kawaguchi, K. Hiramatsu, N. Sawaki, Photoluminescence of Mg-doped GaN grown by metalorganic chemical vapor deposition. J. Vac. Sci. Technol. A **21**(4), 838–841 (2003)
22. J. Neugebauer, C.G. Van de Walle, Gallium vacancies and the yellow luminescence in GaN. Appl. Phys. Lett. **69**(4), 503–505 (1996)
23. C.G. Van de Walle, Interactions of hydrogen with native defects in GaN. Phys. Rev. B **56**(16), R10020–R10023 (1997)
24. P.J. Dean, T. Inoguchi, S. Mito, K.I. Pankove, Y.S. Park, B.K. Shin, Y.M. Tairov, Y.A. Vodakov, S. Wagner, in *Electroluminescence*, ed. by K.I. Pankove Springer, Berlin (1977)
25. Y. Zhang, Y. Liu, Z.L. Wang, Fundamental theory of piezotronics. Adv. Mater. **23**, 3004–3013 (2011)

Chapter 11
Piezo-Phototronic Effect on Electrochemical Processes and Energy Storage

Abstract Photoelectrochemical (PEC) processes are fundamental for photon water splitting and energy storages. The key to the PEC efficiency is dictated by the charge generation and separation processes. In this chapter, we present the piezoelectric on PEC, in which a consistent enhancement or reduction of photocurrent was observed when tensile or compressive strains were applied to the ZnO anode, respectively. The photocurrent variation is attributed to a change in barrier height at the ZnO/electrolyte interface. We also introduce a fundamental mechanism that directly hybridizes the two processes into one, using which the mechanical energy is directly converted and simultaneously stored as chemical energy without going through the intermediate step of first converting into electricity. By replacing the polyethylene (PE) separator as for conventional Li battery with a piezoelectric poly(vinylidene fluoride) (PVDF) film, the piezoelectric potential from the PVDF film as created by mechanical straining acts as a charge pump to drive Li ions to migrate from cathode to the anode accompanying with charging reactions at electrodes. This new approach can be applied to fabricating a self-charging power cell (SCPC) for sustainable driving micro/nano-systems and personal electronics.

Photoelectrochemical (PEC) processes are the fundamental of photon water splitting and energy storages. The key to the PEC efficiency is dictated by the charge generation and separation processes. In this chapter, we present two examples. The first study is about the piezoelectric PEC [1], in which a consistent enhancement or reduction of photocurrent was observed when tensile or compressive strains were applied to the ZnO anode, respectively. The photocurrent variation is attributed to a change in barrier height at the ZnO/electrolyte interface. The second example is a piezopotential driving diffusion of Li ions in a battery for demonstrating the self-charging power cell. It is a process of directly converting mechanical energy into chemical energy that integrates a nanogenerator and a battery into one package.

11.1 Basic Principle of Photoelectrochemical Process

The basic PEC process can be illustrated in Fig. 11.1. The system is made of a n-type semiconductor that is directly interfacing with an electrolyte. The counter elec-

Z.L. Wang, *Piezotronics and Piezo-Phototronics*, Microtechnology and MEMS,
DOI 10.1007/978-3-642-34237-0_11, © Springer-Verlag Berlin Heidelberg 2012

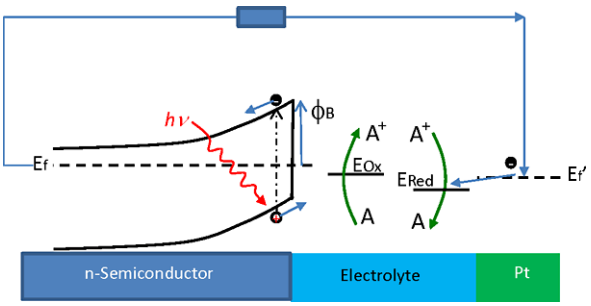

Fig. 11.1 Basic principle of a photoelectrochemical process expressed using a band diagram

trode is Pt. A natural Schottky barrier of height ϕ_B is present at the semiconductor-electrolyte interface. Once a photon with an energy higher than the bandgap of the semiconductor shines at the interface, an electron-hole pair is generated. The excited electron tends to drift toward the semiconductor side in the conduction band owing to the inclined band, which then is transported through the external load to the Pt electrode owing to a difference in Fermi level at the two sides. The hole drifts toward the electrolyte. If the energy possessed by the hole is more than the oxidation potential, it can stimulate an oxidation process to cover an A species into A^+. The electron at the Pt side is then recaptured by A^+ if the reduction potential is lower than the Fermi level of Pt, so that it is reduced into A. This is the process of converting photon energy into electricity through a redox process.

11.2 Piezopotential on the Photoelectrochemical Process

For the process shown in Fig. 11.1, the drift of the hole from the semiconductor to the electrolyte will be impossible of the oxidation potential E_{Ox} is significantly higher than the valence band edge of the semiconductor at the solid-liquid interface. In such a case, no charge exchange will be possible, and thus no redox process (Fig. 11.2(a)). For a piezoelectric semiconductor, if a tensile strain is applied to the semiconductor film so that the side directly interfacing with the electrolyte has a lower piezopotential, the valence band edge is up lifted so that it is close to the oxidation potential E_{Ox}, as shown in Fig. 11.2(b), the hole has enough energy to trigger the oxidation process. At the same time, the steeply raised conduction band at the electrolyte side accelerates the drift of the electron in the conduction band towards the ITO side. Furthermore, the valence band at the ZnO-ITO contact is lowered, reducing the local resistance or threshold voltage for electron transport. All of these processes are favorable for enhancing the efficiency of PEC.

Alternatively, by switching the strain to a compressive strain in the film, the local piezopotential at the electrolyte interface is high, as shown in Fig. 11.2(c), the lowered valance band reduces the energy of the hole so that it may not be effective to stimulate the redox process or at least at a reduced efficiency. Furthermore the flattened conduction band at the electrolyte side reduces the drifting speed of the electron toward the ITO side. The raised conduction band at the ITO side increases

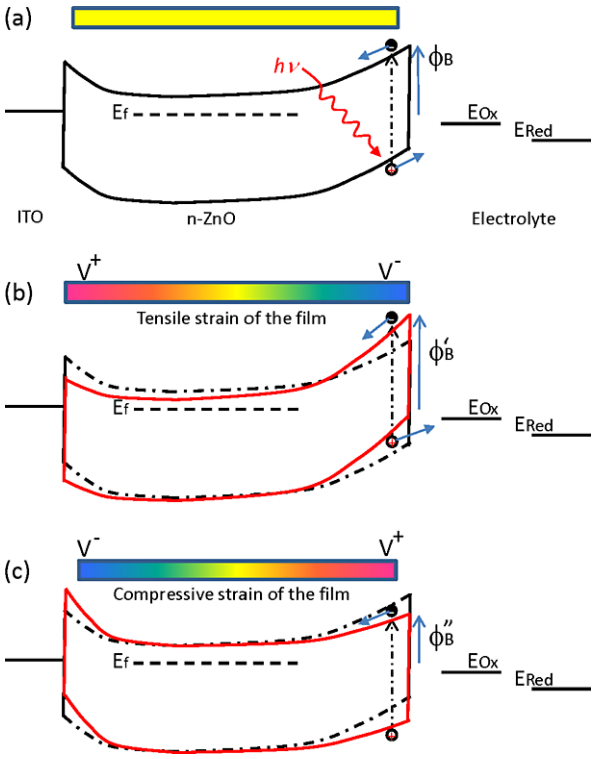

Fig. 11.2 Effect of piezopotential in the semiconductor on the photoelectrochemical process. (**a**) Band structure of the PEC with the absence of piezopotential. (**b**) Band structure of the PEC when the film is under tensile strain so that the side directly interfacing with the electrolyte has a lower piezopotential. (**c**) Band structure of the PEC when the film is under compressive strain so that the side directly interfacing with the electrolyte has a higher piezopotential

the threshold voltage and increases the local resistance. All of these processes can largely reduce the efficiency of PEC.

11.3 Photoelectrochemical Solar Cell

11.3.1 Design of the Cell

The piezoelectric PEC (PZ-PEC) anode was fabricated by sputtering a thin film of ZnO (~1 μm thick) on an ITO/PET substrate. Resistivity of the as-fabricated ZnO film was $\sim 10^7$ Ω cm, which could produce an appreciable piezopotential upon deformation as well as reasonable charge conductance for water oxidation under illumination. The device and measurement setup is schematically shown in Fig. 11.3(A).

The J–V characteristic of the ZnO PZ-PEC anode was measured without and with strain applied to the ZnO anode. At zero strain (black curve in Fig. 11.3(B)), photocurrent density (J_{ph}) of 0.54 mA/cm^2 was obtained at applied potential of 1.5 V versus saturated calomel electrode (SCE) under light intensity of

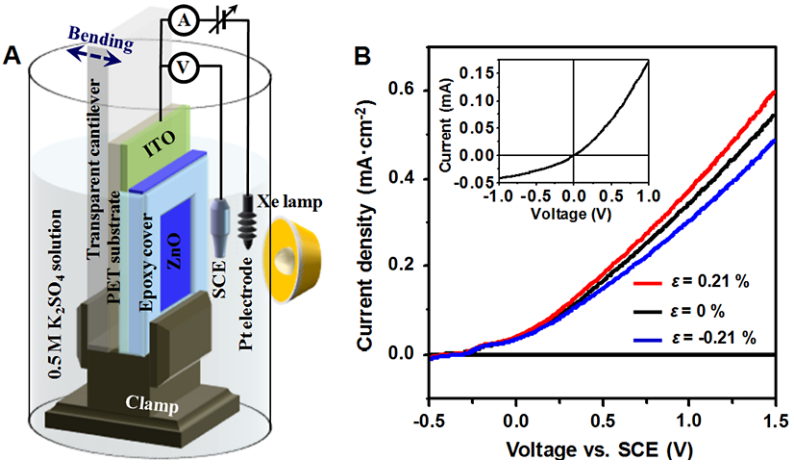

Fig. 11.3 Fundamentals of the PEC cell with piezoelectric ZnO as photoanode. (**A**) Schematic setup of the ZnO-based PZ-PEC half-cell for characterizing the piezoelectric effect-related water splitting reactions. (**B**) J–V curves and dark current density of ZnO PEC cell with and without strain applied to the ZnO thin film (Figure courtesy of [1])

100 mW/cm^2, demonstrating a considerable water oxidation rate. The dark current remained at a very low level (~5 μA/cm^2) under bias potentials between −0.5 and 1.5 V (vs. SCE) indicating the high quality of the ZnO surfaces.

The J–V curves were then collected when the ZnO anode was under strain. As shown in Fig. 11.3(B), an enhanced photocurrent (I_{ph}) was observed when a 0.21 % tensile strain was applied. At applied potential of 1.5 V versus SCE and under light intensity of 100 mW/cm^2, J_{ph} increased from ~0.54 mA/cm^2 to ~0.6 mA/cm^2 due to the tensile strain. The maximum efficiency was calculated from the J–V curves and a ~10.2 % efficiency increase was identified. The opposite effect was observed under 0.21 % compressive strain, which induced reduced J_{ph} (blue curve in Fig. 11.3(B)) and a ~8.5 % maximum efficiency drop (from 0.06 % to 0.055 %).

11.3.2 Piezo-Phototronic Effect on PEC

Figures 11.4(A) and (B) present the J_{ph} measured by the potentiostat when a constant strain was applied to the ZnO anode periodically [1], where the applied external bias was fixed as 1.5 V versus SCE. With a compressive strain of −0.12 %, J_{ph} decreased from 542 μA/cm^2 to 509 μA/cm^2 when the illumination intensity was 100 mW/cm^2. While with a tensile strain of 0.12 %, J_{ph} increased from 269 to 287 μA/cm^2 under a light intensity of 50 mW/cm^2. Small spikes could be observed from the J_{ph} profiles at the moment of applying and releasing strain when the light intensity was 50 mW/cm^2 (Fig. 11.4(B)). Response of J_{ph} on straining is swift and highly reproducible. More importantly, the J_{ph} change (ΔJ_{ph}) is independent of

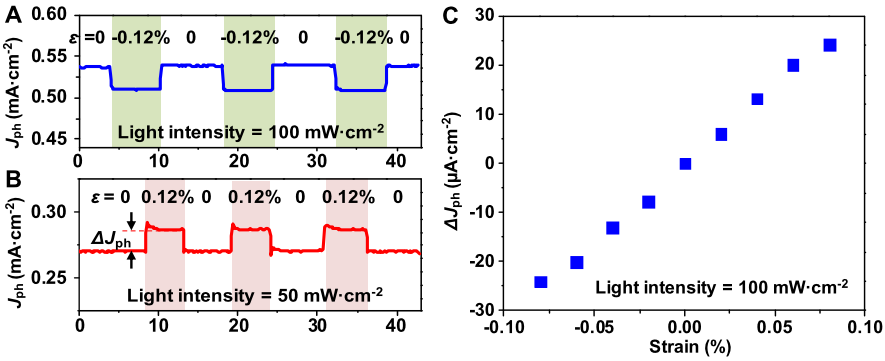

Fig. 11.4 PEC performance when ZnO was under static strains. (**A**) Photocurrent density (J_{ph}) of the ZnO PZ-PEC under periodic compressive strains (−0.12 %) at an applied bias of 1.5 V versus SCE. The strained regions are marked with a shade of light green. J_{ph} was collected under illumination of 100 mW/cm^2. (**B**) J_{ph} under periodic tensile strains when light intensity was 50 mW/cm^2 and applied bias was 1.5 V versus SCE. Current spikes can be observed at the moments of applying and releasing strain due to the lower light intensity. (**C**) Photocurrent density change (ΔJ_{ph}) as a function of applied strain under illumination of 100 mW/cm^2. The background J_{ph} was 540 μA/cm^2 and applied bias was 1.5 V versus SCE (Figure courtesy of [1])

time. No decay was observed during a period extending over hundreds of seconds, as long as the strain was held. Thus, ΔJ_{ph} is defined as the difference between the constant J_{ph} under strain and the J_{ph} base line when no strain was applied. The relationship between ΔJ_{ph} and strain is found to be approximately linear as shown in Fig. 11.4(C), where all data were collected under a light intensity of 100 mW/cm^2.

11.4 Piezopotential on Mechanical-to-Electrochemical Energy Conversion

In general, electricity generation and energy storage are two distinct processes that are accomplished through two different and separated physical units achieving the conversions of from mechanical energy to electricity and then from electric energy to chemical energy, respectively. The nanogenerator is an effective way of converting mechanical energy into electricity. The Li-ion battery [2–4] is one of the most effective approaches, in which the electric energy is stored as chemical energy through the migration of Li ions under the driving of an externally applied voltage source and the follow up electrochemical reactions occurring at the anode and cathode [5]. We have established a fundamental mechanism that directly hybridizes the two processes into one, through which the mechanical energy is directly converted and simultaneously stored as chemical energy, so that the nanogenerator and the battery are hybridized as a single unit [6]. Such an integrated self-charging power cell (SCPC), which can be charged up by mechanical deformation and vibration from

the environment, provides an innovative approach for developing new mobile power source for both self-powered systems and portable and personal electronics.

11.4.1 Working Principle of the Self-charging Power Cell

The working mechanism of the self-charging power cell is an electrochemical process driven by deformation created piezoelectric potential (Fig. 11.5) [6]. At the very beginning, the device is at a discharged state, with $LiCoO_2$ as the positive electrode (cathode) material and TiO_2 NTs as the negative electrode (anode), which is the originally fabricated structure of the device, and the $LiPF_6$ electrolyte is evenly distributed across the entire space, as shown in Fig. 11.5(a). A PVDF film, which has intimate contacts with both electrodes, serves as the separator and it has the smallest Young modulus among all of the components in the device [PVDF in electrolyte solvent: ~1.2 GPa; TiO_2: 100 GPa (Y_a) and 266 GPa (Y_c); $LiCoO_2$: ~70 GPa; Ti Foil: 100–110 GPa; Al Foil: 69 GPa], thus, it suffers from the most severe compressive strain when a compressive stress is applied onto the device, as shown in Fig. 11.5(b). We purposely use the PVDF film with the polarity that results in a positive piezoelectric potential (piezopotential) at the cathode ($LiCoO_2$) side and negative piezopotential at the anode (TiO_2) under compressive strain for separating the charges. Under the driving of the piezoelectric field with direction from the cathode to the anode, the Li ions in the electrolyte will migrate along the direction through the ionic conduction paths present in the PVDF film separator for ion conduction in order to screen the piezoelectric field, and finally reach the anode, as shown in Fig. 11.5(c) (note that a PVDF film is an ionic conductor for Li^+, which is why that PVDF is used as the base for polymer electrolyte and also the binder for electrodes in Li-ion batteries). The decreased concentration of Li^+ at the cathode will break the chemical equilibrium of the cathode electrode reaction ($LiCoO_2 \leftrightarrow Li_{1-x}CoO_2 + xLi^+ + xe^-$), so that Li^+ will deintercalate from $LiCoO_2$, turning it into $Li_{1-x}CoO_2$ and leaving free electrons at the current collector (Al foil) of the cathode electrode. This process is driven by the tendency of establishing new chemical equilibrium. In the meanwhile, under the elevated concentration of Li^+ at the anode, the reaction at the other electrode ($TiO_2 + xLi^+ + xe^- \leftrightarrow Li_xTiO_2$) will move to the forward direction for the same reason, enabling Li^+ to react with TiO_2 so that Li_xTiO_2 will be produced at the anode electrode, leaving the positive charges at the Ti foil as the current collector. During this process, Li^+ will continuously migrate from the cathode to the anode and the device is charged up a little bit owing to the large volume of the device.

During the progress of charging electrochemical reactions at the two electrodes, extra free electrons will transfer from the cathode to the anode, in order to maintain the charge neutrality and the continuity of the charging reaction. There are generally two ways for the electrons to transfer: either inside the battery system in some manner, or through the external circuitry. After comparing the self-charging behavior of

the SCPC with and without an outer circuitry (that is, the electrochemical workstation connected between cathode and anode, to monitor the change of voltage), we suggest that there should probably be some internal mechanisms for the electrons to transfer across the two electrode, although this exact process is still to be further investigated.

Under the mechanical deformation, the piezopotential continues to drive the migration of Li^+ ions until to a point when the chemical equilibriums of the two electrodes are re-established and the distribution of the Li^+ can balance the piezoelectric field in the PVDF film, with no Li^+ drifting through PVDF (Fig. 11.5(d)); that is to say, a new equilibrium is achieved and self-charging process will cease. This is the process of converting mechanical energy directly into chemical energy.

In the second step, when the applied force is released, the piezoelectric field of the PVDF disappears, which breaks the electrostatic equilibrium, so that a portion of the Li ions diffuse back from the anode to the cathode (Fig. 11.5(e)) and reach an even distribution of Li^+ all over the space in the device again (Fig. 11.5(f)). Then, a cycle of charging is completed through an electrochemical process of oxidizing a small amount of $LiCoO_2$ at cathode to $Li_{1-x}CoO_2$ and reducing a bit of TiO_2 to Li_xTiO_2 at the anode. When the device is mechanically deformed again, the process presented above is repeated, resulting in another cycle of charging by converting mechanical energy directly into chemical energy.

In this self-charging mechanism, the role played by the piezoelectric material (PVDF) is similar to the DC power supply used in the conventional charging process of a Li battery. Both of them can be deemed as charge pumps, but the specific mechanisms are different. As for the conventional charging method, the DC power supply will pump the electrons from the positive electrode to the negative electrode through the external circuit and the Li ions will go in the same direction but within the cell, in order to retain a neutral charge balance. Thus the electrochemical reactions on the two electrodes occur and the battery is charged up. But for our SCPC proposed here, the piezoelectric material pumps the Li^+ ions, rather than the electrons, from the positive to the negative electrode, which also accomplishes the charging of the device. This mechanism can also be explained by thermodynamics. According to Nernst's theory, the relative electrode potentials of the two electrodes have the following relationships with Li^+ concentration:

$$\varphi_{Li_{1-x}CoO_2/LiCoO_2} = \varphi^o_{Li_{1-x}CoO_2/LiCoO_2} - \frac{RT}{F}\ln\frac{1}{[a_c(Li^+)]^x},$$

$$\varphi_{TiO_2/Li_xTiO_2} = \varphi^o_{TiO_2/Li_xTiO_2} - \frac{RT}{F}\ln\frac{1}{[a_a(Li^+)]^x}$$

where $\varphi_{Li_{1-x}CoO_2/LiCoO_2}$ and $\varphi_{TiO_2/Li_xTiO_2}$ are actual electrode potentials of cathode and anode, $\varphi^o_{Li_{1-x}CoO_2/LiCoO_2}$ and $\varphi^o_{TiO_2/Li_xTiO_2}$ are standard electrode potentials of these two electrodes, and $a_c(Li^+)$ and $a_a(Li^+)$ are the activities of Li^+ around cathode and anode, respectively, which can be approximately equated to the

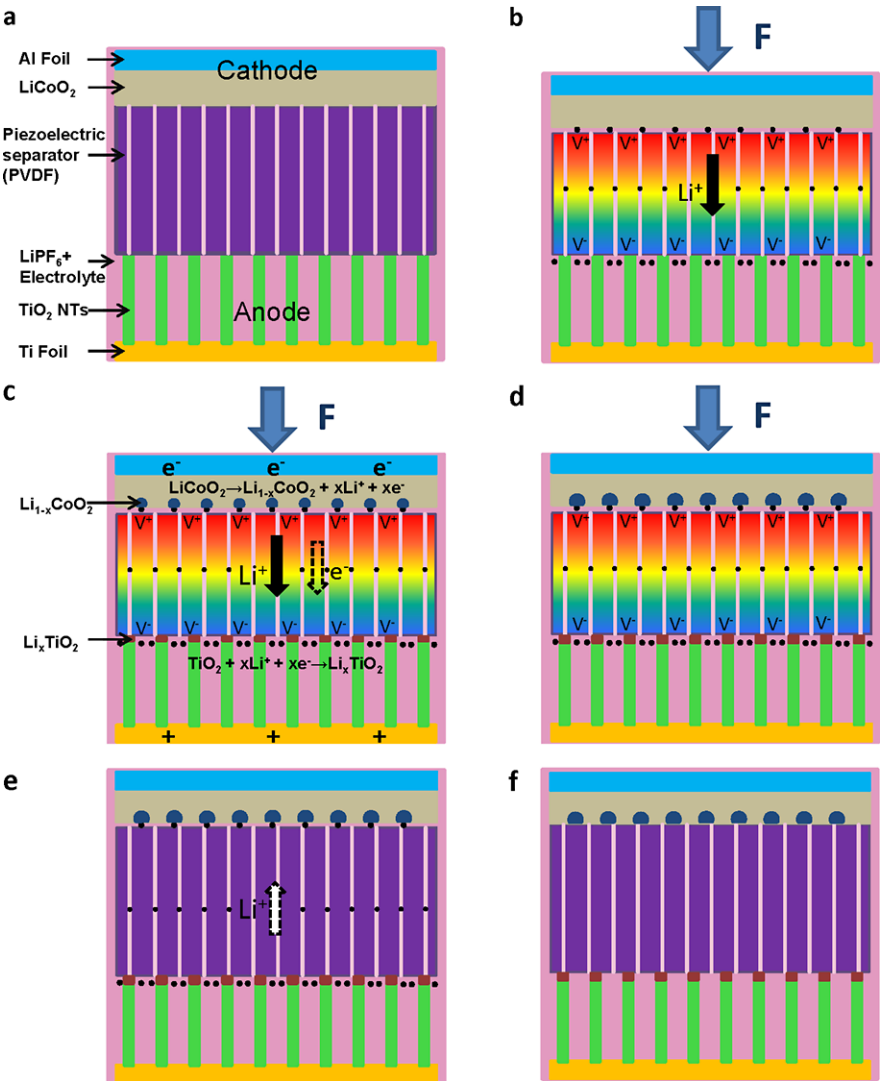

Fig. 11.5 The working mechanism of the self-charging power cell driven by compressive straining. (**a**) Schematic illustration of the self-charging power cell in discharged state with $LiCoO_2$ as cathode and TiO_2 nanotubes as anode. (**b**) When a compressive stress is applied onto the device, the piezoelectric separator layer (e.g., PVDF film) creates a piezopotential, with the positive polarity at the cathode side and negative piezopotential at the anode. (**c**) Under the driving of the piezoelectric field, the Li ions from the cathode will migrate through the PVDF film separator in the electrolyte toward the anode, leading to the corresponding charging reactions at the two electrodes. The free electrons at the cathode and positive charges at the anode will dissipate inside the device system. (**d**) The status where chemical equilibrium of the two electrodes is re-established and the self-charging process ceases. (**e**) When the applied force is released, the piezoelectric field of the PVDF disappears, which breaks the electrostatic equilibrium, so that a portion of the Li ions will diffuse back to the cathode. (**f**) This electrochemical system reaches a new equilibrium, and a cycle of self-charging is completed [6]

concentrations, R is the gas constant, T is the temperature, and F is the Faraday constant. Thus, under the driving of piezoelectric field, because of depleting of Li^+ concentration near the positive electrode, the electrode potential $\varphi_{Li_{1-x}CoO_2/LiCoO_2}$ will decrease; likewise, the elevation of Li^+ concentration will result in an increase of $\varphi_{TiO_2/Li_xTiO_2}$ at the negative electrode. For a conventional Li-ion battery, the electrode potential $\varphi_{Li_{1-x}CoO_2/LiCoO_2}$ is larger than $\varphi_{TiO_2/Li_xTiO_2}$, so that the battery can discharge spontaneously through the reduction of $Li_{1-x}CoO_2$ and oxidization of Li_xTiO_2. But for the self-charging process, because the change of Li^+ concentration will possibly make $\varphi_{TiO_2/Li_xTiO_2}$ larger than $\varphi_{Li_{1-x}CoO_2/LiCoO_2}$, the device is self-charged through the reduction of TiO_2 and oxidization of $LiCoO_2$.

11.4.2 Design of the Self-charging Power Cell

The experimental design of a self-charging process is based on the characteristics of both piezoelectric and electrochemical properties, as schematically shown in Fig. 11.6(a) [6]. The device is based on a sealed stainless-steel 2016-coin-type cell, as shown in the highlight of Fig. 11.6(b). The SCPC is composed of three major components: anode, separator, and cathode. The anode is made of aligned TiO_2 nanotube (NT) arrays that are directly grown on a Ti foil. Instead of using the polyethylene (PE) separator as for traditional lithium ion battery, a layer of polarized poly(vinylidene fluoride) (PVDF) film is located above the TiO_2 nanotube arrays as the separator. This PVDF film can establish a piezoelectric potential across its thickness under externally applied stress, which not only converts mechanical energy into electricity, but also serves as the driving force for the migration of Li ions. The cathodes are $LiCoO_2$/conductive carbon/binder mixtures on aluminum foils. Fig. 11.6(c) is a cross-sectional scanning electron microscopy (SEM) image of the sandwich structure of the device. The TiO_2 nanotube arrays with anatase crystal structure were fabricated on Ti substrate using an anodization method with a post-annealing process in air [6] (Method Summary). The height and diameter of the nanotubes are about 20 μm and 100 nm, respectively, as shown in Fig. 11.6(d). A commercial piezoelectric PVDF film with a thickness of ~110 μm is mainly composed of β phase and α phase, and it has been prior poled before assembly into the battery. After placing $LiCoO_2$ cathode with a thickness of 20 μm on the other side, the system was filled with electrolyte (1 M $LiPF_6$ in 1:1 ethylene carbonate: dimethyl carbonate) and finally sealed for measurements. The galvanostatic charge-discharge measurements, with comparison to traditional Li-ion batteries using PE as separators, proved that the power cells act also as a battery system. Periodic deformations were applied onto the device in order to charge it up (Fig. 11.6(b)), and the voltage and current were monitored simultaneously in both charging and discharging processes.

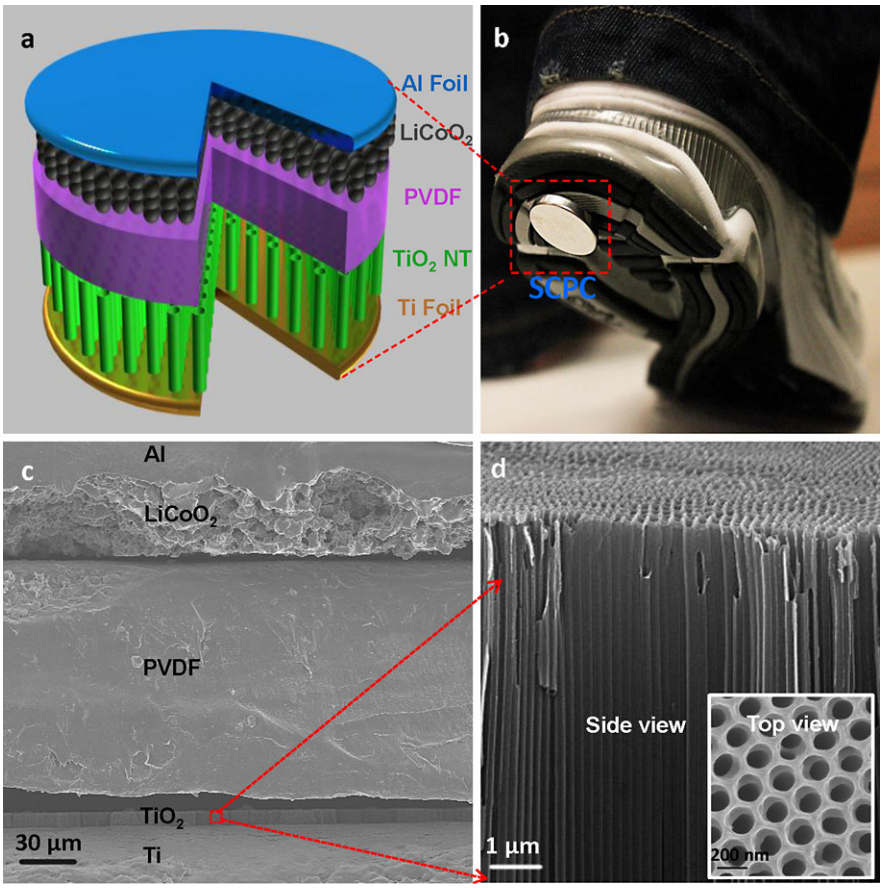

Fig. 11.6 Structure design of a self-charging power cell by hybridizing a piezoelectric nanogenerator and a Li-ion battery. (**a**) Schematic diagram showing the design and structure of the self-charging power cell. The anode is aligned TiO_2 nanotube arrays that are directly grown on Ti foils; a layer of polarized PVDF film performs as the separator; the cathode is $LiCoO_2$ mixture on aluminum foil. This structure is sealed in stainless-steel 2016-coin-type cells, as shown in the inset. (**b**) Sticking a power cell on the bottom of a shoe, the compressive energy generated by walking can be converted and stored directly by SCPC. (**c**) Cross-sectional SEM image of the self-charging power cell, which is composed of aligned nanotubes as anode, piezoelectric polymer film as separator and cathode. (**d**) Enlarged view of the aligned TiO_2 nanotubes. The *inset* is a top view SEM image of the nanotubes [6]

11.4.3 Performance of the Self-charging Power Cell

By using a mechanical setup that can provide a periodic compressive stress onto the device, we demonstrated the self-charging process of the power cell [6]. Figure 11.7(a) is a typical self-charging and discharging cycle. Under the compressive force applied to the SCPC at a frequency of 2.3 Hz, the voltage of the device in-

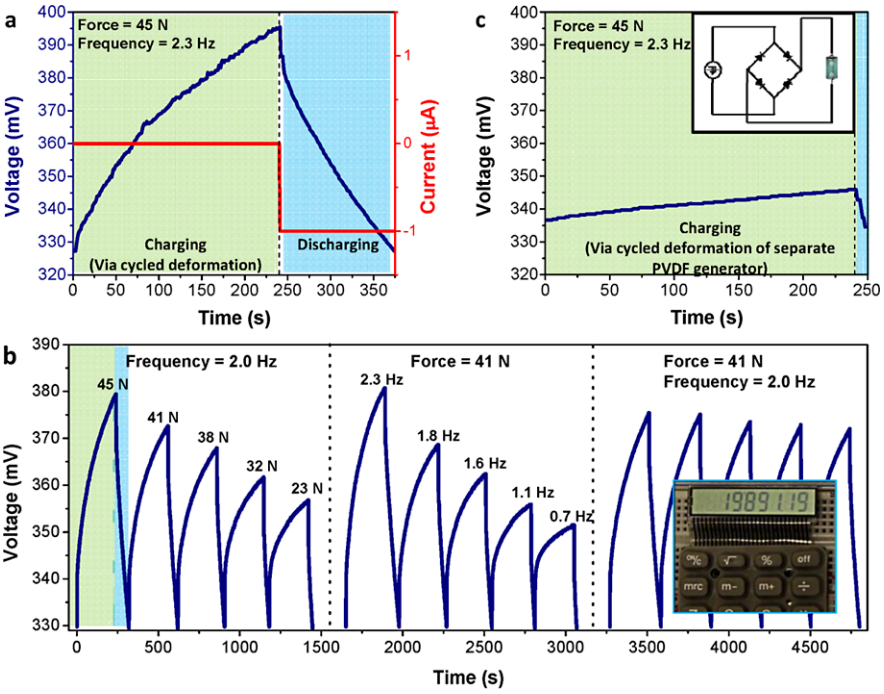

Fig. 11.7 Self-charging process of SCPC under periodic compressive straining and the corresponding discharging process. (**a**) A typical self-charging process simply by applying cycled mechanical compressive strain to the device (green shadowed region), during which the voltage keeps raising, but the current flowing through an external load connected between the cathode and anode remains almost zero, indicating that the charging process is accomplished by the migration of the Li ions in the internal circuit rather than the flow of electrons in the external load. In the discharge process (blue shadowed region), the stored power is released in the form of electron flow in the external load as indicated by the measured current and drop of voltage. (**b**) Self-charging and discharge cycles of SCPC under different force and frequencies, respectively. Note that the force indicated in the figure was the force applied to the entire device, most of which was consumed at the stainless shell of the cell; only a very small fraction of the force reached the PVDF. The inset shows the operation of a commercial calculator using the SCPCs as the power source. (**c**) As a comparison of efficiency, the SCPC is separated into two individual units: a PVDF piezoelectric generator and a Li-ion battery by using PE as a separator. This plot shows the voltage across the battery as being charged by the generator for 4 min under the same conditions as for (**a**), followed by a discharge process under the current of 1 μA. The inset is a schematic circuit of the traditional charging methods with separated generator and storage units connected by a bridge rectifier [6]

creased from 327 to 395 mV in 240 s. After the self-charging process, the device was discharged back to its original voltage of 327 mV under a discharge current of 1 μA, which lasted for about 130 s. So we proved that the proposed power cell can be charged up under the repeated deformation by directly converting mechanical energy to chemical energy. In this experimental case, the stored electric capacity of the power cell was about 0.036 μAh.

From the theory of piezoelectricity, within elastic deformation regime, the magnitude of the piezopotential is linearly proportional to the magnitude of strain, thus also to the magnitude of the compressive force. Figure 11.7(b) shows that, as we solely increased the mechanical force applied to the device, the self-charging effect would be enhanced. Thus, an increased piezopotential can give an enhanced charging effect. In addition, the self-charging effect is also affected by the frequency at which the deformation is applied, as shown in Fig. 11.7(b). Under a constant applied force of impact, a higher frequency resulted in an increased charging voltage simply due to higher input power. When the force and the frequency were both kept constant, the rate at which the voltage was increased was relatively stable. The above results are additional proofs that the self-charging process is due to the piezoelectric effect. We have demonstrated that a series connection of several SCPCs drove the operation of a commercial calculator for more than ten minutes, as shown in the inset of Fig. 11.7(b).

The overall efficiency of our proposed SCPC has two parts—the energy converting efficiency of piezoelectric material and the energy storage efficiency of this mechanical-to-electrochemical process. We compared this with the efficiency of the traditional charging method, which is composed of a separated generator and a storage unit connected though a bridge rectifier (inset of Fig. 11.7(c)). The generator unit was fabricated by sealing the PVDF film in the same coin cell to create a similar straining condition as SCPC. After being charged for 4 min via cycled deformation of the separate PVDF generator, the voltage of the battery has only increased by ∼10 mV (Fig. 11.7(c)), which is a lot lower than that of SCPC (65 mV) (Fig. 11.7(a)). Therefore, the single mechanical to chemical process for SCPC is much more efficient than the mechanical to electric and then electrical to chemical double-processes for charging a traditional battery. This is because our current study demonstrated a new approach for directly converting mechanical energy into chemical energy without going through the generation of electricity as an intermediate state, which saves at least the energy wasted on the outer circuitry, including the rectifying component. This is the innovation of the power cell. In practice, an accurate estimation of the efficiency is largely affected by a number of factors. First, the rigid stainless-steel coin cell, which consumed a large portion of mechanical energy. Second, an accumulation of deformation in PVDF piezoelectric polymer film made it beyond the range of elastic deformation, thus the piezoelectric potential could be degraded a lot. Therefore, through improvement of the device structure and packaging methods, and also using piezoelectric material with higher piezo-coefficient, the performance of the SCPC could be largely enhanced in the future.

As a comparison and control experiment, we measured the response of a conventional Li-ion battery under the same deformation condition, which had the same structure as the power cell except using PE film as the separator instead of the piezoelectric PVDF film. As shown in Fig. 11.8(a), the voltage remained the same at ∼325 mV during the ∼4000 cycles of deformation that lasted for ∼0.5 hour. Thus, the conventional Li-ion battery cannot be charged up at all by applying cycled mechanical deformation. This is because there is no piezoelectric potential that drives

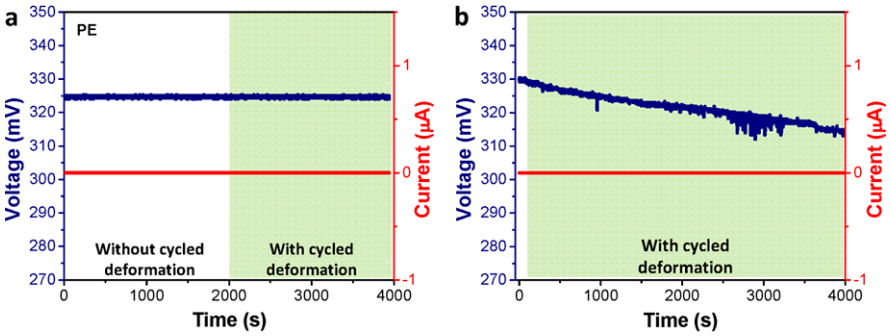

Fig. 11.8 Response of devices of a similar structure as the self-charging power cell, but with different films as separators. (**a**) For a conventional Li-ion battery using PE as the separator, no charging effect is observed by applying cycled mechanical deformation, indicating that the result presented in Fig. 11.7(a) is due to the piezoelectric driven charging process. (**b**) For a device that has the same structure as a SCPC but with the PVDF film having a piezoelectric field pointing from anode to cathode, we have no charging effect either, just as expected from the mechanism presented in Fig. 11.5 [6]

the migration of Li ions. This comparison experiment rules out the possible contribution from the electrostatic noise or the measurement system to the charging process presented in Fig. 11.5(a) for SCPC.

Alternatively, if the piezoelectric polarization as presented in Fig. 11.5 is reversed, the piezoelectric field in the PVDF film is pointing from anode to cathode, which is unable to drive the migration of Li ions from cathode to anode, so that the entire device will not be charged even after many cycles of mechanical deformation. The response of the device fabricated using PVDF film with opposite polarization was measured under the same deformation condition, as shown in Fig. 11.8(b). The voltage slightly decreased from 330 to 315 mV during the ~8000 cycles of deformation that lasted for ~1.1 hour. There was no charging behavior in such a device simply because the piezopotential drove Li ions to migrate in the opposite direction of the charging process, which further confirmed the working principle of the SCPC as proposed in Fig. 11.5.

11.5 Summary

In summary, a new mechanical-to-electrochemical process is proposed by integrating piezoelectric material with an electrochemical system, using which an approach for fabricating a self-charging power cell is demonstrated for converting and simultaneously storing mechanical energy directly as chemical energy, with a significantly higher overall efficiency than the traditional charging method composed of two separated units. By replacing the PE separator as for conventional Li battery with a piezoelectric PVDF film, the piezoelectric potential from the PVDF film created under straining acts as a charge pump to drive Li ions migrating from the

cathode to the anode accompanying with charging reactions at electrodes, which can be defined as a piezo-electrochemical process. Using the mechanism demonstrated here, we have hybridized a generator with a battery for the first time as a sustainable power source. It provides an innovative approach for developing new energy technology for driving personal electronics and self-powered systems.

References

1. J. Shi, M.B. Starr, H. Xiang, Y. Hara, M.A. Anderson, J.H. Seo, Z. Ma, X.D. Wang, Interface engineering by piezoelectric potential in ZnO-based photoelectrochemical anode. Nano Lett. **11**(12), 5587–5593 (2011)
2. C.K. Chan, H.L. Peng, G. Liu, K. McIlwrath, X.F. Zhang, R.A. Huggins, Y. Cui, High-performance lithium battery anodes using silicon nanowires. Nat. Nanotechnol. **3**, 31–35 (2008)
3. Y. Idota, T. Kubota, A. Matsufuji, Y. Maekawa, T. Miyasaka, Tin-based amorphous oxide: a high-capacity lithium-ion-storage material. Science **276**, 1395–1397 (1997)
4. J.M. Tarascon, M. Armand, Issues and challenges facing rechargeable lithium batteries. Nature **414**, 359–367 (2001)
5. M. Wakihara, O. Yamamoto (eds.), *Lithium Ion Batteries: Fundamentals and Performance* (Kodansha Ltd./Wiley-VCH, Tokyo/Weinheim, 1998), pp. 1–10
6. X.Y. Xue, S.H. Wang, W.X. Guo, Y. Zhang, Z.L. Wang, Hybridizing energy conversion and storage in a mechanical-to-electrochemical process for self-charging power cell. Nano Lett. **12**, 2520–2523 (2012)

Appendix
Published Journal Articles by Wang's Group on Nanogenerators and Piezotronics (2006–2012)

2012

[1] Y. Yang, Y. Zhou, J.M. Wu, Z.L. Wang, Single micro/nanowire pyroelectric nanogenerators as self-powered temperature sensors. ACS Nano

[2] G. Zhu, C. Pan, W. Guo, C.-Y. Chen, Y. Zhou, R. Yu, Z.L. Wang, Triboelectric-generator-driven pulse electrodeposition for micro-patterning. Nano Lett.

[3] N. Cui, S. Bai, W. Wu, L. Meng, Z.L. Wang, Y. Zhao, L. Jiang, Y. Qin, Magnetic force driven nanogenerators as a non-contact energy harvester and sensor. Nano Lett. **12**, 3701–3705 (2012)

[4] J.M. Wu, C. Xu, Y. Zhang, Y. Yang, Y. Zhou, Z.L. Wang, Flexible and transparent nanogenerator based on a composite of lead-free $ZnSnO_3$ triangular-belts. Adv. Mater.

[5] X. Xue, S. Wang, W. Guo, Y. Zhang, Z.L. Wang, Hybridizing energy conversion and storage in a mechanical-to-electrochemical process for self-charging power cell. Nano Lett. **12**, 2520–2523 (2012)

[6] J.H. Jung, C.-Y. Chen, B.K. Yun, N. Lee, Y. Zhou, W.Jo, L.-J. Chou, Z.L. Wang, Lead-free $KNbO_3$ ferroelectric nanorods based flexible nanogenerators and capacitors. Nanotechnology

[7] Z.L. Wang, Preface to the special section on piezotronics. Adv. Mater.

[8] L. Lin, Y. Hu, C. Xu, Y. Zhang, R. Zhang, X. Wen, Z.L. Wang, Transparent flexible nanogenerator as self-powered sensor for transportation monitoring. Nano Energy

[9] Y. Yang, J.H. Jung, B.K. Yun, F. Zhang, K.C. Pradel, W. Guo, Z.L. Wang, Flexible pyroelectric nanogenerators using a composite structure of lead-free $KNbO_3$ nanowires. Adv. Mater. **2012**, 5357–5362 (2012)

[10] Y. Yang, K.C. Pradel, Q. Jing, J.M. Wu, F. Zhang, Y. Zhou, Y. Zhang, Z.L. Wang, Thermoelectric nanogenerators based on single Sb-doped ZnO micro/nanobelts. ACS Nano **6**, 6984–6989 (2012)

[11] R. Zhang, L. Lin, Q. Jing, W. Wu, Y. Zhang, Z. Jiao, L. Yan, R.P.S. Han, Z.L. Wang, Nanogenerators as active sensor for vortex capture and air-flow velocity detection. Energy Environ. Sci. **5**, 8528–8533 (2012)

[12] L. Dong, S. Niu, C. Pan, R. Yu, Y. Zhang, Z.L. Wang, Piezo-phototronic effect of CdSe nanowires. Adv. Mater.

[13] Y.S. Zhou, K. Wang, W. Han, S.C. Rai, Y. Zhang, Y. Ding, C. Pan, F. Zhang, W. Zhou, Z.L. Wang, Vertically aligned CdSe nanowire arrays for energy harvesting and piezotronic devices. ACS Nano **6**, 6231–6235 (2012)

DOI 10.1007/978-3-642-34237-0, © Springer-Verlag Berlin Heidelberg 2012

[14] Y. Hu, Y. Zhang, L. Lin, Y. Ding, G. Zhu, Z.L. Wang, Piezo-phototronics effect on electroluminescence properties of p-type GaN thin films. Nano Lett. **12**, 3851–3856 (2012)
[15] Z.L. Wang, W. Wu, Nano-enabled energy harvesting for self-powered micro/nano-systems (invited review), Angew. Chem.
[16] S. Lee, J.-I. Hong, C. Xu, M. Lee, D. Kim, L. Lin, W. Hwang, Z.L. Wang, Toward robust nanogenerator using aluminum substrate. Adv. Mater.
[17] Z.L. Wang, From nanogenerators to piezotronics—a decade study of ZnO nanostructures. MRS Bull.
[18] W. Guo, F. Zhang, C. Lin, Z.L. Wang, Direct growth of TiO_2 nanosheet arrays on carbon fibers for high efficient photocatalytic degradation of methyl orange. Adv. Mater.
[19] N. Cui, S. Bai, W. Wu, L. Meng, Z.L. Wang, Y. Zhao, L. Jiang, Y. Qin, Magnetic force driven nanogenerators as a non-contact energy harvester and sensor. Adv. Mater.
[20] W. Wu, S. Bai, M. Yuan, Y. Qin, Z.L. Wang, T. Jing, PZT nanowire textile nanogenerator for wearable energy harvesting and self-powered devices. ACS Nano
[21] R. Yu, L. Dong, C. Pan, S. Niu, H. Liu, W. Liu, S. Chua, D. Chi, Z.L. Wang, Piezotronic effect on the transport property of GaN nanobelt for active flexible electronics. Adv. Mater. **24**, 3532–3537 (2012)
[22] Y. Zhang, Z.L. Wang, Theory of piezo-phototronics for light emitting diode. Adv. Mater. **24**, 4712–4718 (2012)
[23] Z.L. Wang, Progress in piezotronics and piezo-phototronics. Adv. Mater. **24**, 4632–4646 (2012)
[24] C. Pan, S. Niu, Y. Ding, L. Dong, R. Yu, Y. Liu, G. Zhu, Z.L. Wang, Enhanced Cu_2S/CdS coaxial nanowire solar cells by piezo-phototronic effect. Nano Lett. **12**, 3302–3307 (2012)
[25] Y. Yang, W. Guo, K.C. Pradel, G. Zhu, Y. Zhou, Y. Zhang, Y. Hu, L. Lin, Z.L. Wang, Pyroelectric nanogenerators for harvesting thermoelectric energy. Nano Lett. **12**, 2833–2838 (2012)
[26] F.-R. Fan, L. Lin, G. Zhu, W. Wu, R. Zhang, Z.L. Wang, Transparent triboelectric nanogenerators and self-powered pressure sensors based on micro-patterned plastic films. Nano Lett. **12**, 3109–3114 (2012)
[27] W. Han, Y. Zhou, Y. Zhang, C.-Y. Chen, L. Lin, X. Wang, S. Wang, Z.L. Wang, Strain-gated piezotronic transistors based on vertical zinc oxide nanowires. ACS Nano **6**, 3760–3766 (2012)
[28] G. Zhu, A.C. Wang, Y. Liu, Y. Zhou, Z.L. Wang, Functional electrical stimulation by nanogenerator with 58 V output voltage. Nano Lett. **12**, 3086–3090 (2012)
[29] C. Pan, W. Guo, L. Dong, G. Zhu, Z.L. Wang, Optical-fiber based core-shell coaxially structured hybrid cell for self-powered nanosystems. Adv. Mater. **24**, 3356–3361 (2012)
[30] J.M. Wu, C.-Y. Chen, Y. Zhang, K.-H. Chen, Y. Yang, Y. Hu, J.-H. He, Z.L. Wang, Ultrahigh sensitive piezotronic strain sensors based on $ZnSnO_3$ nanowire/microwire. ACS Nano **6**, 4369–4374 (2012)
[31] J.M. Wu, C. Xu, Y. Zhang, Z.L. Wang, Lead-free nanogenerator made from single $ZnSnO_3$ microbelt. ACS Nano **6**, 4335–4340 (2012)
[32] C.-Y. Chen, T.-H. Liu, J. Song, Y. Zhou, Y. Zhang, Y. Hu, S. Wang, L. Lin, W. Han, Y.-L. Chueh, Y.-H. Chu, J.-H. He, Z.L. Wang, Electricity generation based on vertically aligned $PbZr_{0.2}Ti_{0.8}O_3$ nanowire arrays. Nano Energy **1**, 424–428 (2012)
[33] K.-I. Park, M. Lee, Y. Liu, S. Moon, G.-T. Hwang, G. Zhu, J.E. Kim, S.O. Kim, D.K. Kim, Z.L. Wang, K.J. Lee, Flexible nanocomposite generator made of $BaTiO_3$ nanoparticles and graphitic carbons. Adv. Mater. **24**, 2999–3004 (2012)
[34] A. Yu, P. Jiang, Z.L. Wang, Nanogenertor as self-powered vibration sensor. Nano Energy **1**, 418–423 (2012)
[35] M. Lee, C.-Y. Chen, S. Wang, S.N. Cha, J.M. Kim, L.-J. Chou, Z.L. Wang, Hybrid piezoelectric structure for wearable nanogenerator. Adv. Mater. **24**, 1759–1764 (2012)

[36] K.Y. Lee, B. Kumar, J.-S. Seo, K.-H. Kim, J.I. Sohn, S.N. Cha, D. Choi, Z.L. Wang, S.-W. Kim, p-Type polymer-hybridized high-performance piezoelectric nanogenerators. Nano Lett. **12**, 1959–1964 (2012)
[37] Y. Zhang, Y. Yang, Z.L. Wang, Piezo-phototronics effect on nano/microwire solar cell. Energy Environ. Sci. **5**, 6850–6856 (2012)
[38] Y.-Z. Chen, T.-H. Liu, C.-Y. Chen, C.-H. Liu, S.-Y. Chen, W.-W. Wu, Z.L. Wang, J.-H. He, Y.-H. Chu, Y.-L. Chueh, Taper $PbZr_{0.2}Ti_{0.8}O_3$ nanowire arrays: from controlled growth by pulsed laser deposition to piezopotential measurements. ACS Nano **6**(3), 2826–2832 (2012)
[39] Y. Liu, Q. Yang, Y. Zhang, Z. Yang, Z.L. Wang, Nanowire piezo-phototronic photodetector: theory and experimental design. Adv. Mater. **24**, 1410–1417 (2012)
[40] F. Fan, Z.-Q. Tian, Z.L. Wang, Flexible triboelectric generator, Nano Energy **1**, 328–324 (2012)
[41] C. Xu, C. Pan, Y. Liu, Z.L. Wang, Hybrid cells for simultaneously harvesting multi-type energies for self-powered micro/nanosystems (review). Nano Energy **1**, 259–272 (2012)
[42] J.H. Jung, M. Lee, J.-I. Hong, Y. Ding, C.-Y. Chen, L.-J. Chou, Z.L. Wang, Lead-free $NaNbO_3$ nanowires for high output piezoelectric nanogenerator. ACS Nano **5**, 10041–10046 (2011)
[43] Y. Hu, L. Lin, Y. Zhang, Z.L. Wang, Replacing battery by a nanogenerator with 20 V output. Adv. Mater. **24**, 110–114 (2012)

2011

[44] Z.L. Wang, Self-powered nanodevices and nanosystems. Adv. Mater. **24**, 280–285 (2011)
[45] S.N. Cha, S.M. Kim, H.J. Kim, J.Y. Ku, J.I. Sohn, Y.J. Park, B.G. Song, M.H. Jung, E.K. Lee, B.L. Choi, J.J. Park, Z.L. Wang, J.M. Kim, K. Kim, Porous PVDF as effective sonic wave driven nanogenerators. Nano Lett. **11**, 5142–5147 (2011)
[46] D. Choi, M.-J. Jin, K.Y. Lee, S.-G. Ihn, S. Yun, X. Bulliard, W. Choi, S.Y. Lee, S.-W. Kim, J.-Y. Choi, J.M. Kim, Z.L. Wang, Flexible hybrid multi-type energy scavenger. Energy Environ. Sci. **4**, 4607–4613 (2011)
[47] C. Pan, Z. Li, W. Guo, J. Zhu, Z.L. Wang, Fiber-based hybrid nanogenerators for/as self-powered systems in bio-liquid. Angew Chem. **50**, 11192–11196 (2011)
[48] L. Lin, C.-H. Lai, Y. Hu, Y. Zhang, X. Wang, C. Xu, R.L. Snyder, L.-J. Chen, Z.L. Wang, High output nanogenerator based on assembly of tapered GaN nanowires, Nanotechnology **22**, 475401 (2011)
[49] Y. Yang, W. Guo, Y. Zhang, Y. Ding, X. Wang, Z.L. Wang, Piezotronic effect on the output voltage of P3HT/ZnO micro/nanowire heterojunction solar cells. Nano Lett. **11**, 4812–4817 (2011)
[50] C.-Y. Chen, J.-H. Huang, J. Song, Y. Zhou, L. Lin, P.-C. Huang, C.-P. Liu, Y. Zhang, J.-H. He, Z.L. Wang, Anisotropic outputs of nanogenerator from oblique-aligned ZnO nanowire arrays. ACS Nano **5**, 6707–6713 (2011)
[51] Q. Yang, W. Wang, S. Xu, Z.L. Wang, Enhancing light emission of ZnO microwire-based diodes by piezo-phototronic effect. Nano Lett. **11**, 4012–4017 (2011)
[52] Y. Hu, C.Xu, Y. Zhang, L. Lin, R.L. Snyder, Z.L. Wang, Nanogenerator for energy harvesting from a rotating tire and its application as a self-powered pressure/speed sensor. Adv. Mater. **23**, 4068 (2011)
[53] M. Lee, J. Bae, J. Lee, C.-S. Lee, S. Hong, Z.L. Wang, Self-powered environmental sensor system driven by nanogenerators. Energy Environ. Sci. **4**, 3359–3363 (2011)
[54] Y. Hu, Y. Zhang, C. Xu, L. Lin, R.L. Snyder, Z.L. Wang, Self-powered system with wireless data transmission. Nano Lett. **11**, 2572–2577 (2011)
[55] G. Romano, G. Mantini, A. Di Carlo, A. D'Amico, C. Falconi, Z.L. Wang, Piezoelectric potential in vertically aligned nanowires for high output nanogenerators. Nanotechnology **22**, 465401 (2011)

[56] W. Wu, Z.L. Wang, Piezotronic nanowire based resistive switches as programmable electromechanical memories. Nano Lett. **11**, 2779–2885 (2011)
[57] Y. Zhang, Y. Liu, Z.L. Wang, Fundamental theory of piezotronics. Adv. Mater. **23**, 3004–3013 (2011)
[58] A. Yu, H. Li, H. Tang, T. Liu, P. Jiang, Z.L. Wang, Vertically integrated nanogenerator based on ZnO nanowire arrays. Phys. Status Solidi, Rapid Res. Lett. **5**, 162–164 (2011)
[59] C. Xu, Z.L. Wang, Compacted hybrid cell made by nanowire convoluted structure for harvesting solar and mechanical energies. Adv. Mater. **23**, 873–877 (2011)
[60] J. Bae, M.K. Song, Y.J. Park, J.M. Kim, M. Liu, Z.L. Wang, Fiber supercapacitors made of nanowire-fiber hybrid structure for wearable/stretchable energy storage. Angew. Chem. **123**, 1721–1725 (2011)
[61] M. Riaz, J.H. Song, O. Nur, Z.L. Wang, M. Willander, Experimental and finite element method calculation of piezoelectric power generation from ZnO nanowire arrays grown on different substrates using high and low temperature methods. Adv. Funct. Mater. **21**, 623–628 (2011)
[62] Z. Li, Z.L. Wang, Air/liquid pressure and heartbeat driven flexible fiber nanogenerators as micro-nano-power source or diagnostic sensors. Adv. Mater. **23**, 84–89 (2011)

2010

[63] C. Pan, Y. Fang, A. Mashkoor, Z. Luo, J. Xie, L. Wu, Z.L. Wang, J. Zhu, Generating electricity from biofluid with a nanowire-based biofuel cell for self-powered nanodevices. Adv. Mater. **22**, 5388–5392 (2010)
[64] K.-I. Park, S. Xu, Y. Liu, G.T. Hwang, S.-J.L. Kang, Z.L. Wang, K.J. Lee, Piezoelectric $BaTiO_3$ thin film nanogenerator on plastic substrates. Nano Lett. **10**, 4939–4943 (2010)
[65] Y. Hu, Y. Zhang, C. Xu, G. Zhu, Z.L. Wang, High output nanogenerator by rational unipolar-assembly of conical-nanowires and its application for driving a small liquid crystal display. Nano Lett. **10**, 5025–5031 (2010)
[66] S. Xu, B.J. Hansen, Z.L. Wang, Piezoelectric-nanowire enabled power source for driving wireless microelectronics. Nature Commun. **1**, 93 (2010)

[67] Z.L. Wang, Piezopotential gated nanowire devices: piezotronics and piezo-phototronics. Nano Today **5**, 540–552 (2010)

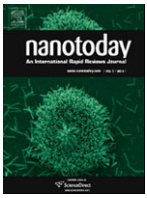

[68] Z.L. Wang, Toward self-powered sensor network. Nano Today **5**, 512–514 (2010)

[69] M.-T. Chen, M.-P. Lu, Y.-J. Wu, C.-Y. Lee, M.-Y. Lu, Y.-C. Chang, L.-J. Chou, Z.L. Wang, L.-J. Chen, Electroluminescence from in-situ doped p–n homojuncioned ZnO nanowire array. Nano Lett. **10**, 4387–4393 (2010)
[70] Z.L. Wang, R. Yang, J. Zhou, Y. Qin, C. Xu, Y. Hu, S. Xu, Lateral nanowire/nanobelt based nanogenerators, piezotronics and piezo-phototronics. Mater. Sci. Eng. Rep. **R70**(3–6), 320–329 (2010)

[71] W. Wu, Y. Wei, Z.L. Wang, Strain-gated piezotronic logic nanodevices. Adv. Mater. **22**, 4711–4715 (2010)
[72] Q. Yang, X. Guo, W. Wang, Y. Zhang, S. Xu, D.H. Lien, Z.L. Wang, Enhancing sensitivity of a single ZnO micro/nanowire photodetector by piezo-phototronic effect. ACS Nano **4**, 6285–6291 (2010)
[73] 王中林 "微纳系统中的可持续自供型电源 - 能源研究中的新兴领域". 科学通报 **55**, 2472–2475 (2010)
[74] C.-T. Huang, J. Song, C.-M. Tsai, W.-F. Lee, D.-H. Lien, Z. Gao, Y. Hao, L.-J. Chen, Z.L. Wang, Single-InN-nanowire nanogenerator with up to 1 V output voltage. Adv. Mater. **36**, 4008–4013 (2010)
[75] 王中林 "压电电子学和压电光电子学". 物理 **39**, 556–557 (2010)
[76] J. Song, H. Xie, W. Wu, V.R. Joseph, C.F.J. Wu, Z.L. Wang, Robust optimizing of the output voltage of nanogenerators by statistical experimental design. Nano Res. **3**, 613–619 (2010)
[77] M. Lee, R. Yang, C. Li, Z.L. Wang, Nanowire-quantum dot hybridized cell for harvesting sound and solar energies. J. Phys. Chem. Lett. **1**, 2929–2935 (2010)
[78] Y. Wei, W. Wu, R. Guo, D. Yuan, S. Das, Z.L. Wang, Wafer-scale high-throughput ordered growth of vertically aligned ZnO nanowire arrays. Nano Lett. **10**, 3414–3419 (2010)
[79] J. Han, F. Fan, C. Xu, S. Lin, M. Wei, X. Duan, Z.L. Wang, ZnO nanotube-based dye-sensitized solar cell and its application in self-powered devices. Nanotechnology **21**, 405203 (2010)
[80] W. Liu, M. Lee, L. Ding, J. Liu, Z.L. Wang, Piezopotential gated nanowire–nanotube hybrid field-effect transistor. Nano Lett. **10**, 3084–3089 (2010)
[81] G. Zhu, R. Yang, S. Wang, Z.L. Wang, Flexible high-output nanogenerator based on lateral ZnO nanowire array. Nano Lett. **10**, 3151–3155 (2010)
[82] Y. Zhang, Y. Hu, S. Xiang, Z.L. Wang, Effects of piezopotential spatial distribution on local contact dictated transport property of ZnO micro/nanowires. Appl. Phys. Lett. **97**, 033509 (2010)
[83] B.J. Hansen, Y. Liu, R. Yang, Z.L. Wang, Hybrid nanogenerator for concurrently harvesting biomechanical and biochemical energy. ACS Nano **4**, 3647–3652 (2010)
[84] Y. Hu, Y. Zhang, Y. Chang, R.L. Snyder, Z.L. Wang, Optimizing the power output of a ZnO photocell by piezopotential. ACS Nano **4**, 4220–4224 (2010); corrections: **4**, 4962–4962 (2010)
[85] Z. Li, G. Zhu, R. Yang, A.C. Wang, Z.L. Wang, Muscle driven in-vivo nanogenerator. Adv. Mater. **22**, 2534–2537 (2010)

[86] X.B. Wang, J.H. Song, F. Zhang, C.Y. He, Z. Hu, Z.L. Wang, Electricity generation based on one-dimensional group-III nitride nanomaterials. Adv. Mater. **22** (2010) 2155–2158.
[87] S. Xu, Y. Qin, C. Xu, Y. Wei, R. Yang, Z.L. Wang, Self-powered nanowire devices. Nat. Nanotechnol. **5**, 366–373 (2010)

[88] Z.L. Wang, Piezotronic and piezo-phototronic effects. J. Phys. Chem. Lett. **1**, 1388–1393 (2010)
[89] C.-T. Huang, J. Song, W.-F. Lee, Y. Ding, Z. Gao, Y. Hao, L.-J. Chen, Z.L. Wang, GaN nanowire arrays for high-output nanogenerators. J. Am. Chem. Soc. **132**, 4766–4771 (2010)
[90] Y. Hu, Y. Chang, P. Fei, R.L. Snyder, Z.L. Wang, Designing the electric transport characteristics of ZnO micro/nanowire devices by coupling piezoelectric and photoexcitation effects. ACS Nano **4**, 1234–1240 (2010)

2009

[91] Z.L. Wang, Ten years' venturing in ZnO nanostructures: from discovery to scientific understanding and to technology applications. Chin. Sci. Bull. **54**, 4021–4034 (2009)
[92] P. Fei, P.-H. Yeh, J. Zhou, S. Xu, Y. Gao, J. Song, Y. Gu, Y. Huang, Z.L. Wang, Piezoelectric-potential gated field-effect transistor based on a free-standing ZnO wire. Nano Lett. **9**, 3435–3439 (2009)
[93] Z. Gao, Y. Ding, S. Lin, Y. Hao, Z.L. Wang, Dynamic fatigue studies of ZnO nanowires by in-situ transmission electron microscopy. Phys. Status Solidi, Rapid Res. Lett. **3**, 260–262 (2009)
[94] S.S. Lin, J.H. Song, Y.F. Lu, Z.L. Wang, Identifying individual n- and p-type ZnO nanowires by the output voltage sign of piezoelectric nanogenerator. Nanotechnology **20**, 365703 (2009)
[95] G. Mantini, Y. Gao, A. D'Amico, C. Falconi, Z.L. Wang, Equilibrium piezoelectric potential distribution in a deformed ZnO nanowire. Nano Res. **2**, 624–629 (2009)
[96] Y. Hu, Y. Gao, S. Singamaneni, V.V. Tsukruk, Z.L. Wang, Converse piezoelectric effect induced transverse deflection of a free-standing ZnO microbelt. Nano Lett. **9**, 2661–2665 (2009)
[97] Z. Gao, J. Zhou, Y. Gu, P. Fei, Y. Hao, G. Bao, Z.L. Wang, Effects of piezoelectric potential on the transport characteristics of metal–ZnO nanowire–metal field effect transistor. J. Appl. Phys. **105**, 113707 (2009)
[98] C. Falconi, G. Mantini, A. D'Amico, Z.L. Wang, Studying piezoelectric nanowires and nanowalls for energy harvesting. Sens. Actuator B **139**, 511–519 (2009)
[99] C. Xu, X. Wang, Z.L. Wang, Nanowire structured hybrid cell for concurrently scavenging solar and mechanical energies. J. Am. Chem. Soc. **131**, 5866–5872 (2009)
[100] Z.L. Wang, Energy harvesting using piezoelectric nanowires—comment on "Energy harvesting using nanowires?" by Alexe et al. Adv. Mater. **21**, 1311–1315 (2009)
[101] Z.L. Wang, ZnO nanowire and nanobelt platform for nanotechnology (review). Mater. Sci. Eng. Rep. **64**(3–4), 33–71 (2009)

[102] M.-P. Lu, J. Song, M.-Y. Lu, M.-T. Chen, Y. Gao, L.-J. Chen, Z.L. Wang, Piezoelectric nanogenerator using p-type ZnO nanowire arrays. Nano Lett. **9**, 1223–1227 (2009)
[103] R. Yang, Y. Qin, C. Li, G. Zhu, Z.L. Wang, Converting biomechanical energy into electricity by muscle/muscle driven nanogenerator. Nano Lett. **9**, 1201–1205 (2009)
[104] Y. Gao, Z.L. Wang, Equilibrium potential of free charge carriers in a bent piezoelectric semiconductive nanowire. Nano Lett. **9**, 1103–1110 (2009)
[105] X. Wang, Y. Gao, Y. Wei, Z.L. Wang, The output of ultrasonic-wave driven nanogenerator in a confined tube. Nano Res. **2**, 177–182 (2009)
[106] R. Yang, Y. Qin, C. Li, L. Dai, Z.L. Wang, Characteristics of output voltage and current of integrated nanogenerators. Appl. Phys. Lett. **94**, 022905 (2009)
[107] R. Yang, Y. Qin, L. Dai, Z.L. Wang, Flexible charge-pump for power generation using laterally packaged piezoelectric-wires. Nat. Nanotechnol. **4**, 34–39 (2009)

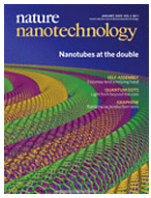

2008

[108] S. Xu, Y. Wei, J. Liu, R. Yang, Z.L. Wang, Integrated multilayer-nanogenerator fabricated using paired nanotip-to-nanowire brushes. Nano Lett. **8**, 4027–4032 (2008)
[109] J. Zhou, P. Fei, Y. Gu, W. Mai, Y. Gao, R. Yang, G. Bao, Z.L. Wang, Piezoelectric-potential-controlled polarity-reversible Schottky diodes and switches of ZnO wires. Nano Lett. **8**, 3973–3977 (2008)
[110] Z.L. Wang, Towards self-powered nanosystems: from nanogenerators to nanopiezotronics (feature article). Adv. Funct. Mater. **18**, 3553–3567 (2008)
[111] J. Zhou, Y. Gu, P. Fei, W. Mai, Y. Gao, R. Yang, G. Bao, Z.L. Wang, Flexible piezotronic strain sensor. Nano Lett. **8**, 3035–3040 (2008)
[112] J. Zhou, P. Fei, Y. Gao, Y. Gu, J. Liu, G. Bao, Z.L. Wang, Mechanical-electrical triggers and sensors using piezolelectric microwires/nanowires. Nano Lett. **8**, 2725–2730 (2008)
[113] Y.-F. Lin, J. Song, D. Yong, S.-Y. Lu, Z.L. Wang, Alternating the output of CdS-nanowire nanogenerator by white-light stimulated optoelectronic effect. Adv. Mater. **20**, 3127–3130 (2008)
[114] Z.L. Wang, Energy harvesting for self-powered nanosystems (review). Nano Res. **1**, 1–8 (2008)
[115] J. Liu, P. Fei, J. Zhou, R. Tummala, Z.L. Wang, Toward high output-power nanogenerator. Appl. Phys. Lett. **92**, 173105 (2008)

[116] Z.L. Wang, Oxide nanobelts and nanowires—growth, properties and applications (review). J. Nanosci. Nanotechnol. **8**, 27–55 (2008)
[117] Y. Qin, X. Wang, Z.L. Wang, Microfiber–nanowire hybrid structure for energy scavenging. Nature **451**, 809–813 (2008)

[118] Y.-F. Lin, J. Song, Y. Ding, Z.L. Wang, S.-Y. Lu, Piezoelectric nanogenerator using CdS nanowires. Appl. Phys. Lett. **92**, 022105 (2008)
[119] Z.L. Wang, X. Wang, J. Song, J. Liu, Y. Gao, Piezoelectric nanogenerators for self-powered nanodevices. IEEE Pervasive Comput. **7**(1), 49–55 (2008)
[120] Z.L. Wang, Self-powering nanotech. Sci. Am. **298**(1), 82–87 (2008)

[121] J. Liu, P. Fei, J. Song, X. Wang, C. Lao, R. Tummala, Z.L. Wang, Carrier density and Schottky barrier on the performance of DC nanogenerator. Nano Lett. **8**, 328–332 (2008)
[122] J. Song, X. Wang, J. Liu, H. Liu, Y. Li, Z.L. Wang, Piezoelectric potential output from a ZnO wire functionalized with p-type oglimer. Nano Lett. **8**, 203–207 (2008)
[123] X. Wang, J. Liu, J. Song, Z.L. Wang, Integrated nanogenerators in bio-fluid. Nano Lett. **7**, 2475–2479 (2007)
[124] Y. Gao, Z.L. Wang, Electrostatic potential in a bent piezoelectric nanowire—the fundamental theory of nanogenerator and nanopiezotronics. Nano Lett. **7**, 2499–2505 (2007)
[125] X. Wang, J. Song, Jin Liu, Z.L. Wang, Direct current nanogenerator driven by ultrasonic wave. Science **316**, 102–105 (2007)

[126] Z.L. Wang , The new field of nanopiezotronics. Mater. Today **10**(5), 20–28 (2007)
[127] Z.L. Wang, Nanopiezotronics. Adv. Mater. **19**, 889–992 (2007)

[128] J.H. He, C.L. Hsin, L.J. Chen, Z.L. Wang, Piezoelectric gated diode of a single ZnO nanowire. Adv. Mater. **19**, 781–784 (2007)
[129] C.M. Lieber, Z.L. Wan, Functional nanowires. MRS Bull. **32**, 99–104 (2007)
[130] Z.L. Wang, Piezoelectric nanostructures: from novel growth phenomena to electric nanogenerators. MRS Bull. **32**, 109–116 (2007)
[131] P.X. Gao, J. Song, J. Liu, Z.L. Wang, Nanowire nanogenerators on plastic substrates as flexible power source. Adv. Mater. **19**, 67–72 (2007)

2006

[132] X. Wang, J. Zhou, J. Song, J. Liu, N. Xu, Z.L. Wang, Piezoelectric-field effect transistor and nano-force-sensor based on a single ZnO nanowire. Nano Lett. **6**, 2768–2772 (2006)
[133] J. Song, J. Zhou, Z.L. Wang, Piezoelectric and semiconducting dual-property coupled power generating process of a single ZnO belt/wire—a technology for harvesting electricity from the environment. Nano Lett. 6, 1656–1662 (2006)
[134] Z.L. Wang, J. Song, Piezoelectric nanogenerators based on zinc oxide nanowire arrays Science **312**, 242–246 (2006)

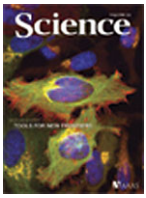

Index

Z.L. Wang, *Piezotronics and Piezo-Phototronics*, Microtechnology and MEMS,
DOI 10.1007/978-3-642-34237-0, © Springer-Verlag Berlin Heidelberg 2012